THE ANALYSIS OF FLOW ON ROUND-EDGED DELTA WINGS

By

SHABUDIN BIN MAT

Dissertation submitted to the Department of Aerospace Engineering, Faculty of Engineering, University of Glasgow, for the Degree of Philosophy

April 2010

To my wife Nor Haizan

To my children; Balqis, Ain & Shahmi

To my family in Perlis, Perak & Kuala Lumpur

PREFACE

The work described in this dissertation was carried out by the author in the Department of Aerospace Engineering of the University of Glasgow during the period October 2005 to March 2010; the dissertation is original in content except where otherwise stated.

Shabudin Bin Mat

April 2010

CONTENTS

List of Figures

List of Tables

ACKNOWLEDGEMENT

First and foremost, I owe an immerse debt of gratitude to my supervisor, Professor Frank N. Coton for his supervision over the past four years. With his support and advice, the research work was carried out smoothly. Without his firm guidance this thesis would never has materialized in anything resembling its present form. He brought me into the International Vortex Flow Experiment group. With his support and encouragement, I have an enjoyable and unforgettable working experienced in Glasgow University.

Secondly, I would like to express my appreciation to my second supervisor Professor Roderick Galbraith, who gave me very valuable suggestions, encouragement and spontaneous advice throughout my study. Professor Coton and Professor Galbraith are the best teachers I have ever had in my life. Keep up your good work.

Third, a special thank must be given to Dr. Richard Green who helped me during the Particle Image Velocimetry experiments. He gave me a very good lesson on how to conduct the PIV experiments for my research work

Fourth, special thanks must be given to Mr. Tony Smedley, Mr. Robert Gilmour, Mr. Ian Brown, Mr. Sandy Erwin, Mr. Alasdair Gilmour, Mr. John Kitching, Mr. Cameron Miller and Mr. Ian Scouller. Their help was very much appreciated and unforgettable. You are the best!!

Finally, I would like to thank my sponsors, the Islamic Development Bank and Universiti Teknologi Malaysia for their financial support throughout my study in Glasgow University.

The encouragement of my wife, my children and support from my family during the write up of the thesis is gratefully acknowledgement.

Thank you everyone.

Shabudin Bin Mat

April 2010

Glasgow, United Kingdom

ABSTRACT

The flow around three-dimensional aircraft wings, including delta-wings is very complicated. Much experimental and numerical work has been performed to discover its complexity. To date, all numerical calculations on delta wings have been carried out for either fully laminar or fully turbulent boundary layers. The transition status of the boundary layer is considered unknown despite several efforts to identify transition from laminar to turbulent flow. One such study, called the International Vortex Flow Experiment – 2 (VFE-2), has been carried out by an international group and mainly focuses on the boundary layers on delta wings. The data from the VFE-2 experimentals potentially provide the location of transition on the upper and lower surfaces of the wing to guide associated numerical studies. The effects of Reynolds number, Mach number, angle of attack and the leading edge bluntness are also investigated.

Almost all delta wing studies to date have involved tests on wings with sharp leading edges and these have led to the conclusion that the flows are relatively independent of Reynolds number. In fact, most real wings have finite leading edge radii. Hence, the flow separation is no longer fixed at the leading edge, thus making the flow dependent on Reynolds number. This particular aspect has been studied extensively by the VFE-2 team.

As part of the VFE-2 project, Glasgow University constructed a delta wing with four different sets of leading edges. Small-, medium- and large-radius edges and a pair of sharp leading edges were constructed in order to compare results from four delta wing configurations. In the current study experiments were carried out on these wings in the 2.65 metre by 2.04 metre, closed circuit, Argyll Wind tunnel of Glasgow University. The models were mounted on a specially designed sting support structure that allowed them to be pitched around a constant centre of rotation throughout the experiments. Tests were conducted at speeds of 20.63 m/s and 41.23 m/s representing Reynolds numbers of 1 x 10^6 & 2 x 10^6 respectively, based on the mean aerodynamic chords of the wings. The tests were conducted in three phases. In the first phase, steady and unsteady forces and moments on all wings were measured at an angle of attack that varied from $\alpha = 10^0$ to 25^0. The forces and moments were captured at two sampling rates; i.e., 100 Hz and 8000 Hz.

The second test series captured flow visualization data on the four wings. In these experiments, a mixture of Ondina oil and paraffin was combined with Dayglo powder and applied to the surfaces of the delta wings. The images of the flow topology on the wings were recorded. The final series of experiments involved Particle Image Velocimetry measurements. A stereo-PIV arrangement was applied in this experiment and two CCD-Cameras were positioned outside the test section for image capture.

The current study has identified interesting features of the interrelationship between the conventional leading edge primary vortex and the occurrence and development of the inner vortex on the round-edged delta wings. The inner vortex was first identified and verified by the VFE-2 team. The effects of Reynolds number, angle of attack and leading-edge radii on both vortices are discussed in detail. The steady balance data have shown that the normal force coefficients are sensitive to leading edge bluntness at moderate angles of attack but are less so at high angles of attack. In relation to this, the flow visualization images have also shown that the primary vortex origin is located further aft on the wing at higher leading edge bluntness. This impacts on the strength of the inner vortex which remains a significant flow feature until the primary vortex approaches the apex. The lateral extent of the inner vortex is very dependent on the primary vortex at the leading edge; i.e. the weakening of the primary vortex has positive effects on the inner vortex. Particle Image Velocimetry shows that the increase in leading edge bluntness significantly decreases the swirl magnitude of the primary vortex.

The results obtained from the current investigation provide considerable insight into the effects of Reynolds number, angle of attack and bluntness on the flow structures experienced by delta wings, with rounded leading edges. This work will, therefore, inform and guide future investigations of delta wing flows and has the potential to impact on future wing design.

NOMENCLATURE

a,b,c,d	Coefficient in first-blending function, φ
CO_2	Carbon Dioxide
C_A	Axial Force
C_D	Drag Force coefficient
C_p	Pressure coefficient
c_R	Wing root chord
C_M	Pitching Moment coefficient
C_N	Normal Force coefficient
d/b	The ration of first-blending function coefficients
f_e	Pitching frequency
f_n	Natural frequency of the vibration of the structure
F_1	Primary Vortex
F_y	Force in y-direction
F_z	Force in z-direction
K	Reduced frequency
L.E	Leading Edge
M	Mach Number
M_x	Wing pitching moment
NO_x	Nitrogen Oxide
PSD	Power Spectra Density
r_{LE}/c_R	Leading edge radius to wing chord ratio
R_{mac}	Reynolds number at mean aerodynamic chord
RL	Large-radius wing
RM	Medium-radius wing
RS	Small-radius wing
S	Sharp-edged wing
S_3	Primary attachment line
S_4	Secondary separation line

t/c_R	Wing thickness to wing chord ratio
u	Velocity component in x-direction
v	Velocity component in y-direction
w	Velocity component in z-direction
x/c_R	Chordwise distance from the Apex
y/c_R	Spanwise distance from the mid-wing
x	Coordinate set perpendicular with the y & z directions
y	Coordinate set perpendicular with the flow direction
z	Coordinate set parallel with the flow direction
α	Angle of Attack
$\alpha 1$, $\alpha 2$	Angle between camera view and Calibration plate
Λ	Delta wing sweep angle
ξ	No dimensional distance parameter, $(x - x_o)/ x_1$
φ	First blending function
x_1	Endpoint longitudinal coordinate of blending function, φ
x	Distance from apex, positive downstream
x_0	Initial longitudinal coordinate of blending function, φ
x_{le}	Longitudinal coordinate of the leading edge
AVT	Advanced Vehicle Technology
CAWAPI	Cranked Arrow Wing Aerodynamics Project International
CFD	Computational Fluid Dynamics
DES	Detached Eddy Simulation
DNS	Direct Numerical Simulation
DLR	Germany's National Research Centre for Aeronautics & Space
EADS	European Aerospace and Defence System
HSCT	High Speed Commercial Transport
KTH	Swedish Royal Institute of Technology
LDV	Laser-Doppler Velocimetry
LES	Large Eddy Simulation

LTPT	Low Turbulent Pressure Tunnel
NASA	National Aeronautics and Space Administration
NLR	Dutch National Aerospace Laboratory
PIV	Particle Image Velocimetry
PSP	Pressure Sensitive Paint
TAI	Turkish Aerospace Industries
USAFA	United States Air Force Academy
VFE-2	Vortex Flow Experiment - 2

Chapter 1

1.0 INTRODUCTION

1.1 Why Delta Wings?

In Aviation, the quest for ever faster speeds led to considerations of dart like wing planform shapes, broadly termed delta wings. The development of fighter aircraft in the 1940's was driven by the need for faster supersonic interceptor aircraft. The Delta wing shape had the advantage that the wing's leading edge remained behind the shock wave generated by the nose of the aircraft when flying at supersonic speed. A second advantage was that, as the angle of attack increased, leading edge vortices formed and these increased the lift of the aircraft and gave the delta wing a very high stall incidence. The concept of vortex lift exploitation has existed since the Second World War. The Concorde was conceived in 1950's and completely relied on vortex lift. An estimation concept of this vortex lift over thin wings was presented by Polhamus in 1966, using leading edge suction analogy. Underneath the leading-edge vortex, a high speed region induces a significant surface suction that can result in additional vortex-induced lift near the leading edge (Buchholz, 2000). Therefore, the actual lift on a delta wing at high angles of attack is dominated by separated vortical structures rather than by attached flow over the convex upper surface of a conventional wing. The lift continues to increase with angle of attack until the leading edge vortex breaks down at an angle of attack much higher than that for conventional wings (Gad El Hak & Ho, 1985). This concept has been applied to many fighter aircraft from the First World War Era to date.

Two English men, J.W Butler and E. Edwards were the first to patent a delta shaped wing with a fuselage in 1897. They proposed a delta wing configuration, fabricated from the wood, for their jet-like aircraft. The modern application of the delta wing, however, came from Alexander M. Lippisch who proposed a rocket fighter to operate in the supersonic region during the 1940s. Later he moved to the

United States and worked for the U.S Air Force on a similar project. The first flying aircraft with a delta wing was the Convair XF-92A. The aircraft was designed with an extremely large vertical tail in order to avoid the leading-edge vortices interfering with the function of the vertical tail. Unfortunately, this layout made the plane almost impossible to control. Another delta wing fighter aircraft was then introduced by Convair to improve the handling qualities. The YF-102 Delta Dagger was introduced in 1953 with a smaller horizontal tail. However, the aircraft produced an immense amount of wave-drag at sonic speed and that caused the aircraft to burn unacceptable large amounts of fuel to go faster. Re-development of the YF-102 was carried out after an accident involving the first prototype in October 1953. To overcome high drag loads at transonic speeds, Convair redesigned the fuselage and wing of YF-102 by introducing the "*area-rule*". This meant that the fuselage resembled a "coke bottle". This enabled reductions in wave-drag.

Other delta-winged aircraft were also developed in the UK, Russia and France during the "cold war". The development of a delta-winged bomber aircraft began in the UK in 1947 with the Avro Vulcan project. The aircraft was proposed for carrying nuclear weapons after the Second World War. The Vulcan was designed as a thick delta wing so as to benefit from sweepback angle effect at transonic speeds. The wing had to be thicker in the root area to accommodate 4 Rolls-Royce engines. Thick wing meant that flow remained essentially attached at large incidences. It would appear that vortex lift was not truly exploited. This is borne out by L/D estimates available. Wind tunnel experiments carried out on a model of the Vulcan suggested that the wing was able to carry heavy loads at higher speeds and higher altitudes than conventional designs of that time. The Vulcan aircraft had a long career until being finally grounded in 1981 and replaced by the Panavia Tornado GR.1. The final service of the Avro Vulcan was during the 1982 conflict.

The French also adopted the delta for their most successful aircraft, the Dassault Mirage III interceptor. The Mirage III was developed almost at the same time as the Vulcan and the YF-102. It also had a 60^0 swept delta wing to offset the transonic effect. Although it was the first aircraft that could fly at more than Mach 2, it suffered from one of the disadvantages of the delta wing in that it needed a longer

take off run and, high landing speed. It also experienced buffeting of the airframe caused by the separation of the boundary layer at low attitude.

Around this time, Russia also introduced the TU-144 supersonic passenger jet and MIG-21 fighter aircraft. The Tupelov-144 was grounded in 1978 when the aircraft was involved in a fatal accident. Many delta winged aircraft were produced in this era such as the A-4 Skyhawk, XB-70, Concorde, Space Shuttle, F-16, Chengdu J-10, and Sukhoi Su 9/11 among others.

The delta wings exhibit some disadvantages that may have caused them to fall out of favour in recent years. The main problems are associated with the flow separation at higher angles of attack. The separated flow can cause the control surfaces fitted to the trailing edge to become less effective. Secondly, the wing produces tremendous induced drag at subsonic speeds (low L/D) compared to conventional tapered wings. This is due to the small wing span or low aspect ratio. The higher drag on the delta-shaped wing is actually induced by the separated flow in the leading edge area itself that is not present on high aspect ratio tapered-wings. These factors affect the aircraft's handling quality. In addition, the aircraft also needs a longer runway for take-off and landing. As a result, delta wing aircraft are effectively limited to high speed and high altitude applications.

Developments in computer flight control have given the delta wing shape new prominence. Delta wings are again a leading concept for fighter aircraft development. Several modern aircraft appearing in the late 1980s to 1990s have incorporated both delta wings and canards. Examples include the Eurofighter typhoon, JAS 39 Grippen, French Rafale, Russian Sukhoi-30 and the American research aircraft, F-16 XL. Delta wings also have the potential to be utilized for future transport aircraft. A new concept of a future high speed civil transport integrates the combination of the double delta wings attached to the fuselage of the aircraft, which is called High-Speed Civil transport.

The goals of future aircraft design are to reduce fuel consumption, reduce Carbon Dioxide (CO_2) by 50% and NO_x by 80% (European Telfona Report in 2005). These challenges can be met by either improving the engine efficiency or by enhancing the aerodynamic properties of the aircraft. The aerodynamic performance can be enhanced in several ways and one of them is by increasing the laminar flow

region on the wing to reduce friction drag at supersonic speeds. Laminar flow needs less energy to move the aircraft through the smooth air without turbulence; thus reducing the fuel consumption. Most efforts have been focused on encouraging laminar flow over the entire wing. One of these projects is called *"F-16XL Supersonic Laminar Flow"*. The F-16-XL is a stretched body version of a full scale conventional F-16 with a larger wing area added in a cranked-arrow shape (see Figure 1.1). Additionally, the sweep angle of the F-16-XL is increased to encourage vortical strength. Several passive and active basic techniques had been applied to the wing to achieve laminar flow conditions. By introducing Porous Titanium on one of the wings during a flight test, laminar flow could be achieved on about half of the entire wing at Mach 2.0.The main function of the Porous Titanium was to suck away the turbulent boundary layer that developed on the wing. More research is needed to improve and extend the laminar flow region to the entire wing (TF-12DFRC (2004)).

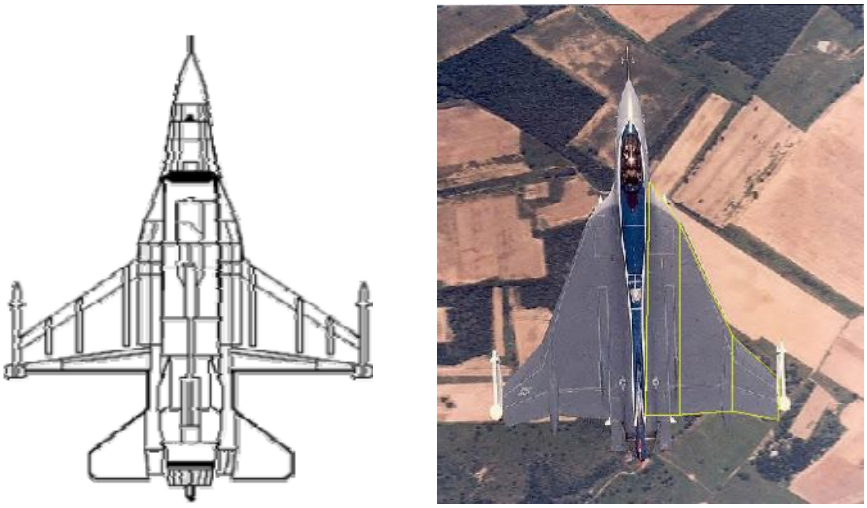

a) b)

Figure 1.1: The wing planform of a) Conventional F-16 & b) F-16-XL

1.2 The Role of the Delta Wing in the Development of Fighter Aircraft

Over the past few decades, early researchers like Fink (1966), Peake & Tobac (1980), Sarpkaya (1971), Leibovich (1978), Pechkam (1958), Elle (1958), Lambourne and Bryer (1961) among others, conducted extensive studies of the flow structures

over delta wings. Their significant contributions to the understanding of delta wing flow physics provided the basis for current work, focusing on the effects of leading edge bluntness, angle of attack, Reynolds number and Mach number. Two research teams called CAWAPI and VFE-2 were established under the NATO-RTO-AVT-113 in 2003 to investigate such effects on the vortical flow of delta wings. The aims of these teams are to increase technology readiness for the development of new military aircraft and also for future transport aircraft (Lamar & Hummel, 2008). Both CAWAPI and VFE-2 are closely related although there are different requirements of each part; for example VFE-2 is focused on experiments and CFD validation. The general objectives of both facets are (Hummel, 2004);

- *F-16XL facet (Cranked Arrow Wing Aerodynamics Project International, CAWAPI)*

  This group aims to perform numerical calculations for the complete F-16-XL aircraft and compare the results with flight test data for various angles of attack and Mach number at full scale Reynolds Number.

- *VFE – 2 Facet (International Vortex Flow Experiment 2)*

  This group performs wind tunnel experiments and numerical calculations on a 65^0 delta wing model in order to understand the vortical flow and uses the experimental results to validate the existing CFD codes.

1.2.1 CAWAPI Facet

Several studies have been carried out over the past two decades, both numerical and experimental into the nature of the vortical flow above the F-16-XL. Many of these have focussed on achieving laminar flow on its wings. This work has been further developed through the CAWAPI facet of NATO AVT-113. It was aimed to perform numerical predictions of the complete F-16-XL fighter aircraft at full scale Reynolds number and compare these with flight test data for various angle of attack

and Mach numbers. Three wind tunnel models of this aircraft had already been tested by NASA simultaneously for comparison. Although the F-16-XL flight test programme was cancelled in 1994 due to funding limitations, the numerical analysis of this aircraft continued to provide useful data for the High Speed Commercial Transport (HSCT) project shown in figure 1.2 (Lamar & Obara, 2008). The HSCT project began in 1990 and was aimed at the design and development of technologies that could carry 300 passengers in a supersonic delta winged aircraft. Due to financial and environmental constraints, the HSCT project was abandoned but the CAWAPI project has continued to provide CFD data to aid understanding of flight and wind tunnel data.

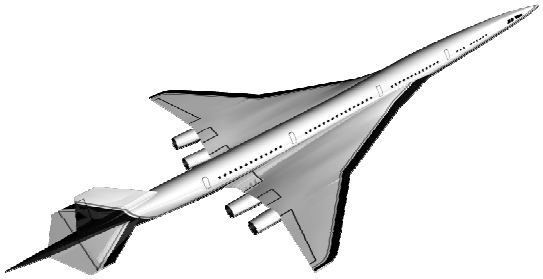

Figure 1.2: High-Speed Civil transport Concept (HSCT)

1.2.2 VFE-2 Facet

The primary objective of the VFE-2 project was to validate and understand the issues around the use of numerical schemes for the calculation of the vortical flow on slender delta wings by comparing the calculations with data from wind tunnel experiments. During the early 1980's, Euler Methods had become the standard technique for the calculation of vortical flow, but they were not well suited to the calculation of the pressure distributions on slender delta wings as the secondary vortices could not be modelled. Further improvements were made in the 1990's to numerical calculations by taking account of viscous effects through solution of the

RANS (Reynolds Averaged Navier-Stokes Methods) equations. This allowed the secondary vortices to be computed. More experimental data are now needed to explore the capabilities of Navier-Stokes calculations. The VFE-2 working group chose a geometry with different leading edge that had previously been tested in the NASA National Transonic Facility and NASA Low Turbulence Pressure Tunnels as the basis for further experiments and CFD validation. The installation of both identical geometry models in the NASA wind tunnels is shown in figure 1.3.

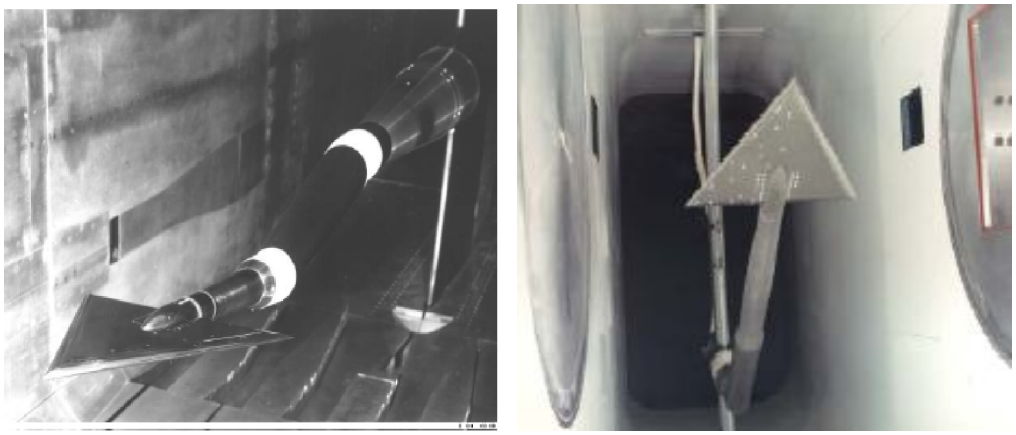

a) b)

Figure 1.3: The Installation of delta wing models in NASA; a) National Transonic Facility (NTF) & b) Low Turbulence Pressure Tunnel (LTPT)

These two experiments were performed in the 1990's as a part of NASA efforts to focus on the effects of leading edge bluntness on the vortical flow on delta wings (Luckring, 1996 & 2008). The results from these experiments such as the starting point of the separation, location of the primary vortex and vortex breakdown data were already available for comparisons. For providing a more robust validation set for the Navier-Stokes calculations, four different flow regions were chosen for comparisons (Hummel, 2004) in the VFE-2 study;

1. Attached flow without vortex formation, $0^0 \leq \alpha \leq 4^0$
2. Separated vortical flow without vortex breakdown, $4^0 \leq \alpha \leq 20^0$
3. Separated vortical flow with vortex breakdown, $20^0 \leq \alpha \leq 40^0$
4. Separated dead-water flow, $40^0 \leq \alpha \leq 90^0$

In VFE-2, two versions of the NASA model (one with sharp and the other with rounded leading edges) were further tested with several new measurement techniques in order to provide a high quality data set for the CFD groups. Furthermore, duplicate models were fabricated based on the analytical geometry descriptions (Chu and Luckring, 1996) and these were tested at research institutions participating in the VFE-2 group. Table 1.1 shows the list of the models including their physical dimensions, owners and the wind tunnels used for the experiments. The third model is the Glasgow University model originally scheduled to be tested in the 2.65 x 2.04 meter Argyll Wind tunnel at Reynolds numbers of 1 and 2 x 10^6.

Model No.	Span (m)	Root Chord, (m)	Tested at	Model Owner	Measurement Techniques	Coordinator
0	0.610	0.653	i) NASA – NTF	NASA-NTF	i) Static Pressure ii) Steady loads	James Luckring
1	0.457	0.490	i)NASA – LTPT ii) DLR-TWG	NASA-LTPT	i) Static Pressure ii) Steady loads iii) Pressure Sensitive Paint iv)PIV	James Luckring & Robert Konrath
2	0.933	0.980	i)Munich Technical University ii) DLR – KKK	Munich Technical University	i) Laser light sheet ii) Oil Flow Visualization iii) Surface Pressure Measurement iv) Hot Wire Anemometry v) Temperature sensitive Paint vi) Infra-red vii)PIV	C. Breitsamter
3	0.987	1.059	Glasgow University	Glasgow University	i) Steady/Unsteady loads ii) Flow Visualizations iii) PIV	Frank N. Coton
4	0.457	0.490	i) ONERA ii) TUBITAK-SAGE	ONERA	i) Pressure Measurement ii) PIV iii) Steady loads	O. Rodriguez
5	0.457	0.490	i) ONERA ii) TUBITAK-SAGE	ONERA	1)Steady Loads 2) Oil Flow Visualization	Suleyman Kurun

Table 1.1: Wind Tunnel models used in VFE-2

Chapter 2

2.0 THE DELTA WING FLOW-FIELD

2.1 Sharp Leading Edge Flow-Field

The flow on the sharp-edged delta wing (Hummel, 2004) at a certain speed and angle of attack can be described as a movement of a part of the flow from the lower to the upper surface into a spiral type of motion. Flow separation will take place at the leading edge near to the apex and primary vortices are formed over the upper surface. The primary vortices basically start as small shear layers at the leading edge and then wrap up in a spiral fashion (Gad-El-Hak and Blackwelder, 1985). The vortices thus originate from a series of smaller vortices shed from the leading edge of the wing. The shear layers rotate around to form a pair of larger vortices called *primary vortices.* The leading edge vortices grow in strength and size extending from the apex to the trailing edge as shown in figure 2.1. The structure of the primary vortex is complex and unsteady with turbulent activity taking place in the area between the separated shear layer and the delta wing leading edge (Honkan and Andreopoulus, 1997). Several early investigations were performed to visualize the three-dimensional flow topology above delta wings such as Nelson & Pelletier in 2003. To date and surprisingly, the detail understanding has been impeded either by the limitations of computational methods, or the constraints of experiments. Hardly, any theoretical models are capable of predicting these complicated flow-fields topology accurately. (Drikakis *et al*, 2003).

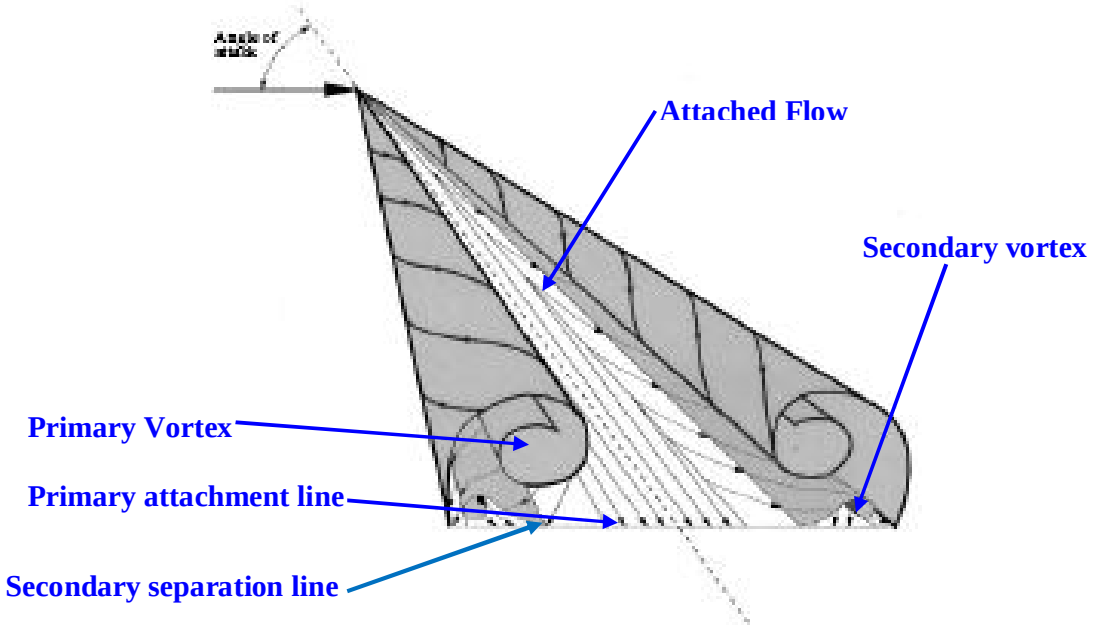

Figure 2.1: Vortex formation over sharp-edged delta wing

The internal structure of the primary vortex itself can be divided into three regions as shown in figure 2.2 (Earnshaw, 1961). The three regions are; *1) the shear layer, 2) rotational core* and *3) viscous sub-core*. The shear layer is generated by a sudden separation of the flow in the leading edge region; the separated shear layer subsequently rolls up to form the primary vortex. The diameter of the outer shear layer increases as the distance from the apex increases. The rotational core, covering about 30% of the local semi span diameter, is a region where the vortex sheet produces only a small variation in longitudinal velocity distribution. Meanwhile the last region; the viscous sub-core, covering about 5% of the local semi span in diameter, is a region where longitudinal velocity is very high and can exceed more than three times the freestream value (Earnshaw, 1961).

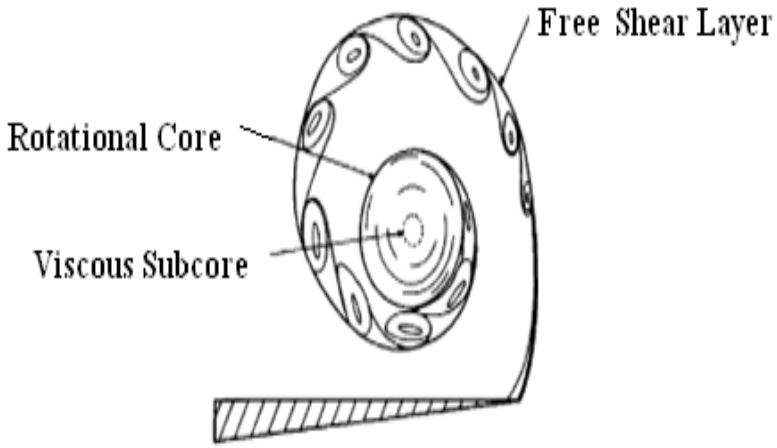

Figure 2.2: Three regions within a leading edge vortex (Earnshaw, 1961)

The free shear layer will roll and make - contact with the wing surface and this situation creates an attachment line all the way from the apex to the trailing edge of the wing (The lines are shown in figure 2.1). The location of the attachment line depends on the angle of attack. From the attachment area, the shear layer underneath the primary vortex is diverted towards the low pressure region in the leading edge area so establishing attached flow below the primary vortex on the wing. After passing the vortex core, the attached shear layer experiences a spanwise adverse pressure gradient that leads to flow separation before the shear layer reaches the leading edge. The adverse pressure then causes this separated flow to spin in the opposite sense of the primary vortex to form another vortex called the *secondary vortex*. The general effect of this secondary vortex (Payne *et al*, 1987) is the displacement of the primary vortex upwards and inwards but the status of the boundary layer on the wing upper surface strongly influences the location of the secondary separation process. In the laminar case, the reduced ability of flow to sustain the adverse pressure gradient, causes the secondary separation process to occur earlier thus making the secondary vortex larger compared with the turbulent case. The shear layer stability of the primary vortex is discussed by Riley and Lawson (1998). They observed that, at low Reynolds number, the shear layer is smooth with

no sign of any instability. Unsteadiness in the shear layer is, however, observed as the Reynolds number is increased.

2.2 Vortex Breakdown

As the angle of attack increases, so does the strength of the primary vortex, the axial velocity in the vortex core can exceed three times the freestream speed. At a certain point aft from the apex, a sudden decrease in the strength of the local primary vortex core occurs. The flow then suddenly becomes stagnant and exhibits large-scale of unsteadiness as shown in figure 2.3 below (Payne *et al*, 1987). The figure also depicts the lost coherence of the primary vortex structure further aft of the wing. This phenomenon is called *vortex breakdown*. In addition to this, Hall (1972) describes vortex breakdown as the stagnation of the swirling flow that causes the flow to develop into a disorganized flow-field. The converged flow also transforms into a reversed and unstructured flow in the vortex core.

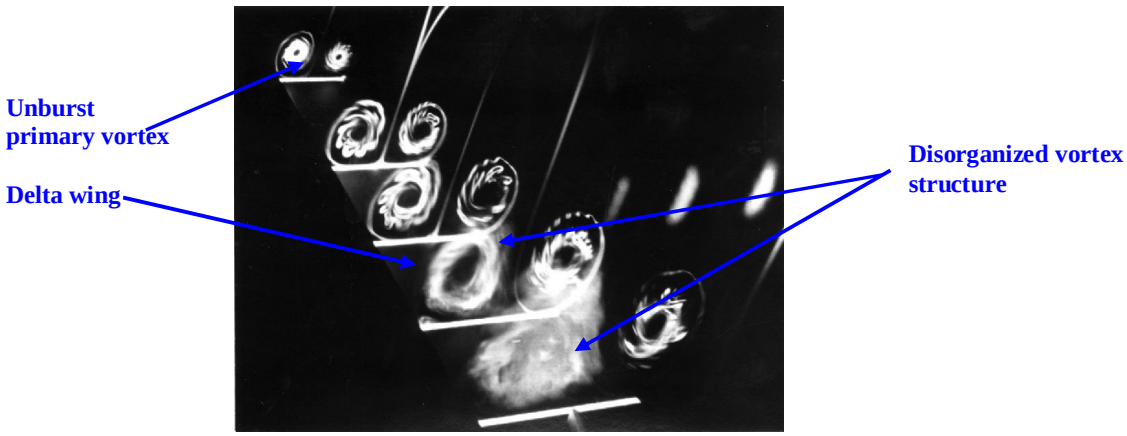

Figure 2.3: Laser light sheet illumination of the cross flow and longitudinal axis of the leading edge above an 85^0 swept delta wing, $\alpha = 40^0$ (Payne, 1987)

The existence of vortex breakdown plays a role in limiting aircraft performance at higher angles of attack due to the decrease in the axial velocity of the vortex core (May & Gutmark, 2005). Vortex breakdown has been the focus of much

research in the aerospace community as it significantly results in the loss of lift and substantial changes in pitching moment, thus affecting the aircraft stability characteristics. The increase in turbulent intensity of the downstream flow also adversely affects the control surfaces such as the fin and rudder of fighter aircraft (Breitsamter, 2008) and (Payne *et al*, 1987).

Amongst the first to record the vortex breakdown phenomenon were Peckham and Atkinson (1957). There were follow-up investigations on this work by investigators including Sarpkaya (1971), Leibovich (1978), Peckham (1958), Elle (1958), Hummel & Srinivasan (1967), Payne *et al* (1987) and Nelson & Visser (1990). Among these, Payne *et al* (1987) showed the development of the breakdown process using smoke visualization on his 70^0 sweep delta wing at high angles of attack. The core region of the vortex expanded rapidly after the breakdown and the flow became highly disorganized. This sudden expansion and unsteadiness of the vortex core was also shown by Wang and Zan (2005) in water tunnel experiments at low Reynolds numbers.

Research has also been performed to investigate the characteristics of the flow after vortex breakdown. Sarpkaya (1971) defined vortex breakdown as an abrupt change in the structure of the vortex core, followed by a growing asymmetric flow (a flow in which the streamlines are not symmetric around the vortex axis). A different perspective on vortex breakdown is discussed by Leibovich (1978) and Garg & Leibovich (1979). They defined vortex breakdown as a disturbance that is characterized by the formation of an internal stagnation point on the vortex axis followed by a reversed flow. Nelson & Visser (1990) described the vortex breakdown as a drastic change in the flowfield arising from the sudden increase in the magnitude of the axial pressure gradient in the vortex core. Hall (1972) showed that the occurrence of the vortex breakdown depended on the magnitude of the swirling flow, the external pressure gradient and the degree of the divergence in the vortex core. The higher adverse pressure gradient and the degree of divergence caused the swirling flow of the vortex core to reduce so contributing to the stagnation of the core. These observations are in good agreement with Elle (1960) who described the breakdown as a failure of the vorticity structure around the vortex core to retain its form.

The breakdown process at high angle of attack, that begins from the wing trailing edge, was discussed by Greenwell & Wood (1992). They divided the separated flow over the delta wing into 4 regions; *1)* unburst vortex or primary core, *2)* Flow Deceleration region, *3)* Bubble formation and *4)* Fully developed breakdown area. The formation and behavior of the primary core *(region 1)* has already been discussed above. Further aft of the apex *(region 2),* the flow decelerates under the influence of the adverse pressure gradient within the vortex core, this occurs in the second region, where the swirling magnitude of the primary vortex reduces. Nevertheless, the flowfield in this region retains the vortex shape but the swirling magnitude becomes less and less further aft. In *region 3*, a further reduction in the swirling magnitude is accompanied by the formation of a bubble like structure with some degree of reversed flow around the vortex core. In *region 4*, fully developed vortex breakdown with large scale turbulent is found and the flow becomes very unsteady and asymmetric.

A later experimental study using a seven-hole probe by Payne *et al* (1989) showed good agreement with Greenwell & Wood (1992). Again, vortex breakdown was found to move upstream towards the apex, as the angle of attack was increased. However, this upstream progression of the vortex breakdown slows down as the angle of attack reaches high values. This can be related to the influence of the pressure gradients along the vortex core. The pressure gradient near to the apex is close to zero at high incidence and so the vortices become stronger and more able to resist the forward movement of the breakdown process (Wentz & Kohlman, 1970).

2.2.1 Types of Vortex Breakdown

According to Lambourne and Bryer (1961), there are two types of breakdown that generally occur on a delta wing; *bubble* and *spiral types*. The bubble breakdown is characterized by the appearance of a stagnation point on the vortex axis followed by an expansion of the vortex core by up to a factor of three as illustrated in figure 2.4 a) by Payne *et al* (1987) and Faler & Leibovich (1977). The associated recirculation zone can be nearly axisymmetric and will grow in size as shown.

Downstream of this bubble breakdown, the vortex is fully turbulent and spreads out rapidly with the distance.

The other type, the *spiral* breakdown, Payne *et al* (1987), is characterized by a rapid deceleration of the vortex core with the size of the core diameter growing before it breaks into large scale turbulence as shown in figure 2.4 b). The flow remains in a spiral mode and rotates in the same sense as the primary vortex but can transform into the bubble type of breakdown and move upstream to the wing apex as the angle of attack is increased.

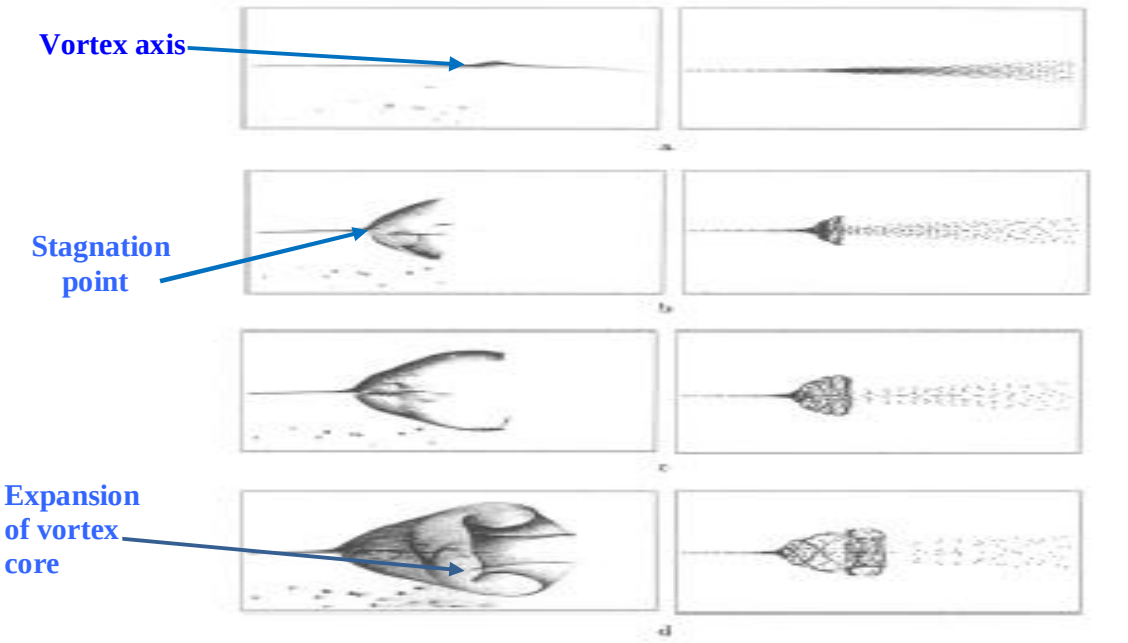

a)

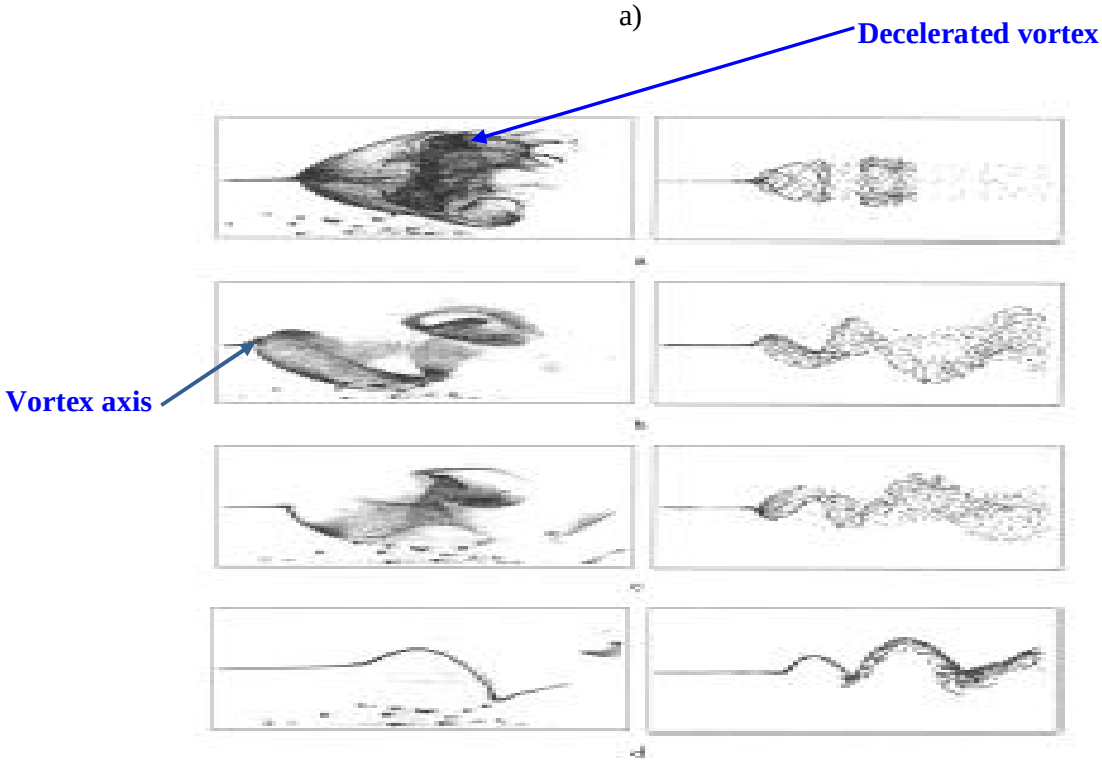

b)

Figure 2.4 a) Bubble breakdown, b) Spiral type of breakdown (Payne et al, 1987)

The detail experimental investigation on the spiral-type breakdown (which is mostly occurred on the delta wing) is well documented by Lambourne & Bryer in 1961. Their water tunnel experiment on the sharp-edged is shown in figure 2.5. They showed after the onset of the bursting, the flow transformed into a large spiral-type vortex structure. This process is followed by a decelerated vortex speed further aft of the wing.

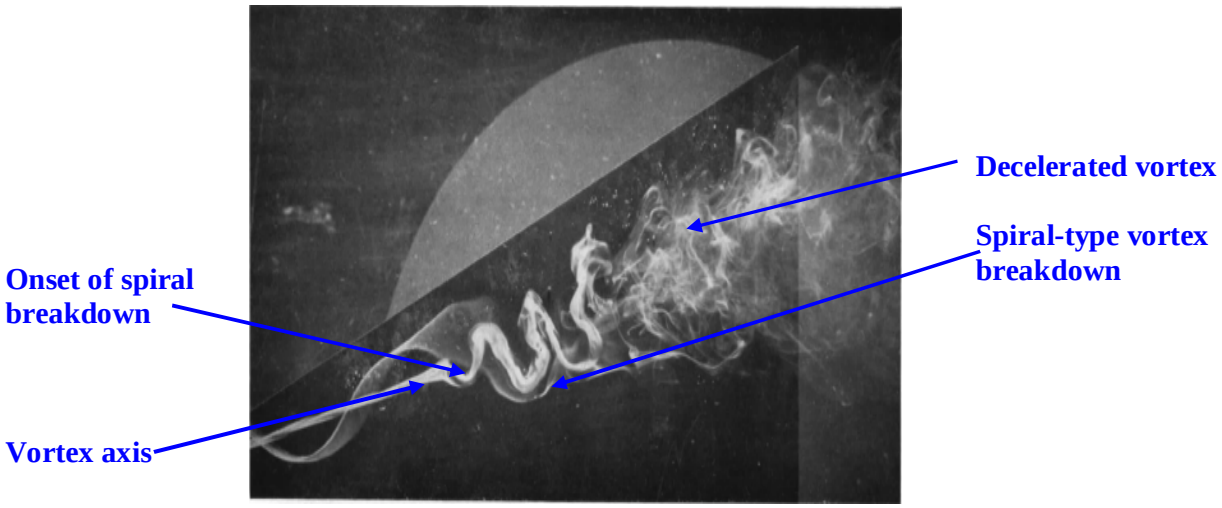

Figure 2.5: Details process of spiral-bursting at the speed 2 inch per second & $\alpha = 40^0$ (Lambourne & Bryer, 1961)

Nevertheless, not many paper discussed the details of the spiral breakdown on the blunt leading edge except the work within the VFE-2 campaign. Numerical analysis performed by Fritz & Cummings in 2008 showed that the onset of the spiral breakdown occurs at about two third of the wing at the test condition as shown in figure 2.6.

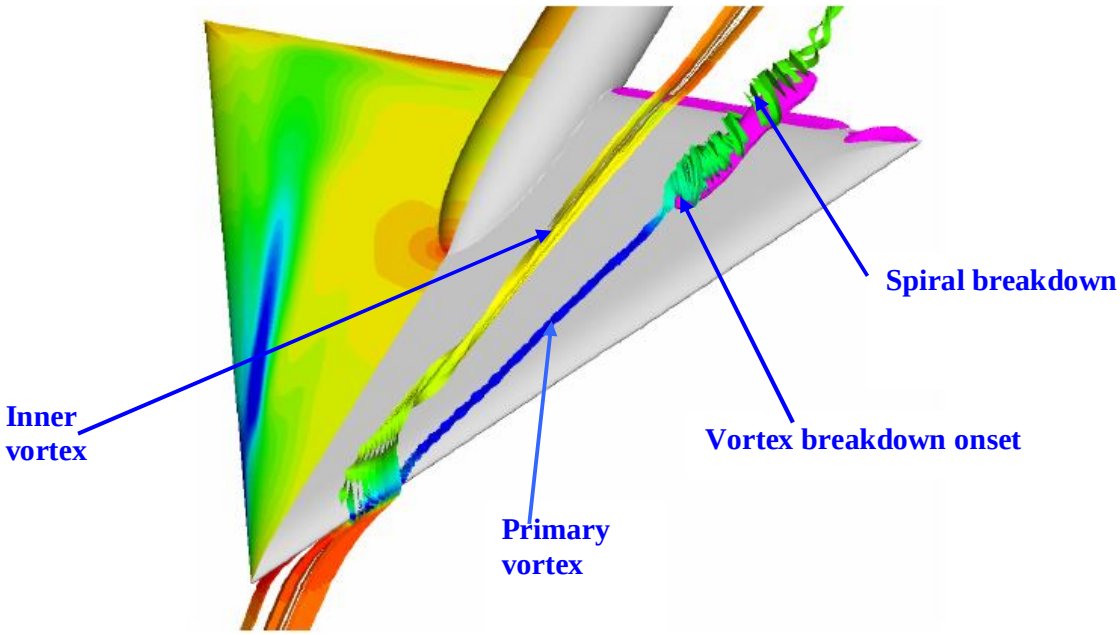

Figure 2.6: Vortex Breakdown on VFE-2 configuration (0.4 Mach number, $\alpha = 18^0$ & 6 x 10^6 Reynolds number)

2.2.2 Factors Influencing the Vortex Breakdown

Several factors influence the position and the strength of the breakdown i.e. wing geometry, Reynolds number, speed and angle of attack. Peckham (1958), Elle (1958) and Hummel & Srinivasan (1967) showed the position of breakdown is mainly dependent on the angle of attack. At a low angle of attack, breakdown occurs at the trailing edge and moves forward toward the apex if the angle of attack is increased. The increase in the adverse pressure gradient within the vortex core as the angle of attack increases, contributes to this phenomenon. The second factor is the wing sweep angle. The detailed effects of the wing sweep angle have been discussed by Nelson & Pelletier (2003) and Kegelman & Roos (1989). They found that an increase in the wing sweep angle delays the vortex breakdown process. The ability of the stronger primary vortex at higher sweep angle to sustain the adverse pressure gradient contributes to this fact.

Another factor influencing vortex breakdown is the leading edge profile. However, there have not been many studies published on this effect. Kegelman & Roos (1989) showed from their experimental results on a 70^0 wing that the upstream progression of the vortex breakdown is delayed for rounded-edged wings compared to the sharp-edged case. In addition, O'Neil *et al* (1989) discussed the onset of the breakdown process is also been delayed by the blunt wings. They showed that the onset of the breakdown reached the wing trailing edge at higher angle of attack compared to the sharp wings. As will be shown later, these is also consistent with the flow visualization images obtained in this study that depicts the progress of the vortex breakdown being delayed by increasing the leading edge bluntness.

Gursul (2004) addressed several other factors such as the geometry of the wing, support structure, model deformation, Reynolds number and blockage. Wentz & Kohlman in 1972 concluded that the vortex breakdown is not much affected by blockage. Recent experiments by Crichton *et al* (2005) and Thomson & Nelson (1992) proved otherwise. They concluded that the effect of blockage is important and should be taken into account. In general, vortex breakdown is shifted upstream when blockage effects are increased.

The effects of vortex breakdown on the steady force coefficients were observed by Hummel & Srinivasan (1967) and Spall (1996). They agreed that breakdown significantly affects the forces and pitching moment of the delta wing. The loss of lift, particularly, was attributed to the loss of coherent vortex structure and its effect on the vortex lift as described by Polhamus (1966).

2.2.3 Vortex Breakdown during Pitching Motion

The breakdown characteristics on a delta wing undergoing pitching motion has also been observed in experiments. Investigations into this was driven by observation that the breakdown process at higher angle of attack is temporarily delayed by pitching motion. A high performance aircraft can take advantage from these unsteady effects for a rapid maneuver at high angle of attack (Le May *et al*, 1990). During testing, the models are normally pitched at constant pitching rate or sinusoidally oscillated. The instantaneous position of breakdown during the experiments depends on the reduced pitch rate or reduced frequency, $K = \Pi.f_e.c_R / U_\infty$; where f_e is pitching frequency, c_R is wing root chord and U_∞ is free stream velocity.

The characteristics of the flow at a higher reduced frequency; where the model is rapidly oscillated show a rapid development of the instability structure of the primary vortex (Atta & Rockwell (1990), Sahin (2002), Le May *et al* (1990) and Cipolla & Rockwell, 1995). In general, an increase in reduced frequency also delays the vortex breakdown process at medium angles of attack. At low reduced frequency, the primary vortex slowly develops during the upstroke and there follows the breakdown process further aft on the wing during the downstroke. Nevertheless, the scope of this PhD study is limited to static experiment only. A rather completed test rig is required for the pitching motion experiments. The system as shown in figure 2.7 (Le May et al, 1990) needs a motorize system to pitch the model at constant pitching rate.

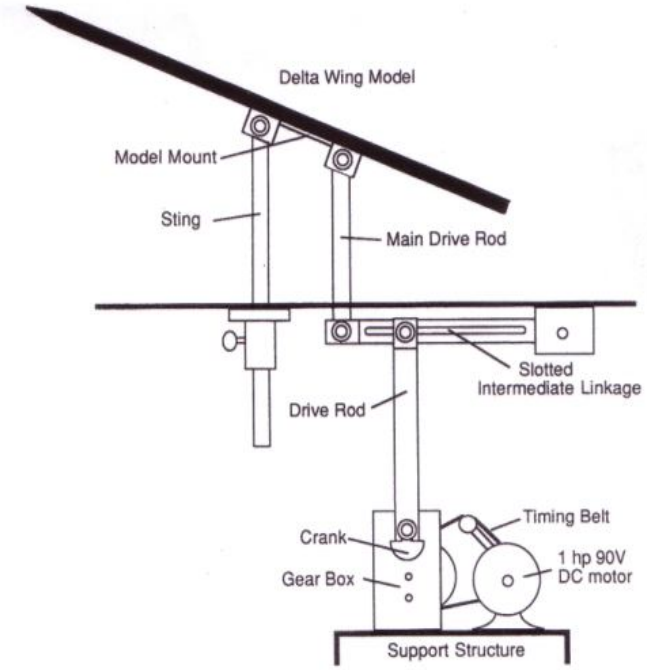

Figure 2.7: Unsteady pitching mechanism (Le May *et al,* 1990)

2.3 Laminar to Turbulent Flow-Field

2.3.1 Impact of Boundary Layer on Vortex Structure

The state of the boundary layer, either laminar or turbulent at separation and underneath the vortex system is another factor that influences the flowfield. Previous studies have shown that the state of the boundary layer at very low Reynolds number is laminar, and it is the laminar separation that leads to the development of the primary vortex (Hummel, 2004). As the Reynolds number increases, transition from laminar to turbulent flow is expected to occur at some position on the wing upper surface. As the Reynolds number further increases, the transition point moves closer to the wing apex. Even at a very high Reynolds number, however, laminar flow may still exist over part of the wing apex region.

This aspect has presented problems for numerical studies, i.e. whether to perform calculations in fully turbulent or laminar flow. The details of transition from laminar to turbulent on the delta wing surface are not very well understood yet, even

for the sharp-edged wing (Hummel, 2008a). The stronger magnitude of the primary vortex for the turbulent case compared with the laminar case is one of the indications that differentiates laminar / turbulent flows. Many attempts either by experiment or numerical analysis have been made, and more work is in progress, to determine the laminar/turbulent transition region. As recent as 2008, knowledge of laminar to turbulent transition remained poor; even with the advent of PSP pressure data (Hummel, 2008a & 2008b). The correct position of transition from experimental work must be replicated for the correct prediction of the vortices on the wing (Fritz, 2008). Fritz showed that the onset of the primary vortex, for the case of a round-edged wing, is slightly over predicted compared with experimental studies when using a fully turbulent assumption. Better results, compared with the experimental study, were obtained by fixing the transition line at 3% along the wing chord position. The principle differences between the laminar and turbulent separation region will be discussed in the next section.

2.3.2 Laminar Flow

At low speeds and small Reynolds number, a smooth laminar flow without turbulence is expected to occur over the upper surface of the wing. In general, laminar flow conditions are hard to achieve and maintain when the speed increases. Several efforts have been made to achieve laminar flow to reduce the drag and consumption of aircraft fuel (European Telfona Report in 2005). Research aircraft appeared in the 1980's to improve the understanding of laminar flow over delta type wings. One of those was the F-16-XL, that was specifically designed to obtain more laminar flow over the wing.

As may be expected and more specific to delta wings, laminar flow can result in laminar separations above the wing. The characteristics of laminar separation have been examined in detail by Hummel (2004) using flow visualization. Hummel reported the existence of a "bigger" primary vortex located more inboard on his sharp-edged wing than would be expected in turbulent flow. Underneath this primary vortex, an adverse pressure gradient occurs between the primary attachment line towards the leading edge. A relatively large secondary vortex is formed due to the

early separation of the flow underneath the primary vortex due to this adverse pressure gradient. The flow underneath the secondary vortex experiences another adverse pressure gradient which leads to a tertiary flow separation (Hummel, 2004). In terms of the strength of the primary vortex in the subsonic region, the primary vortex resulting from laminar separation is weaker in intensity than in the turbulent case (Betyaev, 1994).

To differentiate laminar and turbulent boundary layer above delta wing, Visbal & Gordnier (2003) has performed a numerical calculation at 2 different Reynolds numbers; 5 x 10^4 &1 x 10^5 (Figure 2.8). At low Reynolds number the flow is covered by a smooth laminar flow which extends from the apex to about half of wing. Rough turbulent boundary layer is shown further aft of the wing. By increasing the Reynolds number, turbulent boundary layer extends towards the apex.

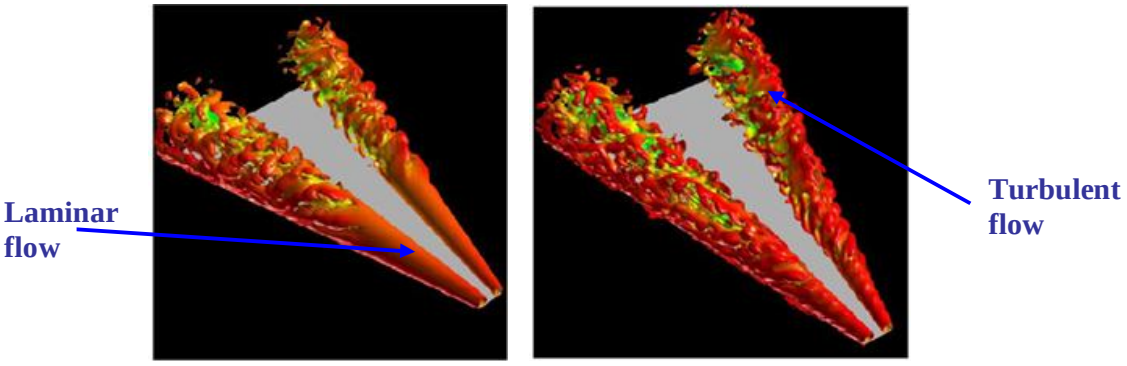

a) 5 x 10^4 Reynolds number b) 1 x 10^5 Reynolds number

Figure 2.8: Flow structure of laminar and turbulent boundary layer

2.3.3 Turbulent Flow

As the speed and Reynolds number increases, turbulent flow initiates on the wing. A “rough” (as shown in figure 2.8) turbulent boundary layer exists when the flow becomes bubbly, irregular, highly mixed, unpredictable and there is increased cross flow compared to the laminar boundary layer case (TF-12DFRC, 2004). This is shown in figure 2.8 above. The turbulent boundary layer gives rise to turbulent separation and creates different characteristics in the flow topology. The primary

vortex is stronger in magnitude and located more outboard than in the laminar case. Underneath this vortex, the ability of the turbulent boundary layer to sustain the adverse pressure gradient leads to a delay in the secondary separation and so a smaller secondary vortex is developed for this condition (Hummel, 2004). In addition, the turbulent boundary layer case exhibits delayed breakdown compared with the laminar case. The turbulent flow also increases the viscous forces thus increasing the drag of the wing.

2.4 Rounded Leading Edge Flow-Field

2.4.1 Attached Flow Region

The round-edged wing exhibits different flow physics compared with the sharp-edged wing especially in the region near the leading edge and the apex. The main difference is due to the attached or non-separated flow covering the wing apex region. The flow stays attached to the wing surface, starting from the apex to a certain chord-wise position which depends on Reynolds number, angle of attack, Mach number and the leading edge profile itself (Hummel, (2004 & 2007) and Luckring (1996, 2002 & 2004a)). Several experiments including surface pressure studies performed by NASA (Chu & Luckring, 1996) show this bluntness effect. From figure 2.9 b), the attached flow region can be recognized by a high suction peak at the leading edge initiated from the apex to a certain chord-wise position on the wing. A vortex-like pressure peak is then noticed at about half of the wing root chord. For the sharp-edged case (figure 2.9 a), the vortex-like pressure is already observed close to the apex. From figure 2.9a, the vortex system is characterised by a suction peak in the vicinity of the leading edge, secondary vortex of the wing followed by a suction peak corresponding to the primary vortex further inboard.

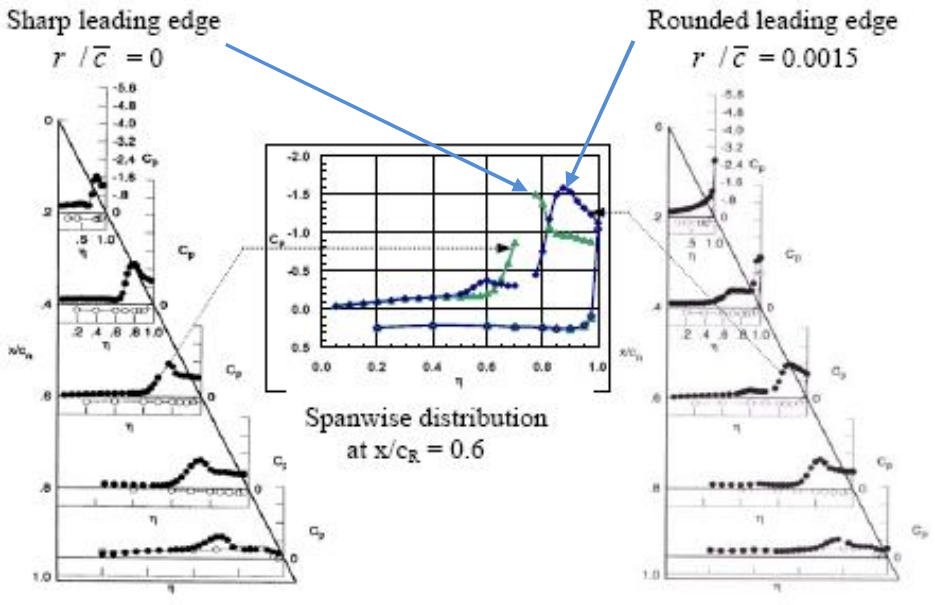

a) b)

Figure 2.9: Effect of Leading edge bluntness on the pressure distribution at Mach number = 0.4, R_{mac}=6 x 10^6 and $\alpha = 13^0$ (Chu & Luckring, 1996).

Later experiment (Particle Image Velocimetry & Pressure Sensitive Paint) together with numerical work on similar wing configurations is shown in figure 2.10. Both results were well agreed with earlier pressure measurement studies; i.e., the primary vortex will only appear at certain chordwise position on the blunt leading edge wing (the onset of the primary vortex is shown in figure 2.10). The flow in the apex region is covered by attached non separated flow to certain chordwise position (also shown in figure 2.10).

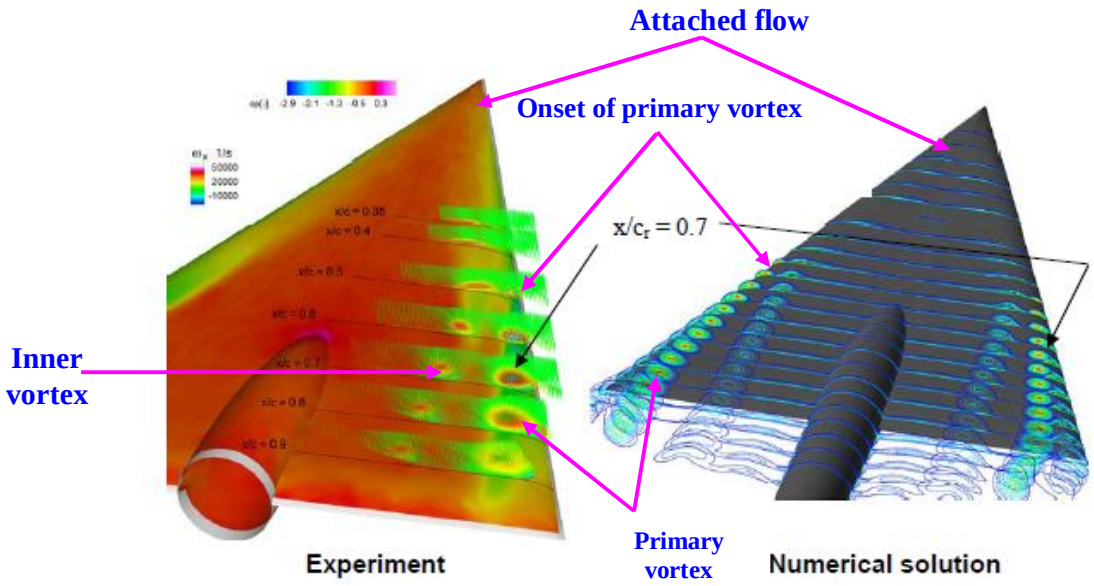

Figure 2.10: Comparison of the experimental with the numerical solution above the VFE-2 Configuration with medium radius for Mach number 0.4, $R_{mac} = 3 \times 10^6$ and $\alpha = 13^0$Hummel 2008b)

Besides these studies, the occurrence of the attached flow region has also been established using several flow visualization studies in water or wind tunnels. These include water tunnel experiments performed at 7×10^3 Reynolds number by Miau *et al* (1995).

The attached flow region exists even at transonic speed as reported by Narayan & Hartman (1998) and Chu & Lamar (1988). From figure 2.11, the attached flow region is associated with the Mach number. At higher Mach number, the leading edge separation can have cross flow shock beneath the primary vortex. This shock can become stronger enough to cause shock-induced separation with promoted upstream progression of the primary vortex, thus reducing the attached flow region.

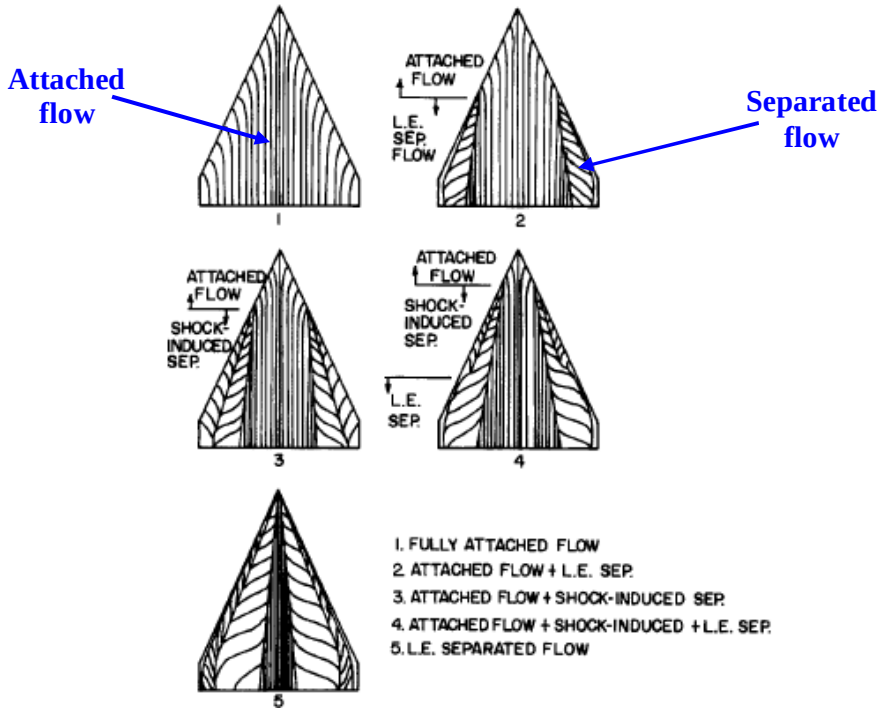

Figure 2.11: Schematic flow patterns on the lee surface of wings with rounded leading edged at transonic speed (Narayan & Hatrman, 1988)

2.4.2 Primary Vortex of the Round-Edged Wing

Downstream of the attached flow region, primary flow separation takes place somewhere near the leading edge caused by the increase in adverse pressure gradient in the flow direction. For the round-edged wing, the primary separation line is no longer fixed to the leading edge but near to it (Hummel, 2004). The principal differences between the sharp and round-edged wing discussed above are summarized in figure 2.12 by Luckring (2004a). The chordwise extent of the primary vortex depends on angle of attack, Mach number, Reynolds number and the leading edge bluntness itself. The properties of the primary vortex also vary with these parameters.

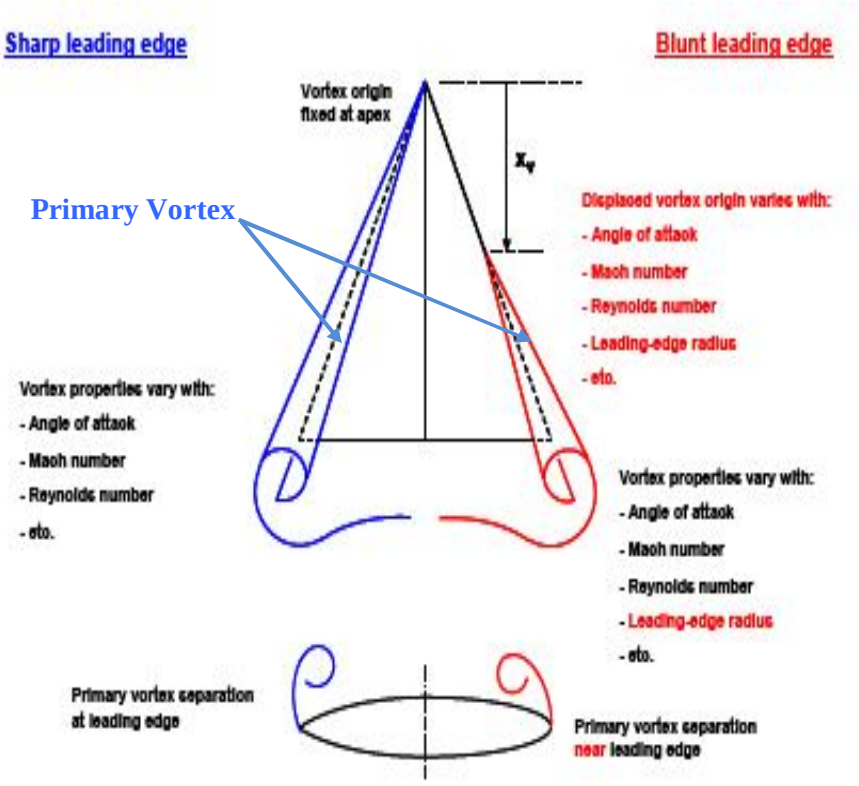

Figure 2.12: Leading edge bluntness consequences for the primary vortex (Luckring, 2004a)

The reason why leading edge separation is initiated at some position down the chord of the blunt leading edge delta wing at moderate angle of attack is now explored. Along the blunt leading edge, the leading-edge radius remains constant, whereas the local half span increases significantly further downstream. This means that the radius to local span ratio decreases i.e. the profile effectively becomes sharper and sharper towards the trailing edge. This causes the suction and corresponding adverse pressure gradient at the leading edge to increase further downstream and finally flow separation takes place in this region (Luckring & Hummel, (2008) and Konrath *et al* (2006)).

Also, the delta wing leading edge upwash distribution increases from the apex to the trailing edge and thus the local angle of attack is higher near to the trailing edge compared with the apex region. The higher angle of attack in the trailing edge area due to its curvature compared with the apex area also increases the corresponding

adverse pressure gradient and promotes separation along the leading edge (Luckring, 2008). Depending on the Reynolds numbers as reported by Furman & Breitsamter (2008) the flow near the trailing edge can be fully turbulent. In this case, the turbulent shear layers of the wing upper and lower surface then roll up along the leading edge (Furman & Breitsamster, 2008) to form a primary vortex in the same way as for the sharp-edged wing. The primary vortex then extends downstream with a stronger magnitude than in the laminar case (Pashilkar, 2001).

At first glance, there are two obvious effects of bluntness observed from figure 2.9. Firstly, the bluntness shifts the position of the primary vortex outboard towards the leading edge compared to the sharp case. Secondly, although not as obvious, the leading edge bluntness decreases the physical size of the primary vortex at constant angle of attack. This is very consistent with Rinoei (1996 a, b) discussion of the bluntness effect. PIV experiments performed by Rodriguez (2008) as shown in figure 2.13 also agreed with this. The PIV results showed that the intensity of the primary vortex on the round-edged wing is weaker than on the sharp-edged wing. Lamar (1990) suggested that the establishment of the attached flow region at the rounded leading-edge as the main factor in delaying the onset and weakening the primary vortex.

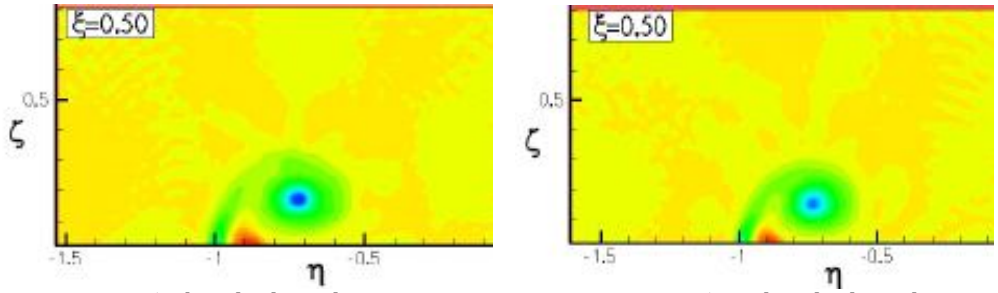

i) Sharp leading edge ii) Medium leading edge

Figure 2.13: Comparison for the size of the primary vortex for the sharp and medium leading edge radius at $\alpha = 24.7^0$, $R_{mac} = 1 \times 10^6$, chordwise position = 0.5 and Mach number = 0.133 (Rodriguez, 2008)

Underneath this primary vortex, a counter rotating secondary vortex is also developed, as it does for the sharp-edged wing (as shown in figure 2.1). This arises from separation induced by the adverse pressure gradient in the flow direction. However, it is not necessarily the case that both vortices will develop simultaneously. The secondary vortex can develop later and further aft of the onset of the primary vortex. Once again, the status of the boundary layer underneath the primary vortex can play a role in this (Rodriguez, 2008). The status of the boundary layer is also a factor influencing the primary separation process. In general, the flow around the leading edge of the round-edged wing is governed by the parameters of Reynolds number and leading edge radius; moving downstream from the apex, several different flow phenomena may be observed at the same angle of attack (Hummel, 2004)

i) Laminar flow around the leading edge without flow separation
ii) Laminar flow around the leading edge followed by the onset of laminar flow separation on the upper surface.
iii) Laminar separation line on the upper surface moves towards the leading edge until laminar flow separations occurs at the leading edge.
iv) Laminar flow separation ends at a certain point along the leading edge and is then replaced by laminar to turbulent transition if the Reynolds number is further increased.

This situation is illustrated in figure 2.14 below. At relatively low Reynolds number, the boundary layer is dominated by a laminar flow while the turbulent is only existed in the tip of the trailing edge. The figure then shows an upstream progression of the turbulent boundary layer with the increase in Reynolds number.

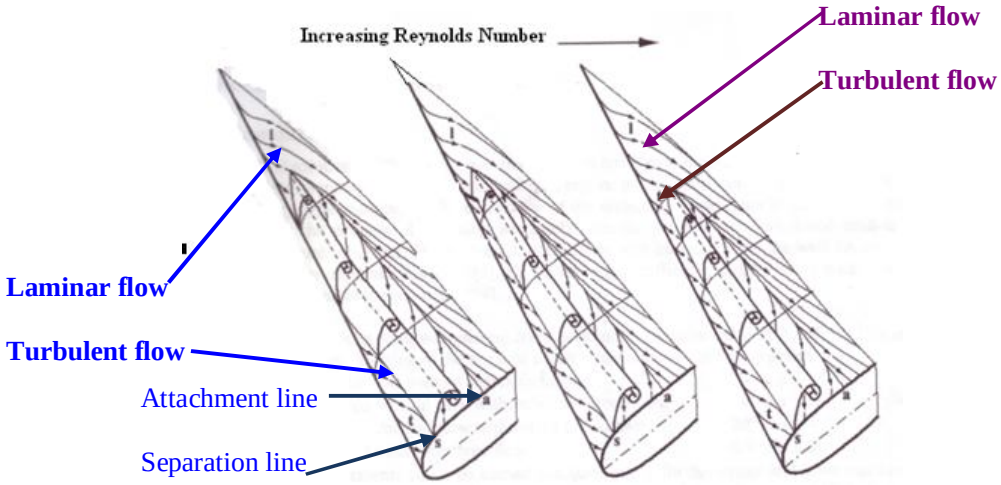

Figure 2.14: Boundary layer underneath the primary vortex (Hummel, 2004)

Increasing Reynolds number moves the transition from laminar to turbulent flow upstream and the region of laminar primary separation is progressively reduced. Finally the laminar primary separation disappears and the whole leading edge is covered by turbulent separation. Since a turbulent boundary layer is better suited to withstand the adverse pressure gradient, the region of attached flow in the apex region is larger for the turbulent case at high Reynolds number compared to the laminar case at low Reynolds number (Bozhkov, 1996 and Hummel, 2004).

2.4.3 The Effects of Bluntness on the Leading Edge Separation

This section will examine the flow topology in the leading edge area in more detail. A closer examination of the leading edge area shows that the separation process occurs at a certain point downstream of the leading edge on the round-edged wing as opposed to "exactly" at the leading-edge for the sharp-edged wing (Luckring (2004a) and Narayan & Seshadri, 1997). At low to moderate incidence, the flow is mostly attached along the blunt-leading edge, but at higher incidences, the flow begins to separate along an appreciable part of the leading edge near to the wing tips. Fink (1966) also illustrates similar flow topologies, i.e. the flow separation on the

rounded edges occurred after a short run of attached flow in the leading edge area. These observations are also in good agreement with Peckham & Atkinson (1960).

Peake & Tobak (1960) also discussed the flow separation on the round-edged wing in two dimensional terms. They described that at a certain angle of attack, the attached flow region extends from the lower surface of the wing to a certain point in the vicinity of the leading edge on the upper surface of the wing, shown as S_1 in figure 2.15. The flow starts to separate at this primary separation point that depends on the flow characteristics from the lower surface. This means that the status of the boundary layer on the lower surface of the wing, either laminar or turbulent, plays a role in determining the location of the primary separation line thus affecting the formation of the primary vortex on the upper surface of the wing. This is also reported by Hummel (2008b). The separated shear layer then rolls up into a conical primary vortex structure as it does for the sharp-edged wing (F_1). Underneath this vortex attached flow is established with another attachment line formed near the wing centre line on the upper surface at point S_4. The flow then re-separates at point S_3 due to the adverse pressure gradient, forming a secondary vortex, as been discussed in the previous chapter. The shear layer zone between points S_4 and S_3 is associated with high turbulence levels (Honkan & Andreopoulus, 1997).

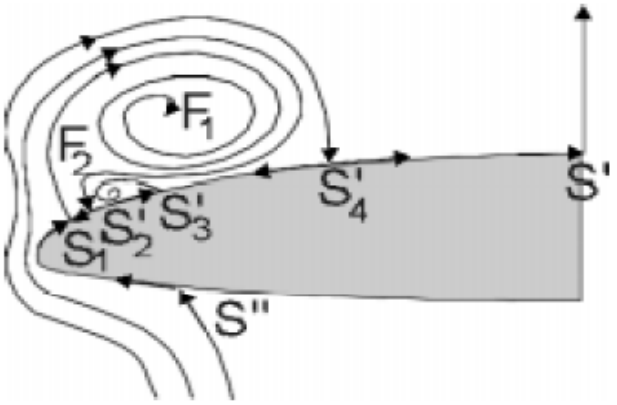

Figure 2.15: Primary vortex topology of the round-edged wing (Lang, 1998)

In addition to the work of Peake and Tobak (1980), a closer examination by Renac (2005) and Jiang *et al* (2000) into the area in the vicinity of the leading edge showed that the primary separation line S_1 of the boundary layer can actually cross

over the lower surface and is not a straight line along the leading edge of the wing. It is located close to the upper surface at the apex and extends towards the lower surface moving from the apex to the trailing edge. This was confirmed by Huang *et al* (2001) who described that the primary separation line is a complex curved line that runs along the leading edge from the apex to the wing tip.

The complexity of these separation lines were also discussed within the VFE-2 campaign as shown in figure 2.16 (Hummel, 2008b). The figure shows the separation line of the primary vortex runs along the leading edge from the onset of the primary vortex extends downstream to the trailing edge. Inboard, the separation and attachment lines of the inner vortex is shown generated further upstream than the primary vortex. Both lines are curved toward inboard downstream of the wing.

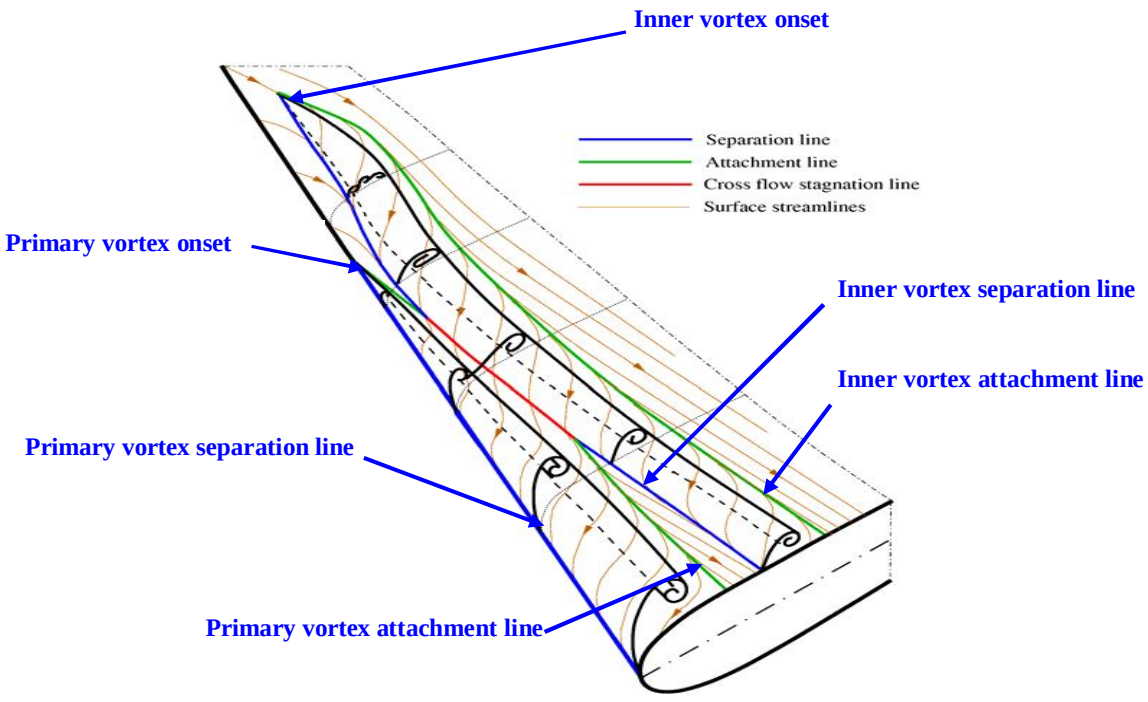

Figure 2.16: Attachment and separation lines on the round-edge delta wing (VFE-2 configuration; Mach number = 0.4, $R_{mac} = 3 \times 10^6$ & $\alpha = 13.3^0$)

Oil flow visualization studies have normally been performed to obtain such topologies over the wing surface. Several researchers used this technique including Lang (1998) and Dieterle (1998) to recreate the surface flow pattern discussed earlier by Peake and Tobak (1980). The flow pattern is generated by viscous stresses acting on the oil surface. The location of attachment and separation lines detected using flow visualization, particularly the secondary separation line, can be used to infer the strength and location of the primary vortex on the wing as discussed previously by Lang (1998).

2.4.4 Inner Vortex

Hummel (2004) also addressed another interesting feature observed in figure 2.4) on the medium-radius wing. At a moderate angle of attack, a weak suction peak is observed, located inboard of the primary vortex. This occurs at about one-third of the wing chord from the apex. This phenomenon provided the focus for some of the initial investigations within the VFE-2 test programme. Numerical and experimental studies were carried out to identify and understand this flow structure. The first numerical results, produced by EADS (Munich) using the *FLOWer* code (Fritz, 2008) were available in 2005 (Hummel, 2006). Transition was fixed at 3 percent of the wing chord on the upper surface of the wing. At a moderate angle of attack, the *FLOWer* calculation shows two vortices spinning in the same sense downstream of the attached flow region. The first one is located close to the leading edge and is the primary vortex, and the other vortex, called the *inner vortex,* develops inboard of the primary vortex. It also appears earlier than the primary vortex at moderate angle of attack as a result of boundary layer separation near to the apex. The inner vortex extends downstream increasing in strength. At the same time, this numerical study also shows that the primary vortex also extends downstream and has a stronger magnitude than the inner vortex. The calculated pressure contours are shown in figure 2.17. This was the first time that the inner vortex had been identified in a numerical solution.

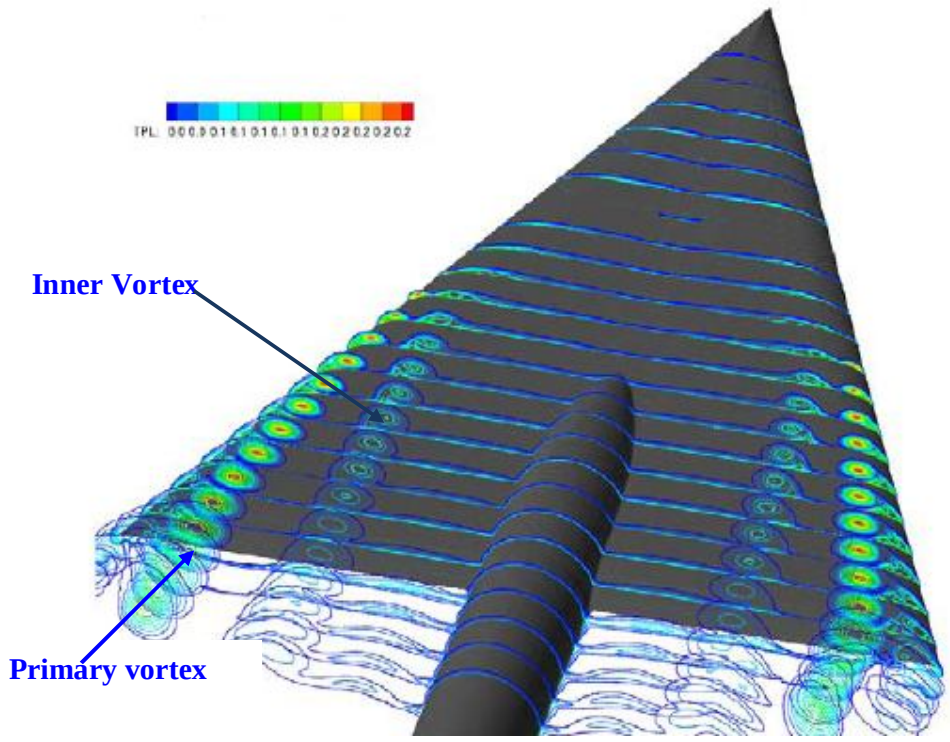

Figure 2.17: Calculated pressure contour on the 65^0 medium radius delta wing at $R_{mac} = 3 \times 10^6$ and $\alpha = 13.3^0$ (Hummel, 2006)

The first experimental results within the VFE-2 group were obtained using Pressure Sensitive Paint (PSP) (Konrath *et al*, 2006 and Klein *et al*, 2006) and Particle Image Velocimentry (PIV), (Konrath *et al* (2006b), Schröder *et al* (2006) and Kompenhans (2007)). A example of the PSP results is shown in figure 2.18 at an angle of attack of $\alpha = 10.1^0$, Reynolds number of 2×10^6 and Mach number of 0.4. A low pressure region representing the footprint of the inner vortex is observed inboard of the primary vortex. It initiates somewhere around half of the wing root chord and extends downstream to the trailing edge area. In the leading edge region, the footprint of the primary vortex is obvious and starts at about half of the wing root chord. For this case both vortices are thought to start at approximately at the same chordwise position.

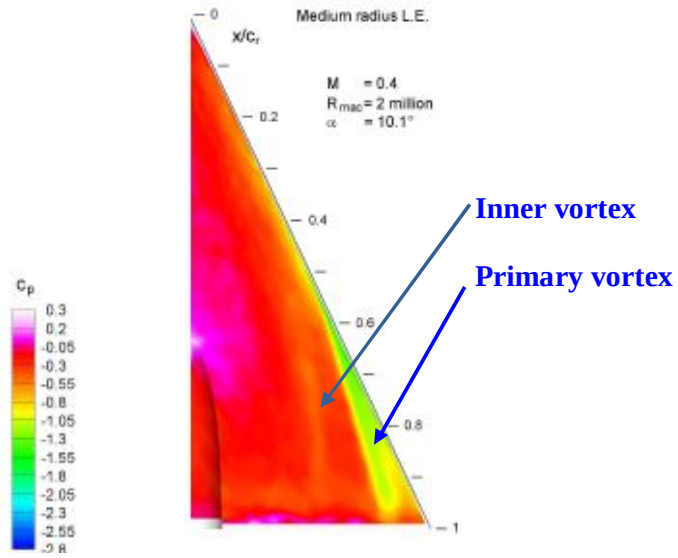

Figure 2.18: Pressure distribution on the medium radius wing at R_{mac} = 2 Million, $\alpha = 10.1^0$ and Mach number = 0.4 (From Konrath, 2006a)

The PIV (Konrath *et al* (2006b) and Schröder *et al* (2006)) results are in agreement with the numerical calculations discussed above; the inner vortex rotates in the same sense as the primary vortex located between the primary vortex and the wing centre line. However, a detailed analysis of the PIV results at a given chordwise position may provide further insight into the nature of this inner structure (shown in figure 2.10). It actually extends downstream with increasing magnitude to a certain chord-wise position only; it then decays in strength as the primary vortex is formed. Both vortices extend downstream and remain apart and do not merge with each other. Both vortices are located close to each other during the initial stage of their development with the stronger primary vortex shifting the inner vortex inboard further downstream on the wing (Konrath *et al*, 2008a & 2008b).

It has been postulated that the inner vortex flow is caused due to a boundary-layer separation bubble. The concept of three dimensional bubble separations as discussed by Dēlery (1992) is strongly linked to the development of the inner vortex. The bubble separation is a type of three dimensional separated flow which originates from a saddle point in the attached flow region. The flow lifts off from the surface forming a flow separation and might roll up to form a spinning flow. As discussed by

Hummel in his report, the flow in the apex region is fully laminar at Reynolds number of 0.88 million that leads to a laminar separation at certain test conditions. The three dimensional laminar bubble separation can occur first on the wing surface in a region close to the apex, where the body is relatively thick compared with the trailing edge area. Simultaneously, the flow in this apex area is smeared towards the low pressure region of the leading edge. The flow then rolls-up to form the inner vortex (Hummel, (2008a) and Furman & Breitsamster (2008)). At the beginning of its development, the inner vortical structure appears as a flat vortex close to the wing surface and grows to form a round vortex as it moves further aft. It then slightly lifts off from the wing surface at a certain chord position (Konrath *et al,* 2008b). Nevertheless, the strength of the inner vortex decays as the primary vortex develops from the leading edge separation. This is because the vorticity shed from the leading edge is fed into the primary vortex, reducing the feeding of the inner vortex. (Luckring & Hummel, 2008).

2.5 The Effects of Angle of Attack, Reynolds Number, Mach Number on Round-edged Delta Wing

The flow physics of the round-edged wing depends on the angle of attack, Reynolds number, Mach number and the bluntness itself (Luckring (2002, 2004b), Engler (1991), Konrath (2006a)). These effects will be further discussed in the next section. The effect of bluntness was discussed in chapter 2.4.3.

2.5.1 Variation of the Angle of Attack

At a low angle of attack, the flow separates in a region close to the trailing edge, where the fraction of the leading edge radius over the wing span is small or the wing is getting sharper in the region. The separated shear flow then wraps up to form a primary vortex in the same way as reported by Gad-El-Hak & Ho (1985) for the sharp leading edge. As the angle of attack is increased, the origin of the primary vortex moves towards the apex of the wing (Narayan & Seshadri, 1997 and Luckring, 2002 & 2004a). At the same time the inner vortex develops further upstream on an inboard section of the wing. As the angle of attack is increased, the origin of the inner vortex structure will show an upstream movement. This upstream movement is caused by the increase in adverse pressure gradient in the flow direction (Luckring & Hummel, 2008). Nevertheless, there is also an adverse effect on the strength of this structure. The strength of the primary vortex increases simultaneously with the angle of attack, whereas the inner vortex strength decays. The reason for this has been discussed in detail by Konrath *et al* (2006a, 2006b & 2008b) and Schröder *et al* (2006); once the primary vortex is developed in the leading edge area, the flow starts to feed the primary vortex and not the inner vortex anymore. As the angle of attack increases further, the magnitude of the primary vortex becomes much stronger compared with the inner vortex.

The angle of attack also affects the position of laminar to turbulent transition flow on the wing although not many publications discuss this. Bozhkov (1975) performed a three dimensional smoke visualization on a round-edged delta wing. He

proposed, on the basis of his observations, that the onset of the turbulent boundary layer moves upstream with increasing angle of attack.

2.5.2 Variation of Reynolds Number

The primary separation of the sharp-edged wing is insensitive to the change in Reynolds number because this separation is fixed at the leading edge (Erickson, (1981) & Hummel, (2004)). For the round-edged wing, Reynolds number is an important factor influencing the flow topology at moderate angle of attack. As discussed by Peake and Tobak (1980), the primary separation occurs in the vicinity of the leading edge on the upper surface, thus Reynolds number strongly influences flow separation. The status of the boundary layer; either laminar, transitional or turbulent, is strongly associated with Reynolds number. The flow on the front part of the wing is usually laminar flow. Transition from a laminar to a turbulent boundary layer will take place at some location on the wing that again depends upon Reynolds Number and the angle of attack. As the Reynolds number increases, the transition point moves towards the apex and the extent of the laminar boundary layer diminishes (Hummel, 2004).

Not many papers discuss Reynolds number effects on the round-edged wing at Reynolds numbers less than 1×10^6. At higher Reynolds numbers, a turbulent boundary layer is expected at some point on the wing. Narayan & Seshadri (1987) suggested that attached flow exists over the leading edge with flow separation taking place afterwards at Reynolds numbers varying from 2.4 to 13×10^6. Leading edge separation occurs, however, near the wing tips since the induced angle of attack is highest at this position. This is associated with the downwash effect to increase the local angle of attack in the trailing edge region. In general, lowering the Reynolds number promotes flow separation at the leading edge and, therefore, the onset of the primary vortex. At a higher angle of attack, the effect of Reynolds number appears not to be significant (Szodruch, 1978).

More specific to the VFE-2 work, PSP results by Konrath in (2006a & 2008) and CFD calculation by Fritz (2008) showed that an increase in Reynolds number delays the onset of the primary vortex. This situation is shown in figure 2.19 below. A

few years earlier, Luckring (2004a) used the leading edge pressure coefficient to identify the passage of the onset of separation at different Reynolds numbers on his medium-radius delta wing. He also showed that the onset of the primary vortex is delayed as the Reynolds number is increased. The main reason for the delay is because the flow becomes progressively more turbulent as the Reynolds number increases. The turbulent boundary layer is able to sustain the adverse pressure gradient to a greater extent without separation compared with the laminar case (Hummel, 2004). The strength of the inner vortex is not much influenced by the Reynolds number, but the onset of the inner vortex may begin earlier at lower Reynolds numbers due to earlier separation.

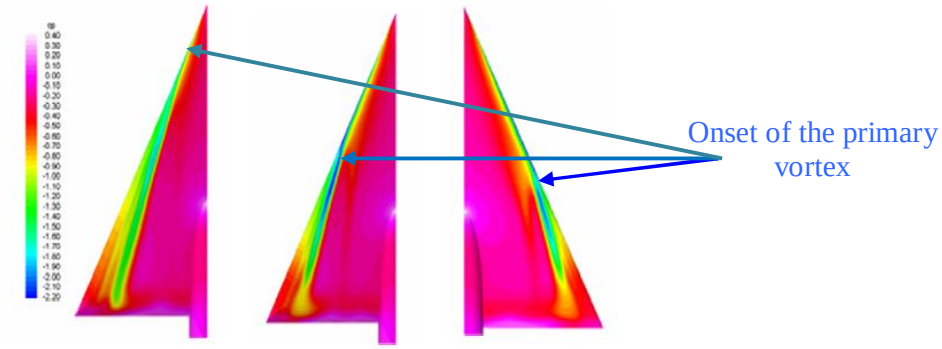

Figure 2.19: Effect of increasing Reynolds number on surface pressure contour for case Mach number of 0.4, R_{mac} = 1, 2 & 3 Million and $\alpha = 13^0$

The Reynolds number also influences the secondary separation process underneath the primary vortex. An increase in Reynolds number will shift the secondary separation line towards the leading edge with a corresponding increase in the strength of the primary vortex.

2.5.3 Variation of Mach Number

Mach number is another factor influencing the flow topology on the delta wing. At high Mach number, compressibility encourages leading edge separation and also enlarges the magnitude of the primary vortex (Luckring, 2008). However, at

higher Mach numbers, shock waves appear on the delta wing (Erickson (1991) and Narayan & Seshedri (1997)) associated with usual abrupt changes in the flow characteristics.

As the Mach number is increases to the fully compressible state, the flow closer to the delta wing surface underneath the primary vortex become completely supersonic and shock waves appear in the flow: their strength increasing with angle of attack. Strong shock waves lie between the primary vortex and wing surface. At high Mach number, the location of the secondary vortex is insensitive to the Reynolds number (Erickson (1991) and Narayan & Seshadri (1997)). Additionally, if the cross-flow reaches supersonic speeds, the secondary separation is caused by a cross flow shock wave and not by the adverse pressure gradient anymore.

Specific to the VFE-2 configurations, strong shock waves are note somewhere in front of the sting fairing and at the trailing edge, where the flow is decelerated from supersonic speed to a low speed (Konrath, 2006a, 2008b). The PSP and PIV results for the VFE-2 configurations show that the leading edge separation and the onset of the primary vortex are both promoted as the Mach number is increased. Flow fields at higher Mach number are generally much more complex with the occurrence of the shock waves; the principle vortex topology remains unchanged except the inner vortex disappears at higher Mach number (Hummel & Luckring, 2008). This is due to the stronger magnitude of the primary vortex at high Mach number that prevents the development of the inner separation.

Compressibility affects the normal force coefficient of the delta wing. The normal force results from NASA-NTF and NASA-LTPT (Luckring, 2008) show that the normal force is slightly higher in the transonic case compared with subsonic flow. This is partly due to compressibility encouraging the leading edge separations.

2.5.4 The Effect of Bluntness on Forces and Moments

A limited number of force and moment measurements have been performed to differentiate the effects of bluntness on the delta wing. A study by Kegelman & Roos (1989) showed that the lift coefficients are insensitive to the bluntness effect. This is in contrast with the wind tunnel experiments of Rinoie (1996a), Wang (2005),

Erickson & King (1992), Fletcher (1958) and Henderson (1976). They showed that, in general, the bluntness lowered the normal force coefficient at all angles of attack when compared with the sharp-edge wing case. The higher normal force on the sharp-edged wing is mainly caused by the extent of the primary vortices over the wing as compared with the round-edged wing. The attached flow region covering the front part of the round-edged wing also contributes to the reduction in the normal force value (Luckring & Hummel, 2008) as will be discussed later.

Not many results have been published on the effects of bluntness on the tangential force and pitching moment coefficients. A sharp leading edge produces a higher drag component (Rinoei, 1996a) and (Wang, 2005). This behavior is, presumably associated with the physically larger vortex structure of the sharp leading edge. The round-edged wing also exhibits lower nose down pitching moment values than the sharp-edged wing (Rinoei, 1996a) and Erickson & King (1992).

Wings with rounded leading edges also experience vortex breakdown further aft on the wing (delaying the vortex breakdown) at all angles of attack compared with sharp-edged wings (Kegelman and Roos, 1989 & O'Neil et al, 1989). In figure 2.20, O'Neil *et al* showed the vortex breakdown appeared in the trailing region at higher angle of attack for the blunt leading edge case compared to the other sharp wing configurations. They also discussed the bluntness of the leading edge delaying the upstream progression of the primary vortex towards the apex.

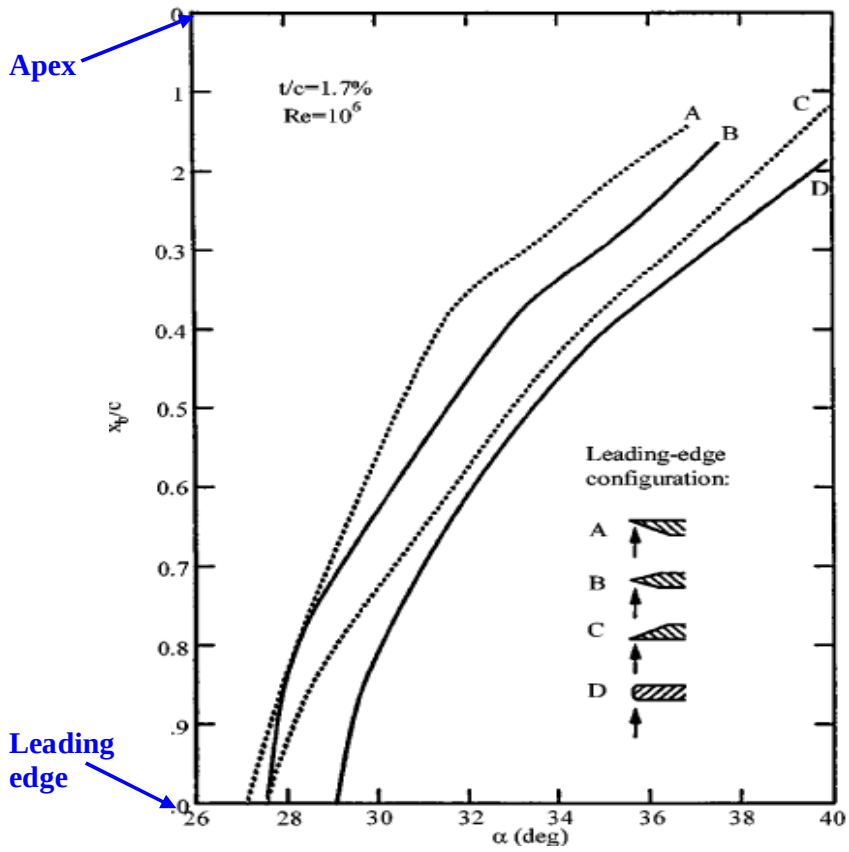

Figure 2.20: Effect of leading edge geometry on vortex breakdown (O'Neil et al, 1989)

2.6 Numerical Studies

This section will provide an overview of the results from numerical studies on delta wing flows. Very significant progress had been achieved in the development and application of numerical methods to simulate the complex flows on real aircraft over the past 30 years. There are several methods that can be used; (Gursul *et al,* 2005b)

1) Euler simulations – This calculation relies on the primary separation line being fixed at a certain location. Euler simulations predict vortex breakdown and vortical flow interactions well but cannot simulate the secondary vortex because the viscous effects (Reynolds number) is not included. For the sharp leading edge, this method of calculation is sufficient to predict the general features of the flow topology above the delta wing.

2) Unsteady RANS – Reynolds Averaged Navier-Stokes methods have the advantage of including viscosity (Reynolds number). Consequently, secondary vortex appears in the results and the flow topology of the sharp leading edge wing is reasonable. However, the methods struggle to fully capture the detail of the vortex formations on the round edged wing.

3) Detached Eddy Simulation (DES) – DES overcomes some of the limitations of the URANS approach by introducing large scale turbulence in the vortex with Large Eddy Simulation (LES). However, DES approach still has difficulty computing correctly the vortex formations on the round edged wing and predicting the flow topology arising from boundary layer transition.

4) Direct Numerical Simulation (DNS) – Direct Numerical Simulation can be used to predict the flow physics at low Reynolds number. It may be a useful tool to predict the flow topology when the flow is (essentially) fully laminar. A fully turbulent and complex geometry such as delta wings are probably the challenges for DNS.

A major difficulty faced by numerical viscous methods is that the accurate prediction of transition is very difficult. Accurate calculation of vortical flow above the delta wing depends mainly on the status of the boundary layer and the appearance of the secondary vortex significantly adds to the complexity of the numerical calculation (Drikakis, 2003). Visbal & Gordnier (2003) used the Euler simulation to calculate the vortex flow above a 75^0 swept sharp-edged delta wing at several different Reynolds numbers. At very low Reynolds number, smooth laminar flow initiated the primary vortex that extended from the apex to the trailing edge. As the Reynolds number was gradually increased, transition appeared in the trailing edge region and extended towards the apex as the Reynolds number was further increased.

To differentiate the effect of laminar and turbulent flow, Agrawal (1992) applied the Navier-Stokes equations, calculating the vortex properties of the sharp-edged delta wing using a fully laminar and fully turbulent assumption. He found several discrepancies between the two cases in terms of the vortex properties. For example, the laminar solution showed a much larger secondary vortex than the turbulent solution. Moigne *et al* (2001) also noted a similar effect, comparing the laminar calculations with experiment.

Within VFE-2, CFD simulations were performed at several research institutions across Europe and the United States on both the sharp and medium-edged wings. Table 2.1 shows the organizations, CFD codes and turbulence models used in the simulations. The vortex systems of the sharp and medium-edged wing were calculated in order to compare with the experimental work. Most of the work within VFE-2 was performed with fully turbulent RANS simulations.

Organization	Grid Type	Grid size	Code	Turbulence Models
EADS	Structured	~ 10 x 10^6	FLOWer	Wilcox k-ω
KTH	Structured	~ 7 x 10^6	EDGE	EARSM + Hellsten k-ω
NLR	Structured	~ 4 x 10^6	ENFLO	TNT k-ω + Vorticity Correction
TAI	Structured	~ 2 x 10^6	TAI-xFlowg	SA
UG	Structured	~ 7 x 10^6	PM3D	TNT k-ω + Vorticity Correction
DLR	Unstructured	~ 16 x 10^6	Tau	SA, Wilcox k-ω
USAFA	Unstructured	~ 26 x 10^6	Cobolts	SA and SA-DES

Table 2.1: Organizations, codes and turbulence models used for CFD simulations

Le Roy & Riou (2008) showed that their numerical calculation at moderate angle of attack and a Reynolds number of 2 x 10^6 differed from the experimental results of NASA (Chu & Luckring, 1996) at similar test conditions. This was typical of the entire VFE-2 activity that showed discrepancies between the numerical and experimental studies. The onset of the primary vortex from their calculation is slightly over predicted compared to the experimental works.

For the medium-edged wing, Fritz & Cummings (2008) compared the numerical results with the Pressure Sensitive Paint (PSP) results from DLR (Konrath *et al*, (2006a)). The first point of comparison was the onset of the primary vortex in order to verify the correctness and accuracy of the CFD simulations. The results are depicted in figure 2.21. It highlights the extent of the challenge for CFD to calculate the flow above the round-edged delta wing. The location of the primary vortex onset varies between solutions and most of them predicted onset further upstream compared with the experiments. Only the results calculated by Fritz (2008) appear to capture the onset of the primary vortex when compared with the PSP results. Another obvious feature from the comparison is that all the numerical studies predicted a very weak inner vortex compared with the experiments. Fritz & Cummings (2008) and Le Roy & Riou (2008) suggested that the very weak inner vortex in the CFD calculations is

caused by the primary vortex being estimated to originate further upstream when compared with the experiments. This delays the development of the inner vortex. It can be concluded from figure 2.21 that an accurate prediction of the inner vortex may depend strongly on an accurate calculation of the primary vortex. More work is still in progress to try to improve the fidelity of the CFD simulations.

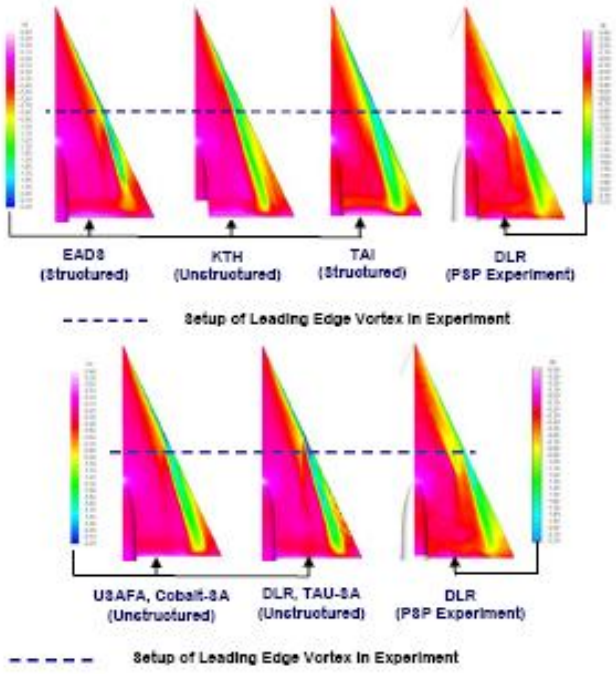

Figure 2.21: Surface Pressure maps and onset of leading edge separation at Mach number 0.40, $\alpha = 13^0$ & Reynolds number of 3×10^6. (Fritz & Cummings, 2008).

Discrepancies in the numerical studies may also arise from the grid resolution and the quality of the turbulence model but the most important parameters is likely to be the location of transition on the round leading edge. Fritz (2008) and Fritz & Cummings (2008) mentioned that the results obtained from CFD can be under or over predicted depending on the location of transition and the actual Reynolds number on the wing. The importance of transition for the CFD simulations was again emphasized by Fritz in related work. Two different turbulent simulations were performed; the first without fixing the transition line and the second with the transition line fixed at 0.3%

of the wing-span from the leading edge. The results (Fritz, 2008) from the first simulation showed that increasing the Reynolds number moved the onset of the leading edge separation upstream. The second experiment, however, showed that increasing the Reynolds number delayed the onset of the primary vortex. This illustrates that the results obtained are very sensitive to the transition location and the accuracy of the primary vortex is only achieved where transition is correctly captured.

In contrast to the above, Crippa (2008) reports that his results at very high Reynolds number compare well to the experimental results of Chu & Luckring (1996). This may be because laminar flow is confined to a very small area close to the apex, with the rest of the wing being covered by turbulent flow.

Despite the issues denoted, good information on the flow evolution has been obtained from the CFD simulations. Gurdamar *et al* (2008) conducted simulations on the VFE-2 configuration at various angles of attack, Mach numbers and Reynolds numbers. These showed the upstream movement of the leading edge separation and the strengthening of the primary vortices as the angle of attack was increased. They also showed that higher Mach number promotes leading edge separation. The general effects of leading edge bluntness on the flow topology above the round-edged wing were also well predicted by Gurdamar *et al* (2008).

CFD can provide considerably more detail on the 3-dimensional flow topology on the round-edged wing than wind tunnel experiments. For example the streamline and pressure field information provided by the simulations of Cummings & Schutte (2008) and Schutte & Cummings (2008) as shown in figure 2.22 provides considerable insight into the bluntness effects on the delta wing. The example shown is at an angle of attack $\alpha = 13.3^{o}$, Mach number of 0.4 and Reynolds number of 3 x 10^{6}. For this case the gross flow topology is similar to that identified in experiments.

Initially, the flow at the apex is attached to the surface of the wing and is smeared into the leading edge suction area. The flow is then diverted towards the leading edge area and separates into a shear layer that rolls up into a swirling flow. This roll up process results in the formation of the inner vortex. This contrasts with the observations of Delery (1992). He described the inboard separation as a "bubble separation" that initiated at a saddle point in the flow. While a bubble separation may occur, the formation of the inner vortex may not depend on this.

In the leading edge region, figure 2.22, separation occurs and rolls up to form a primary vortex downstream from the onset of the inner vortex. On inboard sections of the wing, the inner structure extends downstream and reaches a maximum size and strength at a point near to the onset of the primary vortex. CFD studies also show the strength of the inner vortex then decays, as the primary vortex grows in strength and size. The reason for the decay in the inner vortex strength as the primary vortex develops is discussed by Cumming & Schutte (2008). They agree with the observations of Furman & Breitsamter (2008) as discussed earlier in section 2.4.4. During the initial development of the inner vortex, the leading edge separation from the lower surface feeds and promotes the inner vortex up to a certain distance from the apex. After the primary vortex is fully formed, the separating flow no longer feeds the inner vortex, but rather begins to feed the outer vortex thus reducing the strength of the inner vortex.

The results obtained from the numerical analysis of the VFE-2 campaign reveal a distinct contribution of CFD to well predict the vortical flow above round-edged delta wings.

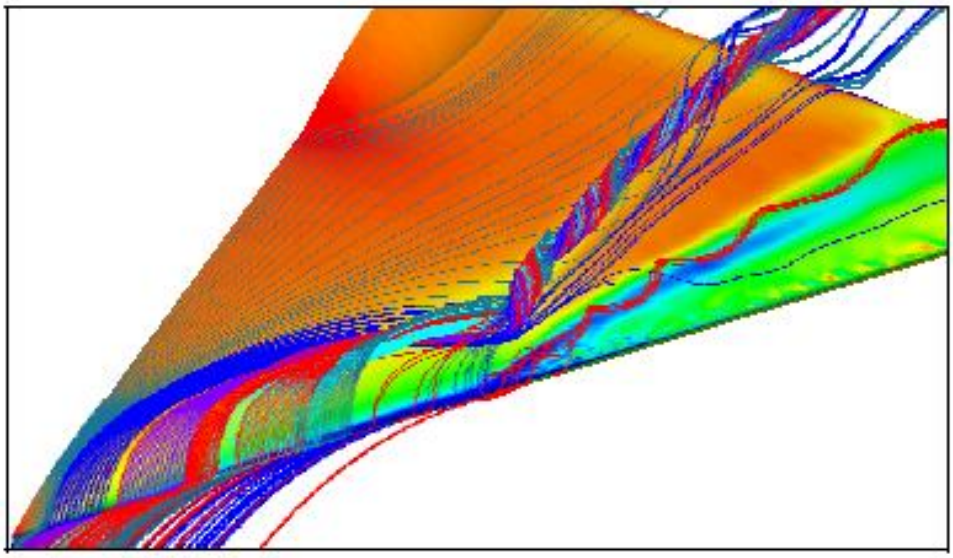

Figure 2.22: Streamlines and pressure distribution calculated using the TAU DLR code at Mach number 0.40, $\alpha = 13.3^0$ & Reynolds number of 3×10^6 (Schutte & Ludeke, 2008)

Three-dimensional flows over the round-edged wing at high speed are complicated by the occurrence of shock waves and the associated sudden decrease in the speed on the wing (Chakrabatty *et al*, 1998). Within the VFE-2 programme, Crippa (2008) calculated that the shock wave occurred at the end of the sting fairing. The complexity of the flow-field with the shock wave is discussed by Schiavetta *et al* (2008) and Fritz & Cummings (2008). The shock wave will interact with the primary vortex and then significantly affect/promote the vortex breakdown as shown in figure 2.23. Schiavetta also reported that there were two other regions for shocks; *1)* the area in the middle between the wing centre line and the leading edge and *2)* near to the trailing edge (Schiavetta *et al* (2008)). These shock wave locations may vary with angle of attack. The main area of the shock-waves on the VFE-2 configurations is shown in figure 2.23.

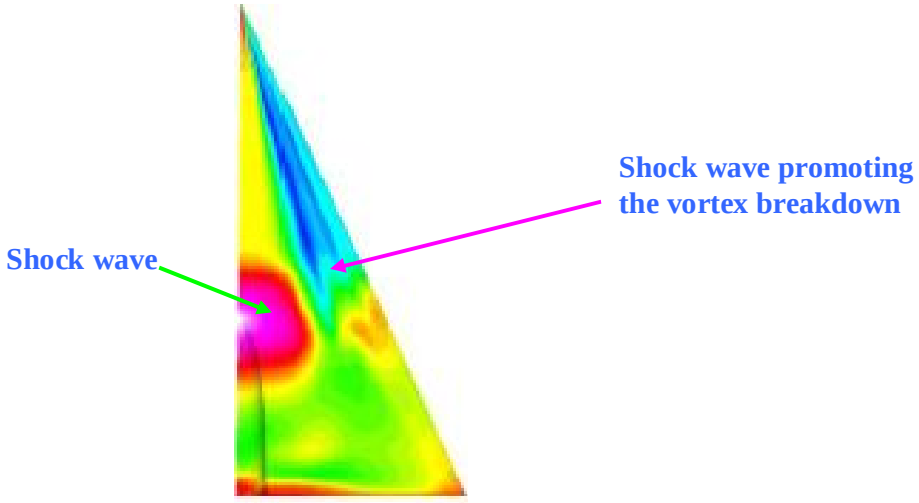

Figure 2.23: Location of shock wave above delta wing at Mach number = 0.85, R_{mac} = 6 x 10^6 & $\alpha = 23^0$ (Fritz & Cummings, 2008).

2.7 Unresolved Issues and the Current Study Programme

Comprehensive experiments and numerical data have previously been published for sharp-edged delta wings. Nevertheless, relatively few experimental or simulation databases are available for round-edged wings outside of the VFE-2 studies. Comprehensive and state of the art results for the round-edged wing (medium case) are available in the VFE-2 virtual library. The difficulties in obtaining the location of transition, the occurrence of the inner vortex and the effect of bluntness on the magnitude of the primary vortex are the issues that this team has identified, as being key to improved understanding of the flow evolution on round-edged delta wings. The researchers conclude that further studies are needed to address these issues. There are few unresolved issues either by experiments or simulation method particularly on the blunt leading edge wings;

1) Further experiments to measure the status of the boundary layer for the VFE-2 configuration with sharp and medium rounded edges. As a starting point, investigations of the boundary-layer state should be performed at an angle of attack $\alpha = 18^0$, where the vortex is fully developed for the sharp-edged wing and where the primary vortex for the medium-edged wing is expected to reach the apex. At this angle of attack, the fact that the flow is expected to be fully separated without breakdown on both wings could simplify the analysis. In addition, a case where the flow is partly separated and partly attached at about $\alpha = 13^0$ should also be studied. PIV will be carried out at Argyll wind tunnel and a detail outlook of the laminar/turbulent status should be determined particularly in the region close to the apex. PIV data in the region close to the apex is not widely available.

2) Leading edge separation on the medium-radius wing is known to initiate at the trailing edge where the thickness ratio of leading edge radius to local half span reduces (Luckring & Hummel, 2008). Despite several experiments dedicated to the development of the primary vortex at low angle of attack, there is still a lack of clarity on its development in the leading edge area. The

detail of the interaction between the leading edge separation and the roll-up process of the inner separation also needs to be clarified and should be further investigated using PIV at low angles of attack and with different bluntness profiles. A better overview of the bluntness effect on the development of the primary vortex can be obtained by comparing the results at different leading edge radius. Regardless of leading-edge radius, the increase in relative sharpness of the wing cross-section as trailing edge is approached should mean that the roll-up process should start there. The leading-edge radius will, however, inevitably influence the phasing of this.

3) Luckring (2008) has compiled CFD and experimental results to characterise the inner vortex; the inner vortex is initiated by a concentration of vorticity around the leading edge near to the apex of the wing. This concentrated vorticity then grows to form the inner vortex. PIV experiments should be used to investigate this interesting feature during the initial development of the inboard separation.

4) The effect of Mach number within the subsonic region also needs further investigation. Even within the subsonic region, the experimental results reported by Furman & Breitsamter (2008) showed that the inner vortical structure totally disappeared at an angle of attack, $\alpha = 18^0$, Reynolds number of 2×10^6 and Mach number 0.37. As will be shown later, the flow visualization studies performed at lower Mach number (0.12) in the current study concluded that the footprint of the inner structure still exists at this angle of attack and can extend up to $\alpha = 23^0$. The differences between the two experiments at this stage are thought to be caused by compressibility effects rather than Reynolds number. An increase in Mach number at constant Reynolds number increases the compressibility effect and so increases the swirling magnitude of the primary vortex. A stronger primary vortex in the leading edge area for the Furman & Breitsamter (2008) case is thought to prevent the development of the inner structure. The effect of Reynolds number may not be significant, since, as will be shown in the current study, the inner

vortical structure appears at 1 x 10^6 Reynolds number as well as at a higher Reynolds number of 4.5 x 10^6 (Cummings & Schutte, 2008).

As mentioned previously, four sets of leading edges, representing sharp, small, medium and large-edged wings have been manufactured for the current study. Although VFE-2 focused on the medium and sharp-edged wings, further insight into the bluntness effect should be gained by considering leading edges with different radii. The current study will provide that insight.

Chapter 3

3.0 EXPERIMENTAL SET UP & WIND TUNNEL TESTING

3.1 Project Overview

The model and the test rig were originally constructed to be part of the Vortex Flow Experiment (VFE-2) campaign. The design was based on the original NASA geometry tested in the NASA-NTF and NASA-LTPT wind tunnels. The geometry of the original NASA model is shown in figure 3.1 and the analytical description of it is shown in appendix A. The model has three main sections; the first is the main flat-plate delta wing without leading or trailing edge. The second part is the leading-edge assembly. There are four sets of leading edges i.e.; sharp, small, medium and large that correspond to ratios of the leading edge radii to the mean aerodynamic chord of 0, 0.05, 0.15 and 0.3 respectively. The final part is the sharp trailing edge portion. For the VFE-2 work, 2 wing models were tested; i.e. the sharp and the medium edged configurations. The small and large-edged wings were subsequently tested to provide better insight into the effects of bluntness.

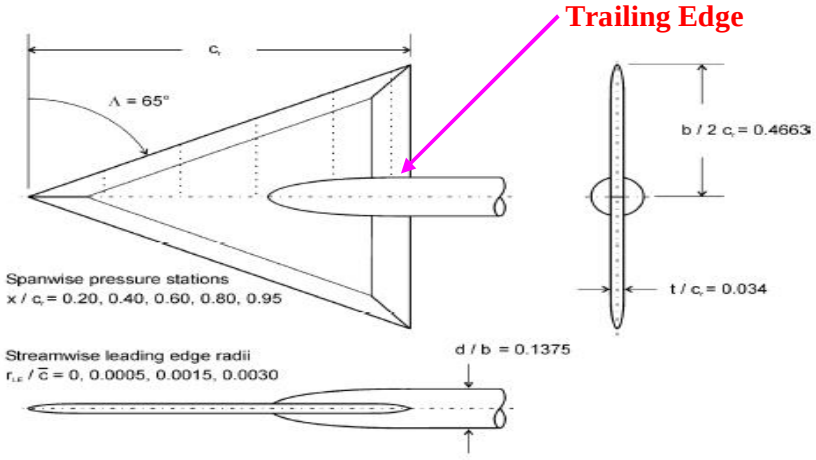

Figure 3.1: The geometry of original NASA (Chu & Luckring, 1996) delta wing showing the interchangeable leading edges

3.2 Glasgow University Model Descriptions

The model constructed for this study replicates the exact NASA (Chu & Luckring, 1996) leading and trailing edge profiles. The model was to be tested in the Glasgow University Argyll low speed wind tunnel. The specifications of the Glasgow University Argyll Wind Tunnel is shown in table 3.1.

Maximum Speed	76 m/s
Test Section	2.65 x 2.04 meter
Moving Ground	3.75 x 1.9 meter
Moving Ground Speed	60 m/s
Mechanical Balance	6-component

Table 3.1: Argyll Wind Tunnel Specifications

The root chord of the model was chosen as 1.059 metres so that the highest Reynolds number of 2 x 10^6 could be achieved at a speed of 41.23 m/s based on the mean aerodynamic chord of 0.70585 metres. The new model had a maximum span of 0.987 metres, a wing area of 0.5223 m^2 and a wing aspect ratio of 0.953 making it the physically largest model in the VFE-2 project. The thickness of the basic flat plate was 36 mm. All four sets of leading edges were manufactured at the same time. A trailing edge was also machined following Chu & Luckring's (1996) analytical function. All the delta wing components were machined from aluminum giving a total model weight of 39.5 kg.

3.3 Conceptual Design of the Sting

The sting structure was designed to replicate the original Chu & Luckring (1996) test rig. The original wing model was positioned in a straight line with the centre of rotation and connected to short sting that was offset by 10^0. The short sting was then connected to another sting section also angled at 10^0 in the opposite sense to this line called the stub sting. The stub sting was then connected to a circular automated arc sector that provided angle of attack changes from negative to positive pitch. The movement of the circular arc was powered by an electrical motor allowing the angle of attack to be controlled automatically. The short and stub sting were covered by an analytically defined fairing according to the functions presented earlier in this chapter. The model angle of attack range that could be achieved using this sting configuration in the Argyll wind tunnel was not sufficient due to the physical constraints of the wind tunnel. The angles of the sting section were, therefore, adjusted to address this issue.

Based on this general configuration, the conceptual design of the Glasgow University sting support structure is sketched in figure 3.2. The key parameters during the initial design stage were; *1)* to minimise the interference from the support structure, the support structure should be positioned at least at two root chord lengths behind the wing trailing edge. *2)* the height of the Argyll wind tunnel is 2.04m., *3)* the model should be able to be pitched up to at least 25^0 *4),* the model chord length itself was 1.059 metres and the model weight was 39.5 kg.

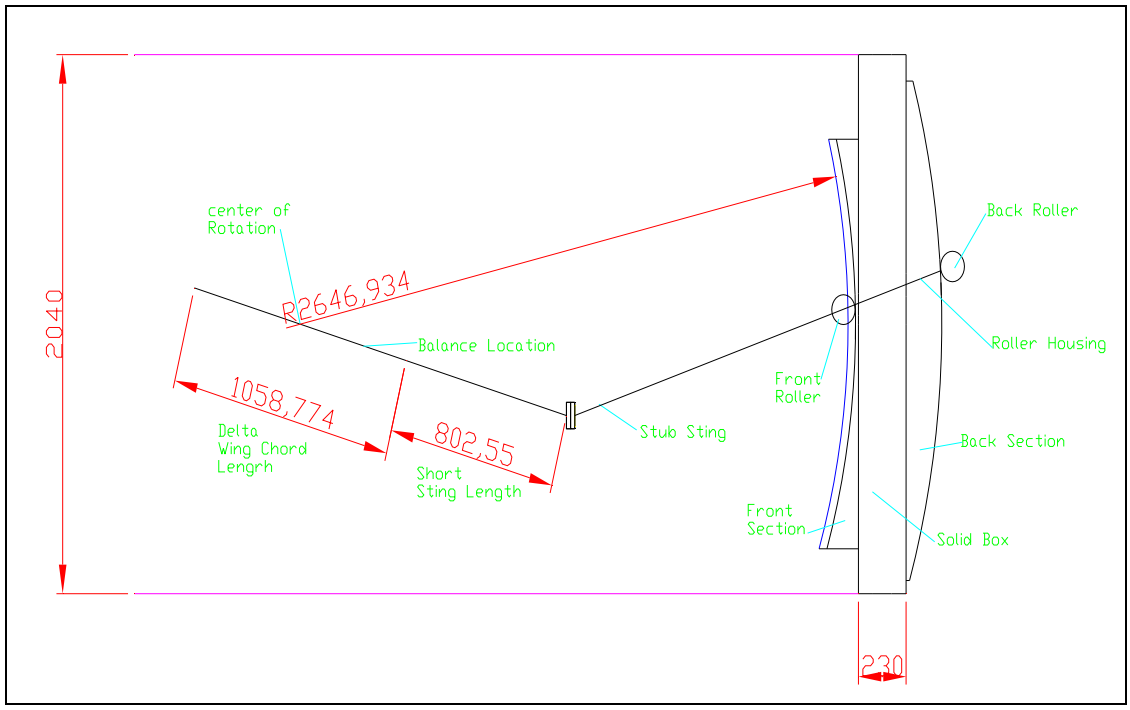

Figure 3.2: Conceptual design of the Glasgow University test rig

The wing/sting assembly consists of 3 main sub components; i.e. the wing, short sting and stub sting. The short sting, closest to the wing, is set at angle of 15^0 to the straight line between the center of rotation and the mounting point on the support section. The short sting is then connected to the stub sting that is offset from the straight line between the mounting point and the centre of rotation by 15^0. The short and stub sting angle were adjusted to 15^0 respectively compared to 10^0 for both stings of the Chu & Luckring (1996) test rig to achieve the desired angle of attack range. To create the interface between the stub-sting and the main support structure, 2 rollers were attached to the stub sting as sketched in figure 3.2. These two rollers were connected to each other by a very strong gas spring arrangement. The main function of these 2 rollers was to ensure the stub component would glide up and down along the 2.65 meter radius. Factory track and cam rollers were used as a back and front rollers respectively and this arrangement is shown in figure 3.3. It should be noted that, unlike the set-up of Chu and Luckring, the radius section used in the current tests

did not move. There was insufficient clearance above and below the wind tunnel for this to occur. This necessitated the sting moving around the radius.

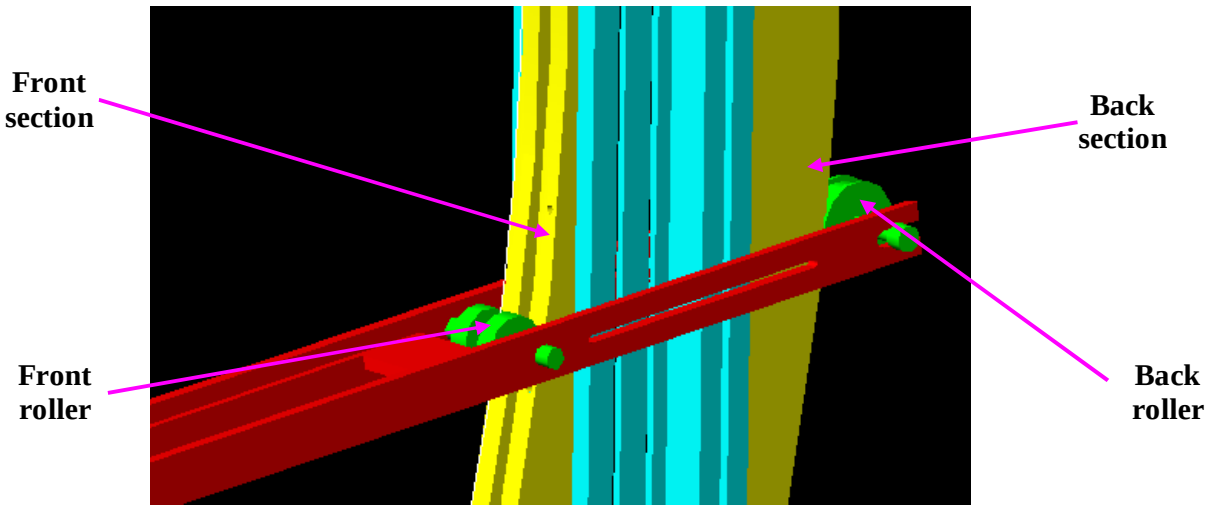

Figure 3.3: The arrangement of the rollers

In the initial design, the two rollers engaged with the front and back of the radius support. The front section had a radius of 2.65 metres and the -aft *section* had a radius of 3.1 metres (also shown in figure 3.3). These two sections created parallel radii originating from the centre of rotation. The angle of attack was determined by moving the stub-sting component around the radius about a constant centre of rotation at the model.

Both sections were bolted to the radius support structure. The support structure located all the way from the roof to the floor of the wind tunnel. Initially, two C-shaped steel structures were proposed as the main support structure. They were to be mounted parallel to each other in the middle of the wind tunnel as shown in figure 3.4.

An H-shaped beam structure was proposed for the stub sting. The H-shaped beam was chosen because of its strength in both; lateral and vertical directions. The front cam roller of diameter 98 mm and back track roller of diameter 96 mm were placed within a cut-out in the H-shaped stub-sting as shown in figure 3.4. Both rollers were attached to each other by a gas spring arrangement. To firmly locate the sting in a specific position, the H-shaped stub-sting was to be bolted through to the radius

support structure as a locking mechanism during the experiment. To reduce the overall weight of the sting structure, two rectangular holes were to be cut out of the H-shaped stub sting as shown in figure 3.4.

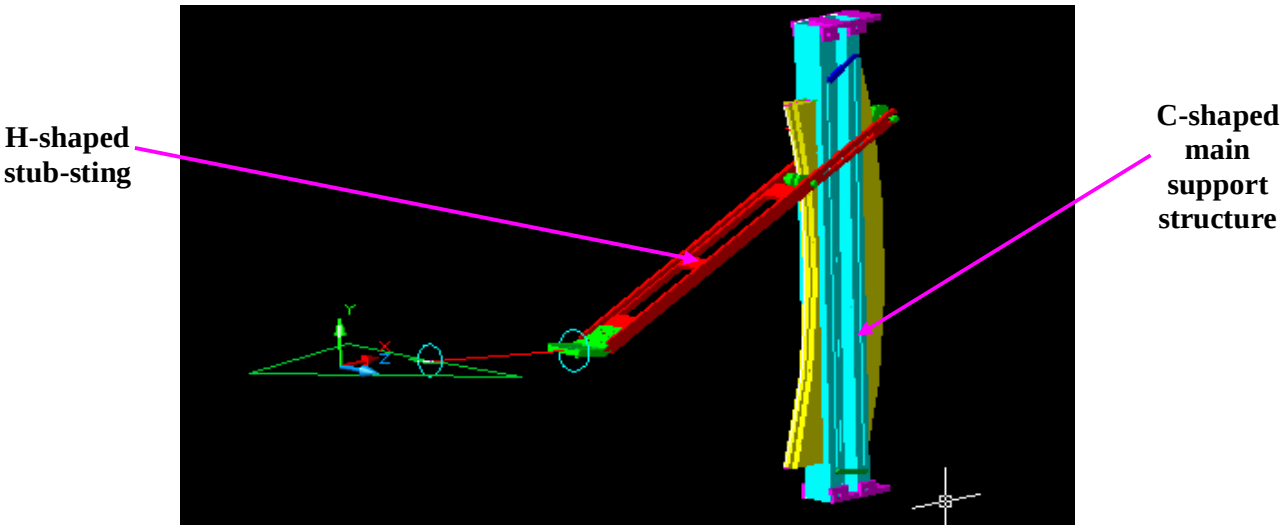

Figure 3.4: The attachment of stub-sting to the section

An H-beam structure was also proposed for the short sting. This structure would be connected to the stub sting through a fabricated connector. This arrangement is shown in figure 3.5. The connector would be fabricated from steel in the Argyll wind tunnel workshop.

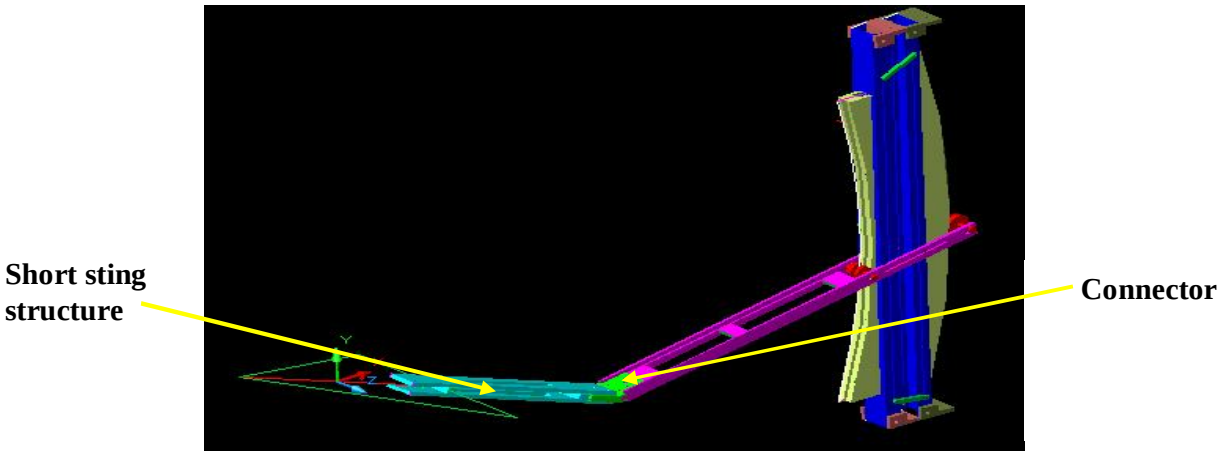

Figure 3.5: Proposed design structure

A 6-component AMTI MC-3 series transducer was chosen to measure the forces and moments of the model. This 6 axis transducer would be placed at the end of the short sting 857 mm from the apex of the wing or 81% of the wing root chord, as shown in figure 3.6. The transducer is a cube of dimensions 76 x 76 x 76 mm with four threaded ¼-20 inserts on the top and bottom surface. Its top surface would have been bolted through to the delta wing whilst the bottom surface would be attached to the short sting. The model pitching moment would be resolved at the two-thirds chord location from the wing apex for consistency with Chu & Luckring (1996). Thus, the moment arm between the transducer reference point and the resolved point is 15.1 cm.

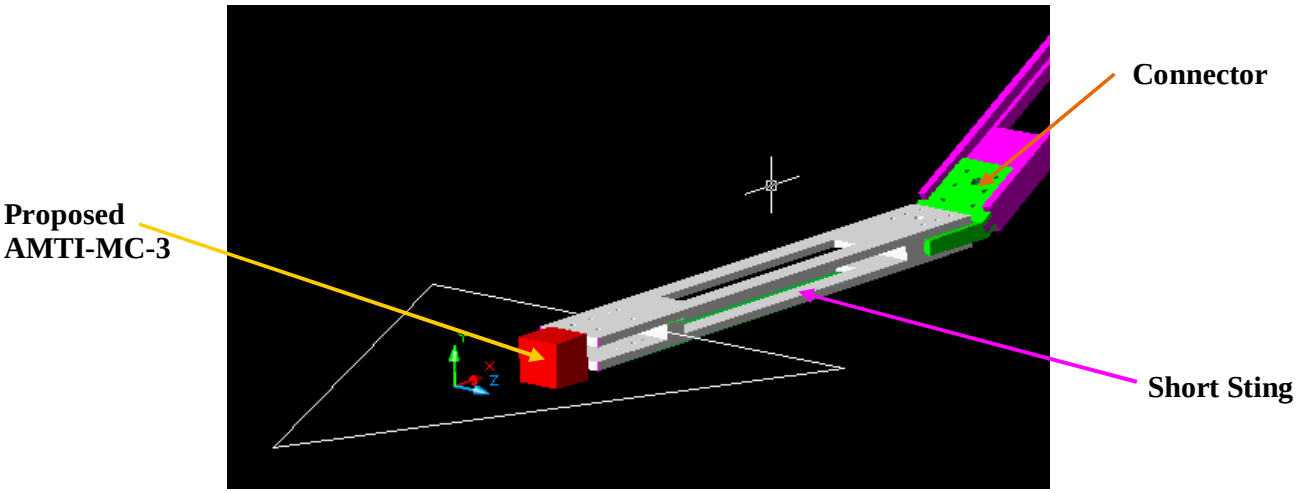

Figure 3.6: Proposed location of the AMTI-MC-3

Finally, the wing and short sting interfaces would be attached to the short sting as shown in figure 3.7. These two components would be machined from the wood into two sections; lower and upper surface.

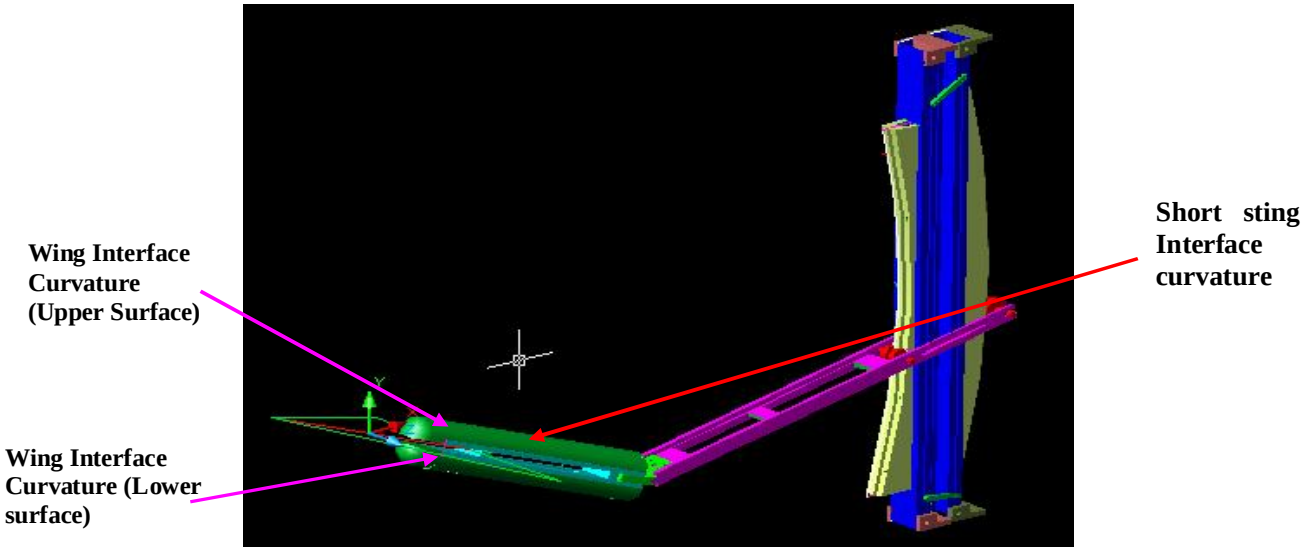

Figure 3.7: The attachment of the short sting and wing interface curvature to the short sting

This preliminary design threw up some issues that required further consideration

- The sting would deflect downwards because of the weight of the model and the sting itself. The required angle of attack, locking mechanism and centre of rotation may be adversely affected by this deflection. A stiffer structure was needed to overcome this problem.

- The second issue was the limited ability of the MC-3 transducer to measure the pitching moment at higher angles of attack and speed; thus several choices of higher capacity transducers were considered.

- The shape of the connector between the sting sections was complicated. This would complicate the machining process, thus a simpler connector design was required necessary to overcome this problem.

- The quality of the C-shaped steel for the main support structure obtained from the supplier was not good.

3.4 Final Design

Several modifications on the design were introduced to address these issues;

- Another structure, called the *roller housing*, was introduced to the design to improve the beam deflection problem and increase the effectiveness of the locking mechanism. The roller housing was set at an angle of zero degrees with respect to the centre of rotation and the wind flow direction. The roller housing would attach to the stub sting that would be set at an angle of 17 degrees. The stub sting would join the short sting that would be set an angle of 15 degrees in relation to a straight line between the centre of rotation and the mounting point on the support structure. The model angle of attack could be set by moving the roller housing around the support section. The centre of rotation would remain constant at half of the wing root chord as proposed earlier.

- The C-shaped support structure was replaced by a solid box section fabricated and assembled from four pieces of aluminium.

- The MC-3 transducer was replaced by a heavier capacity load cell to measure the pitching moment at higher angles of attack and speeds.

3.4.1 Final Design Detail Descriptions

The final design of the sting structure is shown in figure 3.8. The detailed descriptions of each component will be presented in this section.

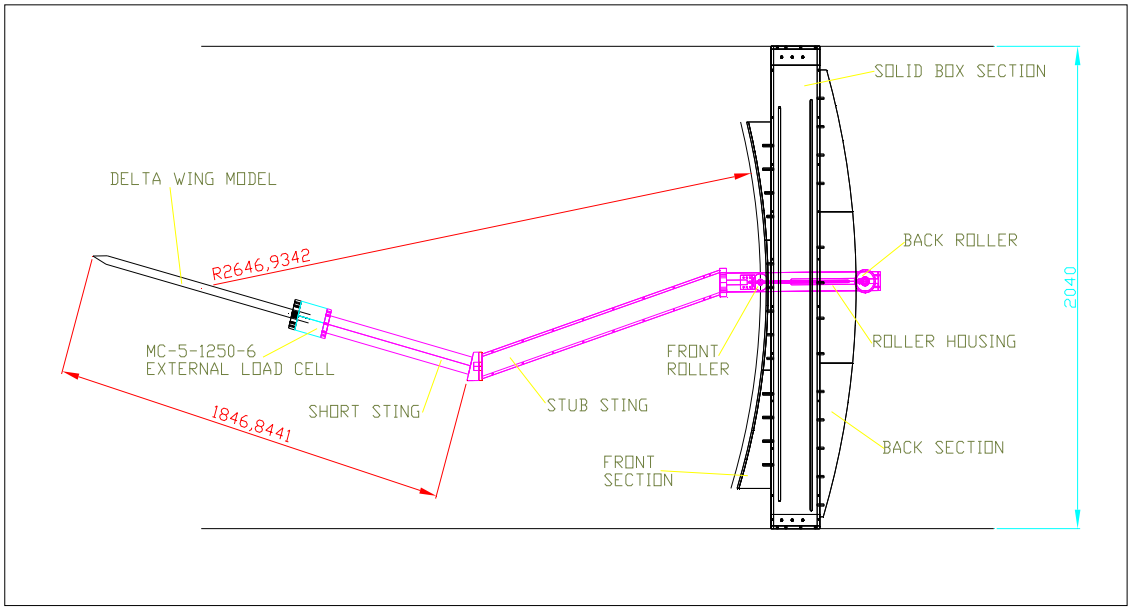

Figure 3.8: Final design of Glasgow University test rig

The model and sting were supported by a strong 15 x 23 cm. solid box section extending all the way from the roof to the floor of the test section as depicted in figure 3.9. Its sides were alluminium plate of length 2040 mm, width 230 mm and thickness 20 mm. These two pieces were positioned streamwise in the test section. Extra 2 pieces of alluminium of height 2040 mm, width 150 mm. and thickness 20 mm were joined to the front and rear faces of the structure to form a solid box. The front and back curved sections of the support were bolted to this box structure.

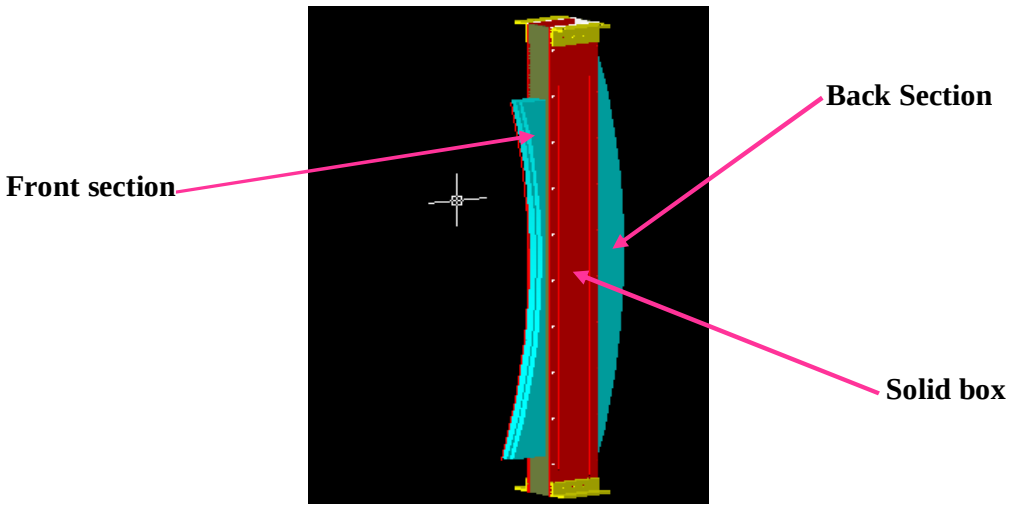

Figure 3.9: Glasgow University's main support structure

Figure 3.10 shows the way of interfacing the roller housing with the main support structure. Two factory cam rollers were embedded in the roller housing creating an interface between the sting structure and the sections. Both rollers were then attached to each other by strong gas springs of diameter 10 mm. The rollers were intended to glide up and down along the 2.65 meter radius allowing the angle of attack to be varied from 0^0 to 25^0. A slit of 10 mm was also machined in the middle part of the roller housing and corresponding 10 mm slits were machined in the box section. A locking mechanism between the sting and the support structure could be engaged by bolting through these slits.

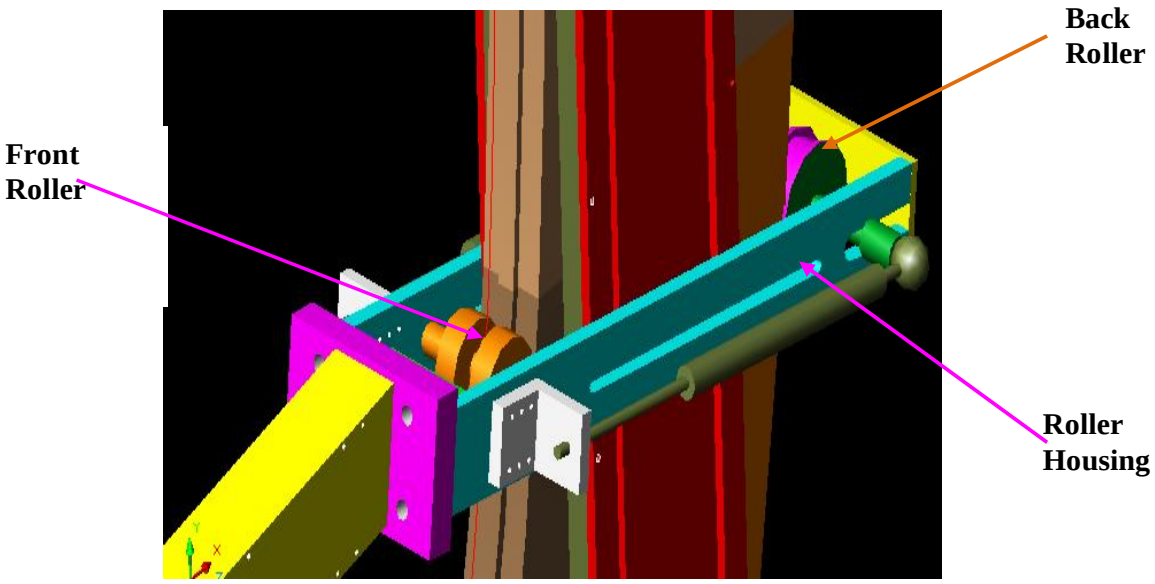

Figure 3.10: Detail arrangement between the rollers, roller housing and support structure

The end corner of the roller housing was welded to a piece of connector fabricated from steel of thickness 12 mm. It was decided to replace the original H-shaped stub sting with a rectangular box section in order to reduce the beam deflection at the rotation point. The stub sting was welded to the steel plate connector. The stub sting was then connected to the 15 degrees short sting, which was the closest component to the model. Two rectangular pieces of metal were used to connect these two stings. In order to simplify the rest of the design from the short sting to the model, a cylindrical alluminium tube of radius 42.3 mm and the length 0.7 m. was used as the short sting.

The MC-3 load cell was replaced by a heavier capacity transducer provided by the AMTI Corporation; the MC-5-1250-6. The factory modified transducer had two advantages compared with the previous load cell. This transducer had a higher moment capability and it was therefore more suitable for the experiments at higher speed and angle of attack. Secondly, it is a cylindrical type load cell with 8 mm. threaded holes on the flat top and bottom surfaces of the load cell. This allowed the bottom surface of the load cell to be bolted directly to the cylindrical short sting and the top surface to be bolted to the wing model. A three-dimensional image of the final

test rig is presented in figure 3.11. The transducer (magenta in color) is placed between the short sting and the model. In order to avoid engagement between the load cell and the wing interface fairing, the transducer was located parallel to the wing trailing edge. This meant that the moment arm between the balance reference point and the force and moment reference point on the wing was 37 cm.

All the components were machined in the Argyll Wind tunnel workshop and the final assembly is shown in figure 3.12. The test rig and the model profile replicate exactly the original Chu & Luckring (1996) geometry from the wing apex to the short sting ends. Nevertheless, several minor changes were made downstream of this in order to simplify the design and manufacturing process. One of them was that a cylinder of diameter 20 cm was used for the stub sting shape. The original NASA sting was curved but no description was provided for this complicated profile in the NASA (Chu & Luckring, 1996) report. Secondly, the Glasgow University test rig was designed so that the offset angle of the short and stub stings were 15^0 and 17^0 compared to 10^0 for both stings in the NASA configuration. This modification was made to achieve the desired angle of attack range in the Argyll wind tunnel.

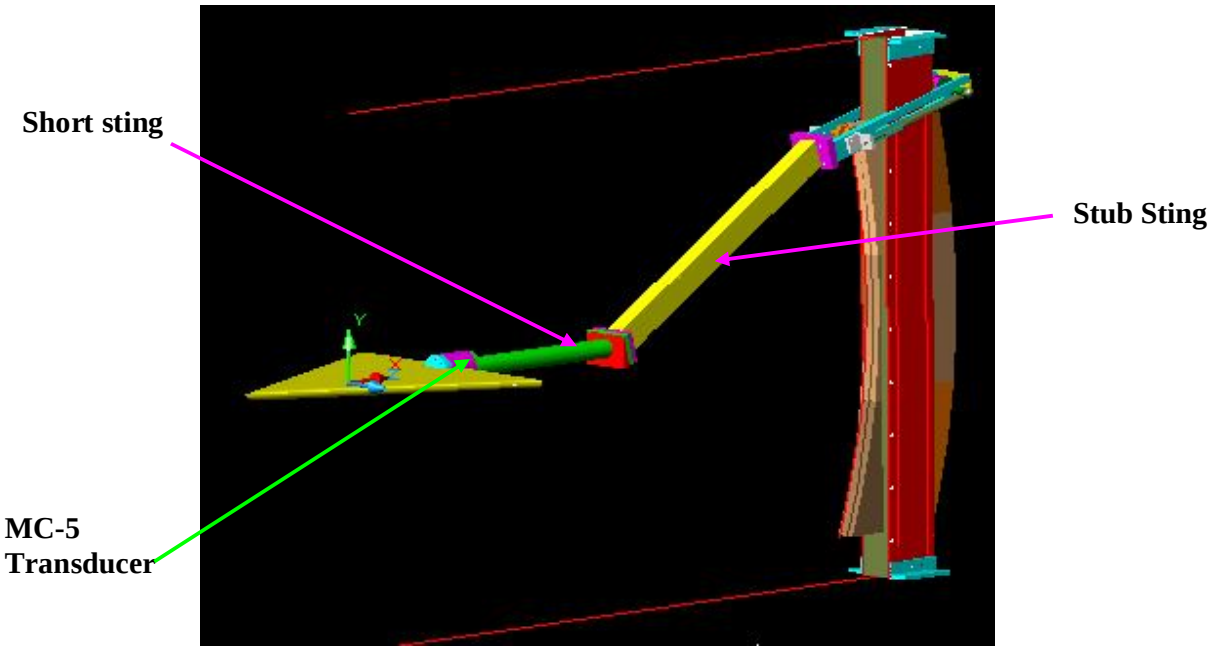

Figure 3.11: 3-D view of the test rig assembly

3.5 Problems During Wind Tunnel Set-Up

Some mechanical problems occurred when the components were assembled in the wind tunnel test section. The main problem identified was that the locking mechanism between the roller housing and the main support structure was inadequate to support the weight of the model and the sting components. The gas spring that was proposed during the design stage was also inadequate to fully engage with the rollers. These two weaknesses caused the sting to slide down without following the curve as expected. Several minor modifications to strengthen the locking mechanism were implemented. Two pieces of steel plate with slits in the middle of them were welded on the top and bottom of the roller housing. With this modification, 4 extra bolts used to engage the roller housing to the support structure. Additionally, a stronger 20 mm. diameter tension spring replaced the original 10mm gas spring.

Another problem found during this stage was the difficulty in maintaining a constant centre of rotation of the sting structure. Two strong winches solved this problem; one winch was attached to the short sting and the other to the stub sting. These two winches were hung from an additional structure located above the roof of the wind tunnel. These winches assisted the rollers to slide up and down on the radius section as the model was manually pitched at the centre of rotation. Both winches were then removed after the roller housing was firmly attached to the support structure.

3.6 Glasgow University Sting Support Structure

The final assembly of the test rig in the Argyll Wind Tunnel of Glasgow University is shown in figure 3.12. The fairings for the short sting and wing interface were manufactured in carbon fibre. These two fairings were then placed on the wing and short sting as shown in the figure 3.12. During the initial experiments, the model exhibited vibration, particularly at higher angles of attack and speeds. In order to resolve this, lateral and vertical bracing wires were attached to the sting providing additional stiffness. These can also be observed in figure 3.12.

Figure 3.12: Glasgow University's delta wing model in the Argyll wind tunnel at high angle of attack.

A problem that arose during the initial experiments was measuring the correct angle of attack during the tests. It was observed that the wing incidences were slightly higher than expected especially at a higher angle of attack and higher speed due to the wind loading. The lateral and vertical bracing wires were used to minutely adjust the planned wing angle of attack before the experiments but the deformation of the rig under load changes this angle. In order to monitor the correct angle of attack during the experiments, a Digital inclinometer with 0.005^0 accuracy was placed on the wing (shown in figure 3.13) under the wing interface fairing.

Another problem that arose during the initial experiments was that the normal force results were lower than expected. The difference was caused by engagement between the transducer and one of the fairings. A minor modification to the short sting and wing interface fairings had to be made to ensure that no transmission of load occurred through the fairings.

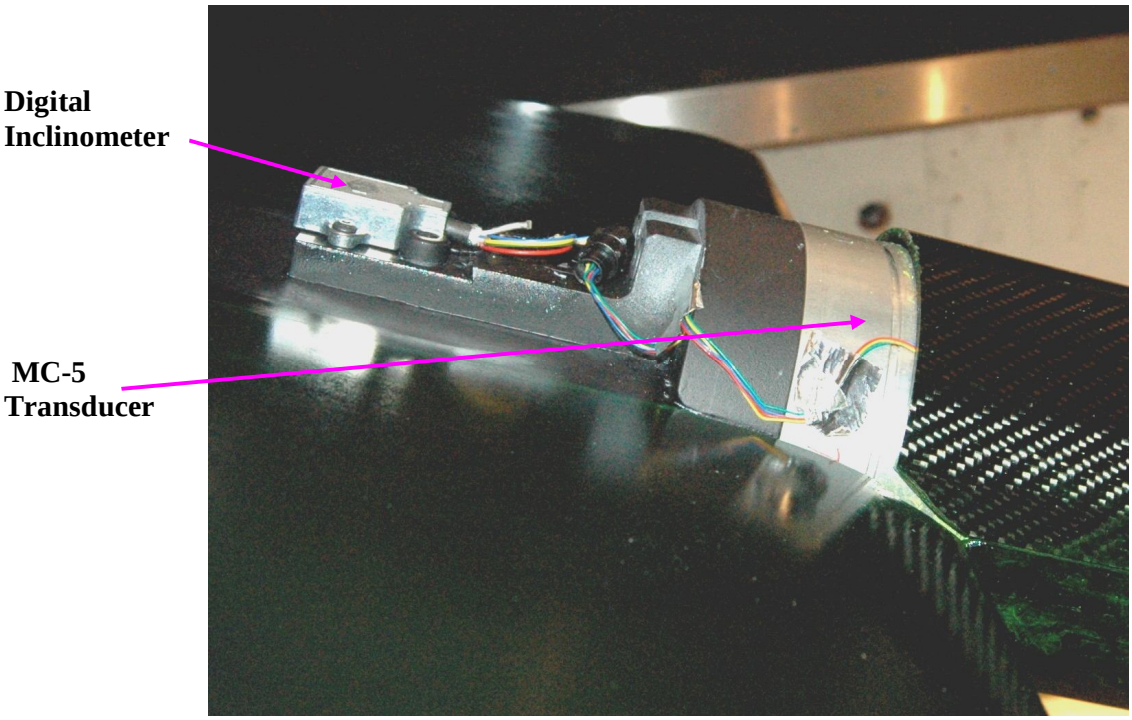

Figure 3.13: Balance and inclinometer attachment to the delta wing.

3.7 Wind Tunnel Testing Techniques

3.7.1 Introduction

There are several experimental techniques that can be used for experimental research in delta wing aerodynamics (Gursul *et al*, 2005b). These include the following:

a. Force balances that provide time-averaged integral quantities but are not naturally useful for understanding detail flow physics.
b. Steady and unsteady pressure measurements including pressure-sensitive paint that provide wing surface measurements but do not provide information on off-surface flow and the nature of the vortices.
c. Surface flow visualization, for example, oil flow visualization that gives an indication of surface flow streamlines but does not provide information on off-surface flow.
d. Off-surface flow visualization (smoke or dye) that provides useful information on shear layer structures and vortex breakdown location but this technique does not provide information on the vortex properties.
e. Multi-hole velocity-probe technique that measures three components of mean velocity.
f. Hot wire anemometry that provides unsteady velocity components.
g. The non-intrusive methods of LDV and PIV that provide information on off-surface flow and the nature of the vortices respectively.

Methods a, c and g are used in the present study. In addition, unsteady balance data were recorded.

3.8 Wind Tunnel Testing at Glasgow University

The experiments in this project were carried out in the 2.65 metre by 2.04 metre closed circuit Argyll Wind Tunnel, with maximum speed of 76 m/s. Tests were conducted at speeds of 20.63 m/s and 41.23 m/s corresponding to Reynolds numbers of 1×10^6 and 2×10^6 based on mean aerodynamic chord respectively. The experiments were conducted in three phases. In the first phase, forces and moments were measured. This was followed by oil flow visualization studies. The final experiments were conducted using Particle Image Velocimetry.

3.8.1 Steady and Unsteady Balance Measurements

The first experiments were the steady and unsteady load cell measurements. These were for all wings; i.e. sharp, small, medium and large-radius wings. Prior to the experiments, the force and moment channels were calibrated with precision weights for their steady characteristics. The calibrations were carried out with three precision weights of 19.62 N, 88.96 N and 222.41 N at each calibration point. During the calibration, these precision weights were placed at three different locations upstream of the MC-5; 20 cm, 50 cm and 70 cm from the balance reference point. For accurate placing of the precision weights, a steel rod of diameter 20 mm was attached in front of the transducer allowing the weights to be mounted. Calibration was performed at sting angles of 0^0 and 15.5^0. The process included the negative and positive directions at these locations upstream of the MC-5 transducer. The raw data obtained from this calibration process were then reduced accounting for balance cross-talk effects. The loads obtained from the balance measurements were then compared with the actual weights applied. The calibration procedure resulted in errors of less than 2% for the forces and moments.

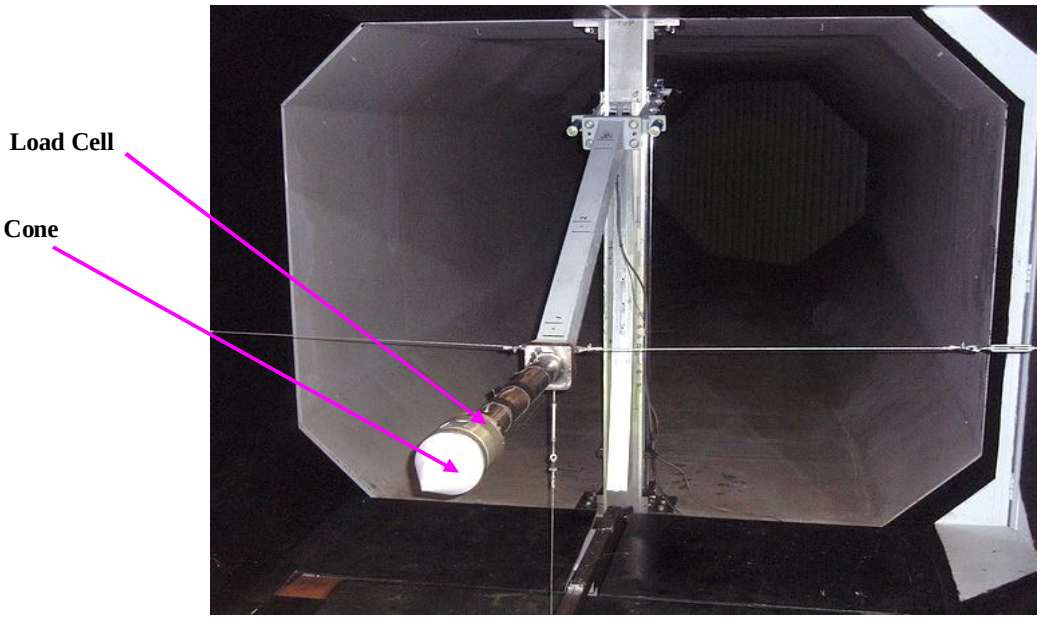

Figure 3.14: Bare test experiments

The balance was also used to examine the unsteady characteristics of the model support structure. There were two stages in doing this, firstly the model was tapped with a mallet with the wind off and the forces and moments were recorded. The data were then analysed to obtain the natural frequency of vibration of the structure. This process was followed by placing a sharp cone in front of the load cell, as shown in Figure 3.14 to prevent any vortex development. Tests were then performed at two speeds, namely 20.63 m/s and 41.23 m/s, and at angles $\alpha = 13.3^0$, $\alpha = 18.5^0$ and $\alpha = 23^0$ to measure the unsteady loads in the absence of the wing. The results of these experiments are discussed in section 4.8.2 & 4.8.3.

After calibration and these initial tests, force and moments were captured at each angle of attack at two sampling frequencies of 100 and 8000 Hz. Each test was repeated five times to determine the repeatability. The results showed an excellent repeatability of forces and moments particularly the forces in the y-direction and moments in the x-direction that corresponded to the model normal force and pitching moment. The results of these tests are discussed in Chapter 4. The maximum capacity of the load cell in the z-direction (5560 N) was very large. This axis provided the model axial force but, as a result of the high range, resolution of this force was not good.

The raw data obtained from each channel was processed using the MC-5 crosstalk matrix. The details of the MC-5 crosstalk matrix are shown in Appendix B and its full range of forces and moments capabilities are shown in table 3.2.

Force and Moment Channels	Maximum Capacity
Fx	±2780 N
Fy	± 2780 N
Fz	± 5560 N
Mx	± 203 N.m
My	± 203 N.m
Mz	± 140 N.m

Table 3.2: MC-5 Full Range Capabilities

The reduced forces and moments from the crosstalk matrix were calculated using a Matlab programme and these are presented in Chapter 4. The analyses of load spectra were also performed using Matlab and the results are also discussed in Chapter 4.

3.8.2 Flow Visualization

The second series of experiments were the oil flow visualization studies. These were also carried out for all wings between $\alpha = 10^0$ to $\alpha = 27^0$ angle of attack at both Reynolds numbers of 1×10^6 and 2×10^6. In this experiment, a mixture of Ondina oil thinned with paraffin was mixed with Dayglo powder before its application to the surface of the wing, as shown in Figure 3.15. During the experiments, extra care had to be taken so that the thickness of the mixture applied to

the wing surface would not affect the actual flow topology, as advised by Squire (1970).

Figure 3.15: The application of mixture onto the delta wing

During the experiment, an ultra-violet light was placed on the roof of the wind tunnel to illuminate the mixture. The images were recorded using a very high definition 3008 x 2000 pixel Nikon D70 digital camera located outside of the wind tunnel on an adjustable tripod on the roof of the wind tunnel in a sequence from the initial to the stabilized oil flow pattern on the wing. Results from these experiments are discussed in Chapter 5.

3.8.3 Particle Image Velocimetry

3.8.3.1 Introduction

The final experiments were carried out using Particle Image Velocimetry. The basic system components for Particle Image Velocimetry are shown in Figure 3.16. Particle Image Velocimetry requires flow seeding, a double-pulsed laser, light sheet optics, a CCD Camera, a timing unit and its software. The main function of each of these is as follows (**www.piv.de**);

a. Seeding – to seed the flow with particles or bubbles.

b. Double-Pulsed Laser – uses two laser pulses to illuminate the particles twice with a very short time interval between the pulses.

c. Light Sheet Optics – to form the laser light into a thin plane across or along the flow.

d. CCD Camera – to record the two flow images exposed by the laser pulses.

e. Timing Unit – highly accurate electronics to control the laser and camera.

f. Software – to capture, analyze and display the results.

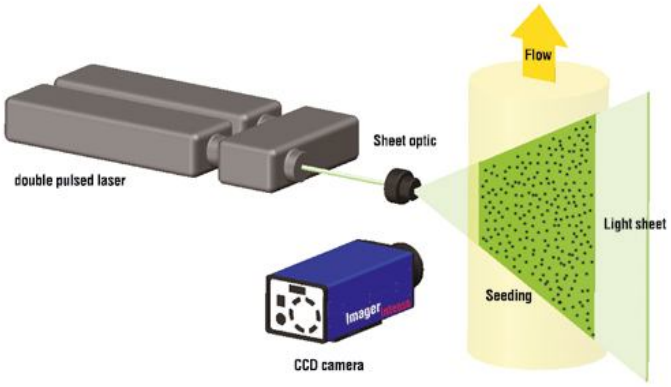

Figure 3.16: Basic system components for Particle Image Velocimetry (Figure taken from www.piv.de)

3.8.3.2 Particle Image Velocimetry at Glasgow University

The arrangement of the stereo Particle Image Velocimetry system in the Argyll wind tunnel is shown in Figure 3.17. The images of the particles were recorded by two 11 Megapixel LaVision cameras with a pair of 300mm focal-length Nikon lenses. Both cameras were mounted on three-dimensional adjustable tripods located outside the test section on the starboard side of the wing model. To obtain good precision of the velocity components, the viewing angles of both cameras should be positioned at $\pm 45^0$. However, due to the limited size of the tunnel window and

required angle of attack, Camera 1 was set at a higher angle compared to Camera 2. This was accounted for during the calibration process.

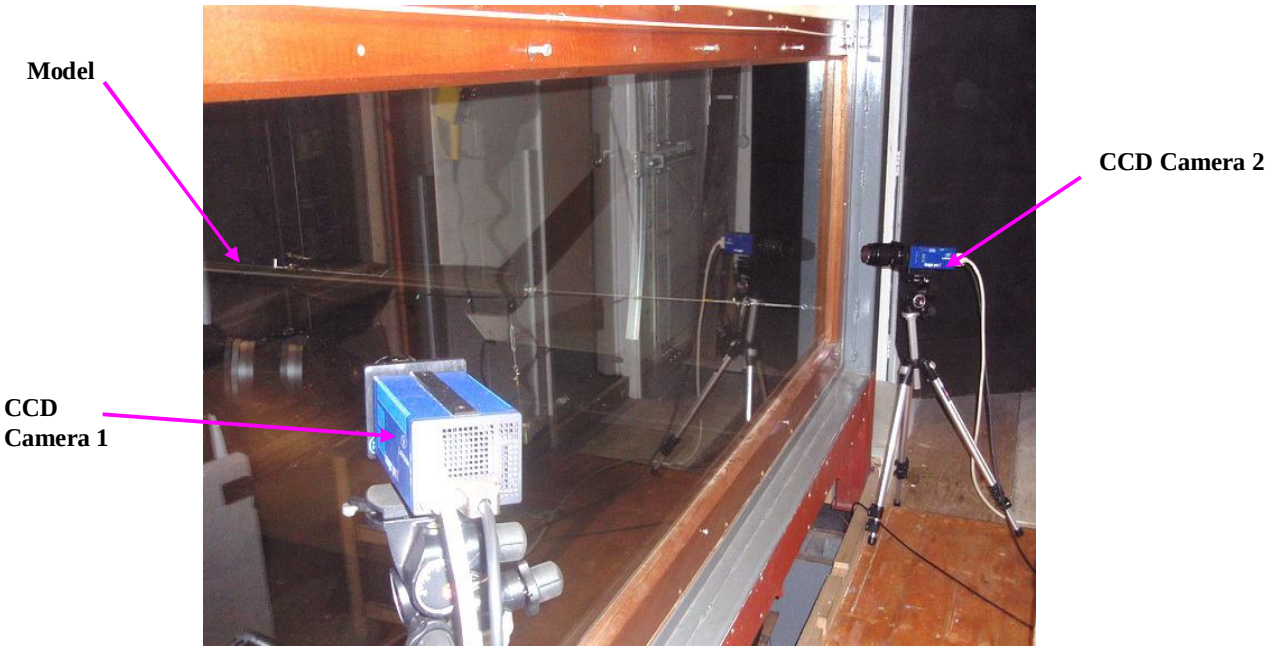

Figure 3.17: Stereoscopic PIV arrangement in the Argyll low speed tunnel showing Camera positions during the experiments

3.8.3.3 Laser Beam and Laser Beam Deflections

The system used to illuminate the droplets in the Argyll tunnel was an Nd: YAG Pulse laser of 250 mJ per pulse. It was located under the floor of the wind tunnel. A beam guide arm fitted with light sheet optics was used to deliver the laser light sheet into the required area, as shown in figure 3.18.

Figure 3.18: Adjustable laser arm and light sheet optics

There were two limitations during the PIV set-up stage; the size of the calibration plate which was only 50 cm by 50 cm and the length of the pulsed laser sheet that was about 50 cm at the wing surface. This was considerably smaller than the span of the wing towards the trailing edge. Thus, it was decided to observe and analyze the vortex system on the starboard side of the wing only. The calibration plate was then placed perpendicular to the wing axis on the starboard side of the model. During the calibration, the light sheet was aligned parallel to the calibration plate, as shown in Figure 3.19, (the model shown in the figure is the large-radius wing). This was necessary to keep the light sheet perpendicular to the wing axis. Any misalignment between the laser sheet and the calibration plate was manually corrected by adjusting the light sheet optics. Since a very thin laser sheet on the wing surface was necessary for good flow images, a piece of reflector paper was utilized to determine the position and sharpness of the sheet.

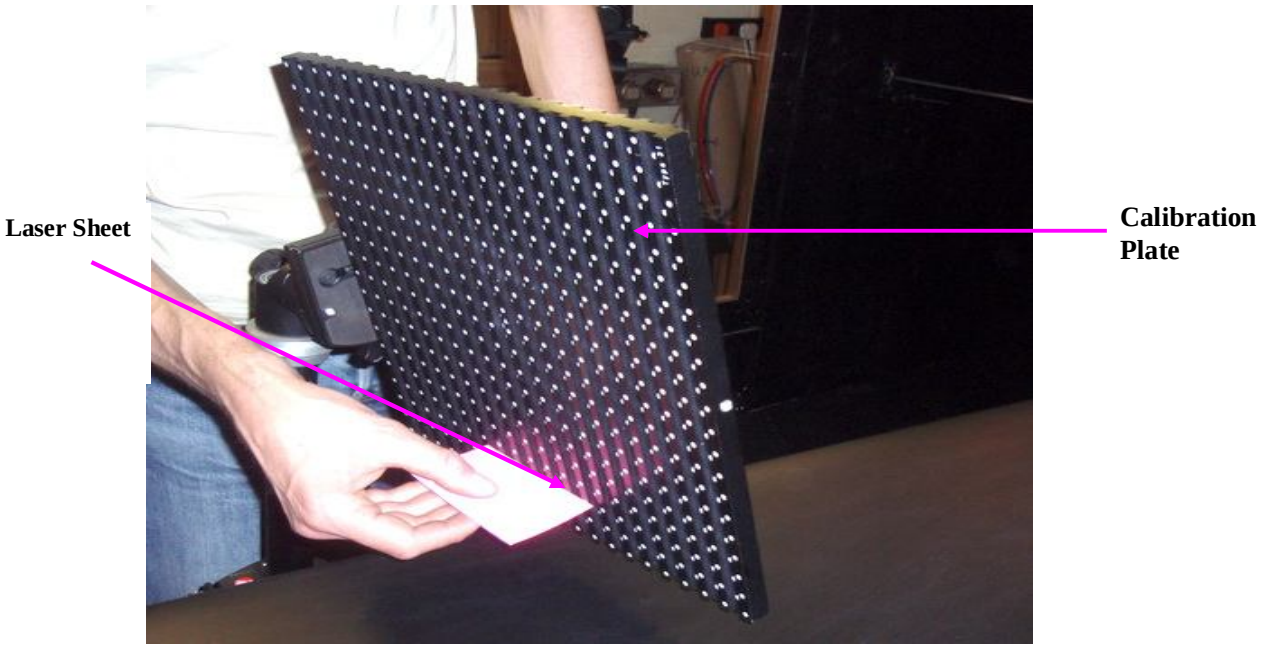

Figure 3.19: Laser sheet adjustments

3.8.3.4 Calibration Process

The most important stage in the stereo Particle Image Velocimetry study was the camera calibration after the laser light was set at a specific position. The calibration process was based on the position and size of the calibration plate. The maximum flow view that could be obtained from these experiments was 50 cm by 50 cm. The calibration plate contained dots spaced at 5 mm along both vertical and horizontal directions. Both cameras were adjusted to obtain full view of the calibration plate. This is shown in figure 3.20. The camera calibration then helped to determine the corrected camera image that arose from the distortion due to the camera position and camera lenses. As mentioned above, during the calibration of the stereo PIV cameras, care had to be been taken to avoid any misalignment between the positions of calibration plate and the laser sheet.

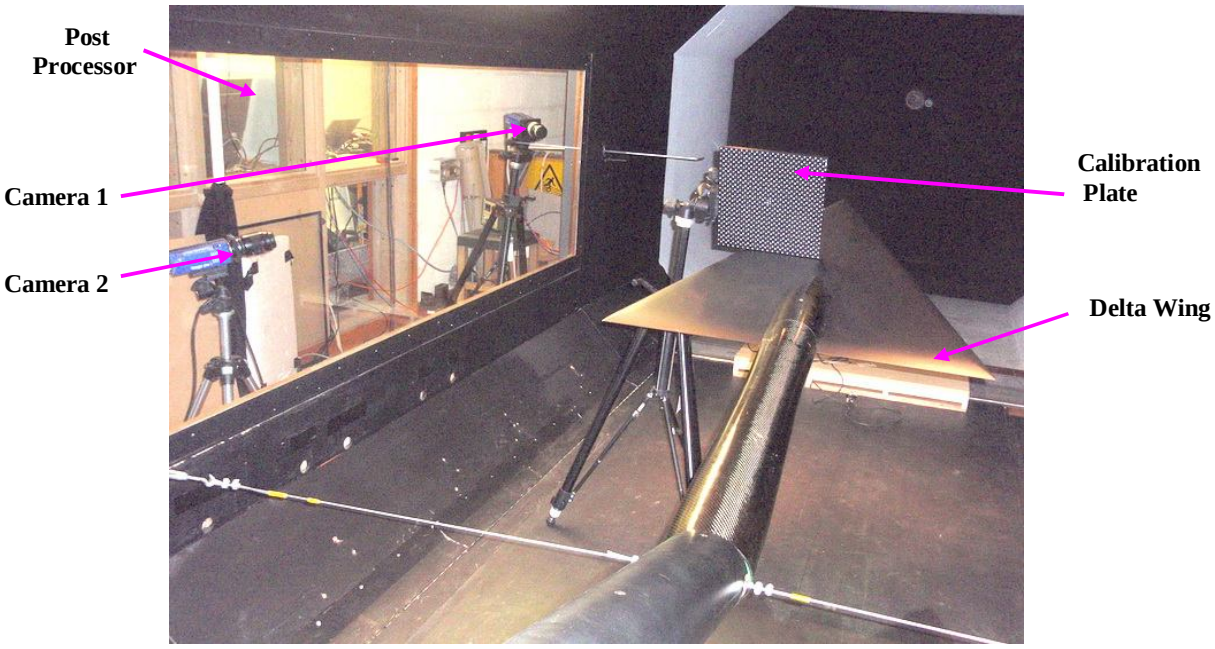

Figure 3.20: Calibration work on Glasgow University Delta Wing

The complexity of applying stereo PIV experiments to the delta wing model in the wind tunnel is illustrated in Figures 3.21 and 3.22. The first problem was that the viewing angle of both cameras was not exactly $\pm 45^0$ with respect to the calibration plate. This was due to the location of the wing in the tunnel and the size of the tunnel window. This caused the viewing angle on the calibration plate of Camera 1 ($\alpha 1$) to be much higher than that of Camera 2 ($\alpha 2$), as shown in Figure 3.21. Secondly, in order to get a better image at positive angle of attack, Camera 1 had to be positioned at a location slightly higher than Camera 2, as shown in Figure 3.22.

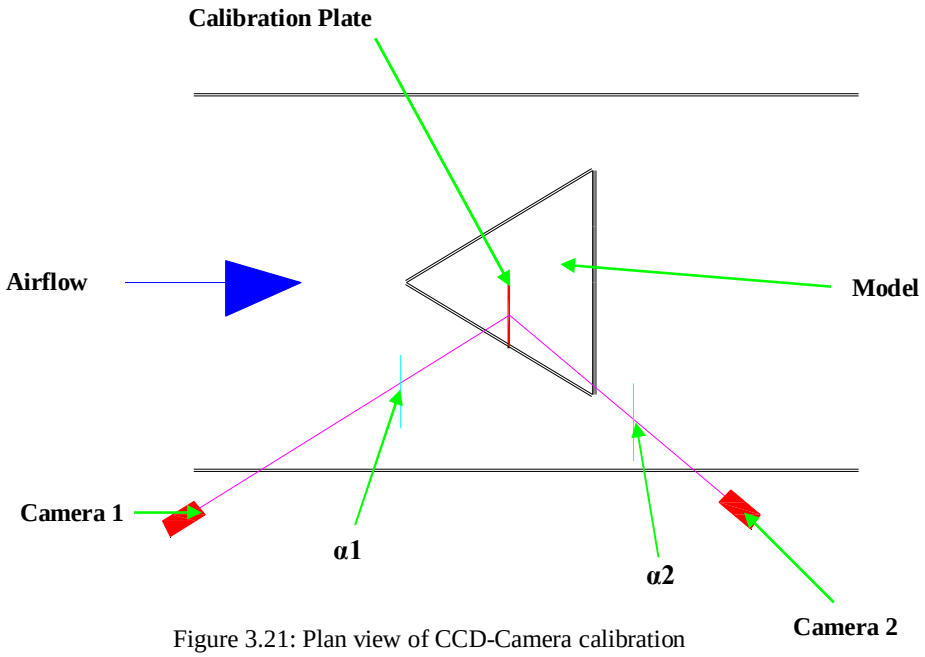

Figure 3.21: Plan view of CCD-Camera calibration

To minimise adverse effects of the glaring, the locations of both cameras had to be manually adjusted and re-adjusted to maximise view of the calibration plate on the LaVison software. The individual lenses were also manually adjusted to get a better view of calibration plate in the software. This calibration process had to be repeated for every change of the angle of attack and measurement plane.

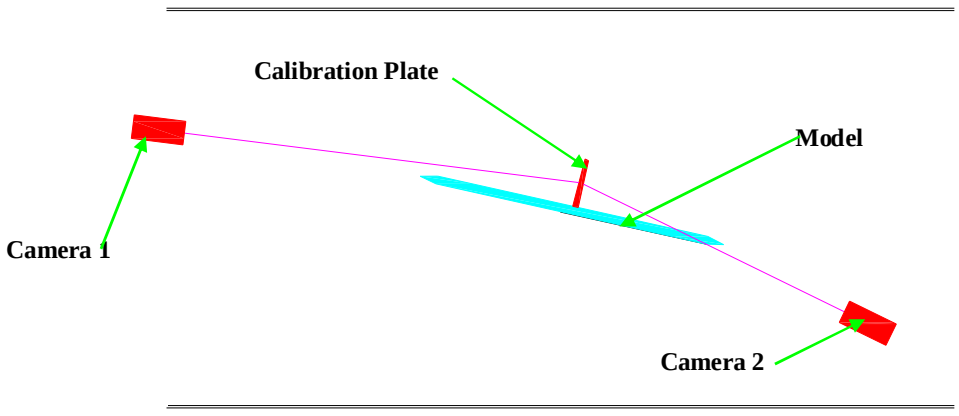

Figure 3.22: Side-view of CCD-Camera calibration

After positioning of the cameras and adjustment of the lenses had been done, the next stage was to obtain three selected dots on the calibration plate to mark as a mapping function of the measurement planes. These three points would become the origin of the calibration on each plane. For instance, the origin of the mapping function for the large-radius wing at $\alpha = 15^0$ and the measurement plane at $x/c_r = 0.5$ was located 36 mm above the wing centre line and 142.5 mm from the leading edge. The mapping function and the cross correlation was calculated from this origin.

The sequence of the dots selected for the mapping function for each camera is shown in Figure 3.23. The images of these three dots on the calibration plate were then recorded by both cameras.

The coefficient of the mapping function was then calculated by the LaVision software. This mapping function was used to evaluate the relation between the coordinates of the point in the calibration plate with the physical space of the measurement plane. The calibration plate was removed after the mapping function had been obtained.

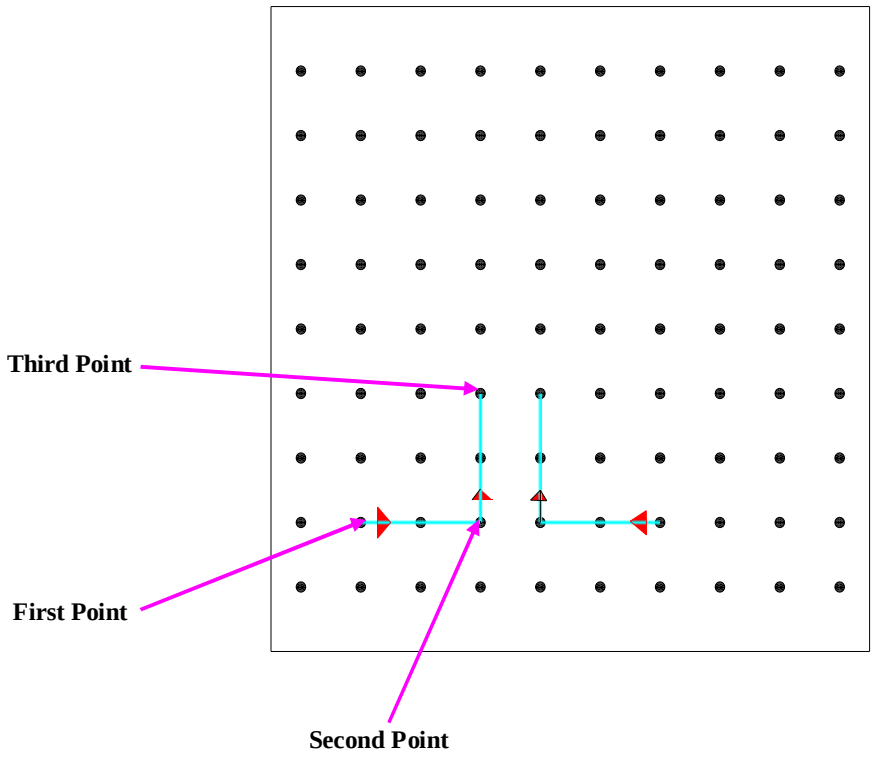

Figure 3.23: Marking function on the calibration plate

A source of light was placed in front of the calibration plate during the calibration process, as shown in Figure 3.24. This was to ensure that the calibration plate was well illuminated during the marking process.

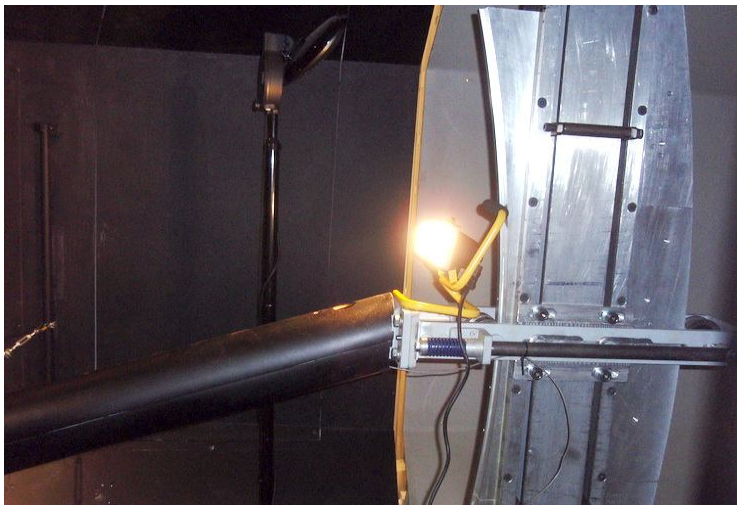

Figure 3.24: Light source during the calibration process

3.8.3.5 Flow Seeding

The final stage before starting the experiments was to ensure a uniform flow seeding in the test section. In this experiment, droplets were produced by a Piv Part 40 Aerosol smoke generator. The seeding material during the experiments was Ondina oil. The generator was placed behind the main support structure of the test rig throughout the experiments. It would be able to produce droplets of diameter around 2 μmm. This smoke generator could be switched on and off manually to control the amount of droplets in the test section, thus homogeneity of particle concentration in the test section could be controlled.

3.8.3.6 The Timing and Generation of Trigger Signals

The time separations between both laser pulses to illuminate the particles were 20 μsecond and 8 μsecond for experiments at Reynolds number of 1 x 10^6 and 2 x 10^6 respectively. The selection of this time separation was based on the light sheet thickness and wind tunnel speed.

3.8.3.7 PIV Measurements at University of Glasgow

After the calibration process was completed, the calibration plate was removed and the experiments at Reynolds number R_{mac} of 1 x 10^6 and 2 x 10^6 were performed. The test cases for the PIV measurements at Glasgow University are shown in table 3.3 and the PIV results are discussed in Chapter 5.

Leading Edge	*Large- and medium-edged wings*
Speed	*20.63 m/s and 41.23 m/s*
Reynolds Number (Mean Aerodynamic chord)	*1 x 10^6 and 2 x 10^6*
Angle of Attack	*10^0, 13^0, $15^0$and 18^0 (Large-Edged)* *13^0, 18^0 and 23^0 (Medium-Edged)*
Cross plane location	*x / c_R = 0.3, 0.5 and 0.75*
Field of view	*50 mm x 50 mm*

Table 3.3: Test cases for PIV measurements in the University of Glasgow Argyll Wind Tunnel

3.8.3.8 Limitations of PIV Experiments

Several problems were faced which limited the effectiveness of the PIV experiments in this study. These included the following;

1) As mentioned earlier, Camera 2 was set at an extreme position because of the physical constraint of the wind tunnel structure and the location of the wing in the test section. Thus, sharp focus from Camera 2 in the plane of view could not be achieved successfully.

2) During the experiments, the shadow and glare effects from the wing surface could not be masked off successfully.

3) Due to these limitations, the PIV experiments were only performed at a Reynolds number of 1×10^6 and 2×10^6 on the large radius wing at $x / c_r = 0.5$.

Chapter 4

4.0 RESULTS – STEADY / UNSTEADY BALANCE MEASUREMENTS

4.1 PART 1: STEADY BALANCE MEASUREMENTS

4.1.1 Introduction to Balance Measurements

This chapter presents steady balance measurements for the round-edged delta wing. The force and moments from the AMTI-MC5 transducer were resolved about the two thirds of chord location in a manner consistent with the original Chu & Luckring (1996) measurements. The experiments were performed at 1 x 10^6 and 2 x 10^6 Reynolds number. In this thesis, normal force (C_N), axial force (C_A) and model pitching moment (C_m) are measured as the forces and moment in Fy, Fz and Mx respectively. This notation is shown in figure 4.1. In this chapter, results will be presented that differentiate the effects of bluntness, angle of attack and Reynolds number.

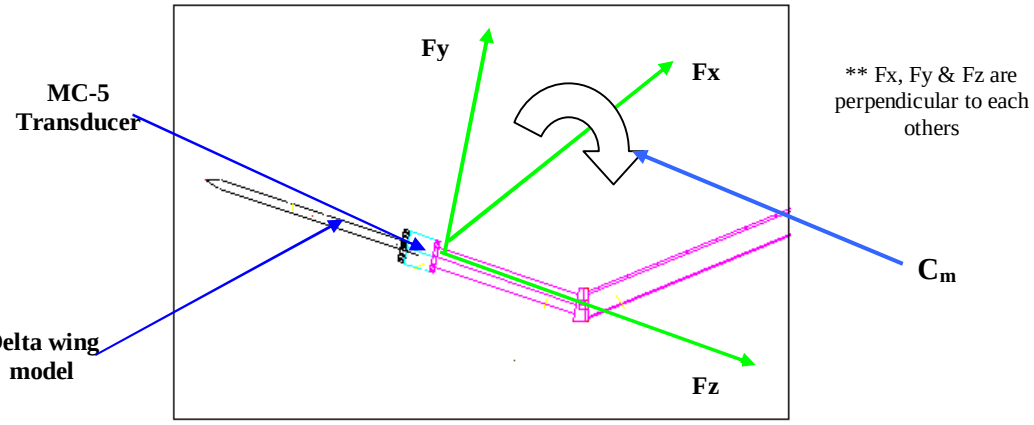

Figure 4.1**:** Force notation used in this experiment (**Fy** measuring the Normal force (**C_N**), **Fz** measuring the axial force (**C_A**) and **Mx** measuring the model pitching moment (**C_M**)

4.1.2 Balance Sensitivity and Cross-Talk

The raw data obtained from the experiments were reduced using a factory specified balance crosstalk matrix. The calculations were performed in MATLAB and the details of the force and moment sensitivities are attached in Appendix B.

The balance system used in the current work was chosen on the basis of a series of constraints that included the anticipated forces and moments on the model, the physical geometry of the sting and balance mounting location and the cost of the balance system relative to the available resources for the project. As a result, it was not possible to procure a balance system that provided high sensitivity on all axes and, as discussed in Chapter 3, a conscious decision was taken to focus on getting fidelity in the normal force and pitching moment. The balance used in this study had a very large range in the Fz (axial) direction resulting in poor resolution of the loads on this axis. The effect of this constraint is explored in the current chapter by comparison with data from other research projects in which the same wing planform has been tested.

4.1.3 Repeatability Test

During the experiments, every data point was recorded five times. Figure 4.2 shows the repeatability that was achieved, for example, in the normal force coefficient at Reynolds numbers of 1×10^6 and 2×10^6. The case shown is for the large rounded-edged wing.

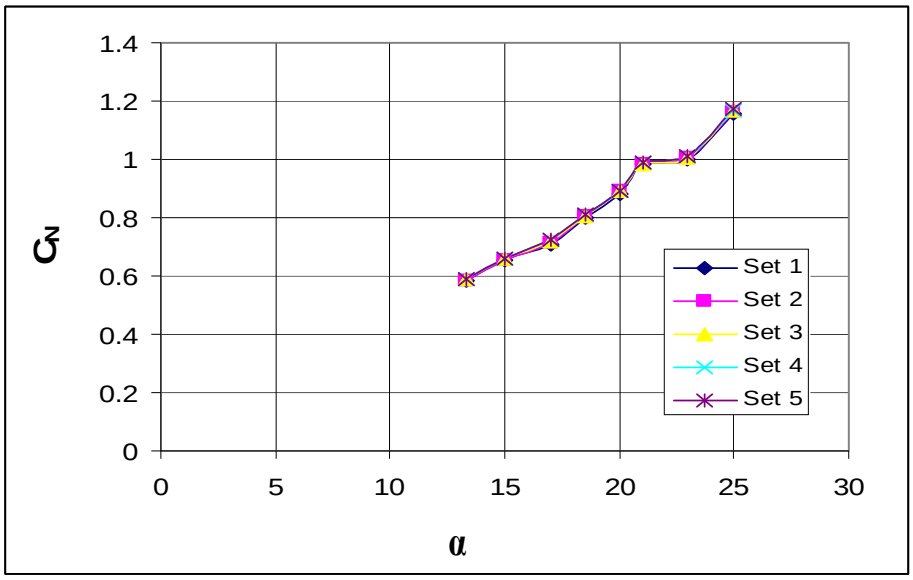

a) Balance repeatability at Reynolds number of 1 x 10^6

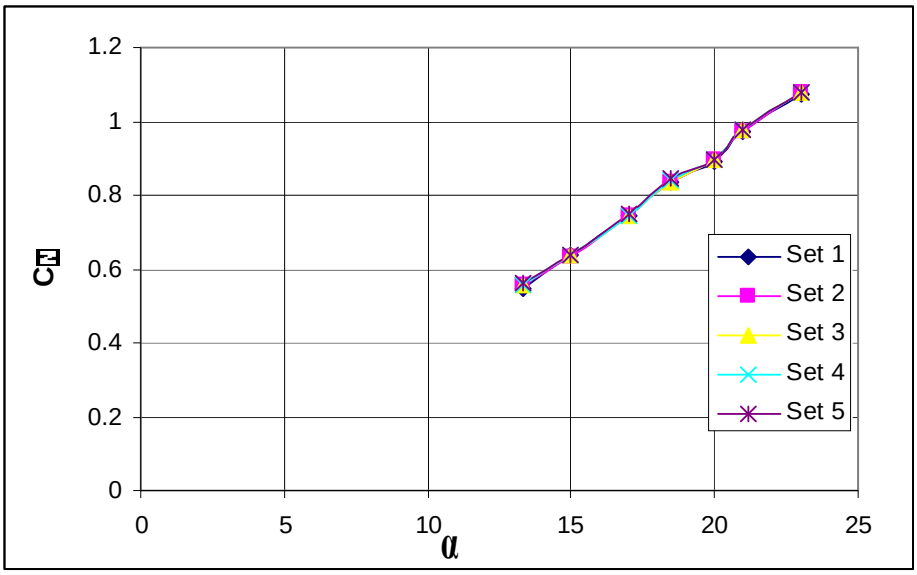

b) Balance repeatability at Reynolds number of 2 x 10^6

Figure 4.2: Repeatability of the normal force coefficients for the sharp-edged wing at Reynolds numbers of 1 x 10^6 and 2 x 10^6.

4.2 The Effects of Bluntness and Angle of Attack on the Steady Forces

4.2.1 The Effect at Reynolds Number of 1 x 10^6

The measured normal and axial force coefficients at one million Reynolds number are presented in Figure 4.3 for the four wing configurations. The normal force coefficients measured for the sharp, small and medium-radius wings are quite similar. The reason for this can be related to early separation of the primary vortex in all of these cases. The dominance of the primary vortex over the entire wing is a major contributor to this similarity. The large-radius wing generally produces less normal and axial force than the other three wings.

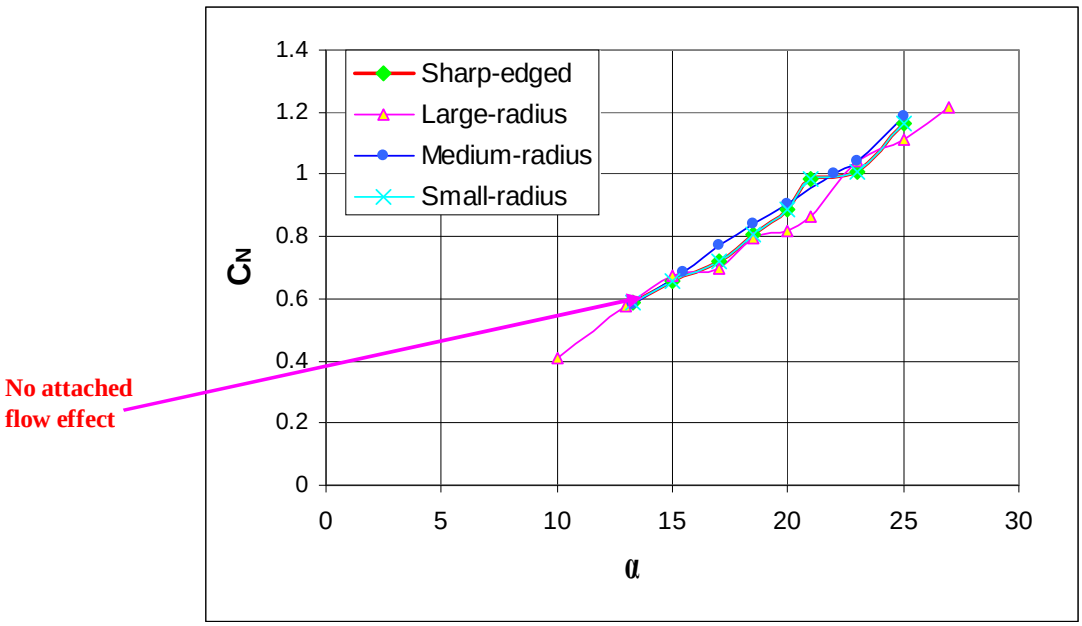

a) Normal force coefficient

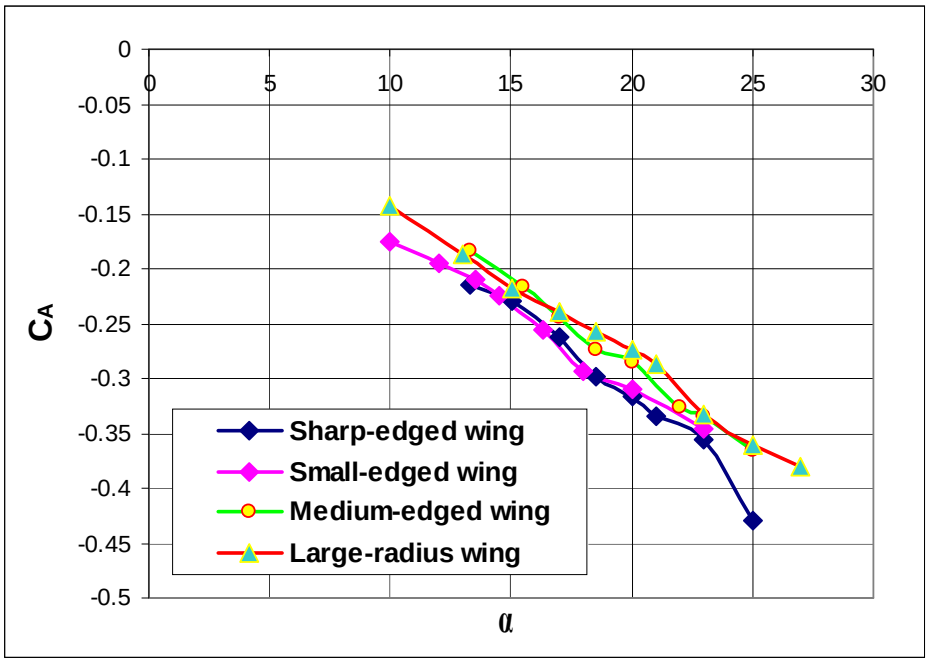

b) Axial force coefficient

Figure 4.3. Comparison of a) normal and b) axial force coefficients for the four wings at R_{mac} = 1 x 10^6.

To access the effect of the poor resolution on the Fz axis, the axial and drag force coefficients (C_A & C_d) obtained from Glasgow University is compared with measurements from ONERA (Rodriguez, 2008) and Tubitak-Sage (Kurun, 2008). Figure 4.4 shows a direct comparison of the axial force coefficients measured in the present study with those of Tubitak-Sage. Figure 4.5 and 4.6 show the effect the measured axial force has on the resolved drag coefficient for the sharp and medium radius wings at a Reynolds number of 1 x 10^6. As discussed in Chapter 3, the range of the load cell in the axial force (z-channel) direction was very large (5560 N); thus, the resolution of this force was not good. The comparison in Figure 4.4 is poor suggesting that the measured axial forces are indeed unreliable. The higher C_d for the Glasgow University case, in Figures 4.5 & 4.6, compared to ONERA and Tubitak-Sage demonstrates the magnitude of the error this creates in the resolved drag coefficient. It should be noted here that, as will be shown later in this Chapter, the normal force coefficients measured at Glasgow compared well with the Tubitak-Sage data and so are not a contributory factor to the error in C_d.

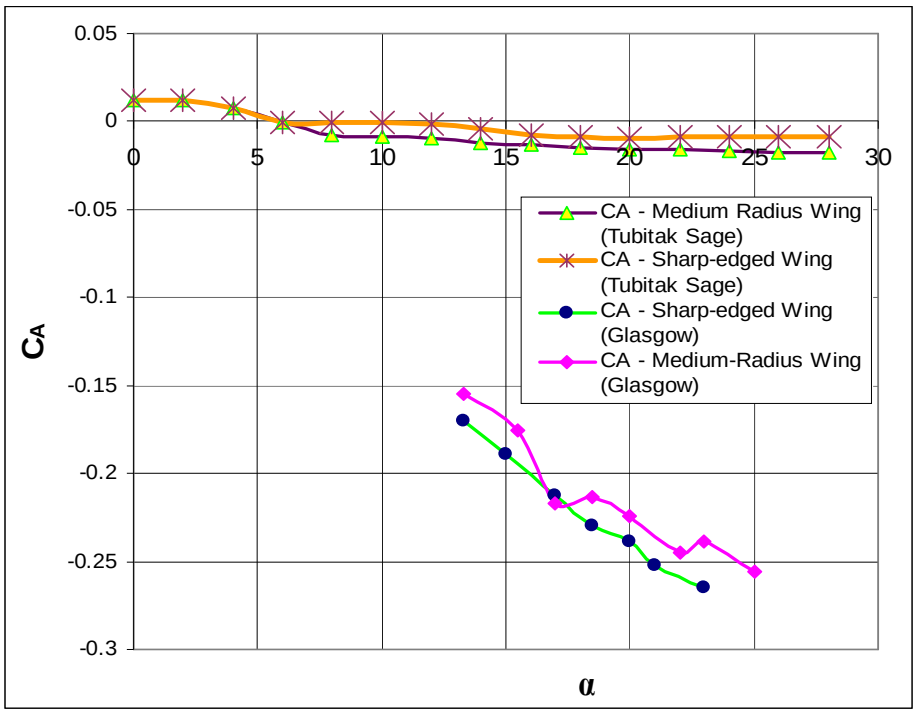

Figure 4.4: The comparison of axial force (C_A) from Glasgow University and Tubitak-Sage (Reynolds Number of 1 x 10^6)

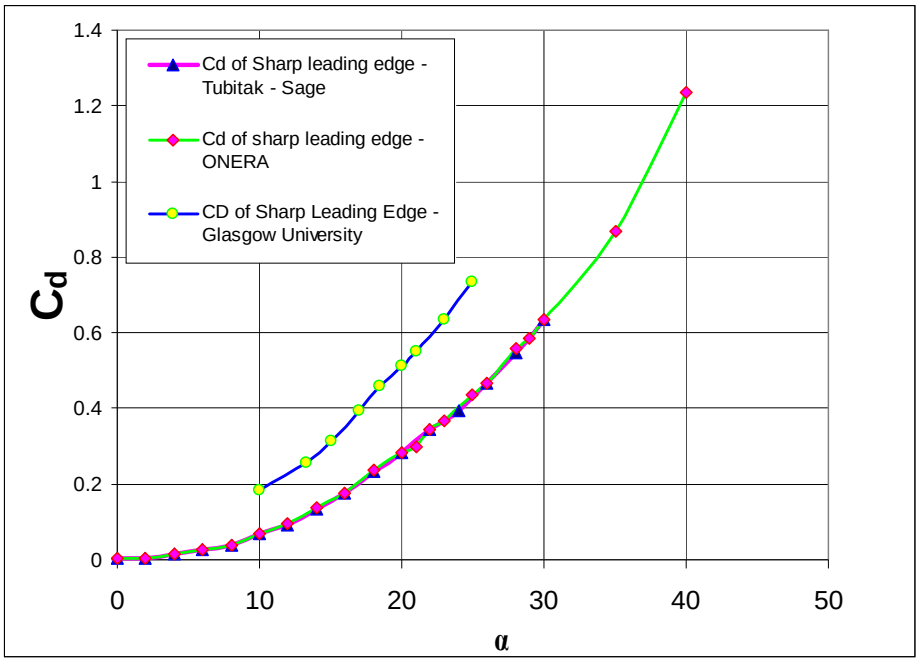

a) Sharp Leading Edge

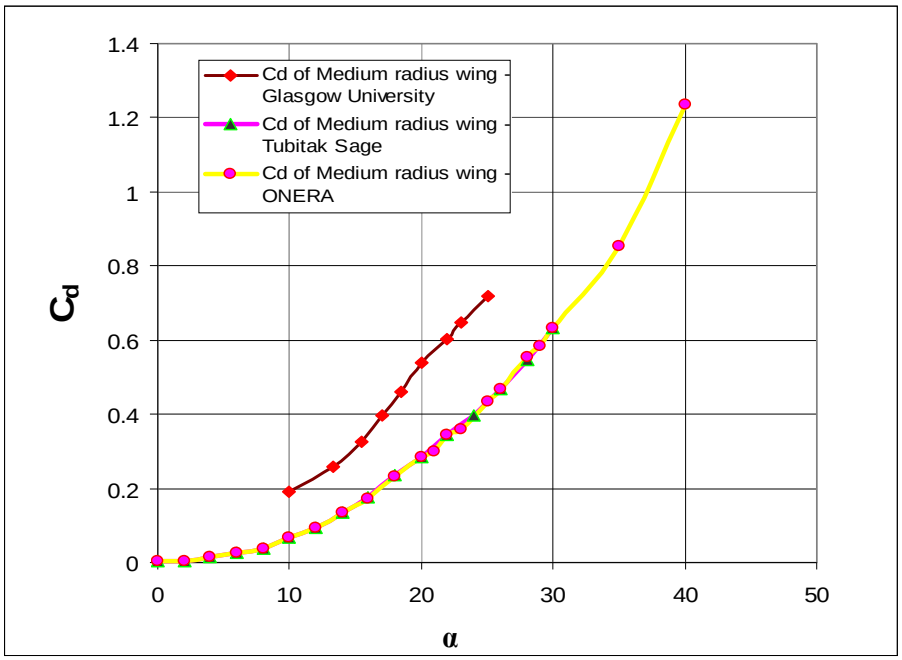

b) Medium Radius Leading Edge

Figure 4.5: The comparison of drag force coefficient of Glasgow, Tubitak-Sage and ONERA Wind Tunnels at the Reynolds number of 1 x 10^6.

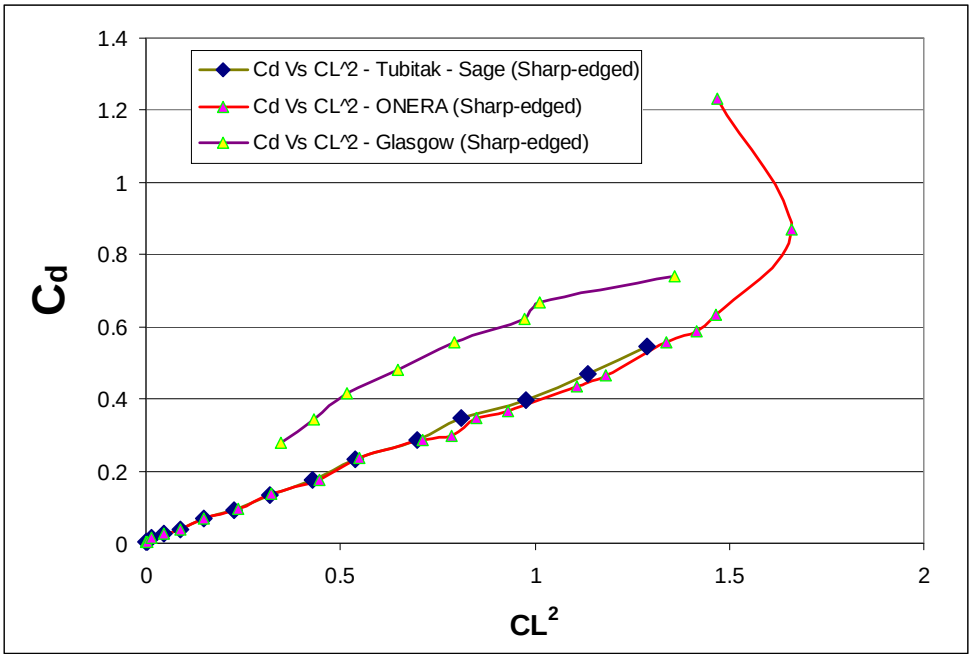

a) Sharp leading edge

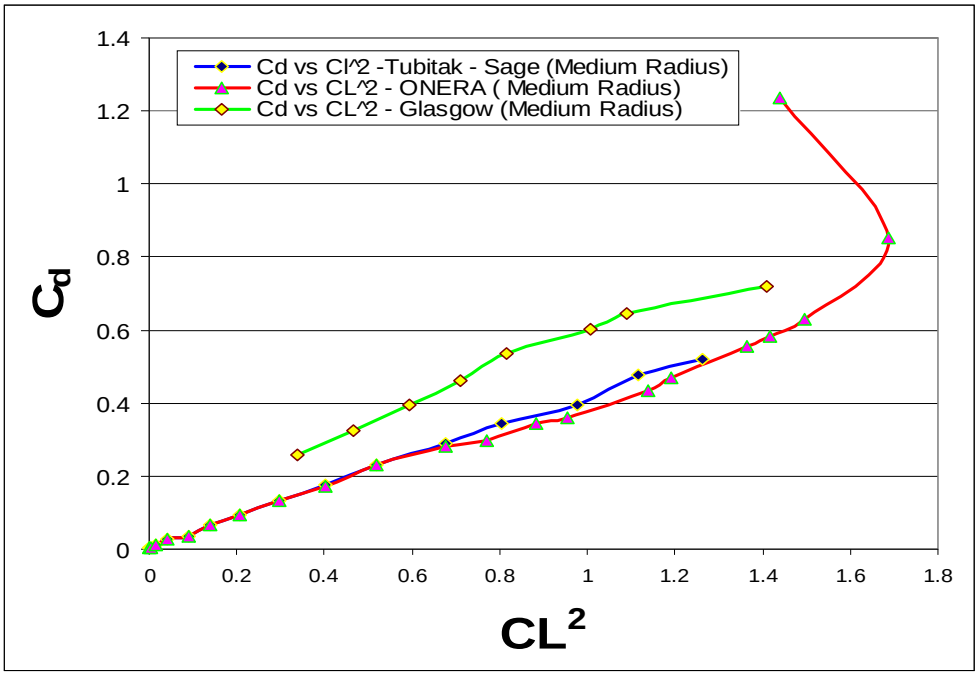

b) Medium radius wing

Figure 4.6: The comparison of C_d vs CL^2 of Glasgow, Tubitak-Sage and ONERA Wind Tunnels (Reynolds number of 1 x 10^6)

These comparisons illustrate that the axial force measurements made in the current study are unreliable. For this reason, these measurements will only be referred to very briefly in the remainder of the thesis. While it has been established that the magnitude of the axial forces are in error, it is not clear whether there is any value in the relative differences in axial force between the different planforms. For this reason, a discussion of these relative differences is retained in the following section but should be treated with caution.

4.2.2 The Effect at Reynolds Number of 2×10^6

The normal and axial force coefficients measured for the four wing configurations at a Reynolds number of $2x10^6$ are presented in Figure 4.7. The figure shows there are obvious differences between the data sets for the four leading edge geometries at a constant Reynolds number. The normal and axial forces are generally higher for the sharp leading edge configuration compared to those from the rounded-edged wings. Both forces tend to decrease slightly in magnitude as the radius of the leading edge is increased although the change in normal force from the sharp to the small and medium-radius wings is marginal. The results in Figure 4.7 a) can be related to flow behavior identified in the flow visualization studies as discussed in chapter 5.

At moderate angle of attack, it can be observed that the normal force acting on the wing decreases as the leading edge radius is increased (consistent with Kurun, 2008 and Gursul *et al*, 2005a). This decrease in normal force is consistent with a decrease in the strength of the primary vortices acting on the wing as discussed in relation to the flow visualization results in chapter 5. The primary vortex is weakened with the increase in leading edge bluntness because the primary separation is delayed following a short run of attached flow in the leading edge region (Peake & Tobak, 1980). The weakening of the primary vortex as the leading edge bluntness increases allows the inner flow structure to develop and increase in size and strength. This, however, does not fully offset the loss in normal force due to the weakened primary vortices. At an angle of attack somewhere near 20^0, the sharp, small and medium-radius wings develop similar normal forces. The flow visualization results indicate

that, at these angles, the flows on the upper surface of these wings are dominated by the primary vortices. This is consistent with Hummel (2004) who reported the primary vortex reaches the apex of the wing at $\alpha = 18^0$ on the medium-radius VFE-2 configuration. Under these conditions, the smaller/weaker inner vortex is only likely to occur on the medium radius wing but is so weak that it has little influence on the normal force.

In the case of the large-radius wing, the normal force only approaches those of the other three wings at approximately 23^0. At this angle, the origin of the primary vortex system reaches the apex of the wings with flow separation occurring along the leading edge and the flow pattern resembles those of the other three wings. It could be expected, under these conditions, that the magnitude of the primary vortices will be similar for all four wings and the effect of leading edge bluntness will be diminished at this Reynolds number.

From figure 4.7 b), the behavior of the axial force coefficients at moderate angles of attack shows similar general behavior to the normal force, i.e. the axial force increases with leading-edge sharpness. It is interesting to note that the axial force associated with the large-radius wing increases substantially when the flow topology on that wing becomes dominated by the primary vortices at high angles of attack.

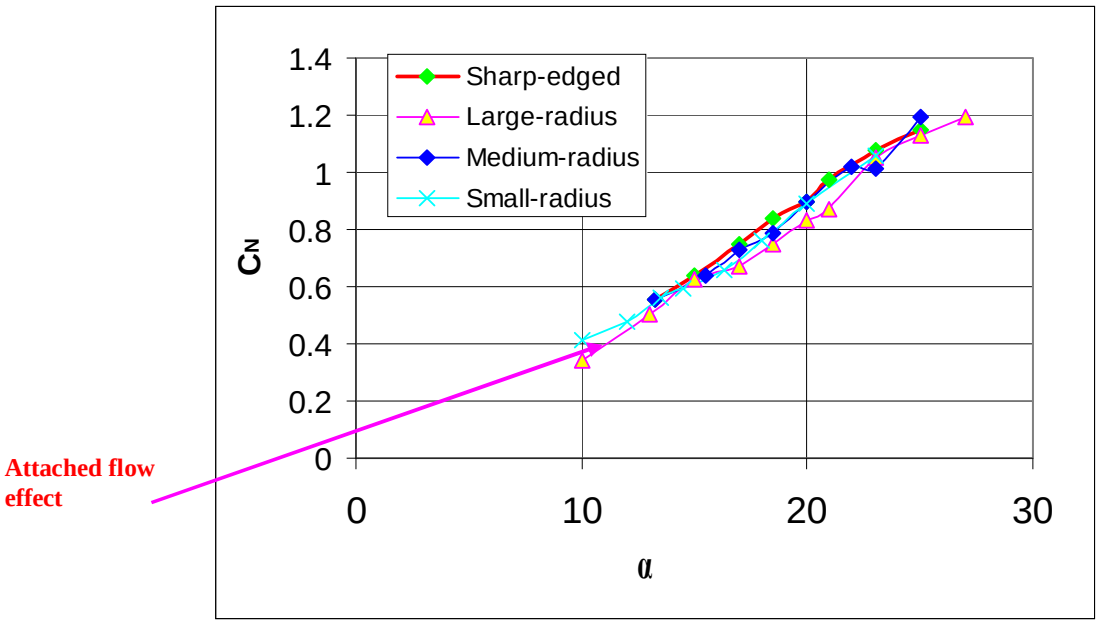

a) Normal force coefficient

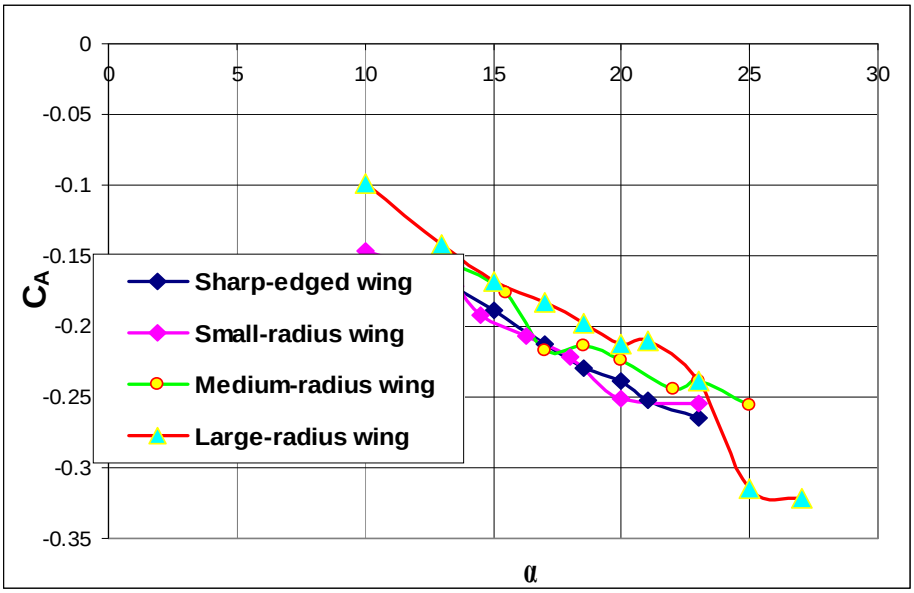

b) Axial force coefficient

Figure 4.7: Comparison of; a) normal and b) axial force coefficients for the four wings at $R_{mac} = 2 \times 10^6$.

4.3 The Effect of Attached Flow on the Normal Force

Figure 4.3 a) and 4.7 a) also shows the effect of the attached flow region, particularly at low angle of attack, on the normal force coefficients. The effect is distinct at 2 x 10^6 Reynolds number where the apex of the wing is covered by an attached flow region as suggested in the previous chapter. Comparing the results for the small and large-radius wings, the normal force of the large-radius wing is lower. The larger portion of attached flow in the apex region, in effect, reduces the normal force. At 1 x 10^6 Reynolds number, the normal force coefficients are similar in all cases. This is very consistent with the flow images presented in the previous chapter which show smaller variations in the flow topology with changes in the leading-edge radius.

4.4 The Effects of Bluntness and Angle of Attack on the Pitching Moment

Figure 4.8 depicts the pitching moment coefficients measured about the two thirds of root chord location at Reynolds numbers of 1x 10^6 and 2x10^6. The results at a Reynolds number of 1 x 10^6 show that the sharp-edged wing exhibits higher nose down pitching moment values than both the large and medium-radius wings. The results for the small-radius wing, at this Reynolds number, are very similar to the sharp-edged wing. It is likely that this general behavior is linked to the greater strength of the primary vortices on the sharper-edged wings although the detail is likely to be complex and will include the effect of the inner vortex structures.

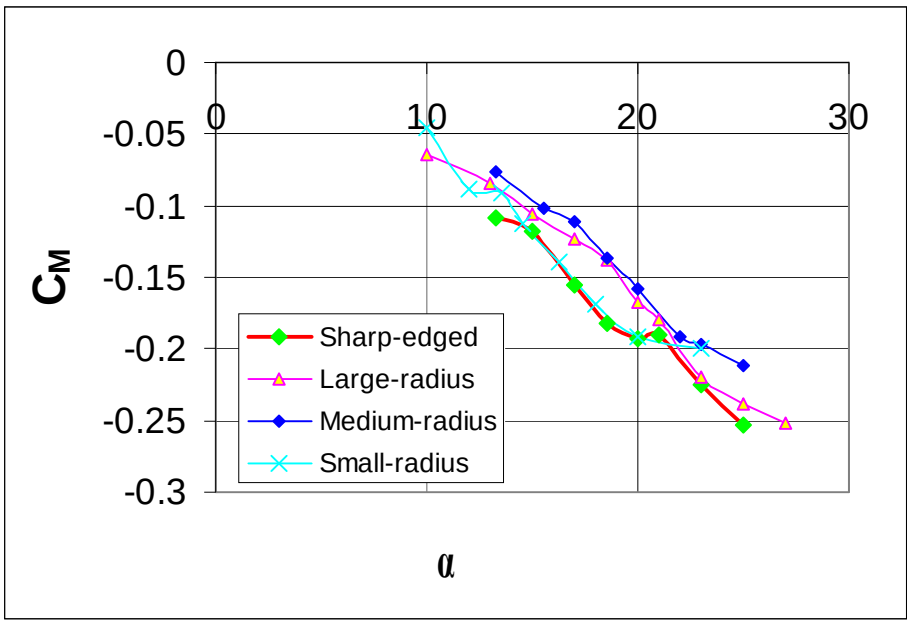

a) Pitching moment coefficients at $R_{mac} = 1 \times 10^6$

Similar general trends can be observed at a Reynolds number of 2×10^6 except that the nose-down pitching moments for the small-radius wing are higher than those of the sharp-edged wing. The stronger pitching moment for the small-radius wing may be linked with the test set-up during the experiments. It is possible that there was load transmission between the wing, the fairings and the balance, thus effecting the measurement of the pitching moment for this case. Even though the results for the small radius wing may be compromised by the test set-up, it does appear that its pitching moment would be close to the sharp-edged wing. The general reduction in nose down pitching moment with increasing leading-edge radius may be related to the attached flow in the apex region and the delayed formation of the tip vortices. Any suction near the apex would reduce the nose-down moment as would weaker primary vortices on the wing surface.

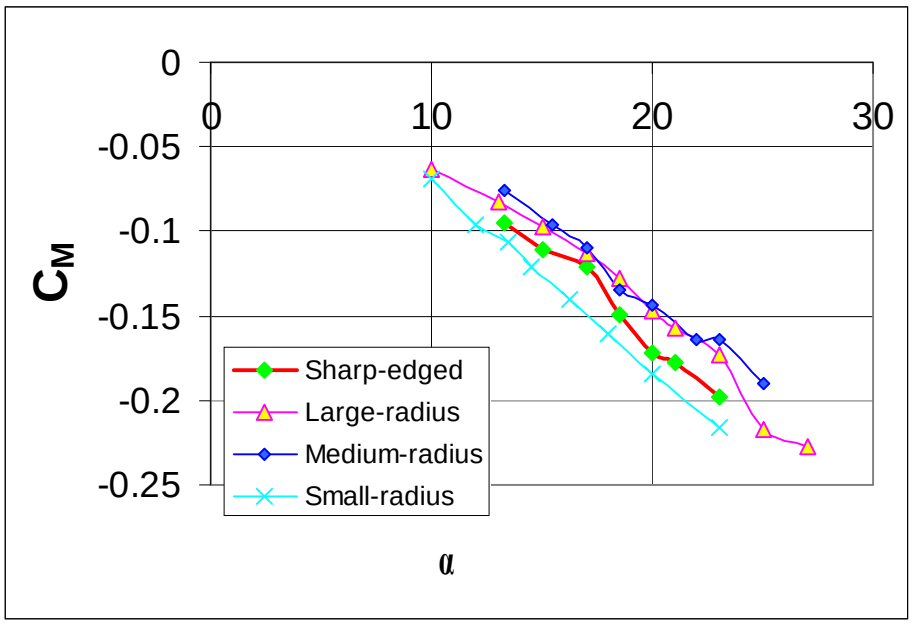

b) Pitching moment coefficients at R_{mac} = 2 x 10^6

Figure 4.8: Comparison of pitching moment coefficients for the four wings at a) at Re_{mac} = 1 x 10^6 & b) at R_{mac} = 2 x 10^6.

4.5 The Effects of Reynolds Number on the Steady Normal Force

Figure 4.9 presents the normal force coefficients (C_N), for all of the wings at Reynolds numbers of 1 x 10^6, 2 x 10^6 and 6 x 10^6 (taken from Chu & Luckring, 1996). It should be noted here that the wind tunnel data from both the current tests and the Chu & Luckring (1996) tests are uncorrected. The figure shows the normal force coefficients do not change with Reynolds number for the sharp wing. Nevertheless there are significant changes in normal force coefficients for all the rounded-edged wings particularly at low to moderate angles of attack up to 15^0. In all rounded-edged cases, higher normal force coefficients are recorded at a Reynolds number of 1 x 10^6. This effect is particularly distinct on the medium and large-radius wings. The influence of the bluntness and Reynolds number on the leading edge separation is the main contributor to these differences.

For the sharp case, the normal force coefficients do not change because the primary vortex is formed at the leading edge and extends to the apex at all Reynolds numbers. The normal force is higher at 1 million Reynolds number (low angle of

attack) on the round-edged wings because the primary vortex at this Reynolds number exhibits similarities with that of the sharp-edged wing. The primary vortex has its origin at the leading edge and extends almost to the apex as discussed in the flow visualization chapter. At higher Reynolds number, the establishment of the attached flow region near to the apex lowers the normal force as observed by Luckring and hummel [final VFE-2 report, 2008]

The results also illustrate why the boundary-layer condition is important on round-edged wings. At lower Reynolds numbers and angle of attack, the laminar flow at the leading edge initiates early separation. At higher Reynolds numbers, the ability of the turbulent flow to sustain the adverse pressure gradient delays the leading-edge separation. At higher angle of attack, the normal force coefficients are quite similar at all Reynolds numbers. This is because flow separation is initiated very close to the leading edge in all cases in the very strong adverse pressure gradient.

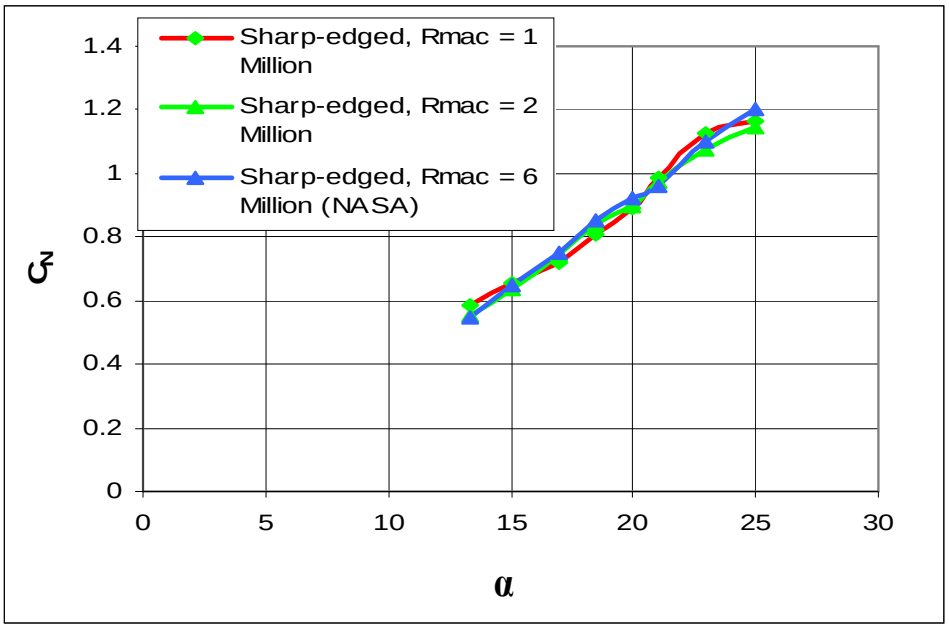

a) Sharp-edged wing

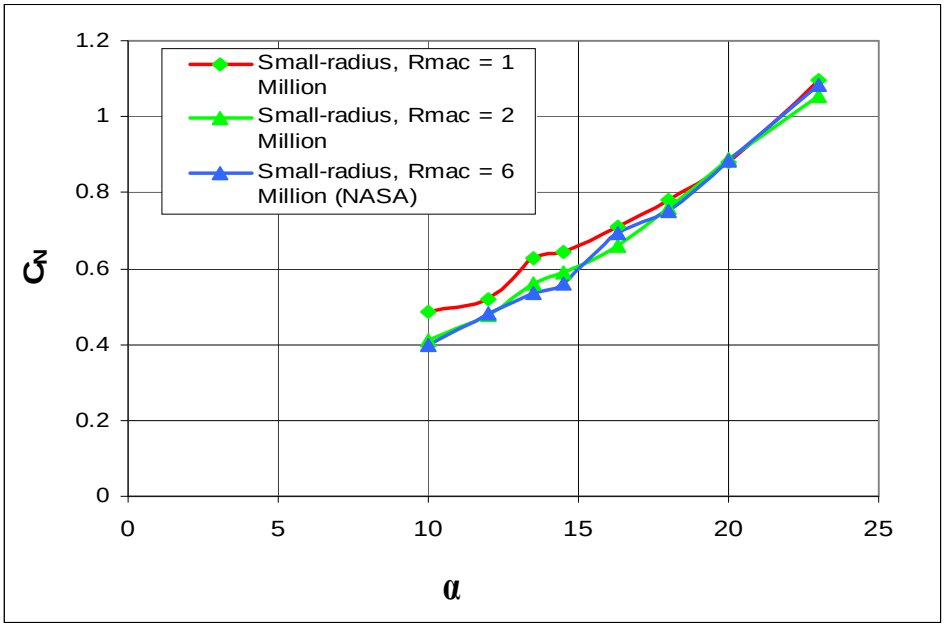

b) Small-radius wing

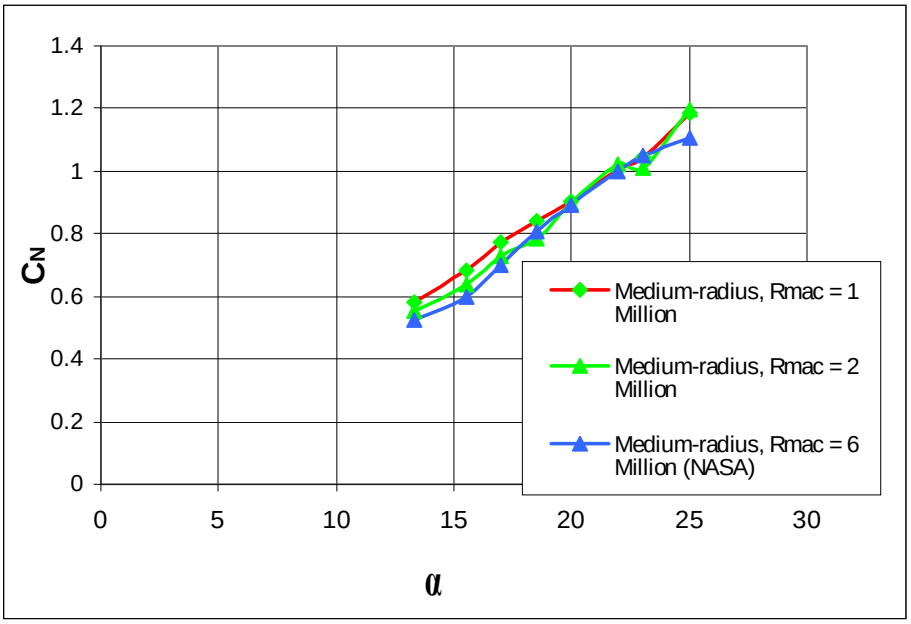

c) Medium-radius wing

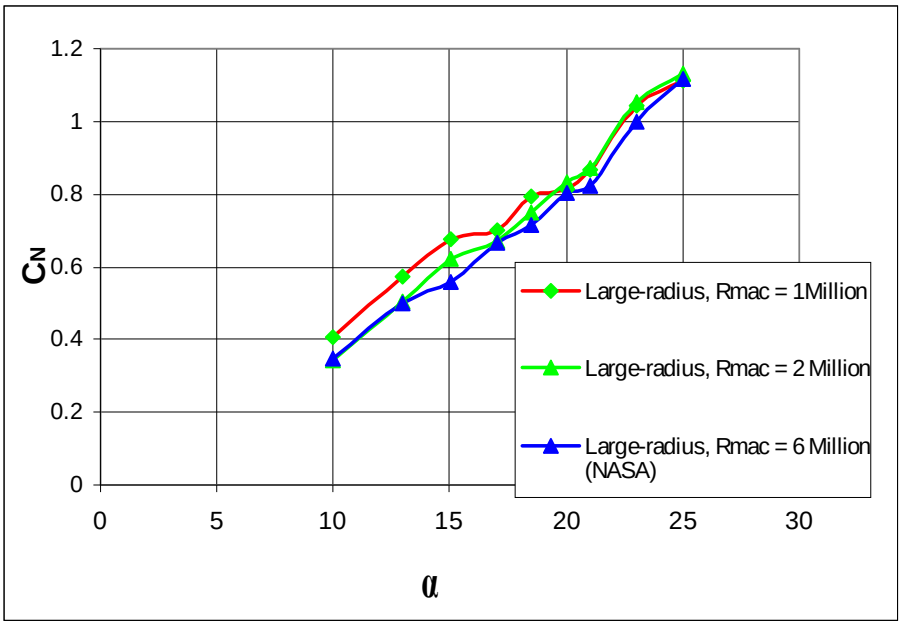

d) Large-radius wing

Figure 4.9: Comparison of normal force coefficients at three Reynolds numbers, $R_{mac} = 1 \times 10^6$, $R_{mac} = 2 \times 10^6$ & $R_{mac} = 6 \times 10^6$ for; a) the sharp, b) the small, c) the medium and d) the large-radius wing.

4.6 The Effects of Angle of Attack and Reynolds Number on the Wing Pitching Moment

Figure 4.10 shows the pitching moment coefficients at 1, 2 and 6 million Reynolds number for all cases of the wing. The results at 6 million Reynolds number are taken from Chu & Luckring (1996). There are significant changes in pitching moment coefficients with Reynolds number. Increasing the Reynolds number significantly decreases the nose down pitching moment in all cases. The differences will be linked with the physical size of the primary vortices and the location of the aerodynamic centre of the wing at these Reynolds numbers. The results at 6 million Reynolds number of Chu & Luckring were also performed in the transonic regime, 0.4 Mach number, while the current experiments at Glasgow were conducted in the subsonic regime. This may also be a factor but there is not enough evidence at this stage to provide a definitive explanation.

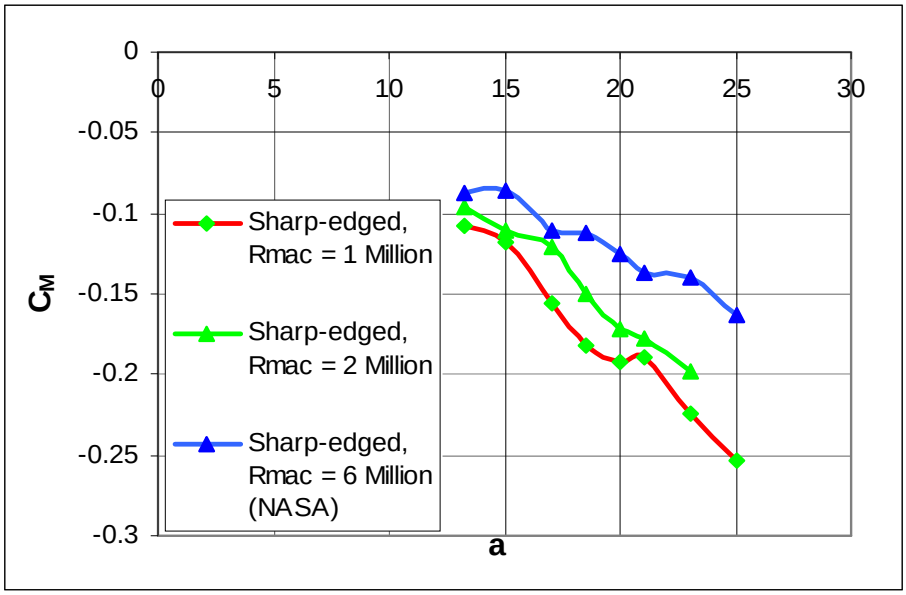

a) Sharp-edged wing

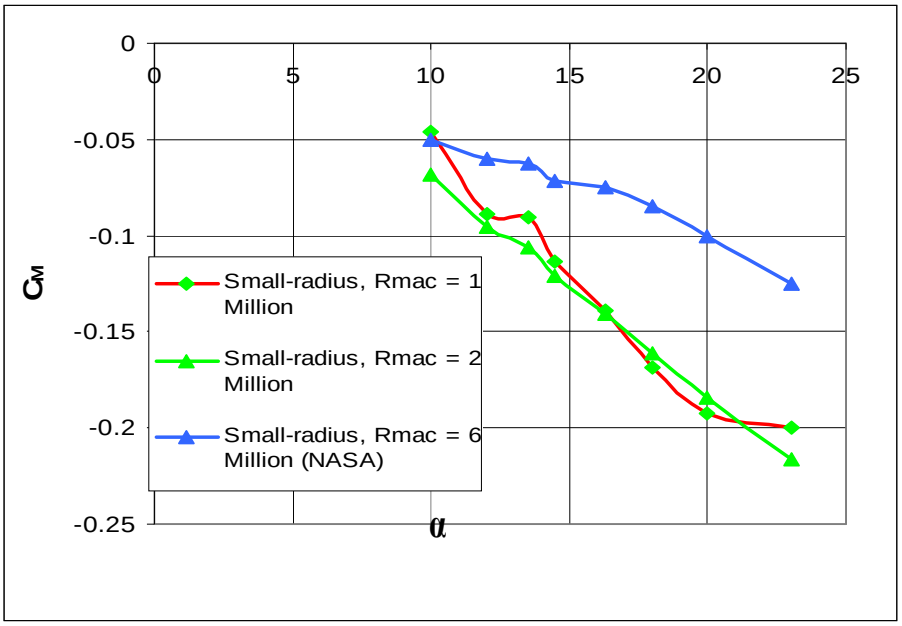

b) Small-radius wing

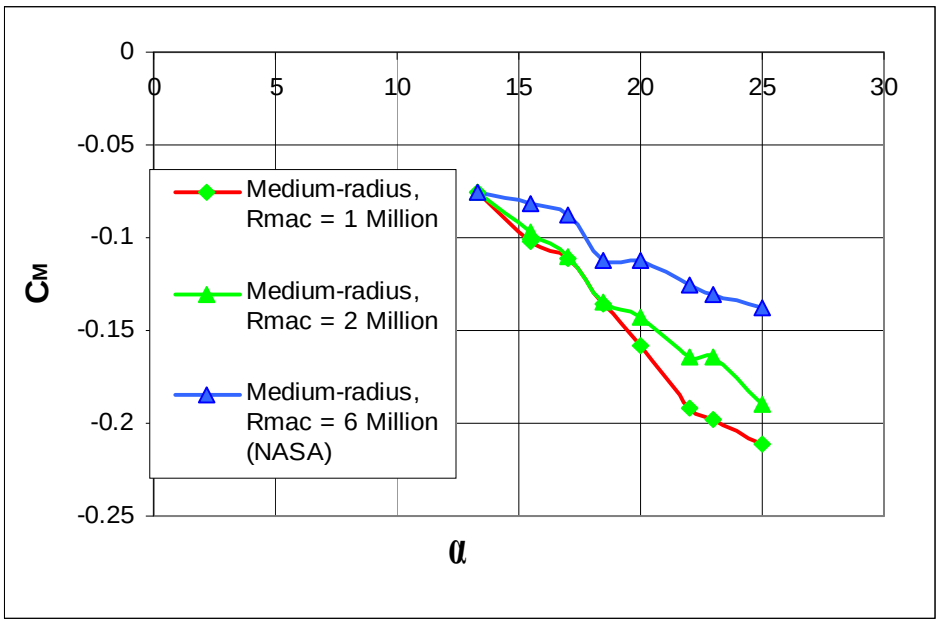

c) Medium-radius wing

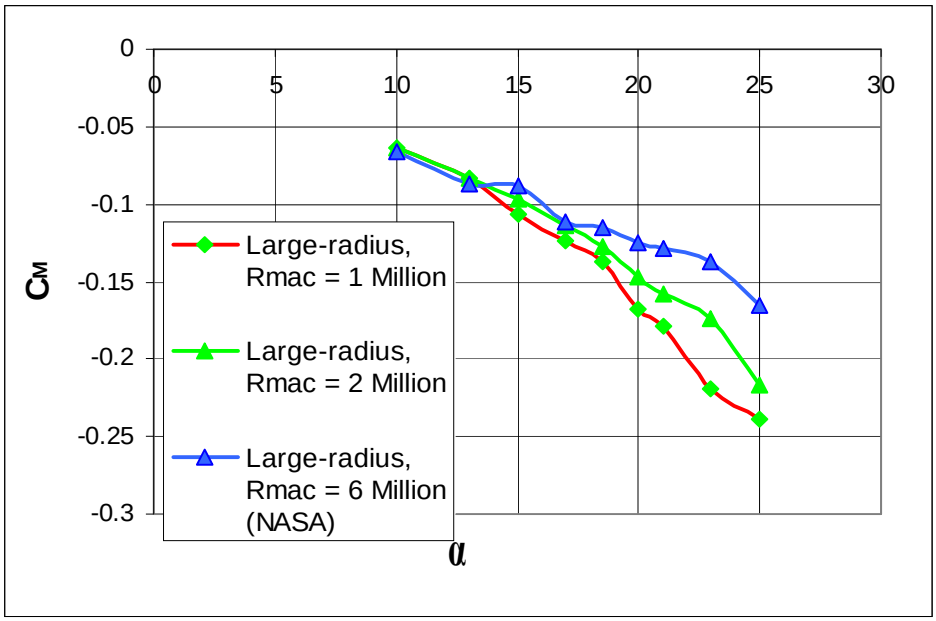

d) large-radius wing

Figure 4.10: Comparison of pitching moment coefficient at three Reynolds numbers, $R_{mac} = 1 \times 10^6$, $R_{mac} = 2 \times 10^6$ & $R_{mac} = 6 \times 10^6$ for; a) the sharp-edged, b) the small, c) the medium and d) the large-radius wing.

The pitching moment coefficients obtained from this experiment were compared with the work of ONERA (Rodriguez, 2008) and Tubitak-Sage (Kurun, 2008). This is done in figure 4.11 for the Reynolds number of $1x10^6$case. The pitching moment results show generally good agreement with ONERA and Tubitak-Sage up to around $\alpha = 20^0$. At higher angle of attack, the blockage in the Glasgow University wind tunnel is very high and this may have contributed to the differences in the measurements.

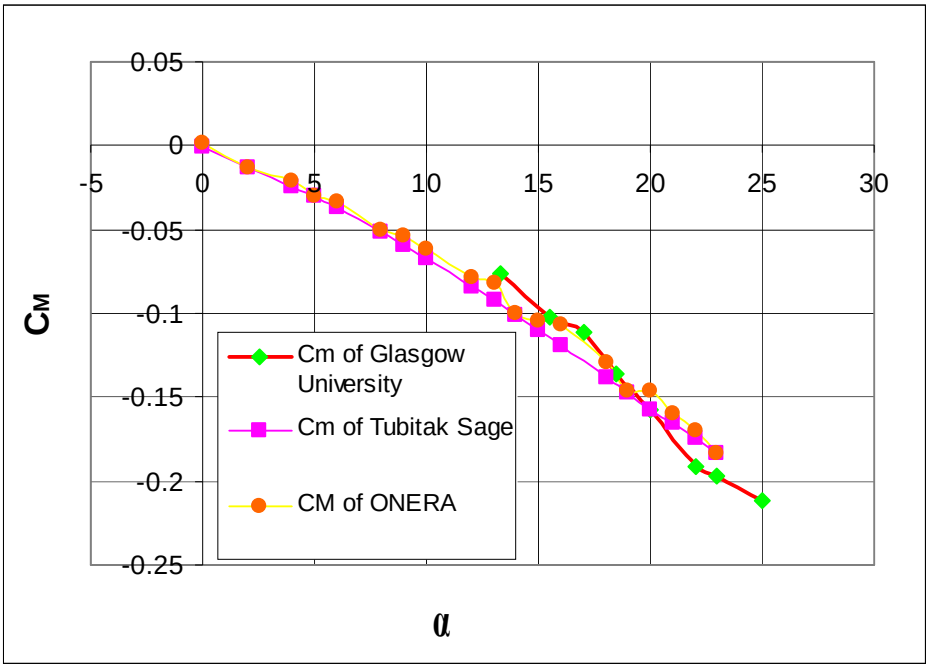

Figure 4.11: The comparison of wing pitching moment coefficients from Glasgow University, ONERA & TUBITAK-SAGE Wind Tunnels at 1 x 10^6 Reynolds Number

The normal force coefficients from the sharp and medium radius wings are also compared with the results of Tubitak-Sage in figure 4.12. This Figure shows a very good agreement between the two data sets considering the data are not corrected for tunnel blockage.

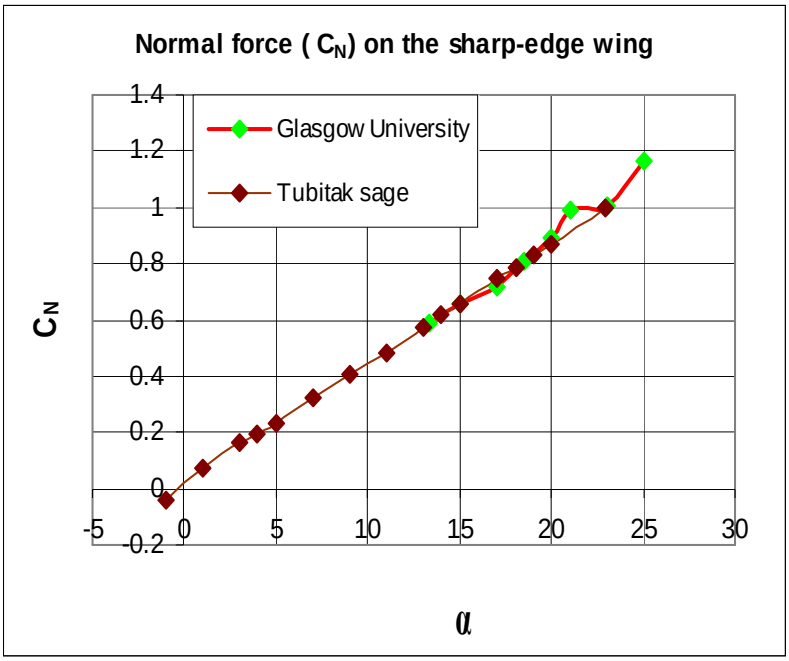

a) Sharp-edged wing

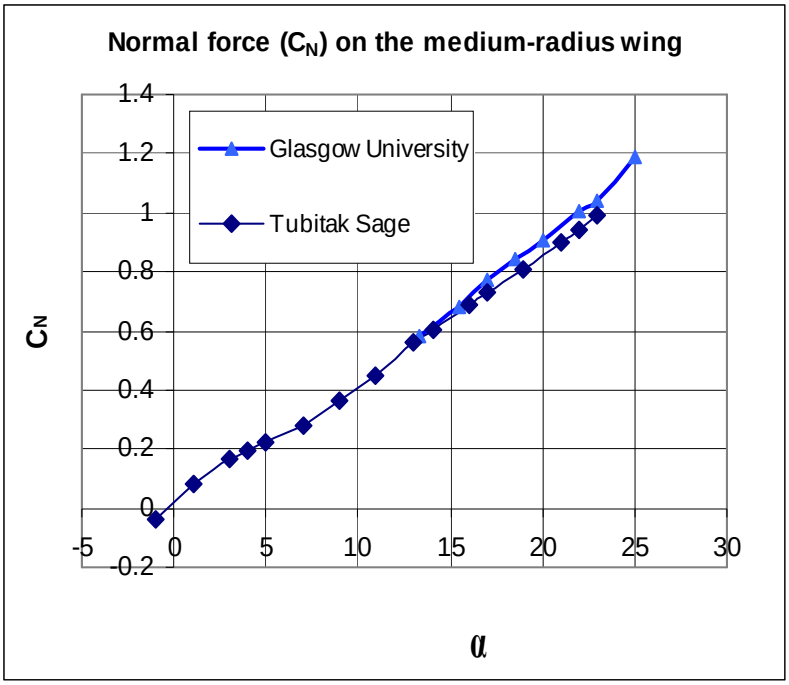

b) Medium-radius wing

Figure 4.12: The comparison of normal force coefficients obtained from Glasgow University and TUBITAK-SAGE wind tunnel for the sharp and medium radius wing at 1 x 10^6 Reynolds number

4.7 PART 11: UNSTEADY BALANCE MEASUREMENTS

4.7.1 Unsteady Forces and Moments

This chapter discusses the unsteady balance measurements made on the delta wing. The effects of Reynolds number, angle of attack and leading-edged bluntness on the load spectra are discussed below.

4.7.2 Bare Test Experiments

The results of the bare experiments discussed in Chapter 3 are shown in Figure 4.13. At a speed of 41.23 m/s (R_{mac} = 2 x 10^6) and a short sting angle of 23^o, no major resonance peak on the data spectrum was observed. Nevertheless, there appears a relatively weak peak at about 63 Hz from the figure. The peak is postulated to be induced by a vortex which develops around the cone at high angle of attack. The bare experiment was carried out by performing several series of experiments without the model (shown in figure 3.14 of chapter 3) in situ to isolate the vibrational characteristics of the isolated support.

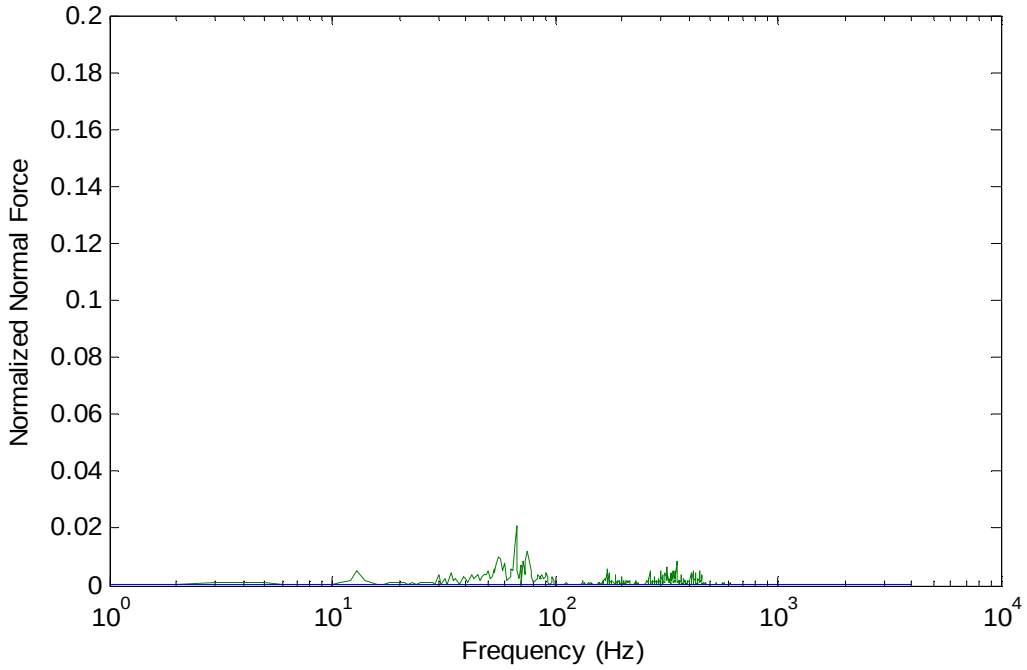

Figure 4.13: Data spectra of normal force of the bare experiments at a speed of 41.23 m/s, $R_{mac} = 2 \times 10^6$ & $\alpha = 23^0$.

4.7.3 Identification of the Natural frequency of Structural Vibration

A sample load spectrum plot calculated for the sharp-edged wing, at $\alpha = 18^0$ and $R_{mac} = 2 \times 10^6$ is presented in Figure 4.14. The figure shows two dominant frequency peaks. A dominant spike at a lower frequency of ~ 6 Hz was obtained in every power spectrum.

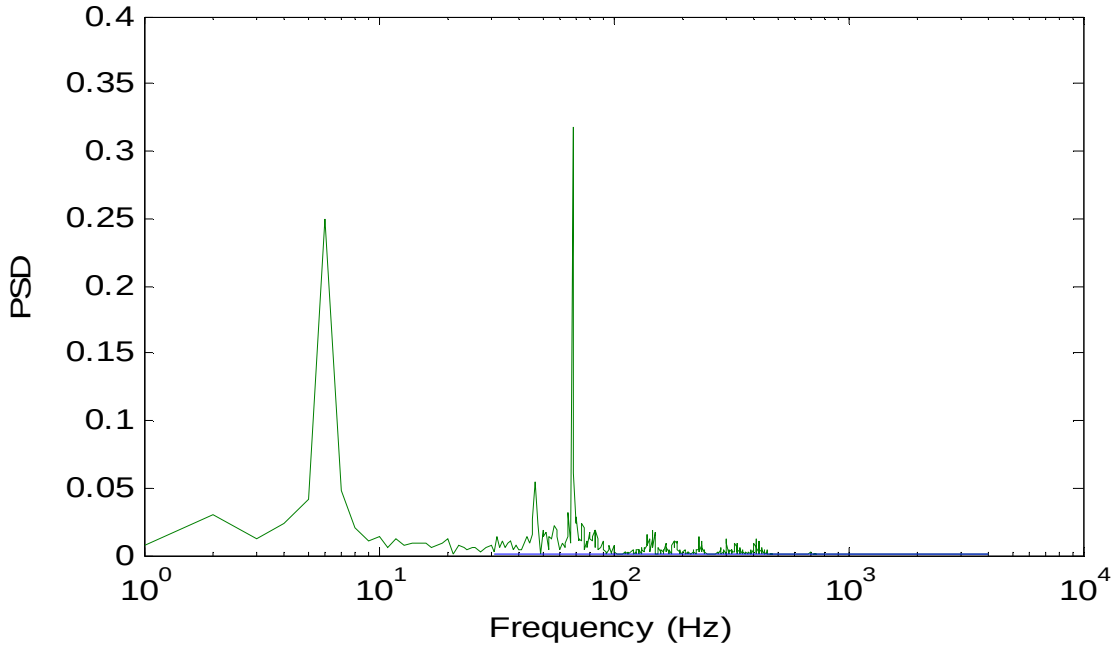

Figure 4.14: Data spectra of normalized normal force for the sharp-edged wing, at $\alpha = 18^0$ & $R_{mac} = 2 \times 10^6$

In order to verify the source of this low frequency, the model was tapped with a mallet with the wind off and the forces and moments were then recorded. The calculated data spectrum of the normal force for this case is shown in Figure 4.15. This produced a single frequency peak representing the natural frequency of the vibration of the structure, f_n at about 6 Hz. Similar practice by Tsang *et al* (2008) also produced a single frequency peak at the natural frequency of vibration of the structure for their aerofoil experiments.

The second large spike at about ~ 65 Hz, in Figure 4.14, was most probably linked to the flow characteristics on the wing. From the literature review of Hummel & Luckring (2008) the flow on the sharp-edged wing at $\alpha = 18^0$ is dominated by the primary vortex extending from the apex to trailing edge. Thus, the spike is strongly suspected to have been induced by the primary vortex. This hypothesis is in agreement with Mabey (1992) and Baban *et al* (1989). They suggested that the spike in the data spectra was indeed due to the separated flow or the vortex system. In

addition, Mabey (1992) also discussed that tunnel resonances would not influence the data spectra.

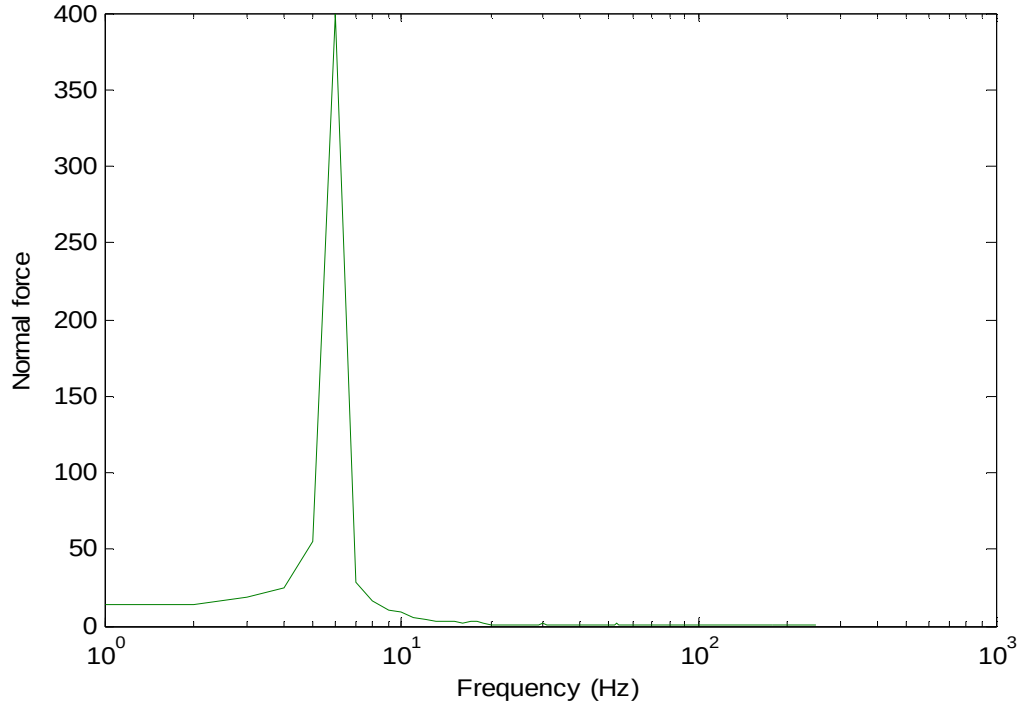

Figure 4.15: Data spectra of the vibration, at $\alpha = 13.3^0$

4.8 The Effects of Leading-Edge Radius on Unsteady Normal Force

The data spectra, at a Reynolds number of 2 x 10^6, for all wings are presented in Figures 4.16, 4.17, 4.18 & 4.19 at $\alpha = 13.3^0$, 18^0 and 23^0 respectively.

4.8.1 The Effects of Leading-Edge Radius at $\alpha = 13.3^0$

In Figure 4.16 i), the dominant frequency of the primary vortex is clearly visible for the sharp-edged wing. Comparing this with the other plots in the same figure, the magnitude of dominant peak associated with the primary vortex is higher for the sharp-edged wing than for the other wings. The reason for this is associated with the dominance of the strong primary vortex on the sharp-edged wing. The result is also consistent with Gursul & Xie (1999) who showed the magnitude of the spectral

peak depends on the strength of the vortex system, i.e. stronger primary vortex induces a higher peak magnitude. For the other wings, the magnitude of the primary vortex peak is reduced. This is consistent with a slightly weaker primary vortex with the increase in leading edge radius.

For the medium-radius wing (figure 4.16 iii)) another significant peak appears at about 45 Hz which may be associated with the inner vortex. On this wing, this secondary peak is weaker than that of the primary vortex, which is consistent with the earlier hypothesis that the inner vortex is weaker than the primary vortex on this configuration.

On the large-radius wing (figure 4.16 iv)), the inner vortex peak increases to become equivalent to the primary vortex peak. The result suggests the inner vortex has a similar magnitude to the primary vortex at this angle of attack. This is consistent with the hypothesis discussed in the steady balance measurement section.

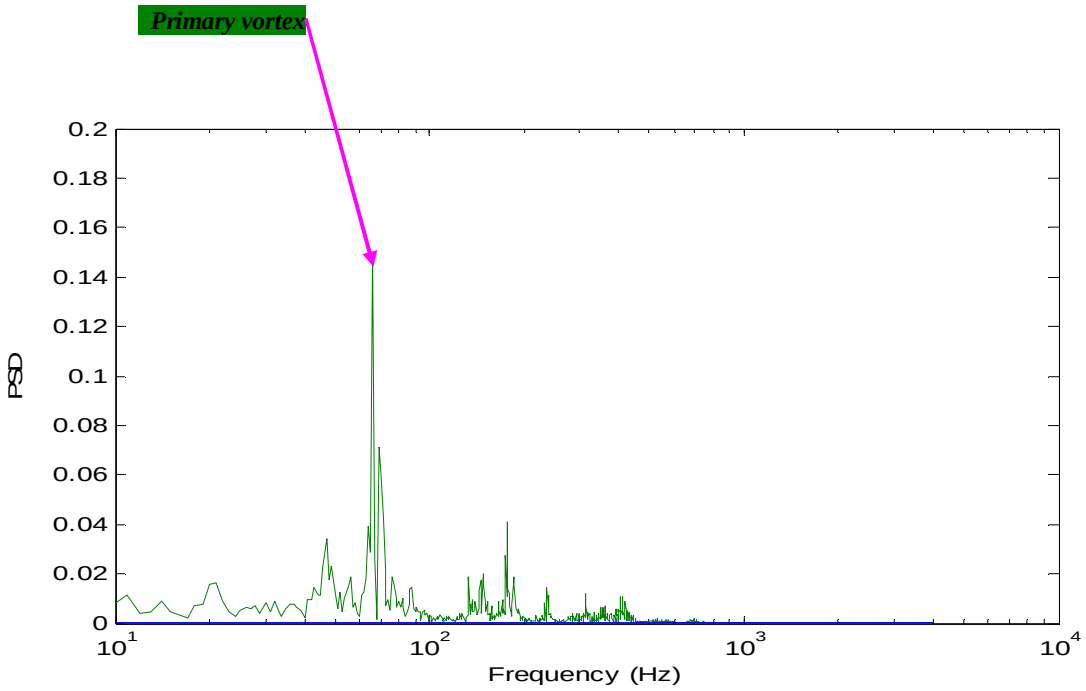

i) Sharp-edged

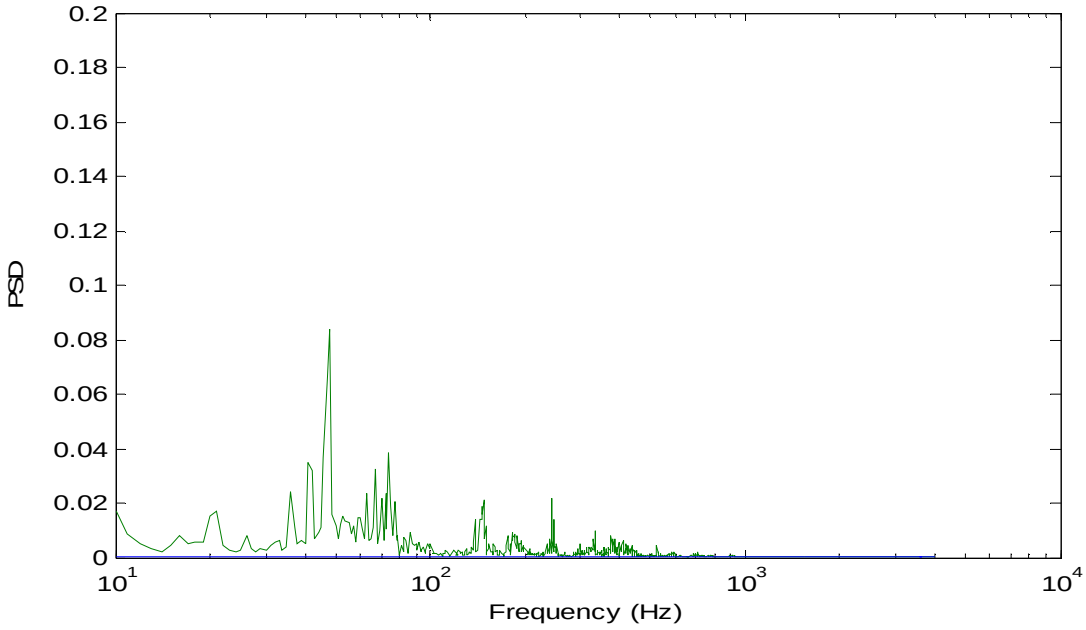

ii) Small-radius

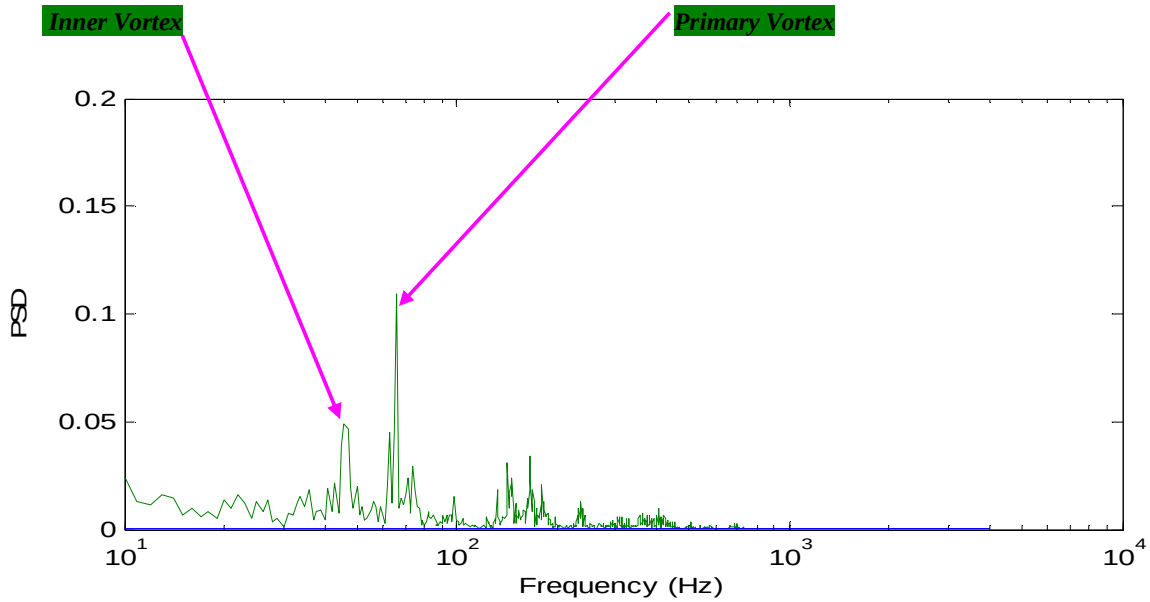

iii) Medium-radius

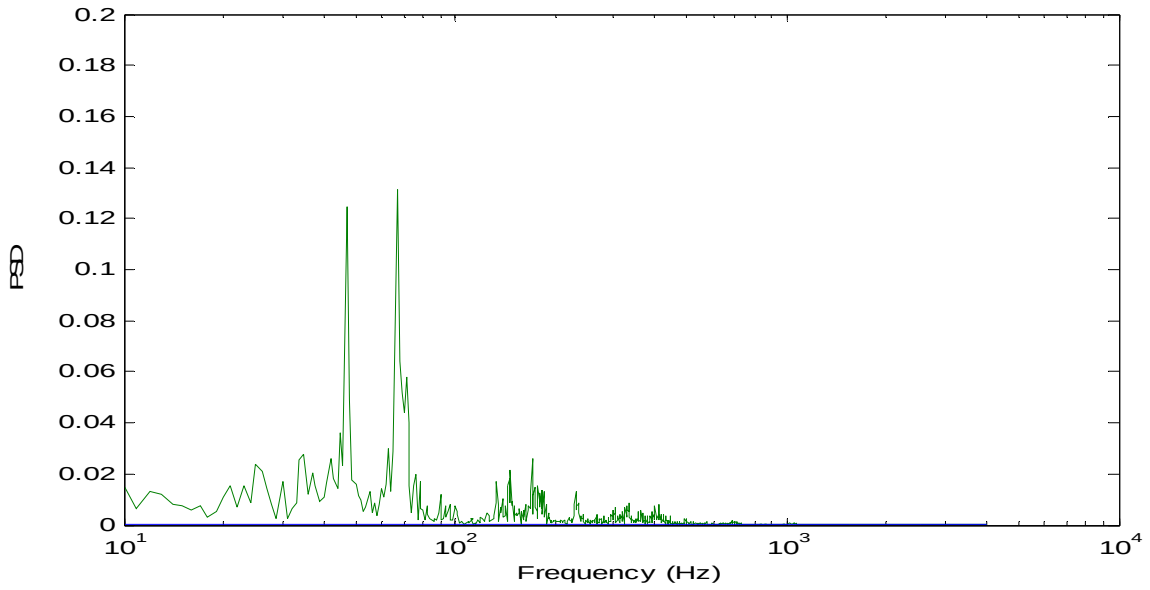

iv) Large-radius

Figure 4.16: The effects of leading-edge radius on normal force spectra, at $\alpha = 13.3^0$ and $R_{mac} = 2 \times 10^6$

4.8.2 The Effects of Leading-Edge Radius at $\alpha = 18^0$

Figure 4.17 shows the effects of leading-edge radius on the data spectra at a Reynolds number of 2 x 10^6 as the angle of attack is increased to $\alpha = 18^0$. The figure shows a dominant peak from the primary vortex for the sharp, small and medium-edged wings. The results in general show that the magnitude of the peak of dominant frequency of the primary vortex decreases with increasing leading edge radius. This is consistent with the weakening of the primary vortex as the leading edge radius is increased.

There was no evidence of the peak associated with the inner vortex for the small and medium-radius wings at this angle of attack. This suggests that the inner vortex identified in the flow visualization studies on the small and medium-radius wings is very weak at higher angles of attack ($\alpha = 18^0$). The results are consistent with those of Luckring & Hummel (2008) which suggested that the flow on the medium-radius wing was fully dominated by the primary vortex; i.e. the origin of the primary vortex had already moved close to the apex of the wing at $\alpha = 18^0$ so diminishing the inner vortex.

Nevertheless, the frequency of the inner vortex was still induced on the large-radius wing but was weaker than in the $\alpha = 13^0$ case.

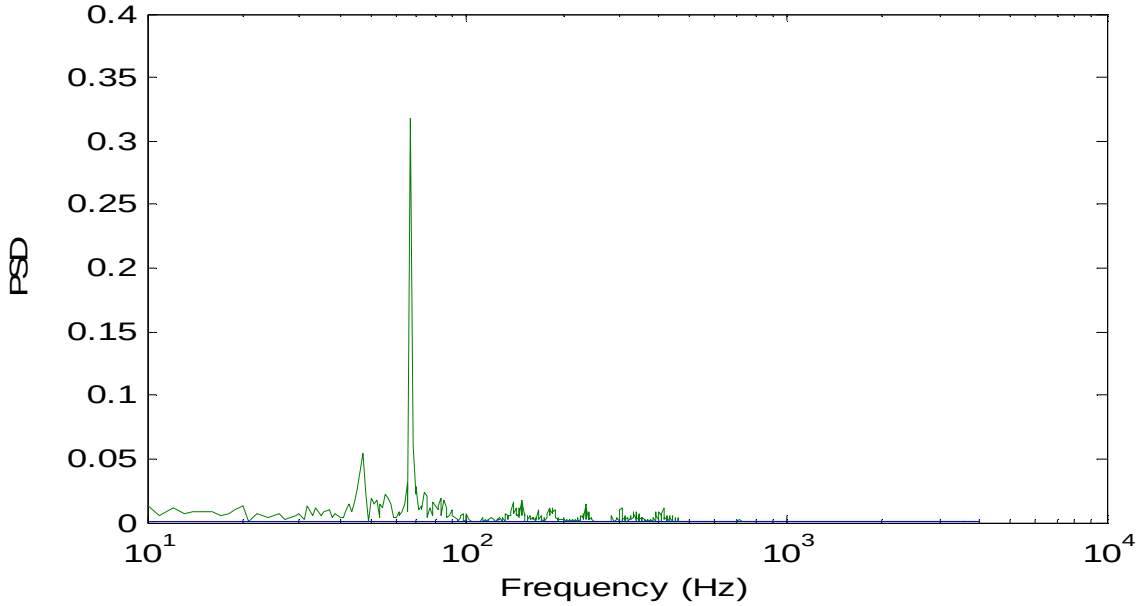

i) Sharp-edged

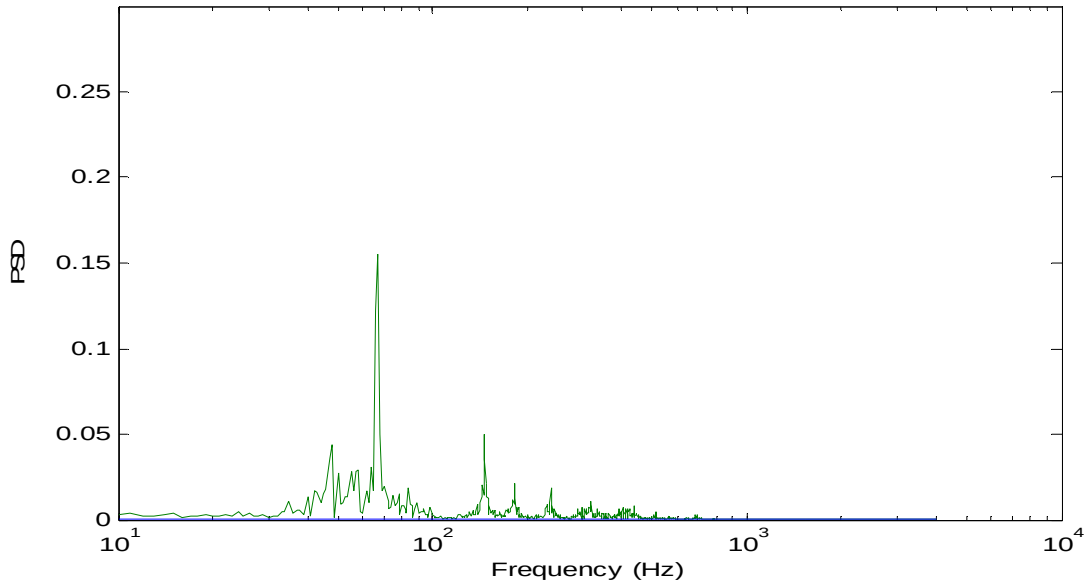

ii) Small-radius

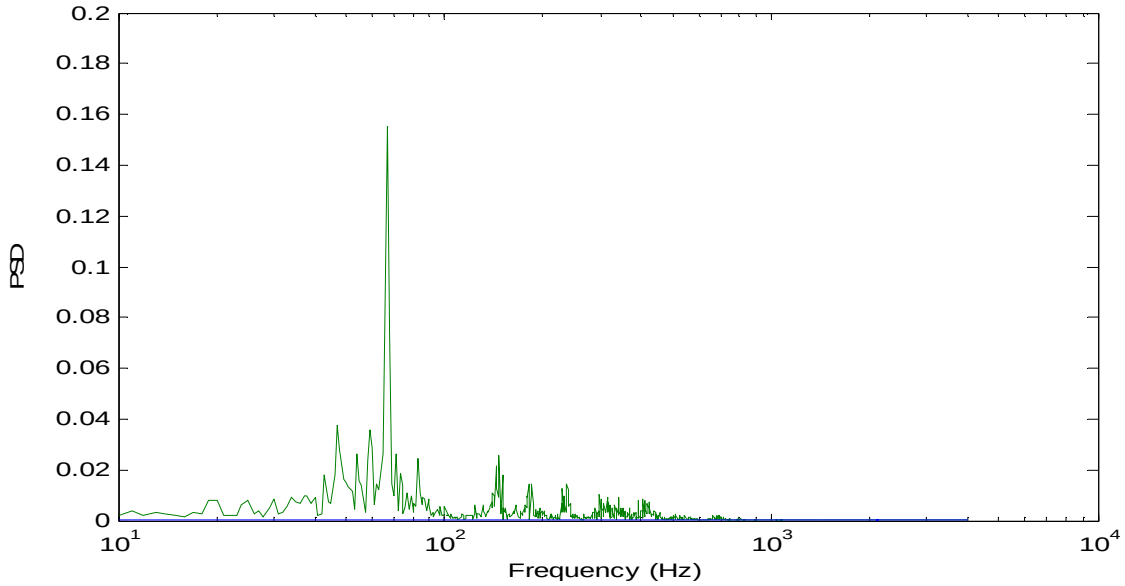

iii) Medium-radius

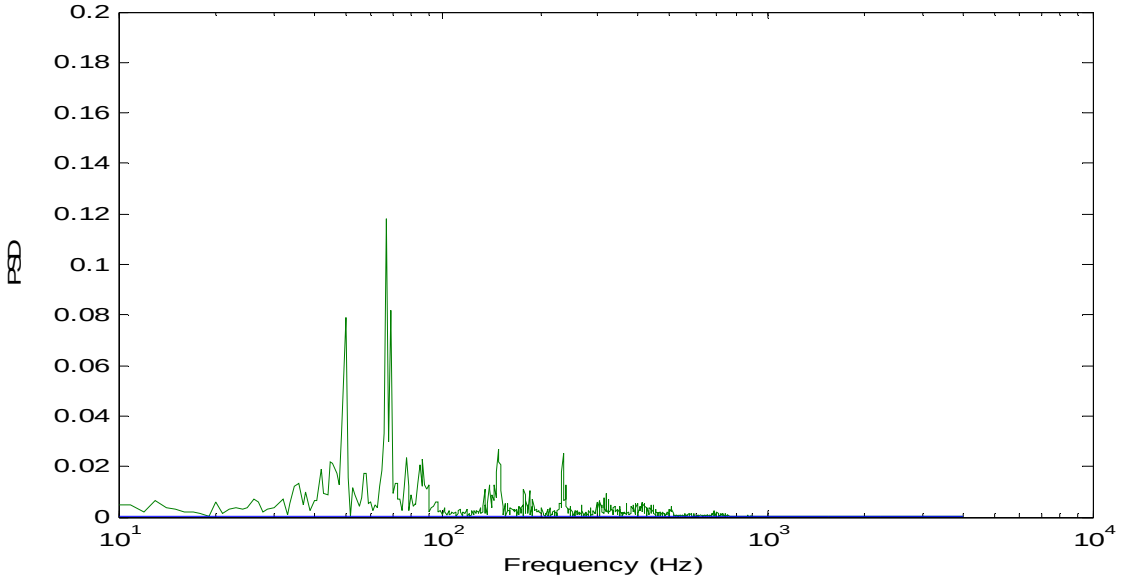

iv) Large-radius

Figure 4.17: The effects of leading-edge radius on normal force spectra, at $\alpha = 18^0$ and $R_{mac} = 2 \times 10^6$

4.8.3 The Effects of Leading-Edge Radius at $\alpha = 23^0$

The characteristics of the unsteady data at the higher angle of attack of $\alpha = 23^0$ for the sharp, small and medium-radius wings are shown in Figure 4.18. The data for the sharp-edged, small-radius and medium-radius wings are quite similar. The first obvious feature in the data spectra is that the dominant frequency is now surrounded by several other smaller peaks and a general increase in unsteady activities. This behaviour can be linked to the loss of coherence of the primary vortex due to the breakdown in the trailing edge region. When this happens, the flow in the trailing edge regions becomes dominated by large scale turbulence in the post-breakdown breakdown region. The data are in good agreement with Luckring & Hummel (2008) who found that the VFE-2 delta wing experienced breakdown of the primary vortex at $\alpha = 23^0$.

Secondly, the data indicated a reduction in the magnitude of the peaks associated with the primary vortex for these three wings. The relative magnitudes of the peaks were much lower compared to those at $\alpha = 18^0$. This can be attributed to the reduced dominance of the coherent primary vortex as vortex breakdown traverses over the wing.

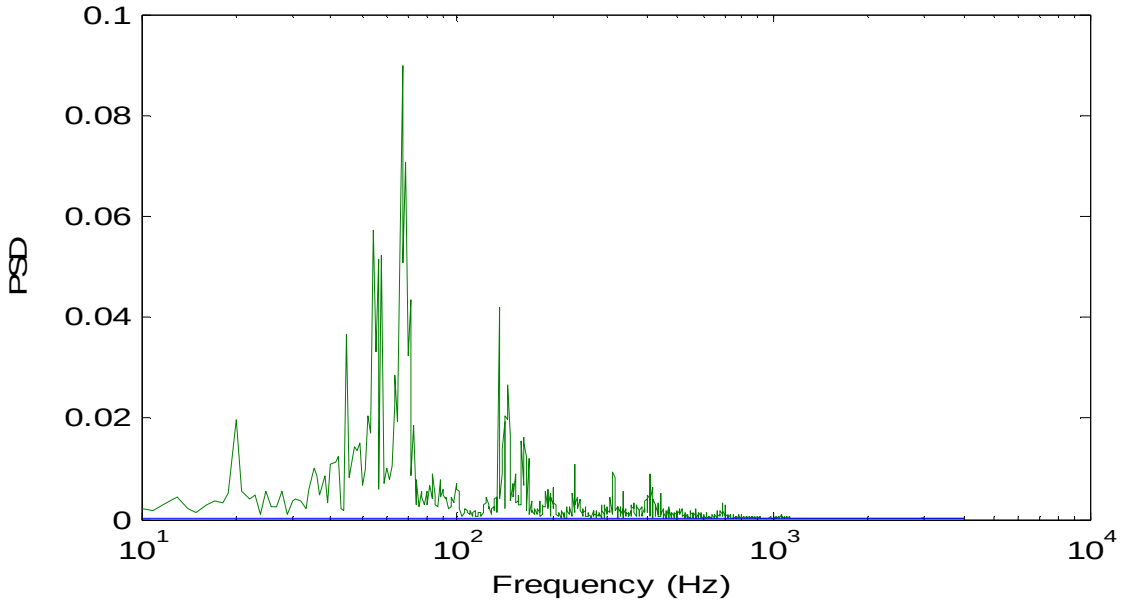

i) Sharp-radius

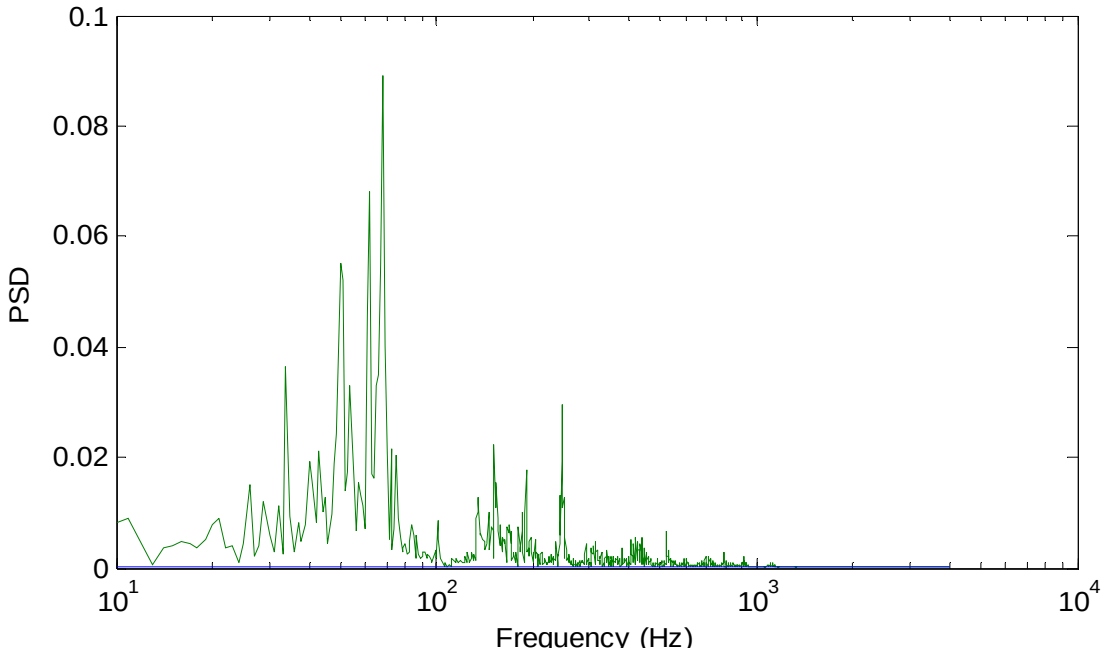

ii) Small-radius

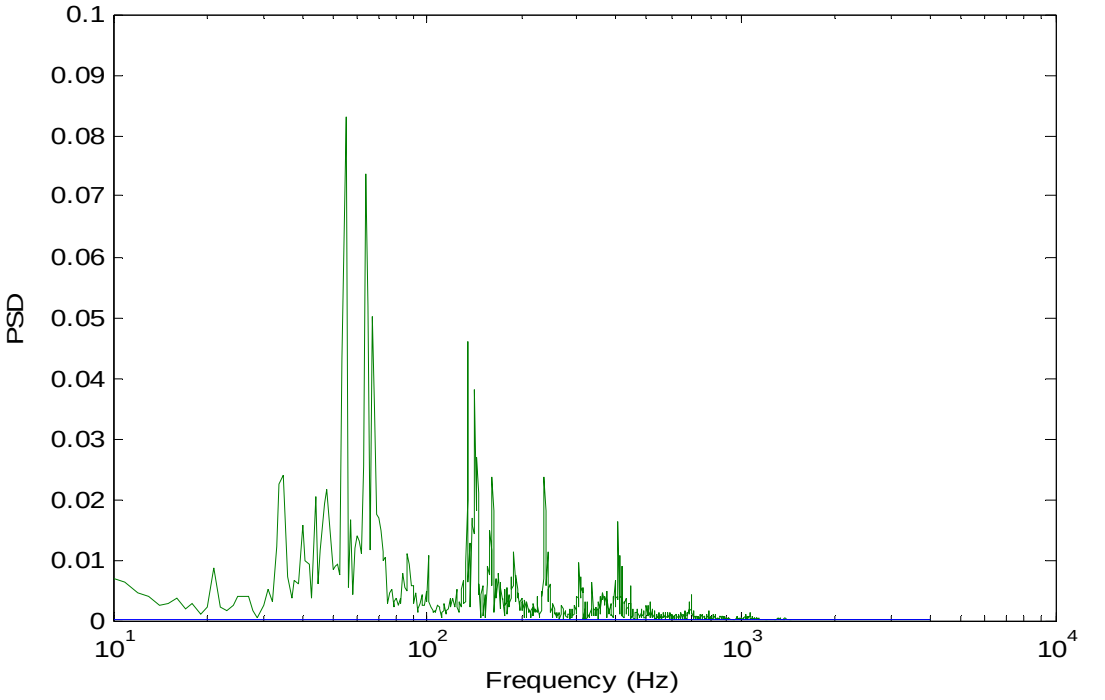

iii) Medium-radius

Figure 4.18: Data spectra of the sharp, small and medium-edged wings at $R_{mac} = 2 \times 10^6$ and $\alpha = 23^0$

The above trends were not observed on the large-radius wing, as shown in Figure 4.19. The results for this wing showed two dominant frequencies still existed at $\alpha = 23^0$. Presumably the flow was still dominated by a double vortex system. The spectral peak of the primary vortex at this angle of attack was higher compared to those from the sharp, small and medium-radius wings. This result is most likely due to vortex breakdown not being as significant for this test condition. This supports the hypothesis discussed in the flow visualization chapter that the increase in the leading-edged radius delays the breakdown of the primary vortex. These finding are in good agreement with Kegelman and Roos (1989) who experimentally showed that vortex breakdown was delayed by increasing the leading-edge bluntness. For this wing, vortex breakdown was expected to occur in the trailing-edge area at angles greater than $\alpha = 23^0$.

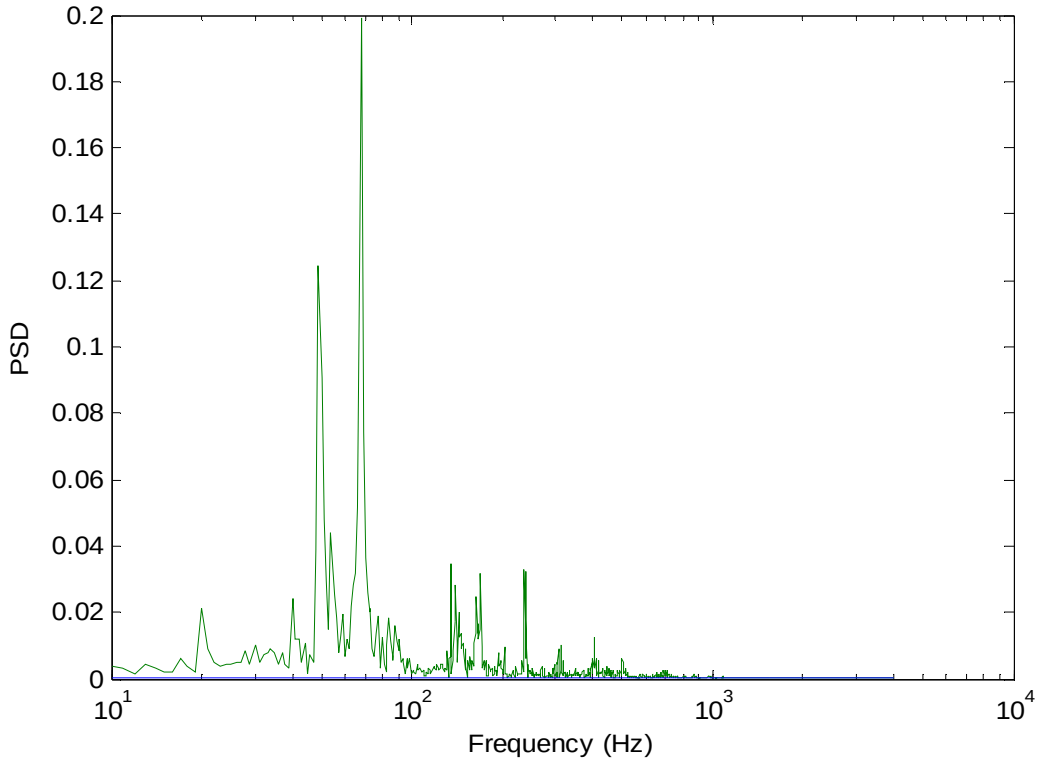

iv) Large-edged

Figure 4.19: Data spectra of the large-edged wing at $R_{mac} = 2 \times 10^6$ and $\alpha = 23^0$

4.9 The effects of the angle of attack on the unsteady normal force

4.9.1 Sharp-edged wing

Figures 4.20 and 4.21 show the way in which angle of attack affects the data spectra for the sharp and blunt leading edge wings respectively. For the sharp-edged wing, the result shows the spectral peak of the primary vortex is increased with an increase in the angle of attack from $\alpha = 13^0$ to $\alpha = 18^0$. The higher peak is caused by the stronger primary vortex at the higher angle of attack. These results are consistent with Baban *et al* (1989), Mabey (1992) and Gursul & Xie (1999) i.e., stronger vortex or separated flow will induce a higher peak in the spectrum.

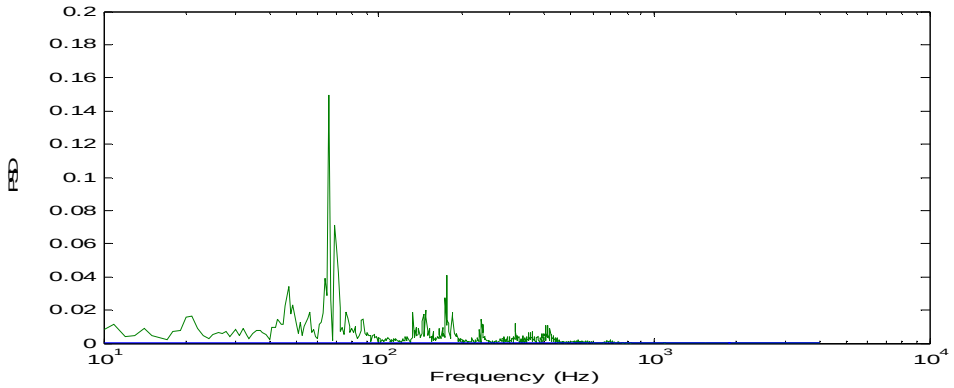

i) Sharp-edged, at $\alpha = 13^0$

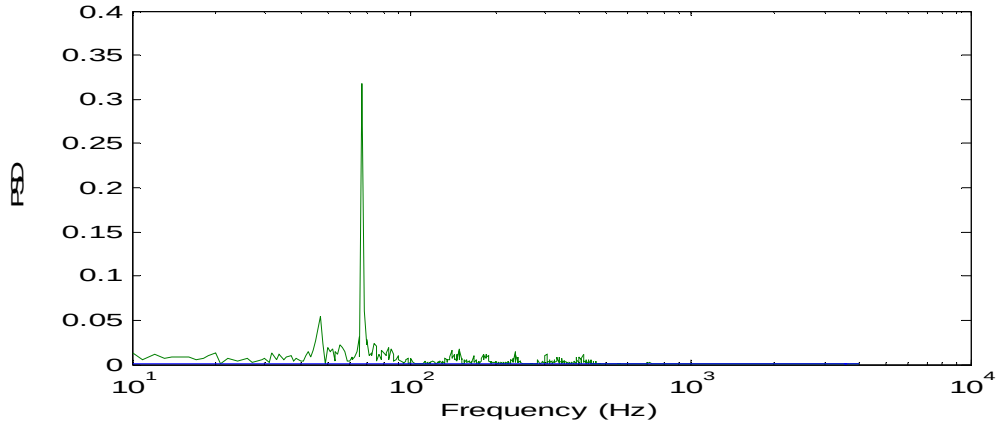

ii) Sharp-edged, at $\alpha = 18^0$

Figure 4.20: The effect of angle of attack on the data spectra for the sharp-edged wing at $R_{mac} = 2 \times 10^6$

4.9.2 Blunt leading edge

The data spectra of the rounded-edged wing, in this case the medium-radius wing, show an excellent agreement with the hypothesis discussed in the flow visualization chapter. At an angle of attack of $\alpha = 13^0$, the shape of the spectrum confirms that the primary vortex is stronger than the inner vortex. An increase in the angle of attack to $\alpha = 18^0$ diminishes the inner vortex, while the primary vortex increases in strength.

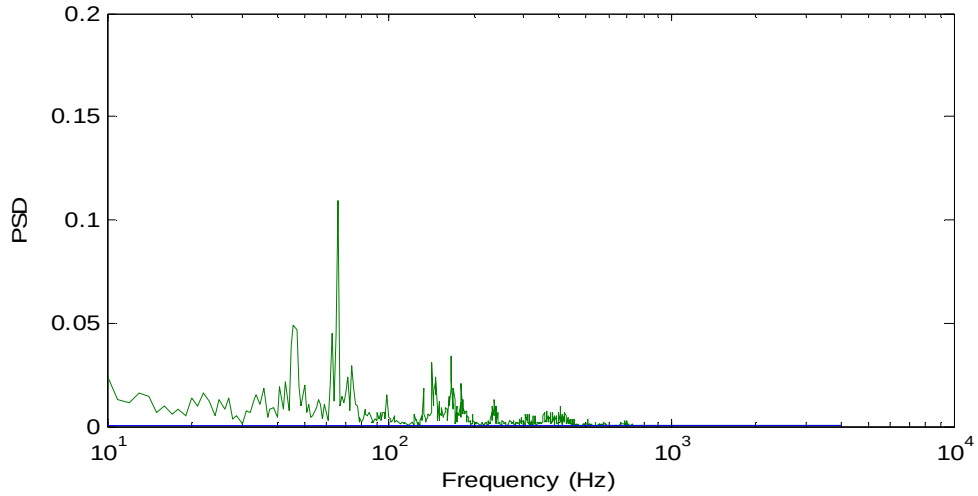

i) Medium-radius wing, at $\alpha = 13^0$

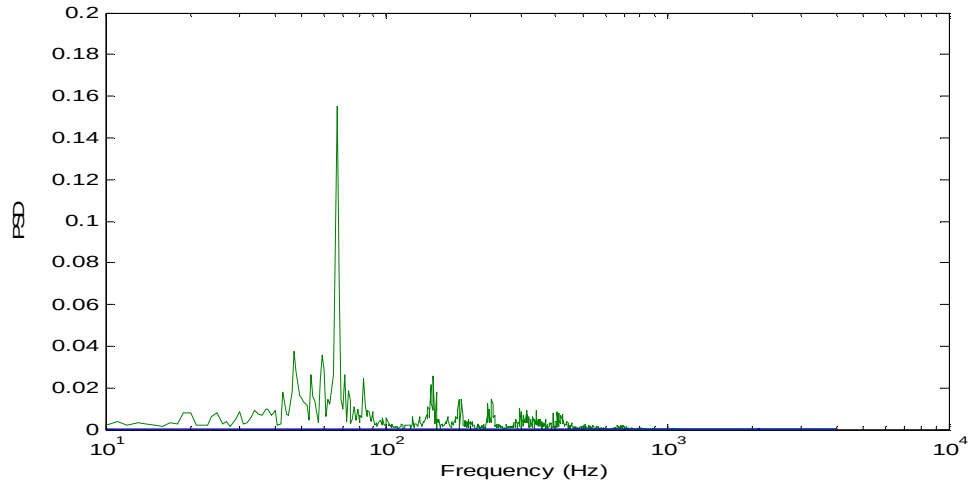

i) Medium-radius wing, at $\alpha = 18^0$

Figure 4.21: The effect of angle of attack on the data spectra for the medium-radius wing at $R_{mac} = 2 \times 10^6$

Chapter 5

5.0 RESULTS – FLOW VISUALIZATION TECHNIQUES

5.1 PART I: OIL FLOW VISUALIZATION STUDIES

This chapter will discuss the effects of bluntness, angle of attack and Reynolds number on the flow topology on delta wings as determined from oil flow experiments.

5.1.1 Sharp Leading Edge Flow Topology

Figure 5.1 highlights some the common features of an established oil flow topology on the sharp-edged wing. This is a useful point of reference for the following discussion in this chapter. On the sharp-edged wing the primary separation is fixed at the leading edge starting in the vicinity of the apex. This separation then rolls-up to form a primary vortex system whose separation and attachment lines are visible on the wing surface. Attached non-separated flow is also observed near the wing centre line extending from the apex to the wing sting interface.

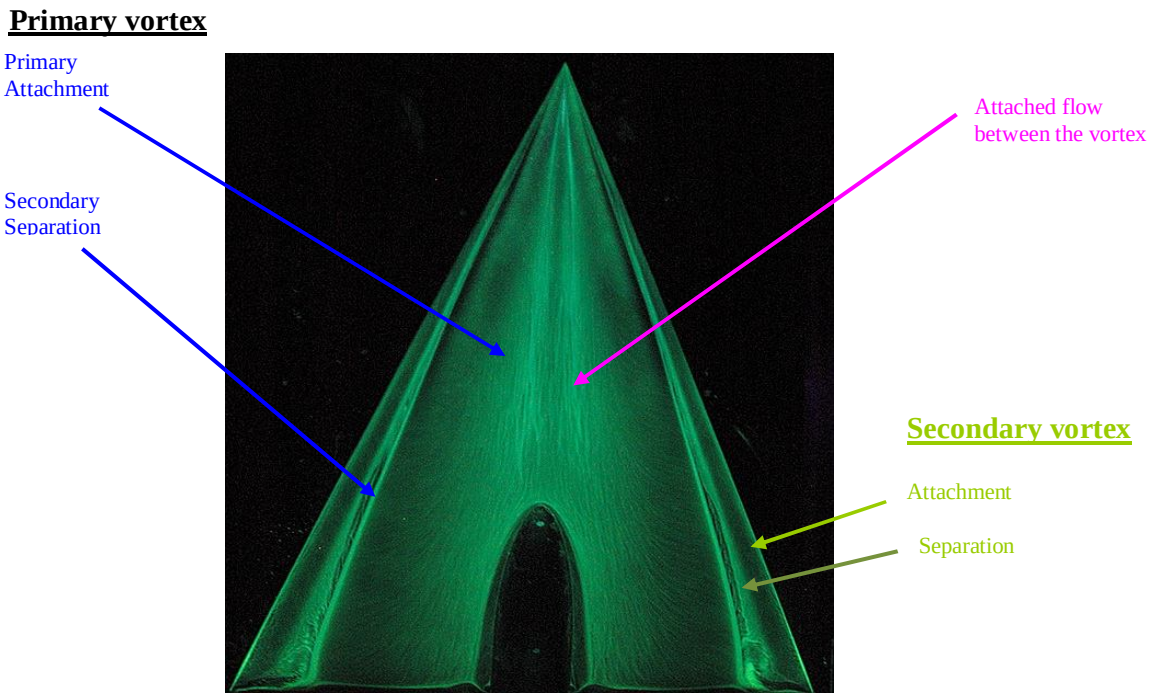

Figure 5.1: Flow topology of the sharp-edged delta wing ($\alpha = 13.3^0$)

5.1.2 Rounded Leading Edge

Figure 5.2 presents the flow topology of a generic round-edged wing. The apex region is covered by fully attached flow up to a certain chordwise distance. The primary vortex then develops further aft of the apex and is accompanied by a secondary system evidenced by clear separation and attachment lines. Inboard on the wing, another flow structure representing the footprint of the inner vortex as discussed by Hummel (2006) and Fritz (2008), is observed. The separation and attachment lines of the inner vortex are shown in the figure. The effect of bluntness, Reynolds number and angle of attack will be discussed in the next sub-section based on interpretation of the oil flow topologies in the same manner as figures 5.1 and 5.2.

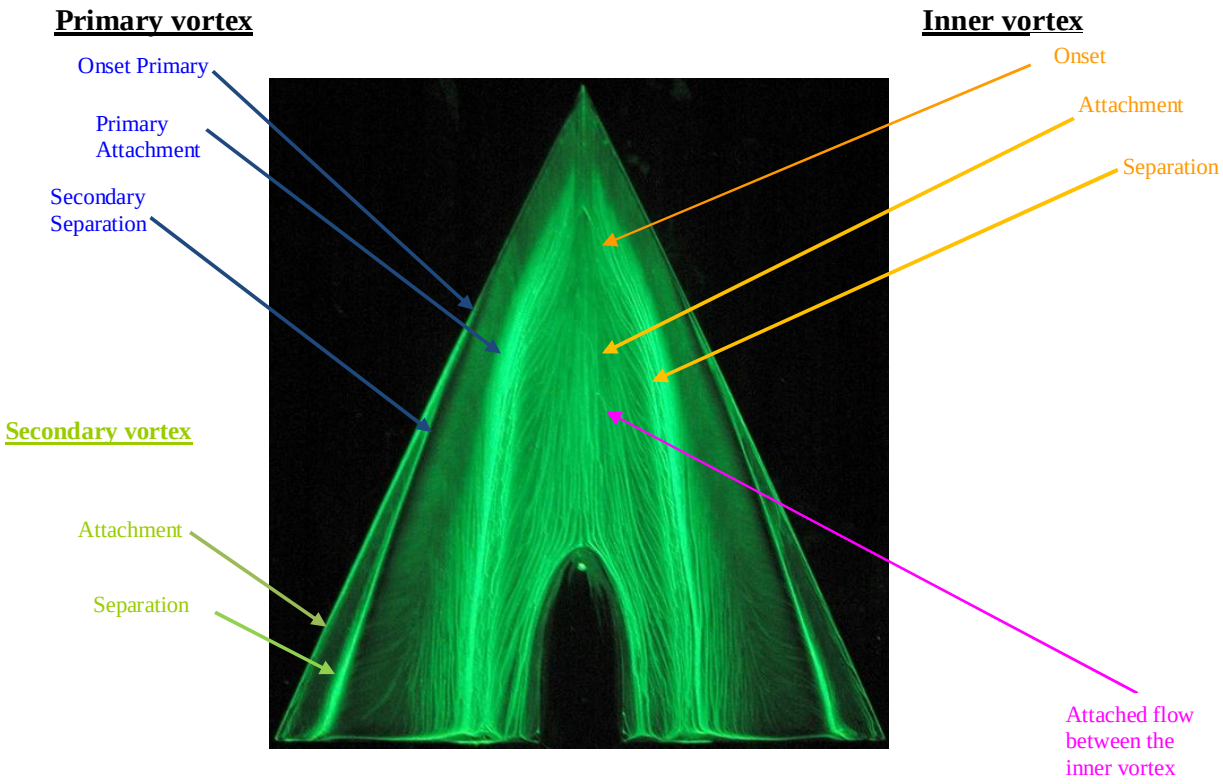

Figure 5.2: Flow topology of the round-edged delta wing ($\alpha = 13.3^0$)

5.2 - Leading Edge Bluntness Effect

Figure 5.3 shows the flow visualization results obtained at a Reynolds number of 1 million for the four different leading edges; sharp, small-radius, medium-radius and large-radius at an angle of attack of 13.3^o. In all cases, the footprint of a vortical structure can be observed near the leading edge. The secondary separation line also clearly delineates the location of the primary and secondary vortex. In all cases, the vortex system appears to originate in the vicinity of the apex of the wing and persists to the trailing edge. The leading edge bluntness does not obviously affect the primary vortex at this low Reynolds number. In fact, a closer examination reveals that this is only true for the sharp-edged wing and the wing with the small-radius leading edge. The dark line emanating from the apex of the medium-radius wing, normally associated with the core location of the primary vortex, exhibits a distinct bend at about 20-30% of root chord. Ahead of this location, the flow in the vicinity of the

leading edge is aligned with the mean flow direction whereas, aft of this location, the flow exhibits the classical orientation of vortical cross-flow. This is even more evident on the large-radius wing where the oil in the apex region appears to be almost wholly aligned with the mean flow direction.

There is also some evidence of an additional structure as reported by Hummel (2006), inboard of the primary vortex on all of the round-edged wings that becomes more distinct as the leading edge radius increases. This structure is not apparent on the sharp-edged wing. It also appears that increasing the leading edge bluntness moves the starting point of this inner vortex further downstream. On the small-radius wing, the inner vortex is initiated closer to the apex of the wing compared with the medium-radius or large-radius wings. In fact, the spanwise location and extent of the inner vortex are also significantly influenced by the leading-edge bluntness. Increasing bluntness moves the vortex separation line outboard and enlarges the physical size of the structure.

In the images below, the inner vortex is generally contained very close to the center of the wing when compared with inner vortex position on the large-radius wing. PIV measurements by Furman & Breitsamster (2008) on the medium radius suggested that the inner vortex disappears at this low Reynolds number. The proximity of the origin of the primary vortex to the apex at this low Reynolds number was thought to prevent the development of the inner vortex according to Furman & Breitsamter (2008). The results from the current study suggest otherwise. This will be discussed further in section 5.4.3.

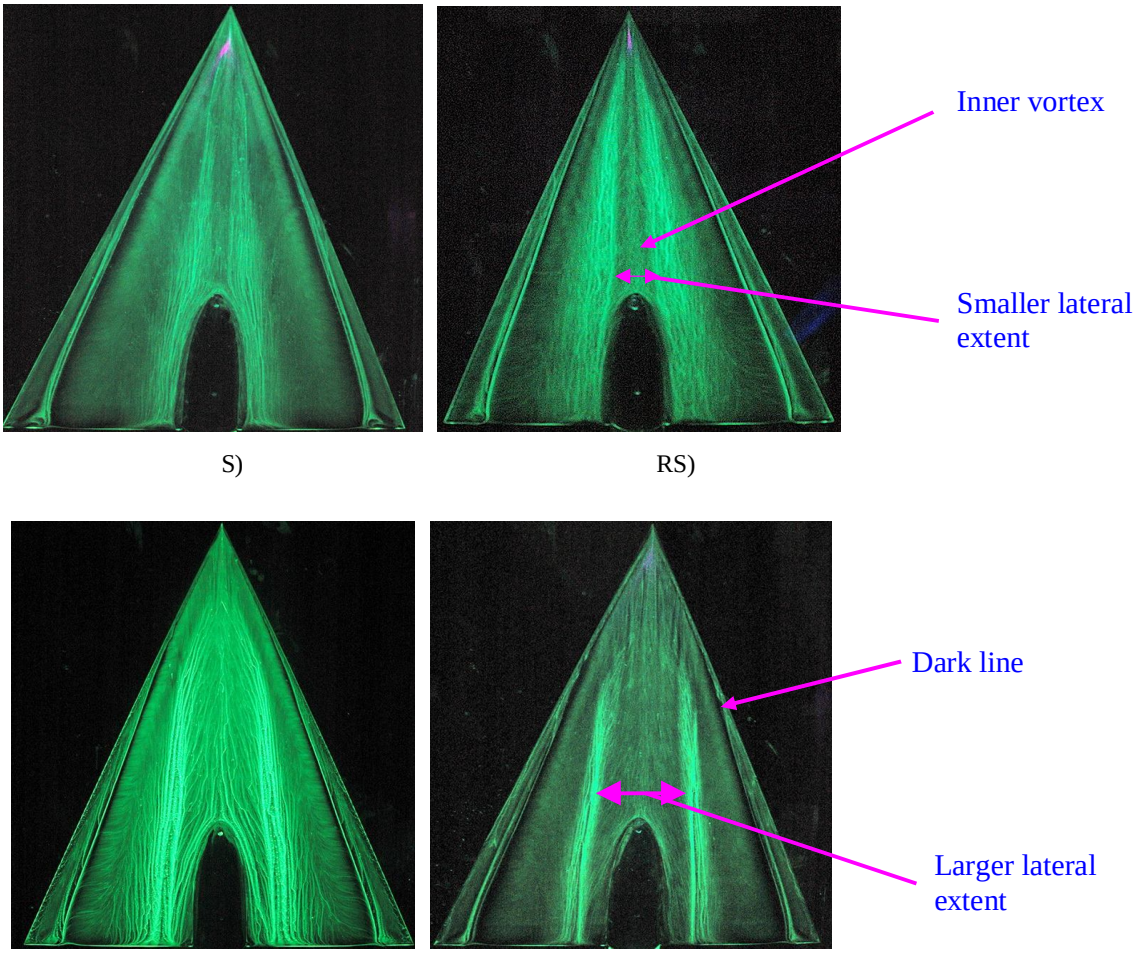

Figure 5.3: Comparison of oil flow topology for the Sharp edged, Small (RS), Medium (RM) and Large (RL) Radius wings at R_{mac} = 1 x 10^6.& $\alpha = 13.3^0$

Several important changes were observed as the Reynolds number was increased to 2x10^6. Figure 5.4 illustrates the comparison at this Reynolds number at the same angle of attack as before for the four sets of leading edges. The first obvious feature is that the primary vortex structures on the medium-radius and large-radius wings clearly no longer begin at the apex as they do for the sharp leading edge and small-radius wing. For the medium-radius wing, the primary vortex appears to have its origin at about 30% of the root chord down the trailing edge. For the large-radius wing, the bluntness causes the origin of the primary vortex to move rearwards to about 45% of the wing root chord. In both cases, upstream of this, there appears to

be attached flow in the streamwise direction in the vicinity of the leading edge followed by a separation front. As at the lower Reynolds number, another feature visible on all the round-edged wings is the footprint of the inboard structure. Again, the increase in the bluntness shifts the separation line of this vortex outboard, so enlarging the size of structure. It is likely that the strength of the primary vortex is related to this behavior. For the sharp-edged wing, the primary vortex is continually fed from the apex and the inner vortex is prevented from developing.

As the bluntness increases, the primary separation on the rounded edges is not fixed to the leading edge as it is on the sharp-edged wing. Rather, the primary separation occurs close to the leading edge after a short run of attached flow in the vicinity of the leading edge (Peake and Tobak, 1980). This both delays the formation of the primary vortex and reduces its strength. Thus, on the small-radius wing, the primary vortex is weaker than on the sharp-edged wing and limited circulation is fed into the inner vortex that forms close to the center-line of the wing. With increasing bluntness, separation is delayed further, particularly in the apex region, and the formation of both the inner and primary vortices is delayed. As the apex of the primary vortex moves downstream, more circulation is fed into the inner structure that grows in size relative to the other vortex structures on the wing. This suggests that the relative strength of this vortex also increases as the radius of the leading edge increases. This is consistent with what appears to be outboard movement of both the primary and secondary vortex structures as the leading-edge radius of the wing increases. Particle Image Velocimetry (PIV) results in section 5.7 will support these hypotheses.

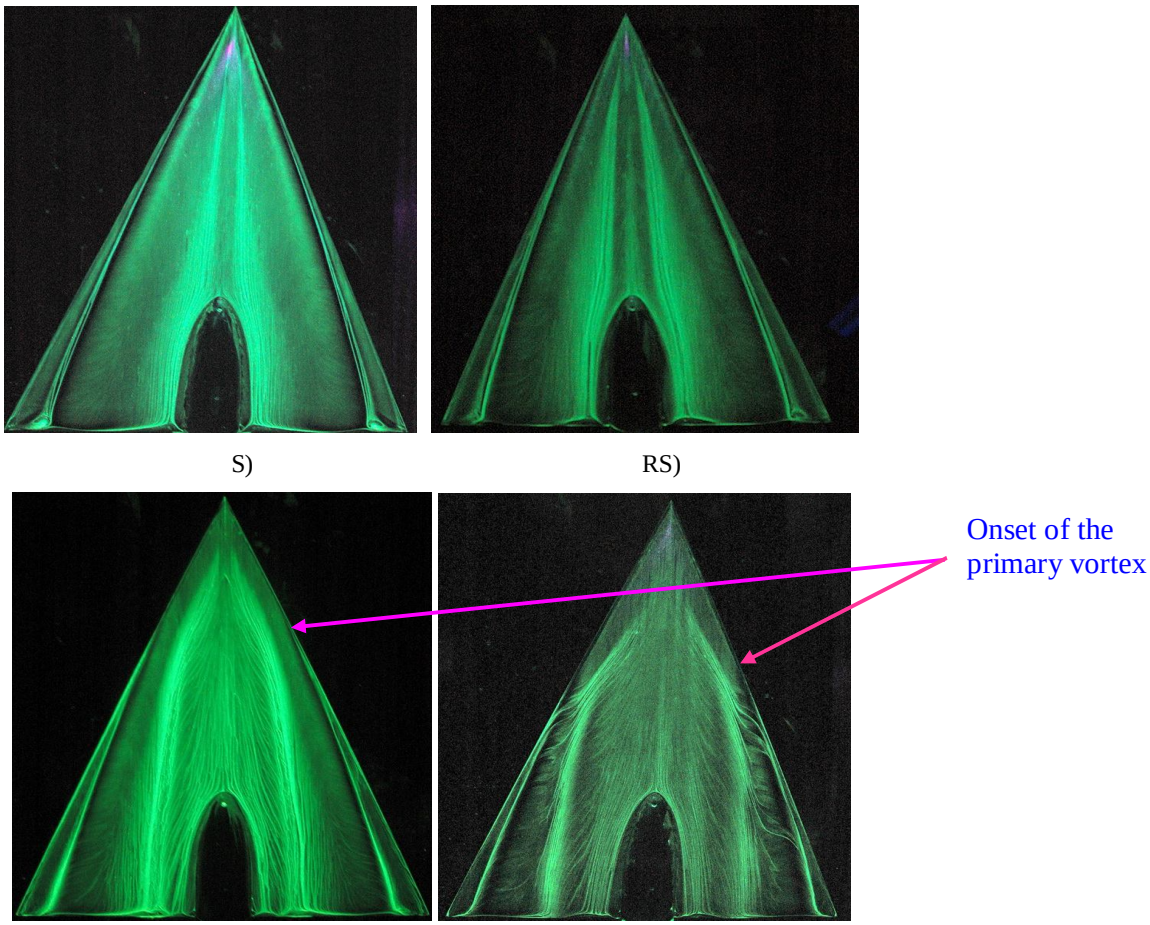

Figure 5.4: Comparison of oil flow topology for the; a) Sharp-edged (S), Small (RS), Medium (RM) & Large (RL) radius wings at $R_{mac} = 2 \times 10^6$.& $\alpha = 13.3^0$

The effects of leading edge bluntness at higher angle of attack ($\alpha = 23^0$ & $R_{mac} = 2 \times 10^6$) are presented in figure 5.5. The results show similar behaviour of the primary vortex for all cases. The primary vortex appears to extend from the apex to the trailing edge on the sharp, small and medium-radius wings and so it seems that the effects of leading edge bluntness are reduced with an increase of angle of attack. Nevertheless, attached flow may still exist near the apex on the large-radius wing for this test condition. In addition, a small inner vortical structure may exist on all of the blunt wings at this angle of attack. This is in agreement with Konrath *et al,* (2008) who reported a weak inner vortex still appeared at higher angles of attack for the higher Reynolds number case. This is possibly due to a very small amount of attached

flow at the apex and a smaller primary vortex compared to lower Reynolds numbers. In this case, there is also evidence of vortex breakdown near the trailing edge.

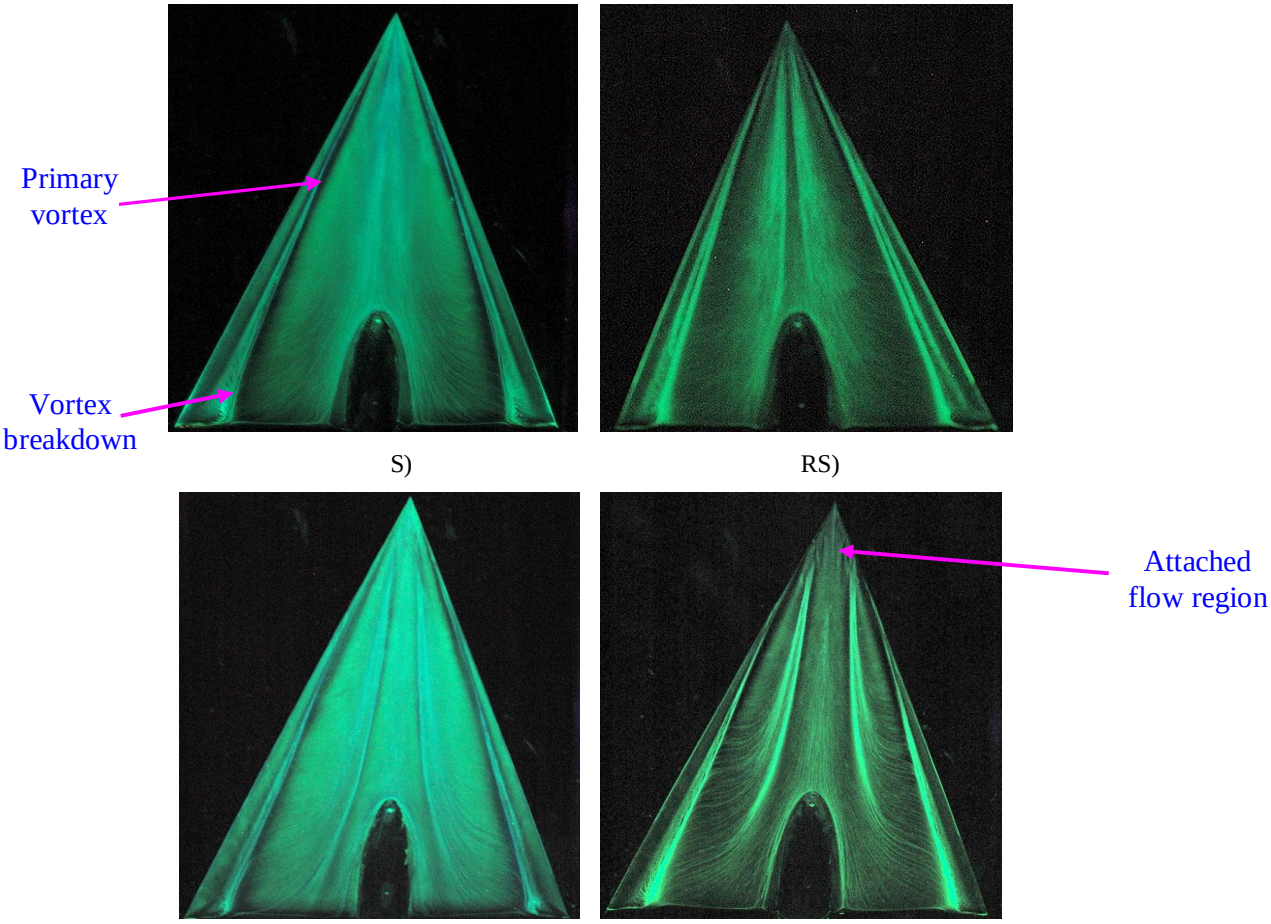

Figure 5.5: Comparison of oil flow topology for the; a) Sharp-edged (S), Small (RS), Medium (RM) & Large (RL) radius wings at R_{mac} = 2 x 10^6 & α = 23^0

5.3 Reynolds Number Effects

Reynolds number effects on the flow characteristics can be illustrated by comparing the flow visualization images at a Reynolds number of 1x10^6 with the corresponding images at 2x10^6. This is done in Figures 5.6, 5.7, 5.8 and 5.9 for each of the wing configurations. The effect of Reynolds number on the sharp-edged wing (α = 10^0) is presented in Figure 5.6. On this wing, the Reynolds number appears to

influence the properties of the primary vortex rather than its onset. At equal to 2 million Reynolds number, the secondary separation line is located more outboard compared to the 1 million Reynolds number case. This is probably by the turbulent boundary layer under the vortex at higher Reynolds number being able to sustain the adverse pressure gradient longer as it travels towards the leading edge. Delayed separation inhibits the development of the secondary vortex, so reducing its size.

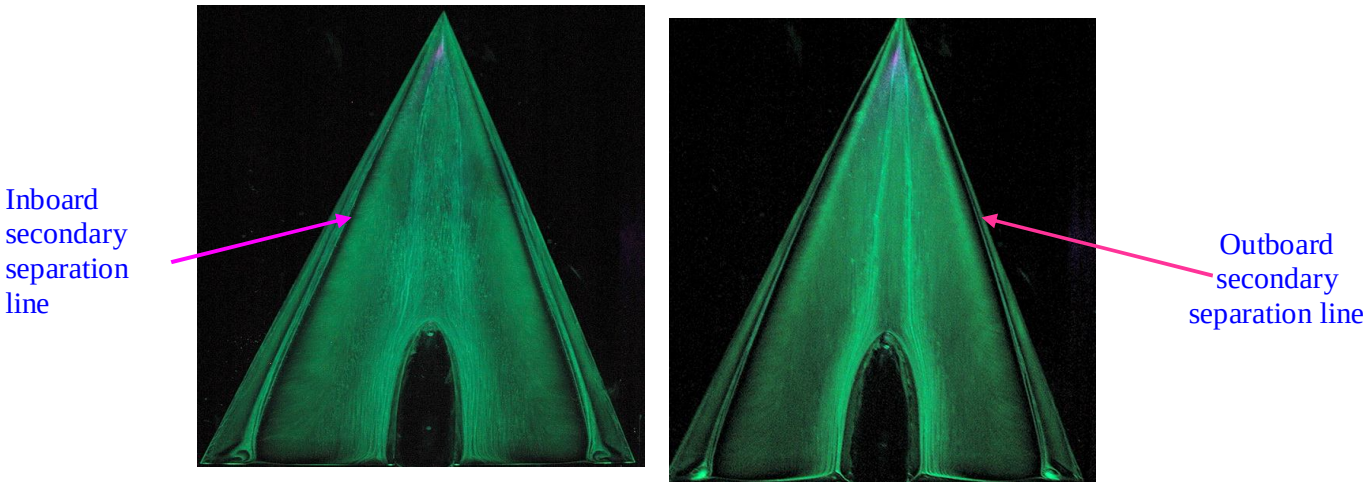

a) b)

Figure 5.6: Comparison of oil flow patterns for the sharp-edged configuration at a) $R_{mac} = 1x10^6$ and b) $R_{mac} = 2x10^6$ & $\alpha = 10^0$

Figure 5.7 shows an example of Reynolds number effects on the small-radius wing. The flow characteristics in the leading edge region exhibit similar flow topology to that presented for the sharp-edged wing in figure 5.6 except that the onset of the primary vortex at 2 million Reynolds number occurs slightly further aft. There is clear evidence of the inner separation in the middle part of the wing for both Reynolds number cases. It develops close to the apex region and has a larger lateral extent at the higher Reynolds number.

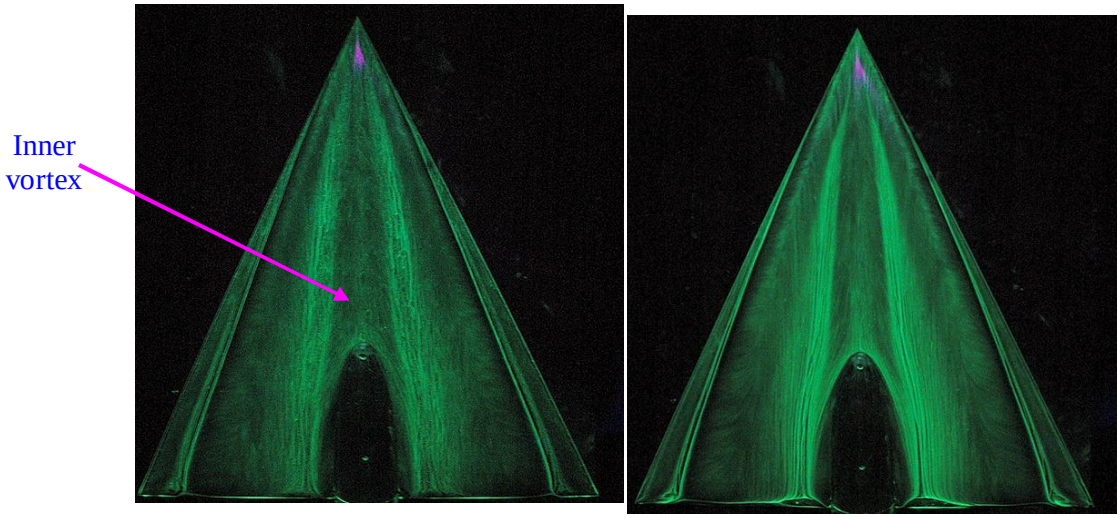

a) b)

Figure 5.7: Comparison of oil flow patterns for the small-radius configuration at a) $R_{mac} = 1x10^6$ and b) $R_{mac} = 2x10^6$ & $\alpha = 12^0$

Figure 5.8 compares the surface oil flow visualizations at Reynolds numbers of $1x10^6$ and $2x10^6$ for the medium-radius wing ($\alpha = 13.3^0$). The figure shows a significant Reynolds number effect compared to previous cases. One of the most obvious features of this figure is the apparent origin of the vortex system in the two cases. At $R_{mac}=2x10^6$ the vortex system appears to originate at approximately 30% of the root chord down the leading edge. Ahead of this, there appears to be no evidence of a vortical structure. In contrast, at $R_{mac}=1x10^6$, at first glance there appears to be continuity of the primary vortical structure almost to the apex of the wing. As discussed previously, closer examination of the dark region inboard of the secondary separation line shows that it has a distinct bend at about 20-30% of the root chord. The secondary separation line itself becomes indistinct at this point. It is likely that this location is, in fact, the origin of the primary vortex on the wing. Upstream of this, laminar separation is initiated near the leading edge but the shear layer does not roll up into a vortical structure. Instead, the shear layer may undergo transition and reattaches close to the leading edge, leaving the footprint of a laminar separation bubble. This phenomenon appears to occur on the two larger-radius wings at 1 million Reynolds number. Examination of the inboard portions of the wing shows that the inner vortical structure is initiated slightly closer to the apex and has a

greater spanwise extent at the higher Reynolds number (shown in figure 5.8). Consequently there is a slight outboard movement of the other vortices on the wing as the Reynolds number increases.

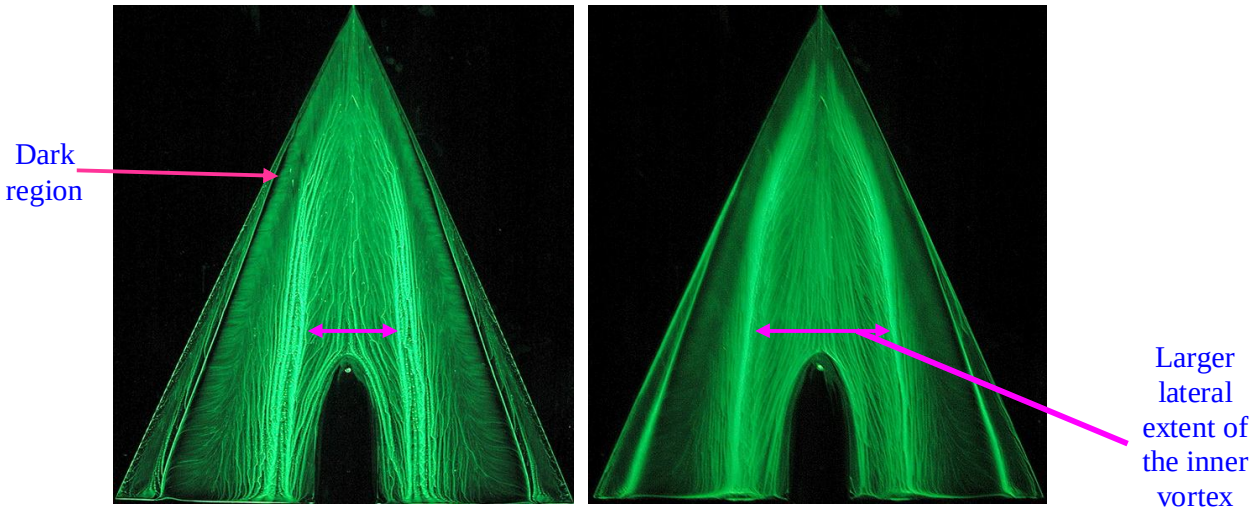

Figure 5.8: Comparison of oil flow patterns for the medium-radius configuration at a) $R_{mac} = 1x10^6$ and b) $R_{mac} = 2x10^6$ & $\alpha = 13.3^0$

Figure 5.9 shows surface oil flow visualizations at Reynolds numbers of $1x10^6$ and $2x10^6$ for the large-radius wing ($\alpha = 10^0$). The flow pattern at $1x10^6$ exhibits some similarities with the corresponding image for the medium-radius wing in Figure 5.8. The main difference is in the chordwise phasing of the flow. In this case, the primary vortex appears to be initiated further downstream at about 50% of the root chord position. A primary vortex is not obvious in the characteristics of the flow pattern at $2x10^6$. An attached flow region aligned with the mean flow exists in the vicinity of the leading edge extending from the apex almost to the trailing edge. This region appears to be truncated by a separation front that becomes increasingly close to the leading edge on aft portions of the wing. The orientation of the oil flow towards the leading edge inboard of this separation front suggests that a weak, but not insignificant, vortical structure may be formed as a result of the flow separation. This appears to originate somewhere between 40 and 50% of the wing chord.

In fact, a closer examination of the leading edge area near to the trailing edge may suggest that a very weak primary vortex has developed at the higher Reynolds number. The primary vortex is generated in this region because the fraction of wing radius over the wing span is very small and so the leading edge is getting relatively sharper in this region. Secondly, the curvature of the trailing edge increases the local angle of attack in the region to promote the primary separation. There is a possibility that the inner separation rolls-up into a vortical structure at its interface with the primary vortex. This remains to be established beyond doubt.

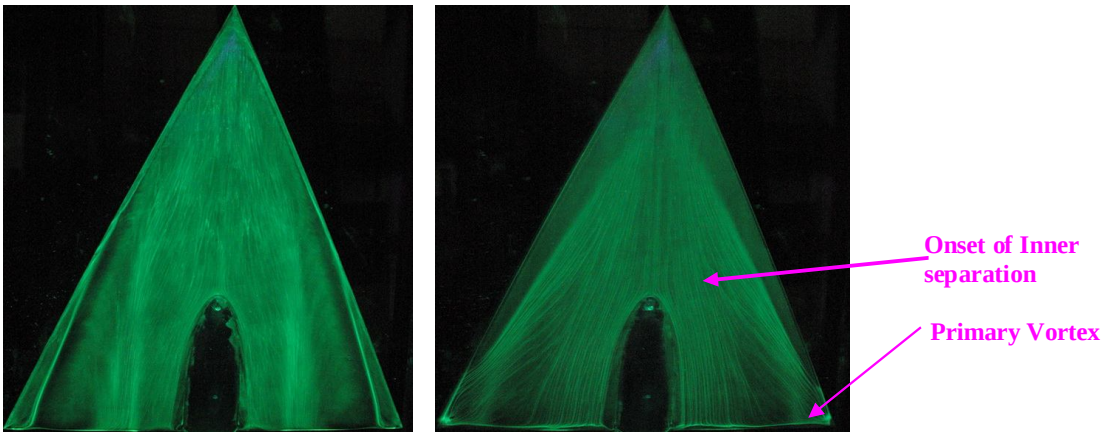

a) b)

Figure 5.9: Comparison of oil flow patterns for the large-radius configuration at a) $R_{mac} = 1x10^6$ and b) $R_{mac} = 2x10^6$ & $\alpha = 10^0$

5.4 Effects of Angle of Attack

This section will discuss the effect of angle of attack on the delta wing flow topologies at the Reynolds numbers of 1 and 2 million.

5.4.1 The Effects of Angle of Attack at a Reynolds Number of 1 x 10^6

Figure 5.10 presents the flow images for the sharp-edged wing at a Reynolds number of 1 million. On this wing, the primary vortex appears to originate near the wing apex and persist to the trailing edge at all angles of attack shown. At around $\alpha = 20^0$, the secondary separation line of the primary vortex is smeared outboard towards

the leading edge. This could be related to transition from laminar to turbulent flow occuring in this area. The images also show the point of transition moving further upstream with increasing angle of attack.

Starting from $\alpha = 18.5^0$, the occurrence of vortex breakdown over the wing is observed in the figure. Vortex breakdown can be recognized by a rupture of the primary and secondary vortex separation lines. At this lower Reynolds number, vortex breakdown appears to occur at slightly lower angles of attack on all of the wings compared the higher Reynolds number case. Further Reynolds number effects on vortex breakdown will be discussed in section 5.5.2

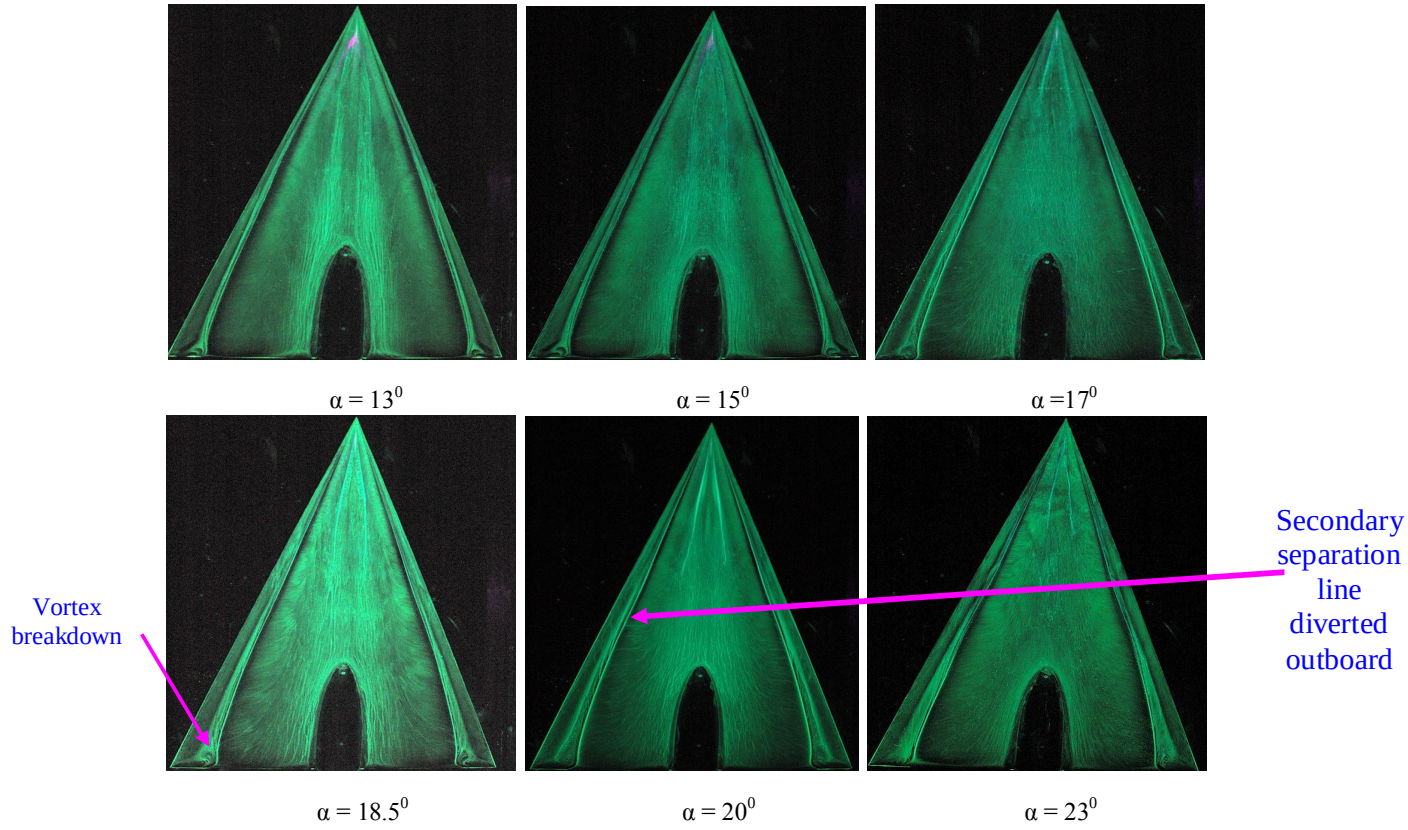

Figure 5.10: Flow topology images for the sharp-edged configuration at $R_{mac} = 1x10^6$ and angle of attack, $\alpha = 13.3^0, 15^0, 17^0, 18.5^0, 20^0$ & 23^0

Figure 5.11 refers to flow images on the small-radius delta wing at a Reynolds number of 1 x 10^6. At $\alpha = 6^o$, the flow in the leading edge region is fully attached extending from the apex to the trailing edge. There is clear evidence of the flow on inboard sections of the wing near the apex smearing outwards without developing any significant vortical structure. There is also evidence here of localized flow separation. The image may suggest that the inboard separated shear layer will not roll-up into a spinning vortex without the primary vortex generated in the leading edge region. This will be discussed further in section 5.4.3. The primary vortex is observed to appear at $\alpha = 8^0$ originating at about 10% of chord from the apex. There is clear evidence of a weak inboard vortical structure developing in the middle part of the wing. The images also show the rapid progression of the primary vortex towards the apex of the wing as the angle of attack increases. The primary vortex reaches the wing apex at an $\alpha = 10^0$. After this angle, the flow in the leading edge region exhibits quite similar behavior to the sharp leading edged wing. Also, as the primary vortex becomes stronger at higher angle of attack its compresses the inner vortex towards the wing centre line.

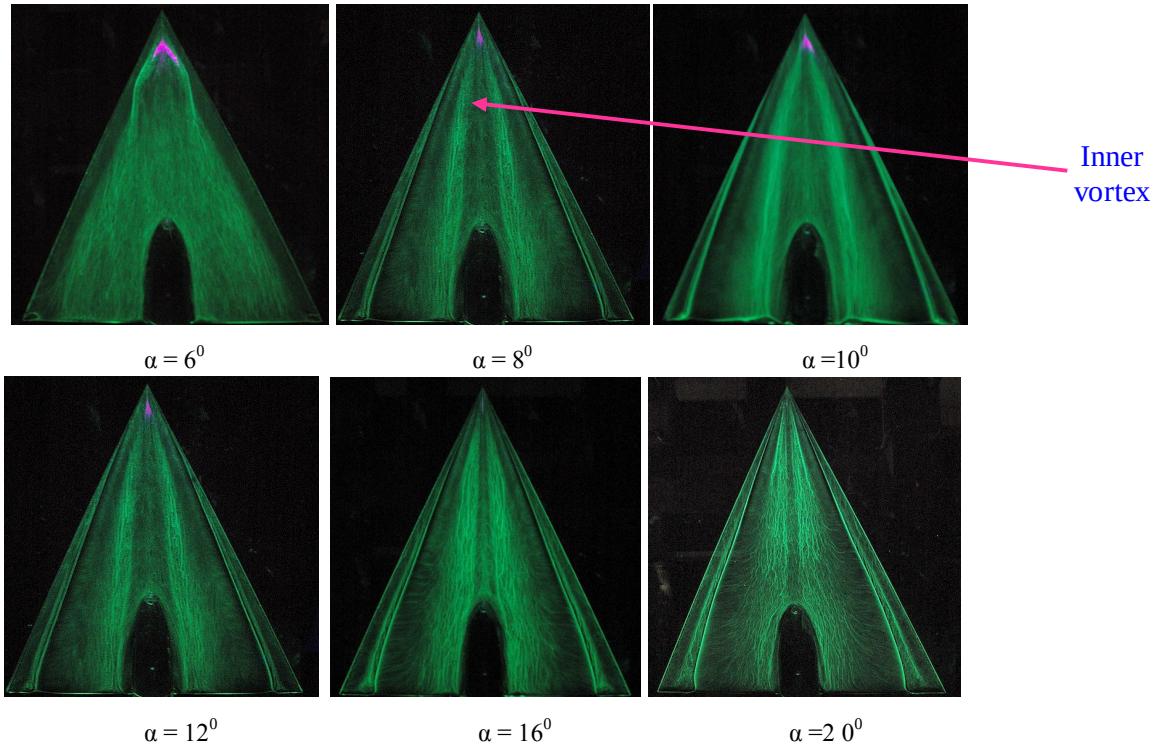

Figure 5.11. Flow topology images for the small-radius configuration at R_{mac} = 1x10^6 and angle of attack, α =6^0, 8^0, 10^0, 12^0, 16^0 & 20^0

Figure 5.12 presents the effect of angle of attack on the medium-edged wing at a Reynolds number of 1 million. The flow topologies on this wing exhibit similarity with the small-radius wing flow characteristics except the bluntness effects and vortex breakdown appear at relatively higher angles of attack compared with the small-radius wing discussed earlier. Again on this wing, the inner vortex is compressed to the wing centre line as the angle of attack is increased. This is associated with stronger primary vortex at high angle of attack. Note that some of the images presented in this figure were taken during the early stages of the research project before the wind tunnel had been painted black; this is why the off-body sections of these photographs are not black.

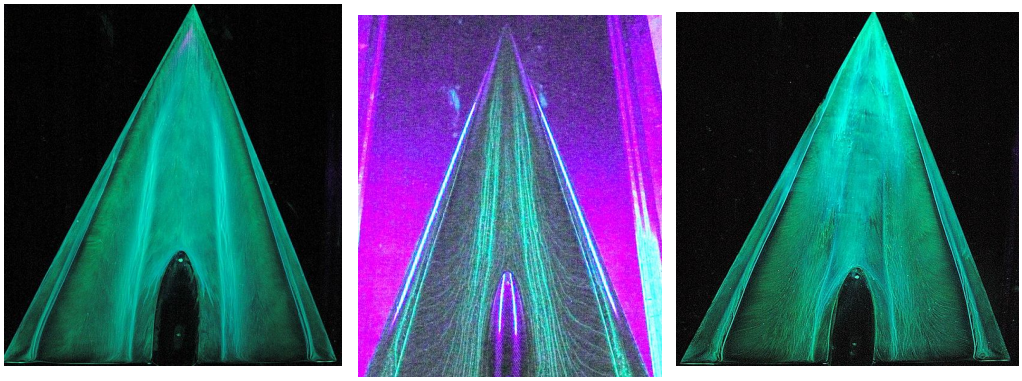

α = 13.3^0 α = 17^0 α =18.5^0

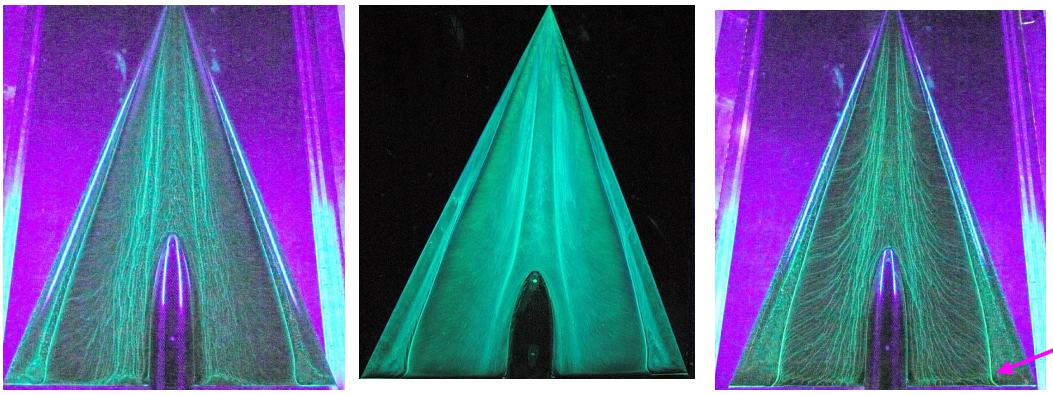

α = 20^0 α = 23^0 α =25^0

Figure 5.12: Flow topology images for the medium-radius configuration at R_{mac} = 1x10^6 and angle of attack, α =13.3^0, 17^0, 18.5^0, 20^0, 23^0, 25^0

Figure 5.13 presents the angle of attack effects for the large-radius wing at the same Reynolds number. The effect of angle of attack appears to be more significant on this wing compared with the previous wings. At α = 10^o, the primary vortex originates at about 40% of the wing root chord. The figure shows a slow upstream progression of the primary vortex origin towards the apex when the angle of attack increases. At α = 13.3^0, the flow in the leading edge region near to the apex is aligned with mean flow direction which indicates that the primary vortex has not developed in this region. The images also depict the progression of an inboard vortical structure with the angle of attack. The upstream movement of the primary vortex again compresses the inner vortex towards the wing centre line. The figure also shows that the inner separation on this wing has a greater spanwise extent compared to the small

and medium-radius wings. This is caused by the weakening of the primary vortex as the leading edge bluntness is increased. This issue will be discussed in chapter 6 (Conclusions and Recommendations).

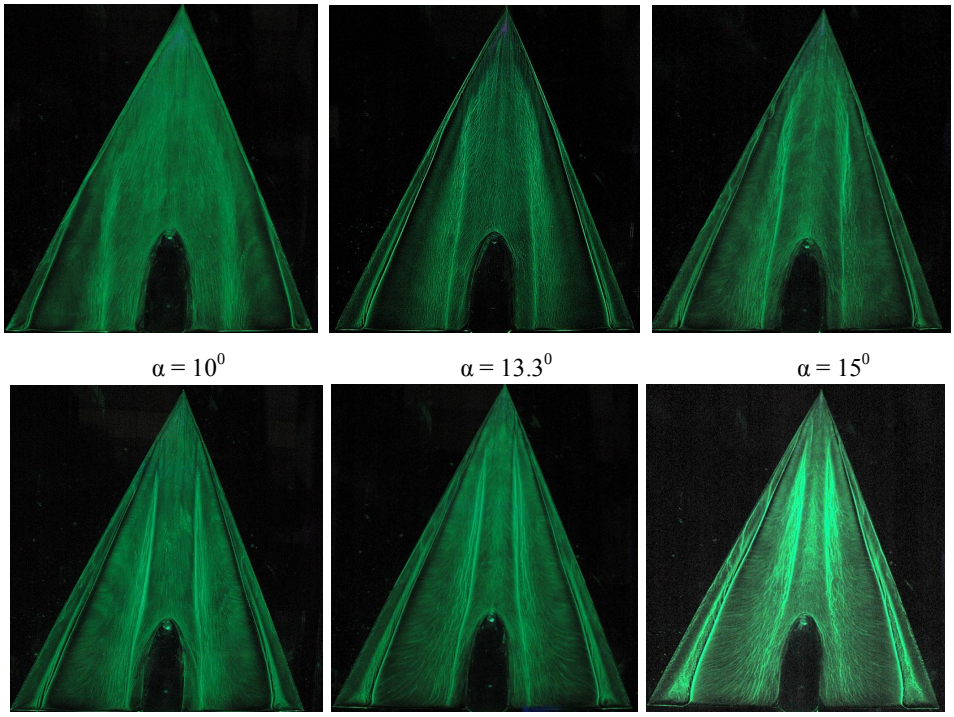

$\alpha = 10^0$ $\alpha = 13.3^0$ $\alpha = 15^0$

$\alpha = 17^0$ $\alpha = 20^0$ $\alpha = 23^0$

Figure 5.13: Flow topology images for the large-radius configuration at $R_{mac} = 1x10^6$ and angle of attack,

$\alpha = 10^0, 13.3^0, 15^0, 17^0, 20^0 \& 23^0$

5.4.2 The Effects of Angle of Attack at a Reynolds Number of 2 x 10^6

Sample flow images recorded on the sharp-edged wing at a Reynolds number of 2 million are presented in Figure 5.14 for α varying from 13^0 to 23^0. At all the angles of attack shown, the sharp-edged wing exhibits a flow pattern consistent with the formation of a large coherent primary vortex that extends from the apex towards the trailing edge. The lateral extent of this vortex increases with angle of attack in line with its increased strength and the secondary vortex behaves similarly.

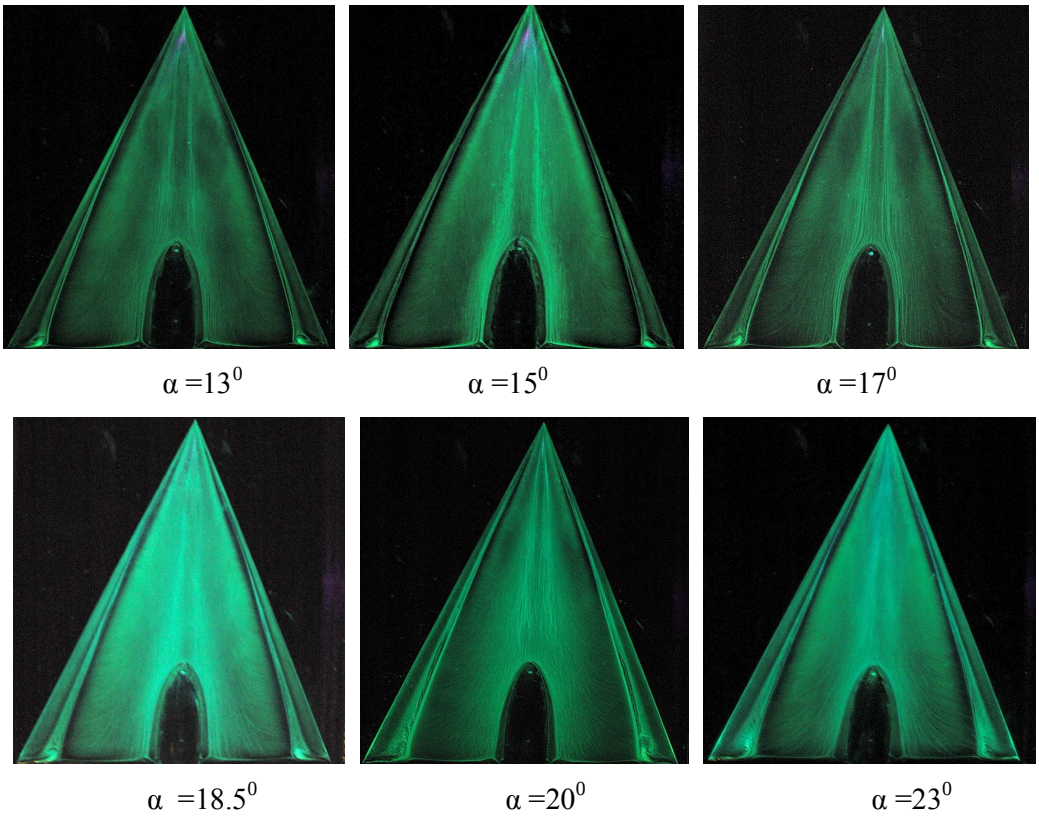

Figure 5.14: Flow topology images for the sharp-edged configuration at R_{mac} = 2x10^6 and angle of attack, α = 13.3^0, 15^0, 170, 18.5^0, 20^0 & 23^0

At similar angles of attack to the cases presented above, the small-radius wing exhibits very similar flow behavior to the sharp-edged wing. This is not, however, the case at lower angles of attack where the effect of leading edge rounding becomes more significant. Figure 5.15 presents the flow topology on the small-radius wing at α = 6^0,8^0, 10^0, 12^0, 16^0 and 20^0 and at a Reynolds number of 2 x 10^6. At the lowest angle, α = 6^0, attached flow appears to exist from the apex to the trailing edge of the wing. In fact, there is a small region of separation close to the apex of the wing that does not develop into anything of significance. The primary vortex only appears at α = 8^0 and is accompanied by, what appears to be, a relatively weak and large inboard vortical structure that has its origins in the previously identified separation region at the apex of the wing. When the angle of attack is increased further to 10^0, there is a significant change in the flow topology on the wing. The origin of the primary vortex

moves almost to the apex of the wing and the inboard structure becomes confined to a region close to the centerline of the wing.

The simultaneous appearance of the primary vortex and the inner vortex at $\alpha = 8^0$ would be consistent with the earlier proposition that the separated flow only rolls-up to generate a spinning vortex inboard on the wing once it interfaces with the primary vortex. This is not the explanation from Hummel & Luckring (2008). They suggested that the inner vortex develops from a three dimensional laminar bubble type separation upstream on the wing. At higher angles of attack, the flow in the leading edge region behaves similarly to the behavior observed on the sharp leading edged wing.

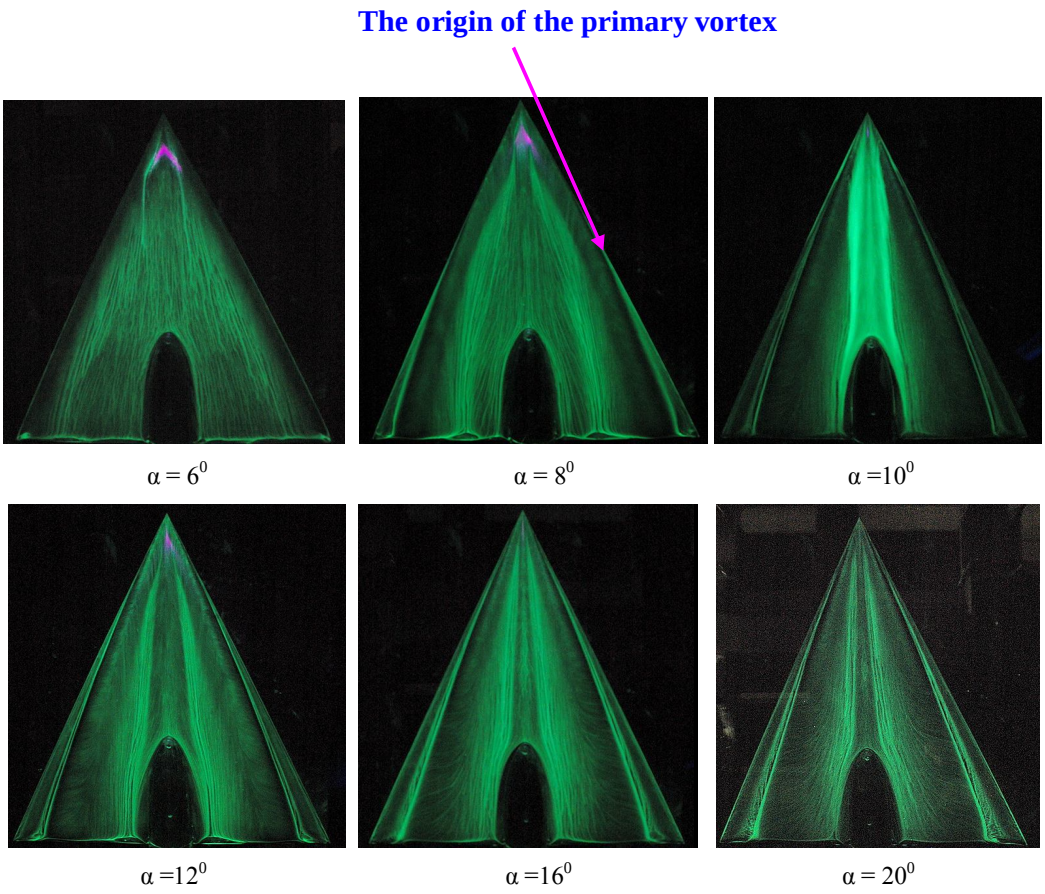

Figure 5.15: Flow topology images for the small-radius configuration at R_{mac} = 2x10^6 and angle of attack, α = 6^0, 8^0 10^0, 12^0, 16^0 & 20^0

Figure 5.16 illustrates the variation in the flow pattern on the medium-radius wing as the angle of attack increases from 13.3^0 to 25^0. The figure shows the progressive movement of the origin of the primary vortex from about 30% of the root chord location towards the wing apex as the angle of attack is increased. The inboard vortical structure is distinct and extensive at low and moderate angles of attack but appears considerably weakened and spatially constrained at the highest angle of attack. This is witnessed by a clear inboard shifting of the separation line of the inner vortex with increasing angle of attack. The reason for this can be related to the strengthening of the leading edge vortex as the incidence increases. This result, although exhibiting the same general trend, differs slightly from that of Furman and Breitsamter (2008) of T.U. Munich. They reported that the inner vortex disappeared at

$\alpha = 18^0$ at the same Reynolds number (Their PIV result is shown in figure 5.17 where the inner vortex is not observed inboard of the wing). The current experiments were at Mach number of 0.12 compared with 0.37 for the Munich tests. It is possible that the Mach number difference or tunnel interference could account for this anomaly. Regardless of this, by $\alpha = 25^0$, there is still a tangible sign of the weak inner vortex. The forward progression of the vortex breakdown can be identified on the images starting at $\alpha = 20^0$.

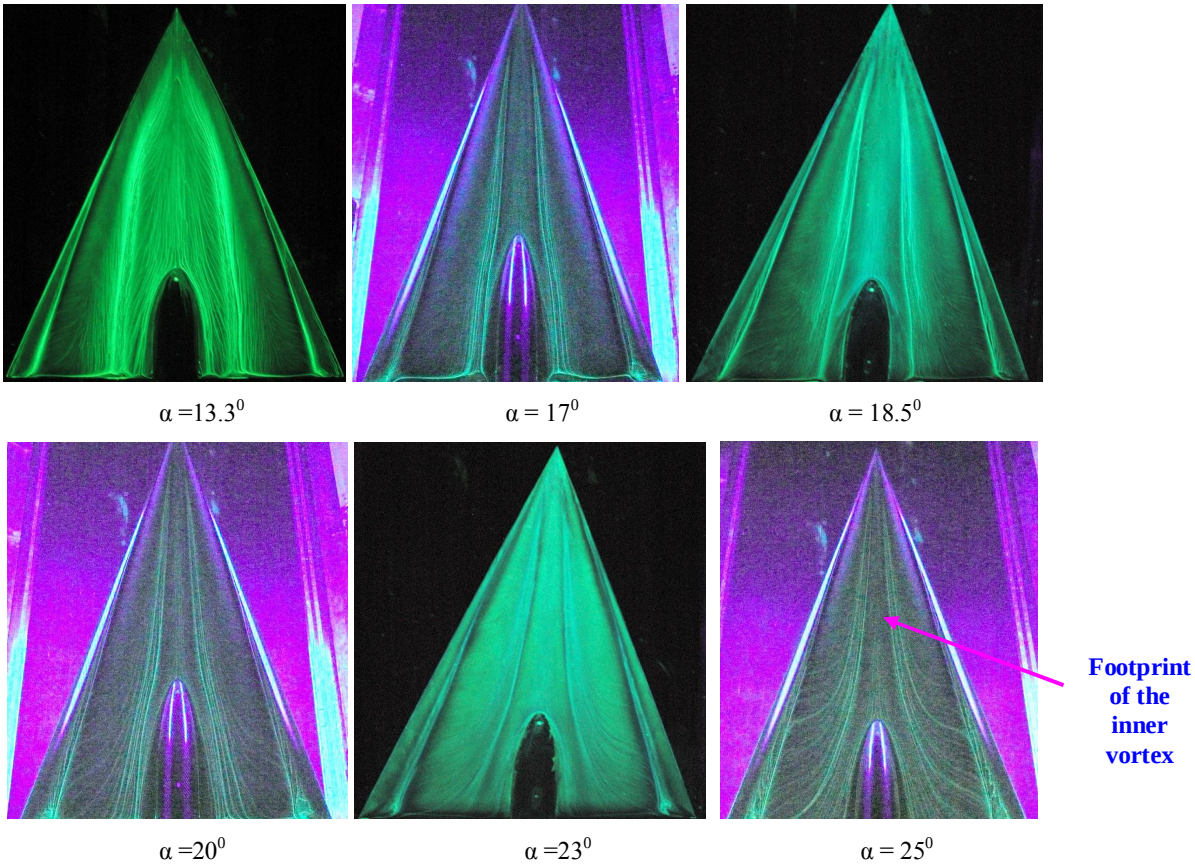

Figure 5.16: Flow topology images of the medium-radius configuration at $R_{mac} = 2x10^6$ and angle of attack, $\alpha = 13.3^0, 17^0, 18.5^0, 20^0, 23^0$ & 25^0

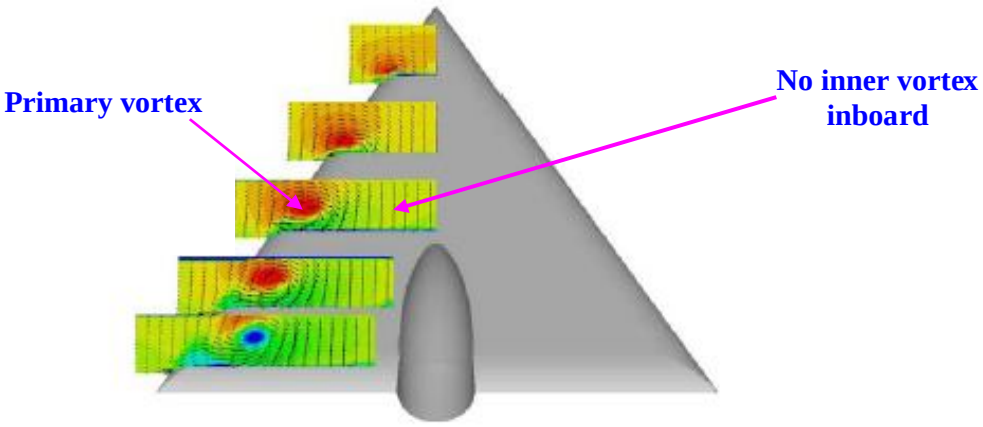

Figure 5.17: Mean flow distribution at R_{mac}= 2 x 10^6, α = 18^0 & Mach number of 0.37 for the medium-radius wing (Furman & Breitsamter, 2008)

Figure 5.18 presents examples of the oil flow structures visualized on the large-radius wing as the angle of attack increases. At the lower α = 10^0, as discussed previously, only the inner vortex is obvious. By α = 13°, a primary vortex structure has clearly formed on the wing, originating at around 40% of the root chord, with the inner structure apparently originating just ahead of this. At the highest α shown in the figure the primary vortex structure appears to originate in the region of the apex and extend to the trailing edge. Similar to the case of the medium-radius wing, there is little evidence of the inner structure in this image.

The figure also illustrates rather well, the dependence of the inner vortex on the angle of attack. From the figure, the onset of the inner vortex moves upstream when the angle of attack increases. It has its origin towards the rear of the wing at α =10^0 and this moves to about 10 % of chord from the apex at α = 15^0. The lateral extent of the inner vortex is reduced with the upstream progression of the primary vortex. In fact, at moderate α, the upstream progression of the primary vortex compresses the inner vortical structure to the wing centre line.

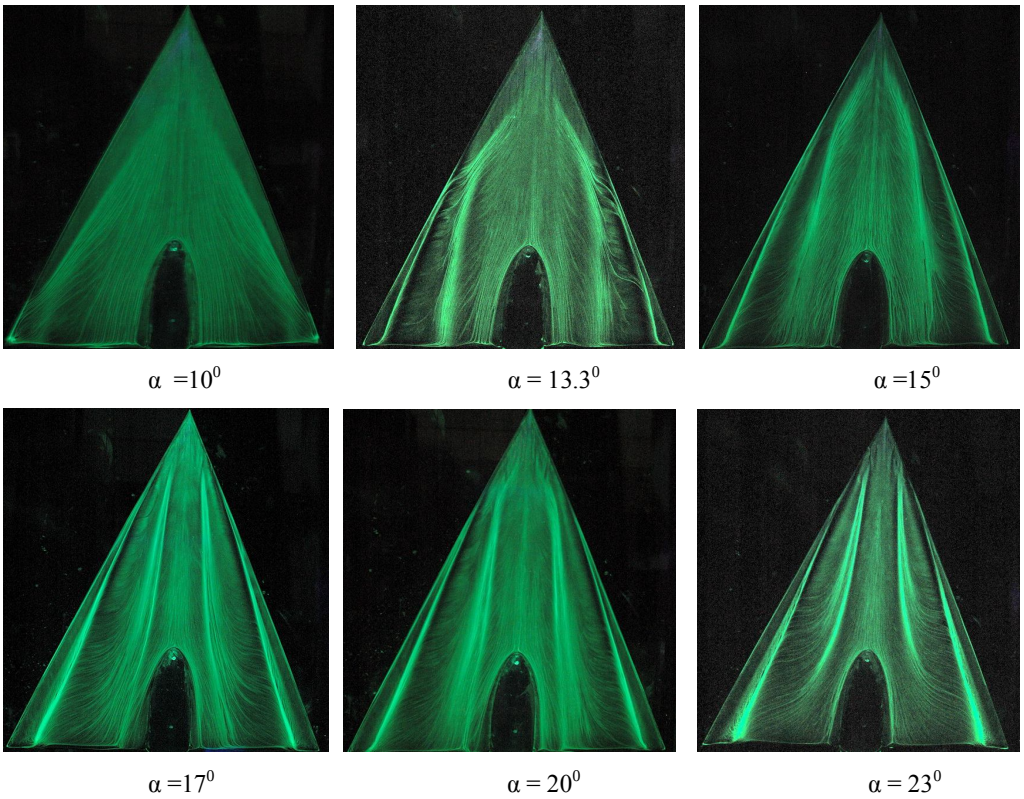

α =10^0 α = 13.3^0 α =15^0

α =17^0 α = 20^0 α = 23^0

Figure 5.18: Flow topology images for the large-radius configuration at R_{mac} = $2x10^6$ and angle of attack = 10^0, 13.3^0 15^0, 17^0, 20^0 and 23^0.

5.4.3 Development of the Inner Vortex

The detailed development of the inner vortex is examined in figure 5.19 by comparing the images at low angle of attack from the small-radius wing at α = 6^o and 8^o with an image of the large-radius wing at α = 10^o (R_{mac} = 2 x 10^6). On the small-radius wing at α = 6^o, the flow on inboard sections of the wing near to the apex tends to smear towards the suction region of the leading edge. At this angle of attack, this smearing process does not develop into any significant flow characteristics. As the angle of attack increases to α = 8^o, the image suggests that this flow will roll-up to form a vortical spinning structure interfacing with the primary vortex that is generated in the leading edge area.

This effect is more obvious on the large-radius leading edge wing at α = 10^o. On this wing the primary vortex is just beginning to form in the leading edge area

near the trailing edge area. A weak inner vortex is simultaneously developing inboard of this structure. This may suggest that the inner vortex can only exist on the wing when a primary vortex is present.

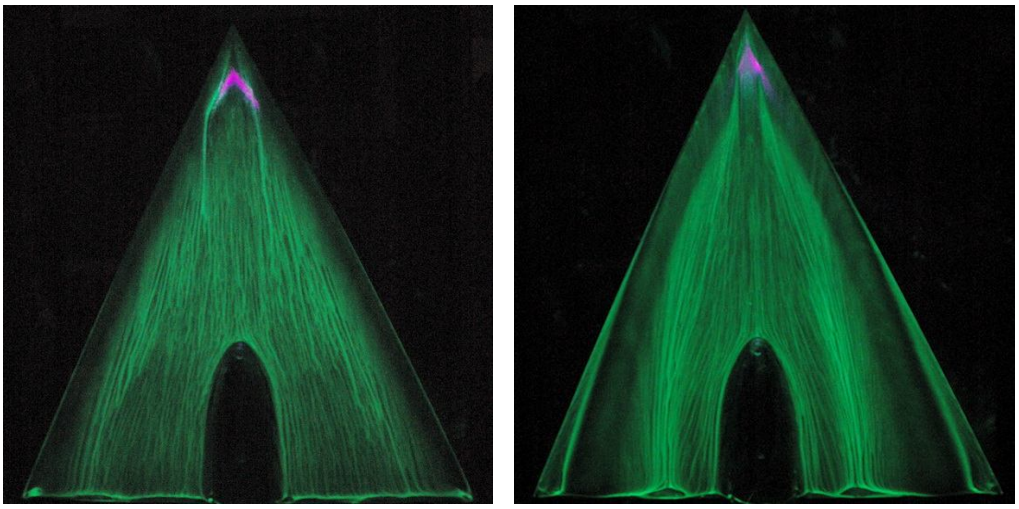

$\alpha = 6^o$ $\alpha = 8^o$

a) Small-radius wing, at $\alpha = 6^o$ & 8^o and Reynolds number of 2×10^6.

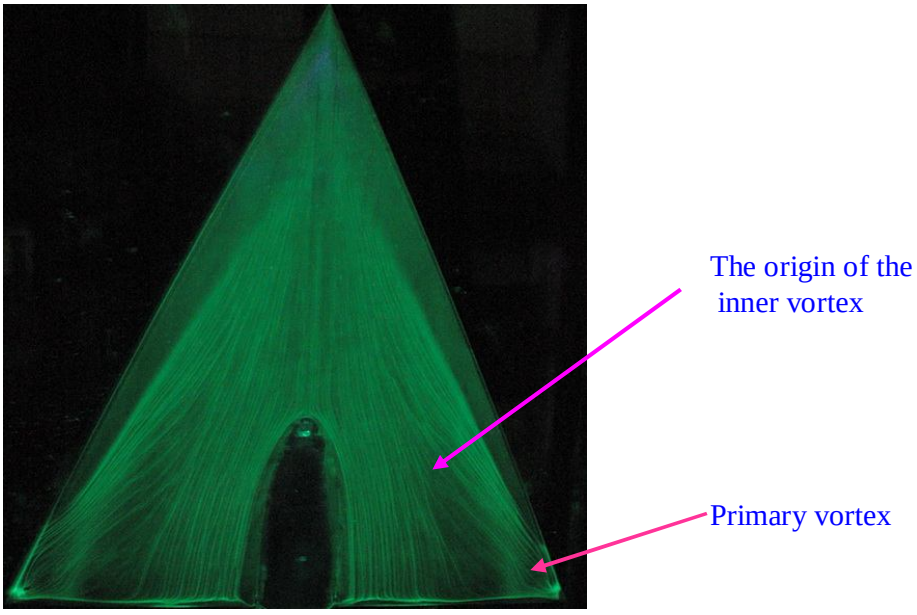

b) Large-radius wing, $\alpha = 10^0$ & Reynolds number of 2×10^6

Figure 5.19: Detailed development of Inner Vortex

5.4.4 Laminar to Turbulent Flow Transition

The status of the boundary layer can be deduced from the oil flow visualization images in some cases. Figure 5.20 presents images from all wings at a low angle of attack and Reynolds number (α = 13.3^0 & R_{mac} = 1 million). The secondary separation line of the primary vortex is straight and extends from the onset of the primary vortex to the trailing edge. This suggests that the boundary layer at this test condition is fully laminar on the entire wing. This is consistent with oil flow studies of Hummel (2004) at a Reynolds number of 0.88 million on the sharp-edged VFE-1 wing.

For the medium and large-radius wing, the oil flow structure upstream of the primary onset is aligned with the main flow direction that indicates the flow is attached to the wing surface in the region. Laminar separation then develops further downstream of this attached flow. This flow may re-attach to the surface upstream of the primary onset.

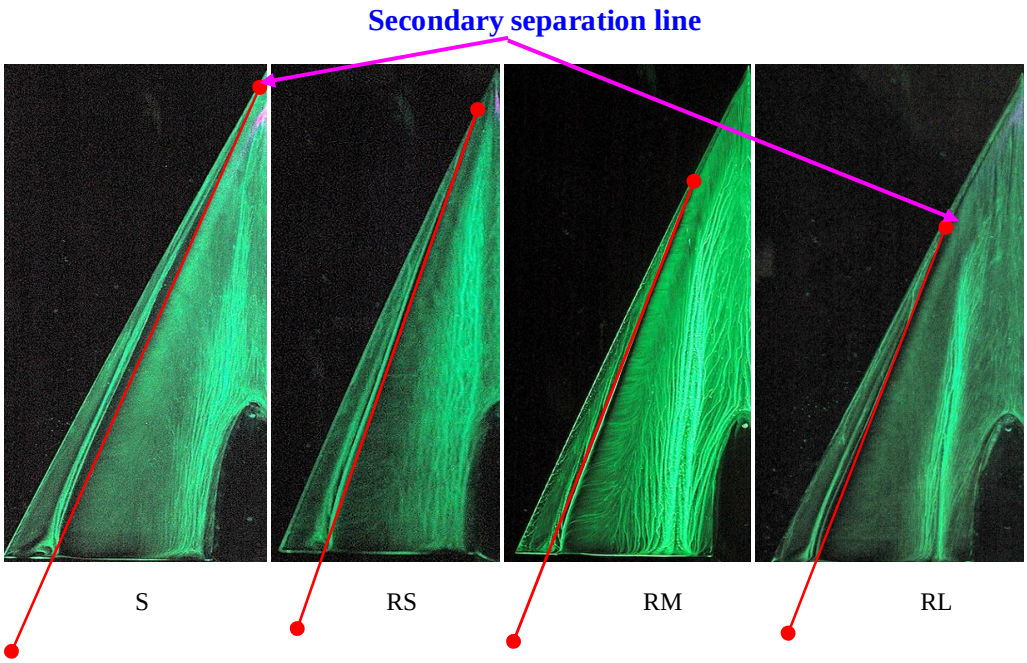

Figure 5.20: Oil flow patterns for all wings at R_{mac} = 1 x 10^6 & α =13.3^0

Transition from laminar to turbulent flow is expected to occur in the wing boundary layer at high α. Figure 5.21 shows the secondary separation line for the sharp-edged and large-radius wing for R_{mac} = 1x 10^6 & α =23^0. This line is straight up to a certain point noted in the figure. After this point, the secondary separation line is diverted outboard which indicates that transition from laminar to turbulent flow may has occured. This outboard movement occurs because the turbulent boundary layer is more able to resist the adverse pressure gradient and delaying the secondary separation process. The images also show that leading edge bluntness delays the transition process slightly.

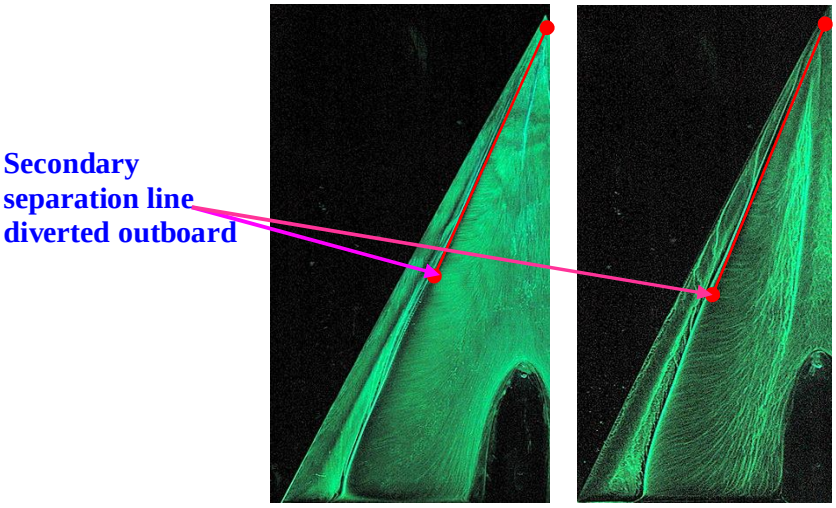

Figure 5.21: Oil flow patterns of the sharp and large-radius wings at 1 x 10^6, $\alpha = 23^0$

Several significant changes are observed as the Reynolds number increases to 2 x 10^6, figure 5.22. The secondary separation line is located further outboard compared with the previous case along the leading edge. This indicates that the flow is mostly turbulent from the apex to the trailing edge. In addition, the secondary separation lines for the sharp and small radius wings are curved away from the leading edge downstream of the middle part of the wing. The secondary vortex formation in these cases is the likely cause for this behaviour. The secondary vortex is stronger and, hence, larger on the sharper edged wings and its growth is responsible for the inward displacement of the secondary separation line.

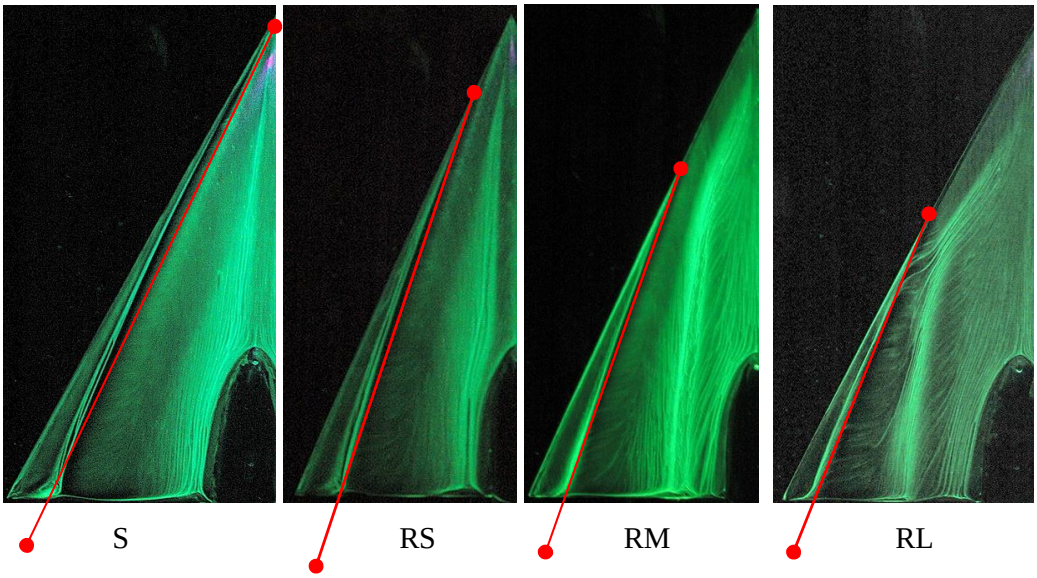

Figure 5.22: Oil flow patterns of all wings at R_{mac} = 2 x 10^6, α=13^0

5.5 Vortex Breakdown

At higher angles of attack, vortex breakdown should be expected to reach the trailing edge region. From the flow images, vortex breakdown can be recognized by strong smearing in the area between the primary and secondary vortices. This is caused by a weaker primary vortex in the region. The starting point of the vortex breakdown is shown in figure 5.23, 5.24 & 5.25.

5.5.1 The Effects of Bluntness on Vortex Breakdown

Figure 5.23 presents the effect of leading edge bluntness on breakdown properties for all wings at $\alpha = 23^0$ and Reynolds number of 2 x 10^6. The flow topologies show the breakdown process is delayed as the leading edge bluntness is increased. These results show an excellent agreement with experimental results of Hummel (2008b), Renac (2005) and Kegelman & Roos (1989). All revealed that increases in leading edge profile radius significantly delayed the vortex breakdown. Renac (2005) suggested that the shear layers on the rounded leading edges are relatively smooth compared with a sharp one, thus, reducing the instability of the

shear layer. Besides, the flow having a short run of attached flow in the leading edge region and slow separation also reduce the instability of the shear layer. A more stable shear layer is strongly suspected to delay the vortex breakdown for the blunt wing. For the sharp case, a rough and unstable shear layer, generated by a sudden separation in the leading edge region, increases the instability of the shear layer. The instability promotes a sudden decrease in the speed of the outer shear layer. The axial flow in the core is then decreased and this promotes a spiral type of breakdown. Within the VFE-2 project, Hummel (2008) also reported the spiral type of breakdown occurring on the wing at such angle of attack of $\alpha = 23^0$.

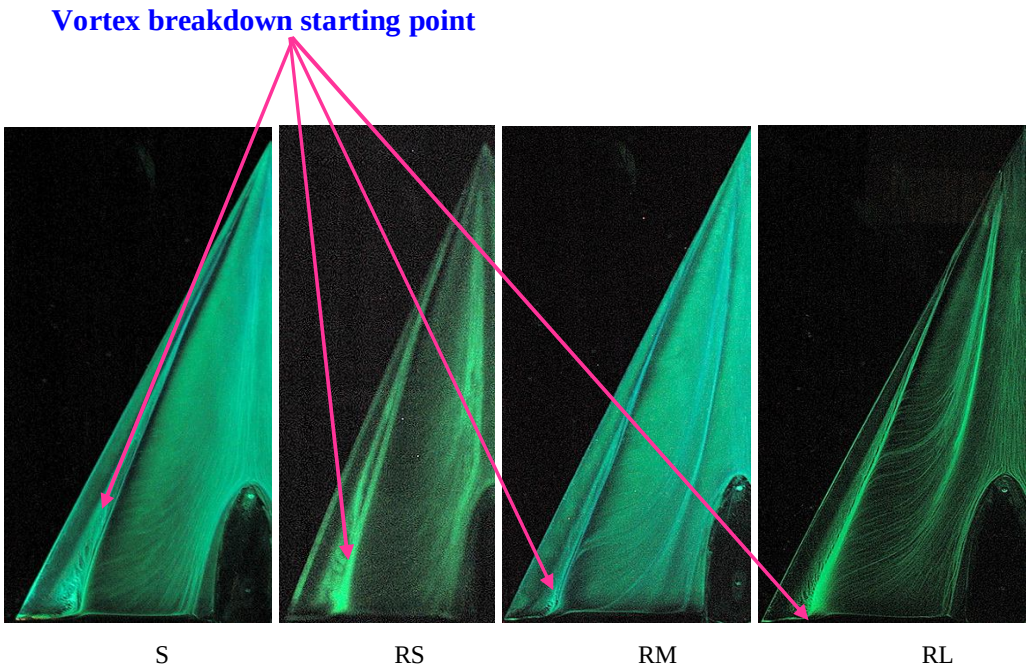

Figure 5.23: Location of vortex breakdown on various leading edges at the Reynolds number of 2 x 10^6& $\alpha=23^0$.

5.5.2 The Effects of Reynolds Number on Vortex Breakdown

Figure 5.24 and 5.25 show the Reynolds number effects on the onset of the vortex breakdown for the sharp-edged and the large radius wing. Both figures show the increase in Reynolds number from 1 to 2 x 10^6 delaying slightly the onset of vortex breakdown. The results obtained can be related to Szodruch (1978). He

described that the pressure level underneath the primary vortex decreases with increasing Reynolds number. Consequently, the flowfield underneath the primary vortex becomes stronger and more turbulent. The higher ability of turbulent flow to endure the adverse pressure gradient, slightly delays the vortex breakdown process in the higher Reynolds number case. These results are consistent with Hummel (2004). He revealed that the flow at Reynolds number 1 x 10^6 was mainly laminar but it was mostly turbulent at 2 x 10^6. This is also consistent with Renac (2005). He mentioned that the vortex breakdown position is only independent of the Reynolds number for high values of Reynolds number; i.e. where the flow is fully turbulent at the Reynolds number of higher than 2 x 10^6. Thus at higher Reynolds numbers, the onset of vortex breakdown will not be much influenced by the Reynolds number.

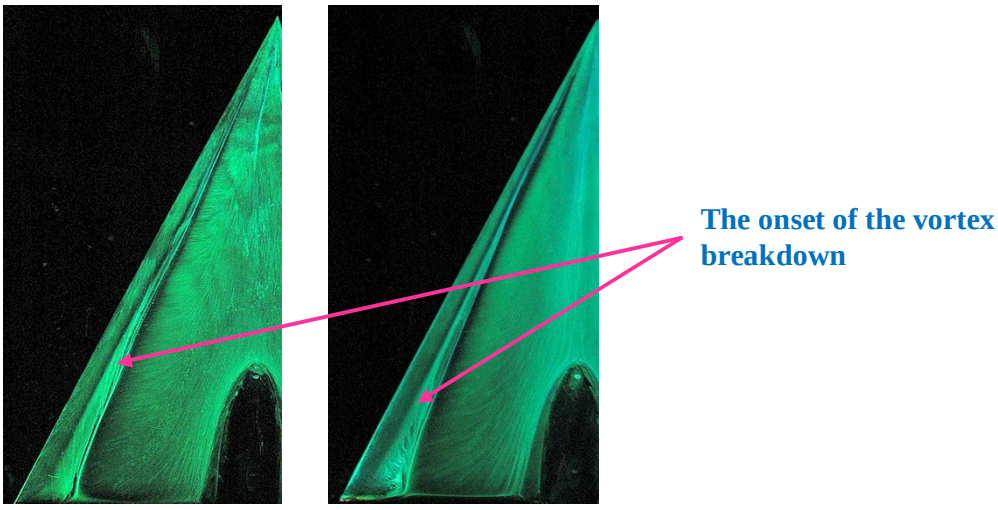

a) R_{mac} = 1 x 10^6 b) R_{mac} = 2 x 10^6

Figure 5.24: The effect of Reynolds number on the position of vortex breakdown on the sharp-edged wing

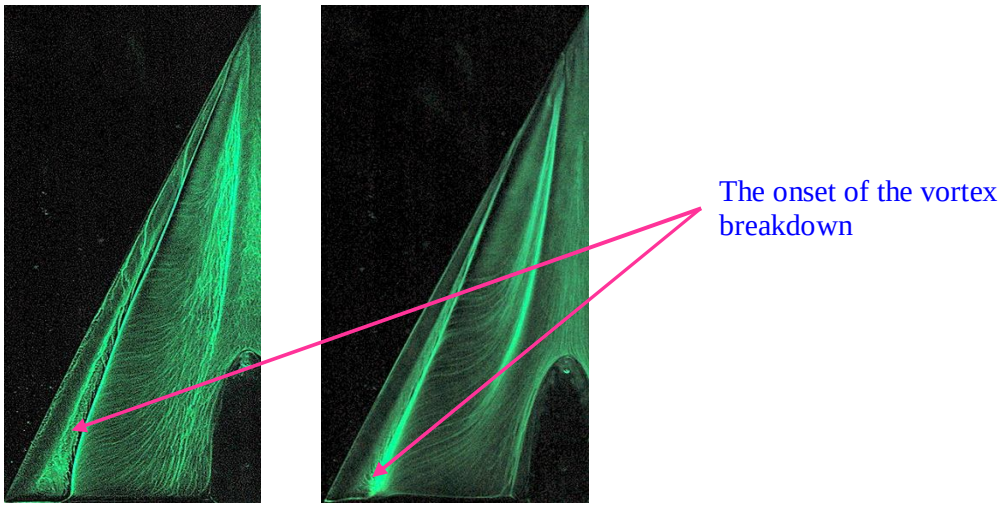

a) $R_{mac} = 1 \times 10^6$ b) $R_{mac} = 2 \times 10^6$

Figure 5.25: The effect of Reynolds number on the position of vortex breakdown on the sharp-edged and large radius wing

5.6 Comparison of Flow Visualization with Other VFE-2 Activity

The comparison of flow visualization studies were also made with the work of Furman & Breisamter (2008) of Munich Technical University. The results show an excellent agreement with the hypothesis made earlier;

i. In all cases as shown in figure 5.26 and 5.27, the vortex breakdown is observed at higher angle of attack. ($\alpha = 23^0$ for both figures)
ii. On the medium-radius wing, the onset of the primary vortex is been delayed further chordwise position (as shown at angle of attack of $\alpha = 13^0$)
iii. The lateral extent of the inner vortex is also decreased with the increase in the angle of attack.

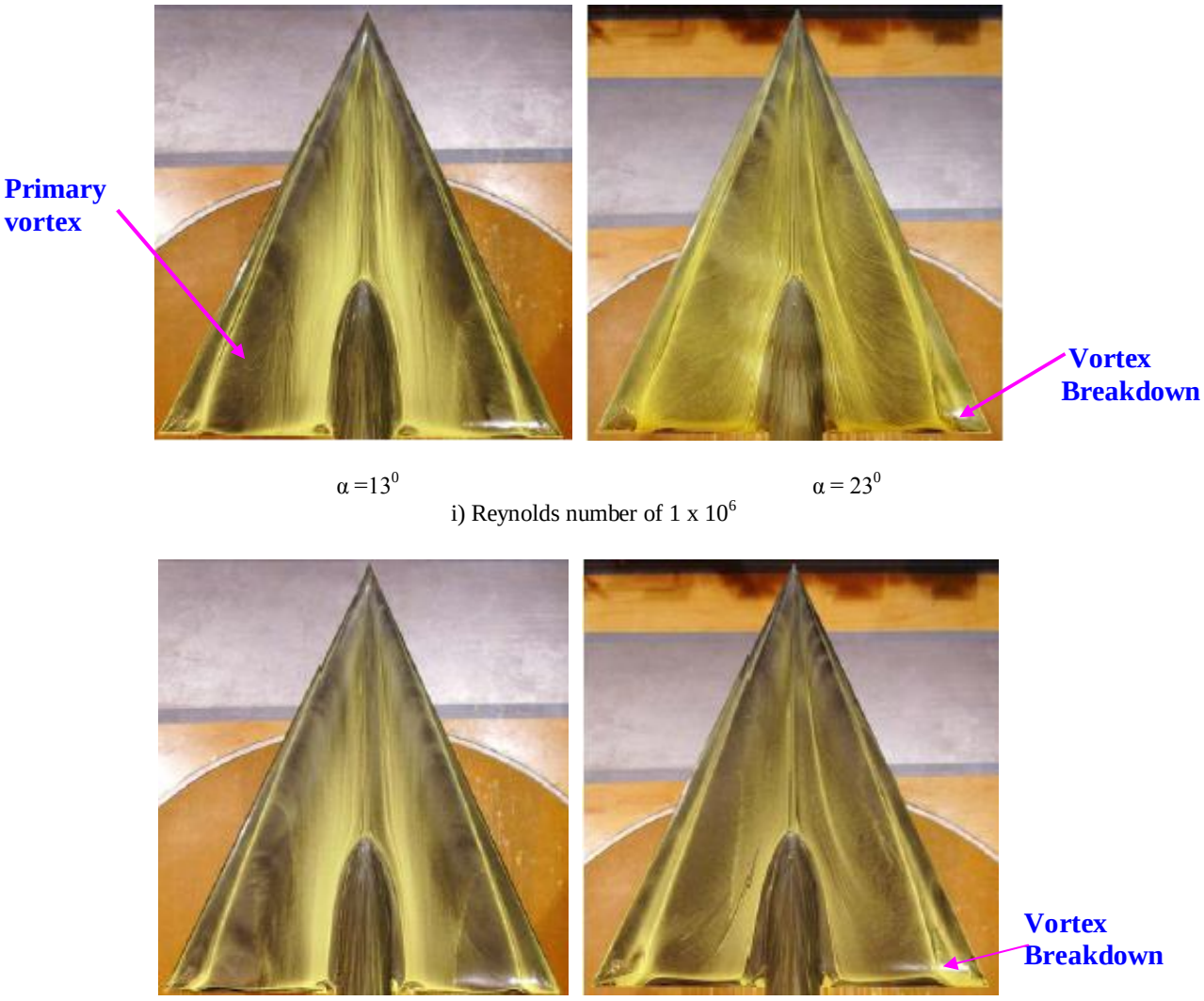

Figure 5.26: Surface oil flow visualization on the Sharp leading edge at the Reynolds number of 1 and 2 x 10^6 at Munich Technical University (Furman & Breitsamter, 2008)

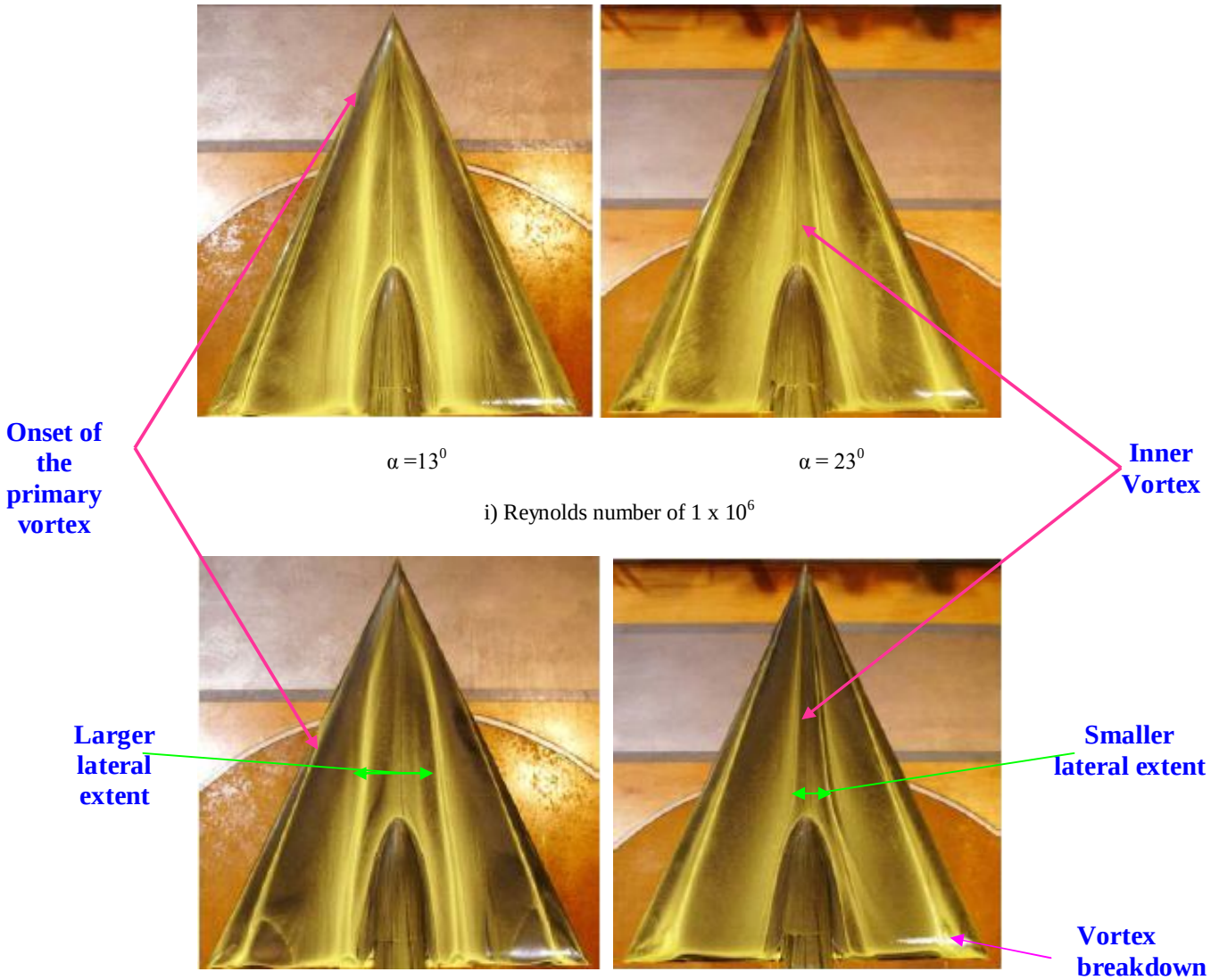

Figure 5.27: Surface oil flow visualization on the Medium leading edge at the Reynolds number of 1 and 2 x 10^6 at Munich Technical University (Furman & Breitsamter, 2008)

5.7 PART II: PARTICLE IMAGE VELOCIMETRY

5.7.1 Introduction

This chapter discusses the Particle Image Velocimetry results obtained from the large-radius wing at Reynolds numbers of 1 x 10^6 and 2 x 10^6 and taken at x/c_r = 0.5. The coordinate system used for the data analysis is shown in Figure 5.28. The origin of the coordinate system was at half of the wing thickness above the leading edge. The (x, y) plane was set coincident with the laser sheet, while the z-direction was set parallel with the flow direction.

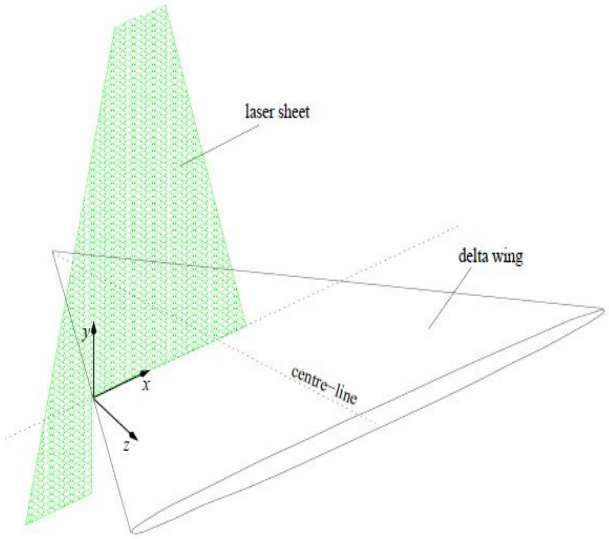

Figure 5.28: Coordinate system used to interpret PIV results

As discussed in chapter 3, there were significant constraints in the PIV tests. As a result, the time averaged velocity and vorticity distributions obtained from the experiments contained several artifacts. Low resolution of camera 2 due to its extreme position during the experiment was the main factor that contributed to the artifacts. The shadow and glare effects from the wing surface and other unwanted illuminations could only be partially masked off.

5.7.2 PIV Results at a Reynolds Number of 1 x 10^6

The time averaged velocity distribution from x = - 40 mm to 100 mm, that focuses on the leading-edge area, at 1 x 10^6 Reynolds number is shown in Figure 5.29. The primary vortex is well developed and centered at a height of about 40 mm above the wing surface and 48 mm inboard of the leading edge. The figure also shows the path of the flow from the lower to the upper surface of the wing at position x less than -20 mm. Nevertheless, the velocity region between y less than 0 mm and x more than -20 mm should be ignored because it was developed from the model surface.

Also in this figure, since the stereoscopic cameras were set to look on the x-y plane, the output background velocity is the velocity in the z-direction (w-component) or the velocity of the flow parallel to the wind tunnel.

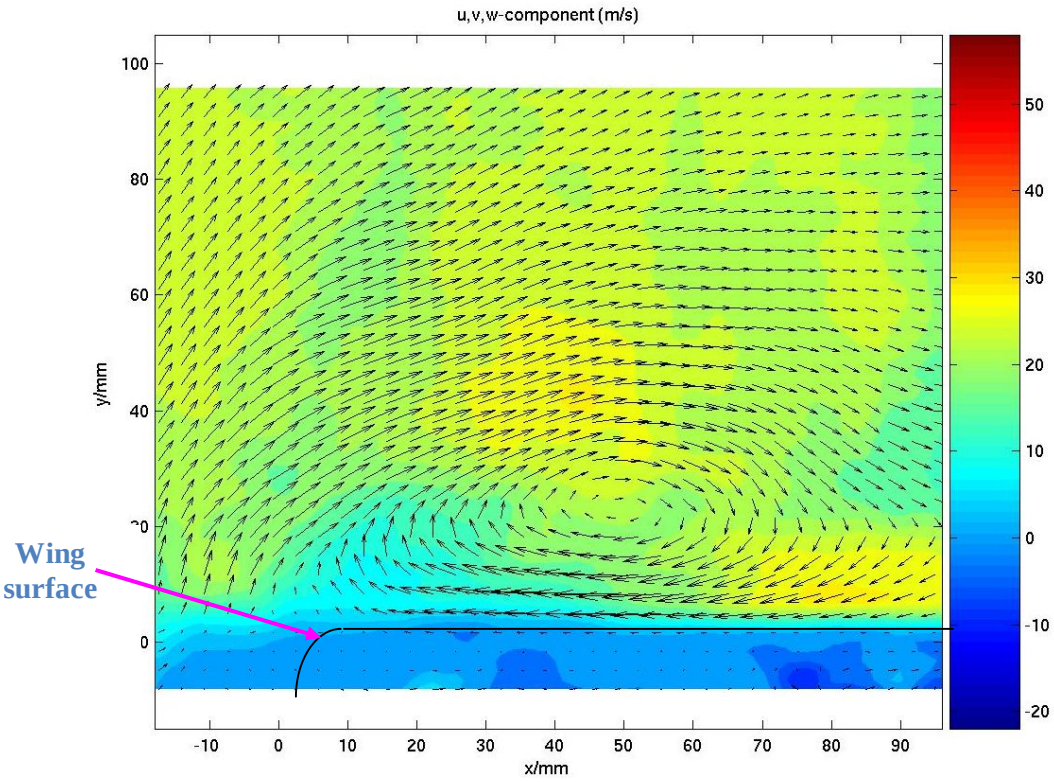

Figure 5.29: Velocity field in the leading-edged area of the large-radius wing, at $x/c_r = 0.5$, Reynolds number of 1 x 10^6 and $\alpha = 15^0$.

The vorticity distribution for the same measurement region is shown in Figure 5.30. Note that the positive vorticity along the line around y = 0 should be ignored as it is caused by reflection from the model surface in the recorded images. Negative vorticity appears in the primary vortex region, and the high negative vorticity coincides with the region of the vortex centre.

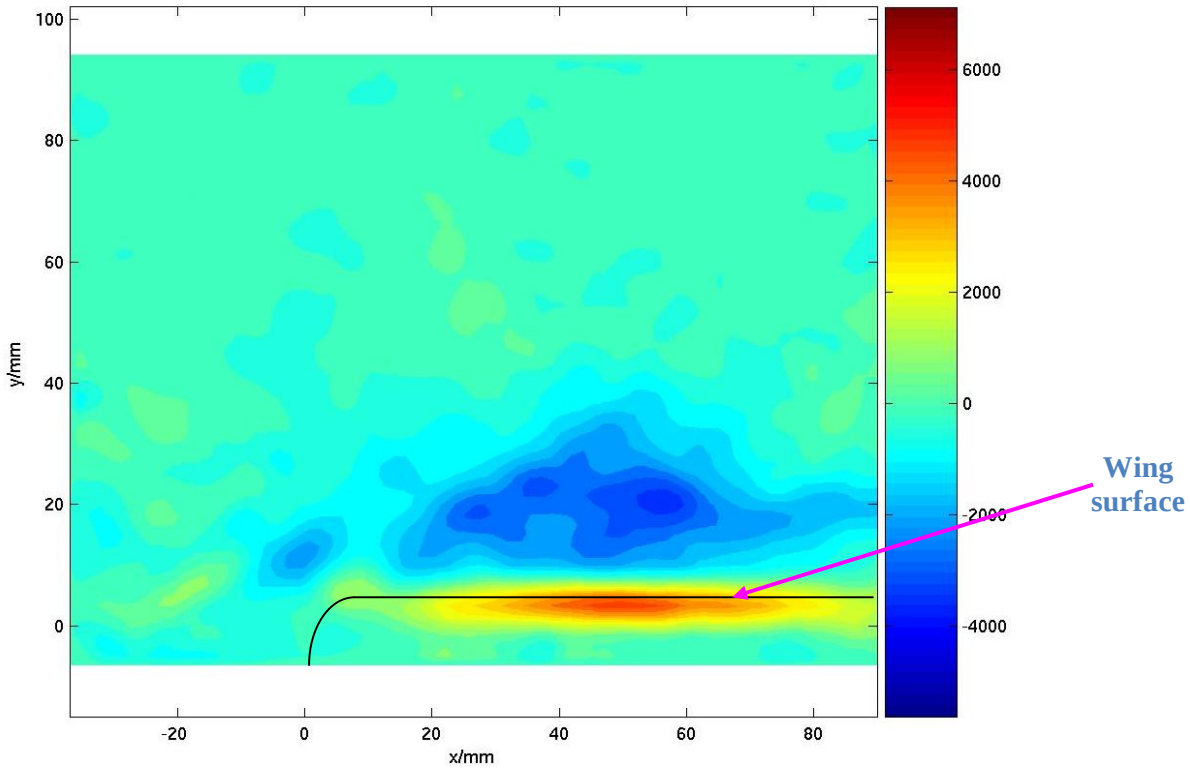

Figure 5.30: Vorticity in the leading edge area of the large-radius wing, at $x/c_r = 0.5$, Reynolds number of 1×10^6 & $\alpha = 15^0$.

Figure 5.31 shows the time averaged velocity taken from x = 40 mm to 240 mm at a Reynolds number of 1×10^6. In this figure, two vortices can be identified with a very weak inner vortex located well inboard and rotating in the same direction as the primary vortex. This inner vortex is centered about 200 mm from the leading edge. The result is in contrast to the experiments performed by Furman & Breitsamster (2008) as part of the VFE-2 programme. In that case, the inner vortex did not develop on either the sharp or medium-edged wing at this Reynolds number.

The reason for this is discussed in section 5.8. Note that the results presented in this figure in the region x = 80 mm to 105 mm were contaminated by shadowing, this was unavoidable due to restricted optical access to the test section. The figure also shows that the averaged vector velocity of the primary vortex extends to about x = 80 mm. Inboard on the wing, the figure shows that the diameter of the inner vortex extends from about x = 190 to 200 mm and that it has a height of about 25 mm.

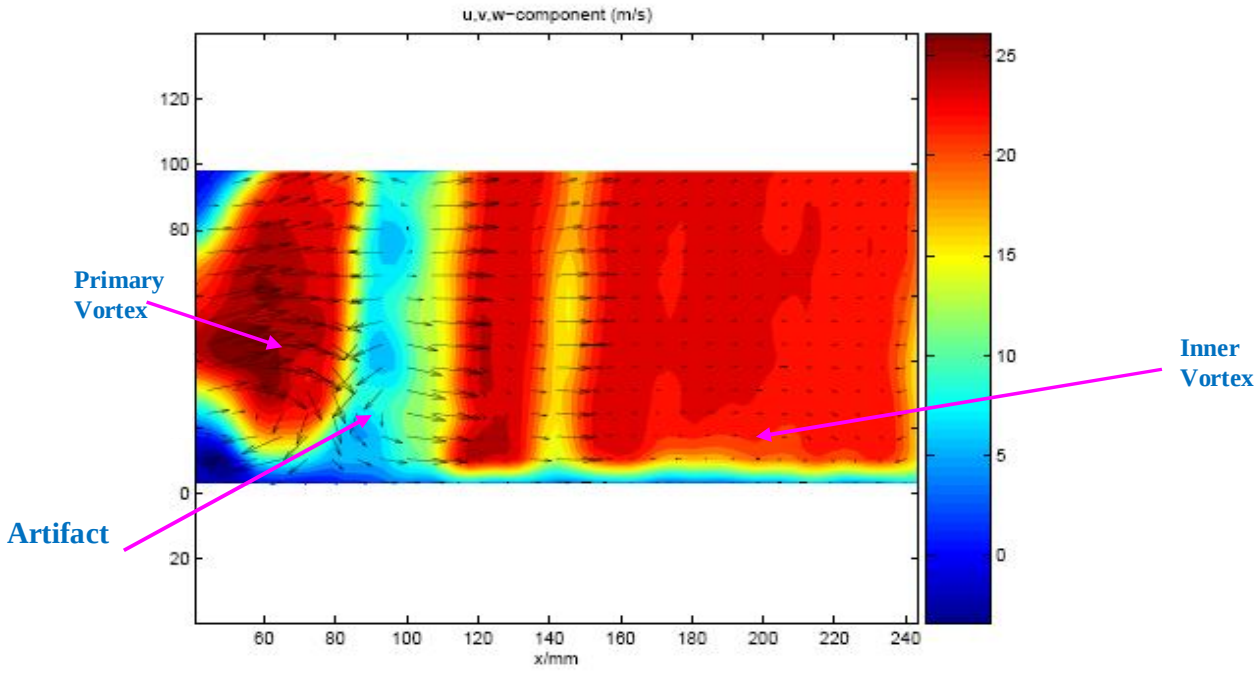

Figure 5.31: Velocity field inboard on the wing for the large-radius wing, at $x/c_r = 0.5$, Reynolds number of 1×10^6 & $\alpha = 15^0$.

The results obtained are well consistent with the experiments performed in DLR (Konrath *et al*, 2008) on the medium radius wing. As shown in figure 5.32, they also showed that the primary vortex developed in the leading edge region while the inner vortex is well generated inboard of the wing.

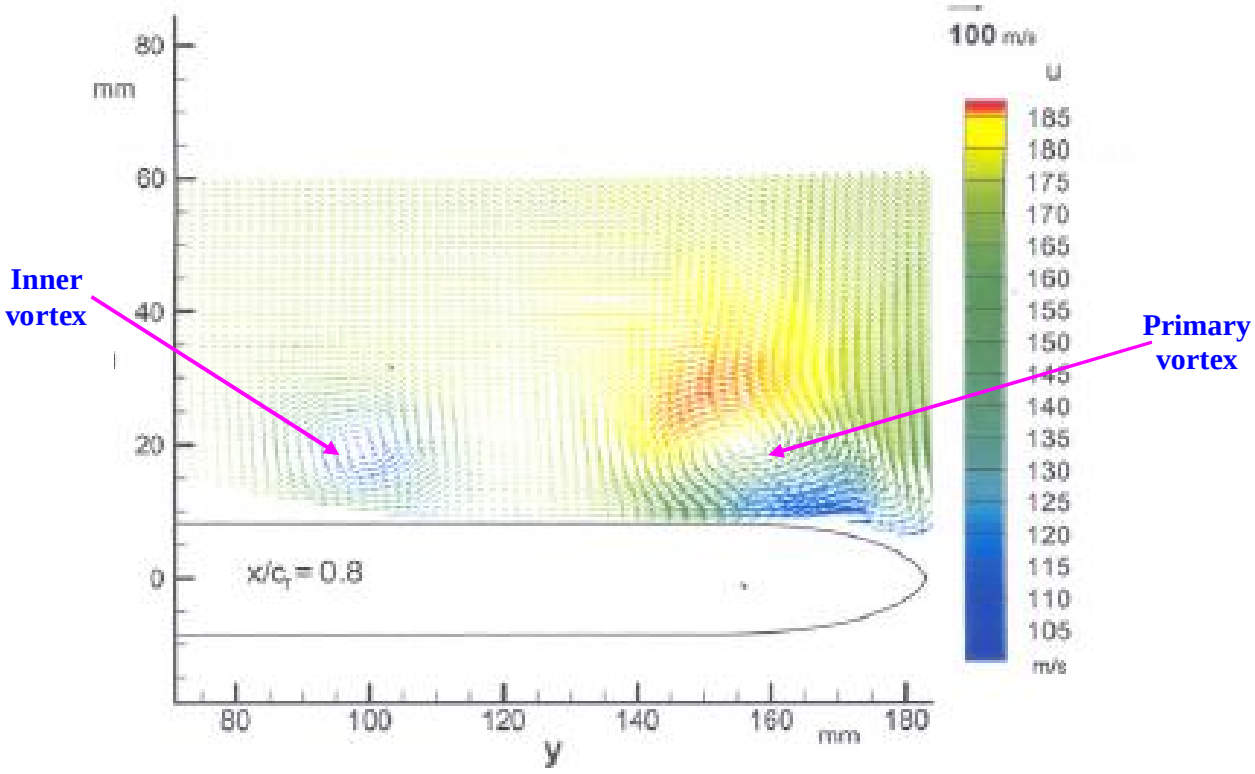

Figure 5.32: Time average velocity at $x/c_r = 0.8$, medium leading radius, Mach number = 0.4, $R_{mac} = 3 \times 10^6$ & $\alpha = 13.3^0$ of DLR experiment (Konrath *et al*, 2006)

5.7.3 PIV Results at a Reynolds Number of 2 x 10^6

The time averaged velocity distribution at a Reynolds number of 2 x 10^6, in the leading-edged region of x = -40 mm to 100 mm, is shown in Figure 5.33. In this case, the primary vortex has developed at a height of about 60 mm from the wing surface and is centered at about 40 mm from the leading edge.

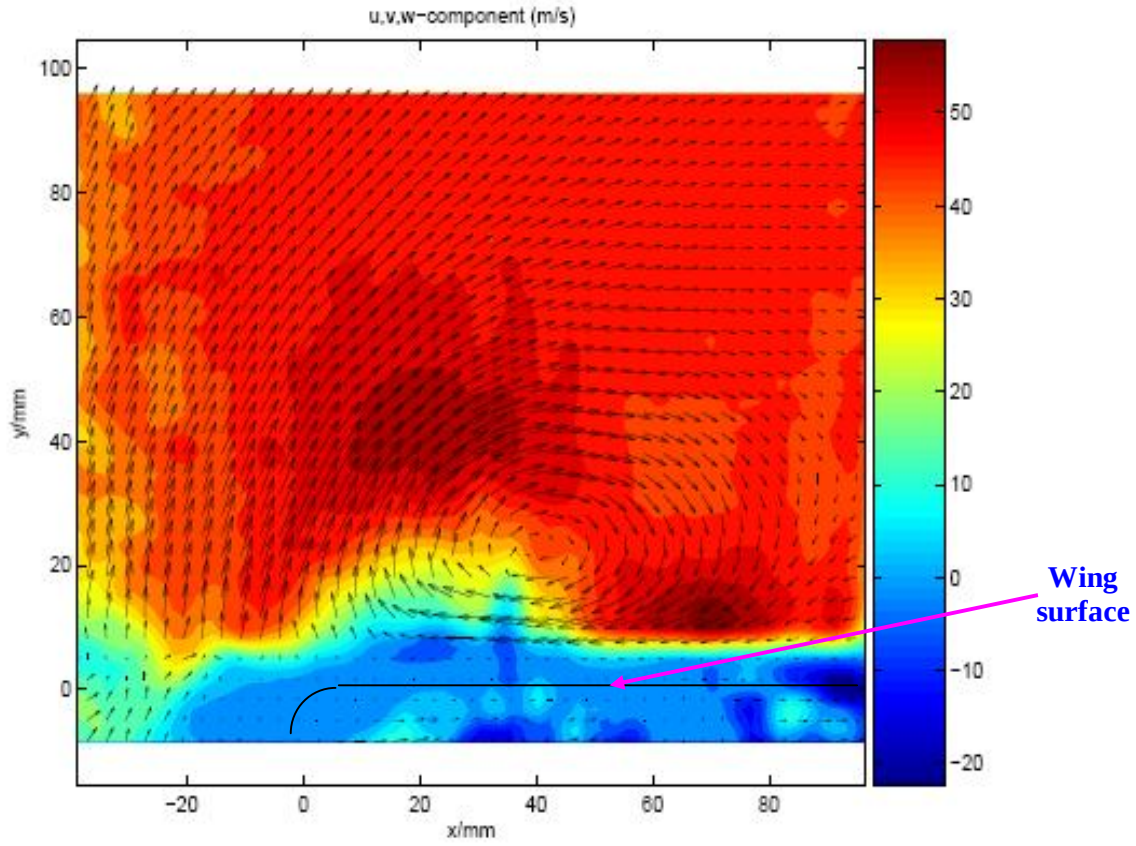

Figure 5.33: Velocity field in the leading-edged region of the large-radius wing, at $x/c_r = 0.5$, Reynolds number of 2×10^6 &$\alpha = 15^0$.

The vorticity distribution on the same plane is shown in Figure 5.34. In this case, the results again show negative vorticity within the primary vortex coinciding with regions of low velocity magnitude in the vortex centre. As before, the positive vorticity in the proximity of the model surface should be ignored. In comparison to the lower Reynolds number, the vorticity in figure 5.30 shows that the size of the primary vortex is slightly smaller in this case.

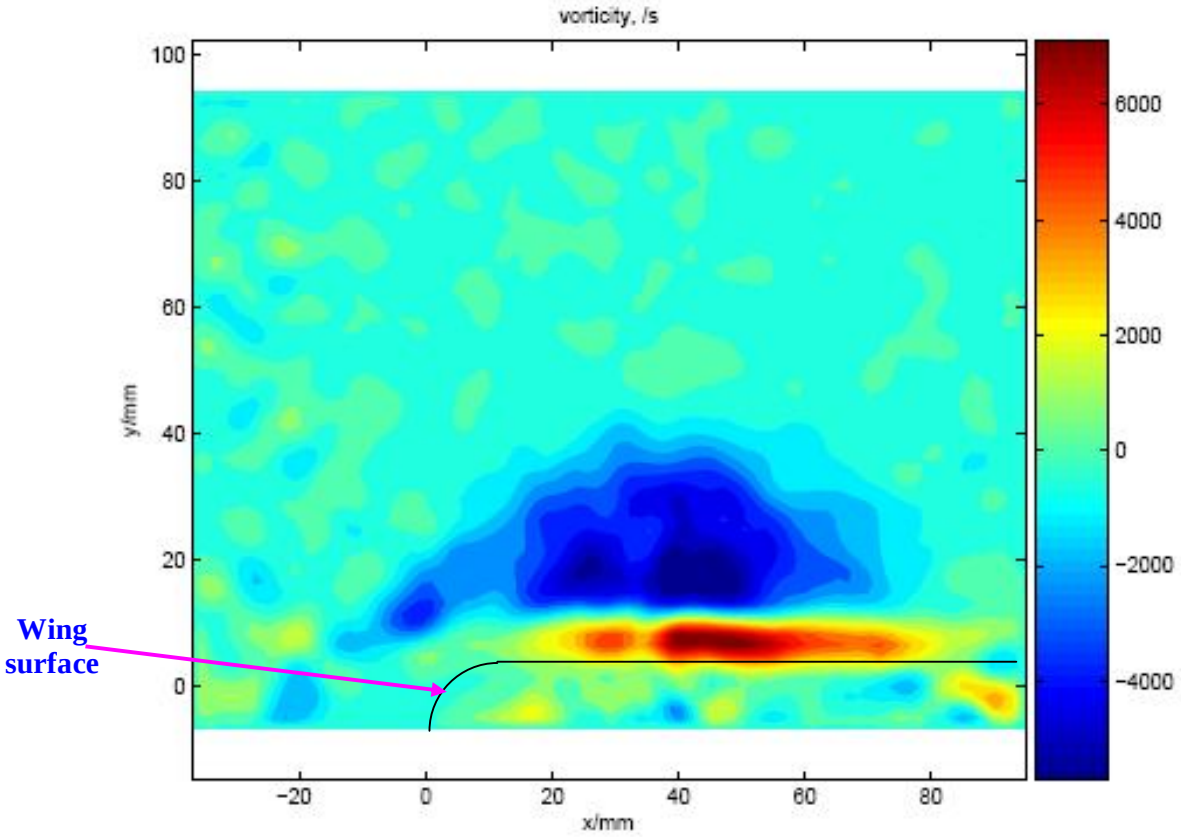

Figure 5.34: Vorticity in the leading-edged area of the large-radius wing at $x/c_r = 0.5$, Reynolds number of 2×10^6 & $\alpha = 15^0$.

Figure 5.35 shows the time averaged velocity distribution from x = 40 to 240 mm at a Reynolds number of 2×10^6. For this test condition, both vortices are again observed but the size of the inner vortex is larger in comparison to the previous case. The reason for this is discussed in section 5.8.

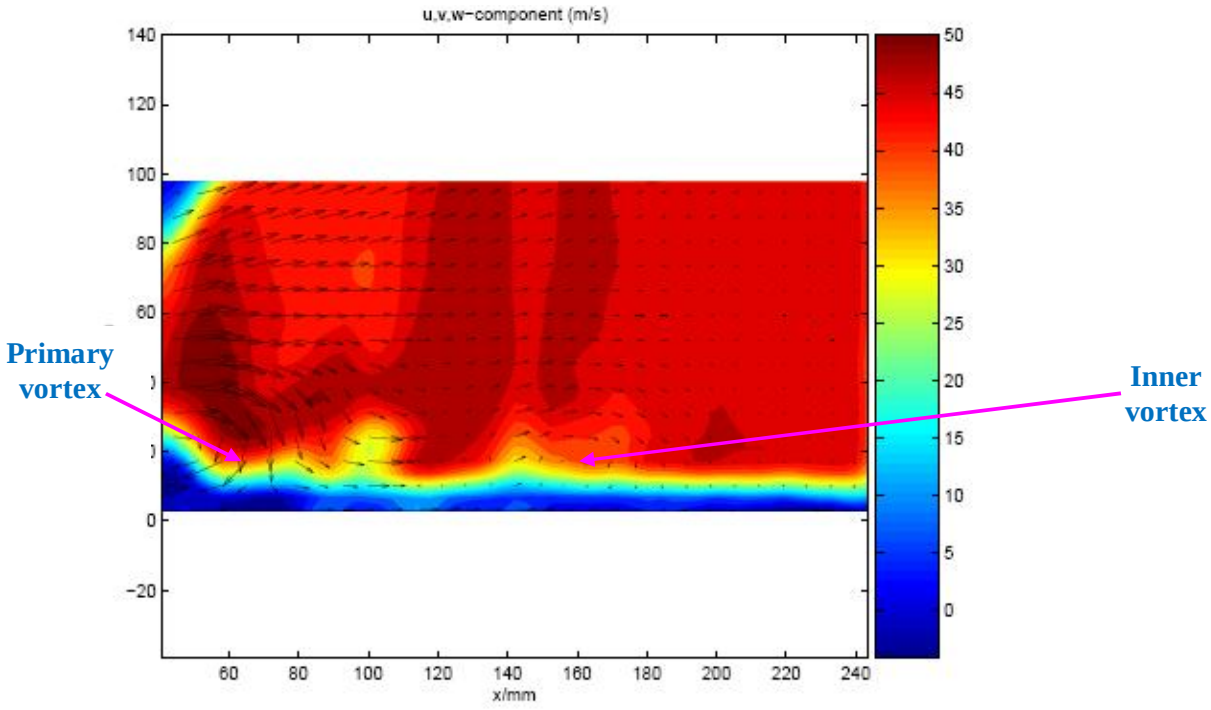

Figure 5.35: Velocity field inboard on the wing for the large-radius wing, at $x/c_r = 0.5$, Reynolds number of 2×10^6 & $\alpha = 15^0$.

The vorticity distribution for the same case is shown in Figure 5.36. The figure shows that the flow is dominated by the primary vortex until about x = 65 mm inboard of the leading edge. Another significant region of negative vorticity is centered about 160 mm from the leading edge. At this test condition, the vorticity plot shows the inner vortex is slightly smaller in size than the primary vortex. The vorticity also shows that the inner vortex is weaker in magnitude than the primary vortex. In section 5.4.2, the flow visualization also indicated an inner vortex existed but was weakening at $\alpha = 15^0$. The large area of positive vorticity at around x = 65 to x = 100 mm appears to be a secondary off-surface structure associated with the interaction of the two co-rotation vortices.

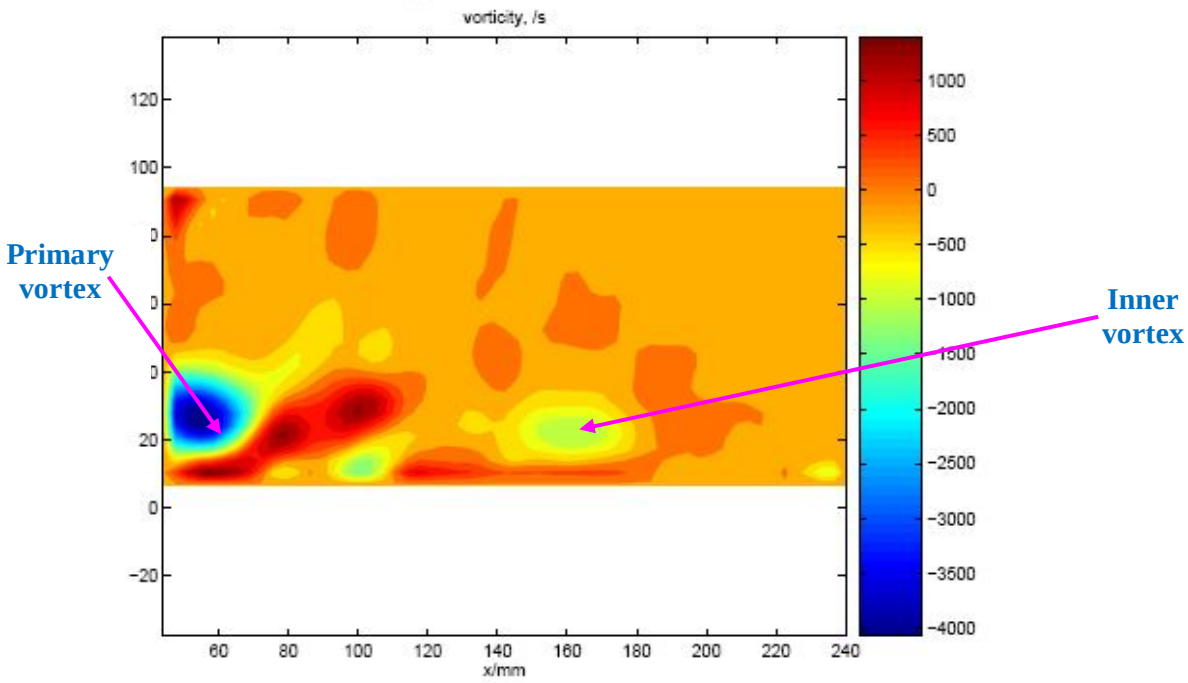

Figure 5.36: Vorticity inboard on the wing for the large-radius wing, at $x/c_r = 0.5$, Reynolds number of 2×10^6 & $\alpha = 15^0$.

5.8 Conclusions from Particle Image Velocimetry Study

Even though the experiments carried out produce results with several artifacts caused by light shadow and camera imperfection, the results are consistent with observations made in earlier sections, specifically;

a. At low Reynolds number ($R_{mac} = 1 \times 10^6$), a very weak inboard vortical structure is present on the large-radius wing at $\alpha = 15^0$. This vortex is located about 200 mm from the leading edge at $x/c_r = 0.5$. This is, however, in contrast with experiments conducted at a similar Reynolds number by Furman & Breitsamster (2008) on the medium-radius wing where no inner vortex was observed. This would suggest that the bluntness of the leading edge is a significant factor. A very weak inner vortex develops on the large-radius wing because the primary vortex is weakened as the leading edge radius is increased. The detailed

development of this inner vortex is shown in figure 5.37. The transport of the vorticity inboard of the wing starts near to the apex. The vorticity from this region extends downstream and smears towards the low pressure region of the leading edge. This vorticity then interfaces with the primary vortex that has already developed in the leading edge region. The flow inboard of the primary vortex rolls-up to form the inner vortex in this case. This result is consistent with the flow visualization images which show the inner vortex develops at a Reynolds number of 1 x 10^6 as discussed earlier in section 5.4.3.

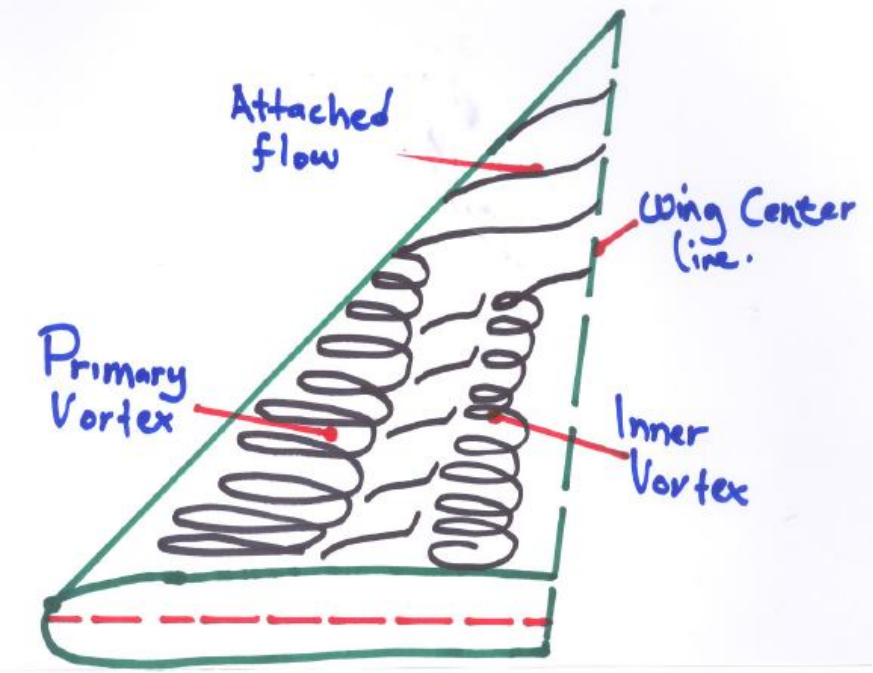

Figure 5.37: The transport of the vorticity inboard of the delta wing

b. At R_{mac} = 1 x 10^6, the time-averaged velocity field in the leading-edge area (Figure 5.29) indicates that the centre of the primary vortex is located about 48 mm inboard of the leading edge. At a Reynolds number of 2 x 10^6, however, (Figure 5.33) the vortex centre is shifted outboard about 40 mm from the leading edge. The reason for this difference may be

associated with the boundary layer state. As discussed in the flow visualization chapter, the flow at a Reynolds number of 1 x 10^6 was mostly laminar while the flow at a Reynolds number of 2 x 10^6 was suspected to be turbulent shifting the primary vortex in an outboard direction. This is also in excellent agreement with the observations of Hummel (2004). Nevertheless the correct prediction of the transition status above the wing is not fully resolved and it has become a difficult aspect for numerical analysis particularly at low Reynolds number.

c. The vorticity field in Figure 5.30 shows a relatively larger primary vortex at the lower Reynolds number compared with the higher Reynolds number case in Figure 5.34. The reasons for this could also be related to the laminar and turbulent characteristics of the flow. The results are again consistent with those of Hummel (2004). He indicated that by increasing the Reynolds number, the turbulent intensity of the flow would increase correspondingly. The greater ability of the turbulent boundary-layer to endure the adverse pressure gradient at higher Reynolds number is strongly suspected to delay the growth of the primary vortex at the higher Reynolds number. This result is again consistent with the flow visualization studies.

d. By comparing Figures 5.31 and 5.35, the time averaged velocity distribution shows that the size of the inner vortex increases as the Reynolds number increases. Although the measurements at 1 x 10^6 Reynolds number are compromised by the test set-up, it does appear that the strength of the inner vortex may also increase as the Reynolds number increases. This will be linked to the boundary layer state which, as discussed above, reduces the size of the primary vortex in the higher Reynolds number case. This, as is borne out by the flow visualization images in figures 5.13 and 5.18 for the 15^0 case, creates room for the inner to expand. Again from figures 5.13 and 5.18 the origin of the primary

vortex is further downstream in the higher Reynolds number case suggesting that higher levels of vorticity may be fed into the inner vortex.

e. The time averaged velocity field also shows that the centre of the inner vortex is shifted outboard as the Reynolds number is increased from 1×10^6 to 2×10^6. It was located at about x = 200 mm from the leading edge at 1×10^6 Reynolds number and at about x = 160 mm from the leading edge at 2×10^6 Reynolds number case. This is linked to the reduction in size of the primary vortex at the higher Reynolds numbers as discussed above.

f. The vorticity and average velocity show that the primary vortex of the large-radius wing develops as an oval-shaped structure compared to the more circular vortex on the medium-radius (Konrath, 2006a & 2008b) and sharp-edged wings (Furman & Breitsamter, 2008). The leading edge profile will be a significant factor here with the delay in leading edge separation influencing the shear layer trajectory and the subsequent roll up process. The separation inboard of the leading edge will have a shallower trajectory consistent with more oval shape of the primary vortex. More comparison with Numerical analysis on the large radius wing is required in the future to verify this.

g. The results obtained from the large-radius wing at a Reynolds number of 2×10^6 case also show that the maximum speed of the shear layer was 66 m/s at the freestream speed of 41.23 m/s. Thus the vortex core velocity is about 1.57 that of the freestream speed. On the medium-radius wing, the vortex core velocity is about 1.90 times the freestream speed (the experiment was performed by Konrath (2006b) as a part of VFE-2 activities at similar Reynolds number, Mach number = 0.4, $\alpha = 13.3^0$). For the large-radius wing, the delay of separation compared with the medium-radius case has initiated a smooth separation; thus weakening the primary vortex. This supports the hypothesis discussed in Chapter 4 and flow

visualization studies that the increase in leading edge bluntness decreases the strength of the primary vortex.

Chapter 6

6.0 CONCLUSIONS AND RECOMMENDATIONS FOR FUTURE WORK

The flow around a delta wing is extremely complicated and exhibits some flow features that are not fully understood. This thesis has presented experimental work performed at Glasgow University as part of the International Vortex Flow Experiment -2 (VFE-2) campaign that aimed to further investigate the three-dimensional flow around delta wings. Results are presented from four measurement techniques; i.e. flow visualization, steady balance, unsteady balance and Particle Image Velocimetry (PIV) measurements on a delta wing model with various degrees of leading-edge roundness (bluntness). A number of interesting features in the data have been highlighted particularly with respect to the effects of bluntness, Reynolds number and angle of attack on the conventional primary vortex. The occurrence and evolution of a relatively recently newly found phenomenon, the inner vortex, on the blunt-radius configurations have also been discussed in detail. It has been shown that the inner vortex is stronger and spatially more extensive for wings with higher leading edge roundness at moderate angles of attack. The current study has provided new insight on the effects of bluntness on the flow topology of delta wings.

6.1 Conclusions

1. In this study, four delta wings configurations which could be differentiated by their leading edge profiles; sharp-edged, small-, medium- and large-radius were tested. Within the VFE-2 group, only two wings were tested; the sharp-edged and medium-radius wings. On the radiused leading edge profiles, two vortices were found, representing the conventional primary vortex in the leading edge area and an inner vortex further inboard on the wing. The results presented show that as the leading edge radius increases the magnitude of the

primary vortex decreases but the magnitude of the inner vortex increases.

2. The precise nature and location of transition from laminar to turbulent flow on a wing is complex to resolve accurately. Several experimental techniques were performed within the VFE-2 campaign such as pressure-sensitive paint, infrared thermography; flow visualization, PIV, temperature sensitive paint, steady and unsteady load measurements but even this extensive database did not provide adequate information on the location of transition. This information is essential if numerical studies, especially at low Reynolds number, are to be properly validated. Once again, in this study, information on transition was somewhat qualitative although flow visualization results from the current study at Reynolds number 1×10^6 suggested that transition appeared under the primary vortex in the middle part of the wing. It then progressively extended towards the apex with increasing angle of attack.

3. The results presented here show that the formation of conventional leading edge primary vortex is very much dependent on the leading edge bluntness, Reynolds number and angle of attack. An increase in leading edge bluntness and Reynolds number can delay the formation of the primary vortex towards the aft portions of the wing. Nevertheless, increasing the angle of attack prompts an upstream movement of the origin of the primary vortex. The results obtained from the PIV experiment in the current study also show that an increase in leading-edge bluntness significantly decreases the swirl magnitude of the primary vortex.

4. This thesis has discussed in detail the development of an inner vortex. The inner vortex was first identified by Fritz in 2005. Initially, the inner vortex was thought to have developed on the front part of the

wing resulting from a three-dimensional separation bubble transition mechanism. Results from the current study suggest that roll-up of the inner vortex does not depend on a separation bubble being formed but rather arises from the complex interaction between separating flow in the apex region and the already forming primary vortex.

5. The normal force was found to be sensitive to leading edge radius but this sensitivity was not consistent across the angle of attack range. At low angle of attack an increase in leading edge radius would decrease the normal force coefficient significantly. This could be associated with the decrease in magnitude of the primary vortex. The analysis of the data spectra was also consistent with this finding. Nevertheless, at higher angles of attack, the normal forces on each of the wings were similar to each other that strongly suggested that the magnitude of the primary vortex was similar for all cases; i.e. the effect of bluntness was diminished at higher angle of attack. The axial forces measured in this study were found to in error. This issue has been discussed in chapter 4.

6. The effects of Reynolds number and leading edge bluntness on the attached flow region were discussed in this study. The flow visualization images showed that the attached flow region enlarged with increases in Reynolds number and leading edge bluntness. The results of the steady balance tests showed that this and the associated effect on the primary vortex had reduced the normal force coefficient significantly at higher Reynolds numbers. Transition appears to be a significant factor that influences the extent of the attached flow. At higher Reynolds number, the ability of the turbulent flow to endure the adverse pressure gradient enlarges the attached flow region in the apex area.

7. The results from the flow visualization studies on the large-radius wing at an angle of attack 10^0 strongly suggest that the primary vortex develops earlier than the inner vortex. For this case a concentration of vorticity in the leading edge area had rolled-up to form a weak primary vortex near the trailing edge. It is suggested that the vorticity inboard on the wing had then rolled-up as it interfaced with this primary vortex already existing at in the leading edge. Further examination of this phenomenon will be required to fully confirm this hypothesis.

8. Within the VFE-2 activities, PIV data were only available on the sharp- and medium-radius wings. Most of the data were concentrated in the middle part of the wing. The data in the apex and trailing edge region were not available due to the physical constraints of each tunnel. This study provided a further insight into the effect of leading edge bluntness by providing PIV data for the large radius wing. These data at Reynolds number of 1×10^6 showed that the inner vortex was established on the wing despite not being present at a similar Reynolds number on the medium-radius wing (Furman & Breitsamter, 2008). The stronger primary vortex on the medium-radius wing appears to have prevented the development of the inner vortex on the wing

6.2 Recommendations for Future Work

1. As stated in Section 6.1, the distribution of laminar and turbulent flow in the boundary layer of a delta wing is difficult to resolve experimentally and to predict computationally even for sharp-edged wing. Several efforts were made during the VFE-2 activities to obtain more insight into this although insufficient detail was generally obtained. Flow visualization studies from the current study have shown that the secondary separation line was smeared outboard towards the leading edge in the middle part of the wing at high angle of attack and

low Reynolds number. This could be related to transition in this area at a Reynolds number of 1×10^6. Nevertheless, further measurements are required to verify the boundary layer status. It is suggested that work should focus on the sharp-edged wing and the medium-radius wing at an angle of attack of 18^0, where the primary vortex is well developed over the entire wing for both configurations. Additional tests on the large-radius wing at the lower angle of attack of 13^0, where the flow is partly attached and partly separated, should also be carried out. A detailed study of the location of the transition fronts in these cases would provide extremely valuable information for validation of CFD methods in the future.

2. For the delta wing used in the VFE-2 studies, the trailing edge is consistently sharp from the wing tip to the wing centre line. The details of the flow in this region could not be captured using PIV due to the physical constraints on camera positioning in each tunnel that took part in VFE-2. As suggested by Breitsamter (2008), the flow in the tip region near the trailing edge is likely in most cases to be fully turbulent and the separation of the turbulent boundary layer here initiates the primary separation. In addition the work in this thesis suggests that the inner vortex only rolls-up as a coherent structure due to interaction between the vorticity inboard on the wing and the primary vortex generated earlier in the tip region. The primary vortex develops in the trailing edge area due to the curvature of the trailing edge itself that results in the local angle of attack in the trailing edge being higher than the model angle of attack. It would be extremely valuable if the detail of the interaction between the primary and inner vortex, at its formation, could be captured via PIV and validated by numerical modelling. Thus, PIV data during the development of the primary vortex in the leading edge area is required in the future.

3. The formation of the inner vortex is dependent on the Reynolds number, Mach number and leading edge radius. The experiments by Furman & Breitsamster (2008) on the medium-radius wing showed that the inner vortex did not form at a Reynolds number of 1×10^6, but it developed at the slightly higher Reynolds numbers of 2×10^6 to 4×10^6 (Konrath, 2006b & 2008a). At low Reynolds number, the extension of the primary vortex up to the apex region, due to early laminar separation, appears to have prevented the development of the inner vortex. At high Mach number, the development of the inner vortex was also prevented by a stronger primary vortex. Nevertheless, the current experiment carried out on the large radius wing at Reynolds number of 1×10^6 showed that the inner vortex did form for this test condition, with the bluntness of the leading edge being the primary factor that contributed to this. Further experiments are still, however, required to investigate the influence of Reynolds number and bluntness on the nature of the inner vortex. Smoke flow visualization may be a suitable method to investigate this nature. The experiments could be performed at various Reynolds numbers, say, from 0.7×10^6 to 1.5×10^6 with the smoke being injected from the wing surface near the primary attachment line of the inner vortex.

4. The effects of Reynolds number, angle of attack and the bluntness on a delta wing undergoing pitching motion should be studied. To date, very little information is available on the flow behaviour during pitching motion on a round-edged delta wing. It is known that pitching motion can have a significant effect on the primary vortex structure of a sharp-edged delta wing and that it influences the progression of vortex breakdown. The flow on the round-edged wings is significantly more complex and the extent to which this complex flow will be altered by pitching motion is almost completely unknown. Experiments to measure the strength and locations of the vortex structures during pitching motion would be extremely valuable as

would understanding the effects of reduced frequency. Results from these types of study would have particular significance to manoeuvring aircraft. Pitching motion experiment on the blunt leading edge wing is required to verify this in the future.

5. Steady balance data at a Reynolds number of 2 x 10^6 showed the normal forces were similar for all wings at about $\alpha = 23^0$. The results suggest that at higher angles of attack, the flow is dominated by the primary vortex on all of the wings. The magnitude of the primary vortex is thought to be identical for all wings and the onset of the primary vortex is located in close proximity to the apex, thus eliminating the effect of leading-edge radius. Unfortunately, there is no PIV data at high angles of attack available, even from the VFE-2 work, for confirmation of this. This is again due to the physical constraints of the wind tunnels used. Further PIV with surface flow visualization and force correlations at high angles of attack, on all of the wings, would be required to verify this.

6. The effects of leading edge bluntness on the vortex breakdown process needs further investigations. Even though the current study shows consistency with previous work on the delay of vortex breakdown, a detailed non-intrusive study in the region of breakdown was not possible here or in the other VFE-2 activities. Unsteady force data on the large radius wing suggested that, at $\alpha = 23^0$, vortex breakdown did not occur or was less extensive on the wing. Vortex breakdown was expected to occur on this wing at higher angles of attack, thus further experiments are required to verify this.

7. The current study has shown that the large-radius wing produced an oval shaped primary vortex, in contrast to the rather circular shape of the primary vortex for the medium-radius wing (Konrath, 2006b & 2008a). Again, the bluntness is likely to be the main factor that

contributed to this. PIV results from the current study suggested that the increase in leading edge radius had decreased the magnitude of primary vortex significantly. It was postulated, on the basis of the force data, that the strength (and possible the shape) of the primary vortex on the large radius wing would tend to that on the sharp-edged wing at higher angle of attack. A detailed experiment and numerical studies of the effects of angle of attack on the primary vortex of the large-radius could provide verification of this.

REFERENCES

1) Agrawal, S., Barnett, R.M., Robinson, B.A. 1992. ***Numerical Investigation of Vortex Breakdown on a Delta Wing.*** AIAA Journal, Vol. 30, No. 3. Page 584-591.

2) Atta, R. & Rockwell, D. 1990. ***Leading-Edge Vortices Due to Low Reynolds Number Flow Past a Pitching Delta Wing.*** AIAA Journal, Vol. 28, No 6, Page 995-1004.

3) Baban, F., So, R.M. & ötugen. 1989. ***Unsteady Forces on Circular Cylinders in a Cross-flow.*** Experiments in Fluids 7, Page 293 – 302.

4) Betyaev S.K & Brysov O.P. 1994. ***Delta Wing in a Subsonic Flow.*** *Mekhanika Zhidkosti I Gaza*, .Vol29, No2**.** Page 282-284.

5) Bozhkov V.M, Mozol'kov A.S. & Shalaev, V.I.1975. ***Visual Study of the Three-Dimensional Flow Diagram around a Delta Wing in Subsonic Stream.*** Mekhanika Zhidkosti I Gaza. Page 334-338.

6) Breitsamter, C. 2008. ***Unsteady Flow Phenomena Associated with Leading-Edge Vortices.*** Progress in Aerospace Sciences. Vol 44. Page 48-65.

7) Buchholz, M.D. & Tso, J. 2000. ***Lift Augmentation on Delta Wings with Leading-Edge Fences and Gurney Flap.*** Journal of Aircraft. Vol.37, No. 6, Page 1050-1057.

8) Chakrabarty, S.K., Dhanalakshmi, K. & Mathur, J.S. 1998. ***Navier-Stokes Analysis of Vortex Flow over a Cropped Delta Wing.*** Acta Mechanica 131, Page 69-87.

9) Chu, J. & Lamar, J.E. 1988. ***Force and Pressure Study of Thick Cambered/Twisted 58 deg Delta Wings.*** Journal of Aircraft. Vol. 25, Page 69-75

10) Chu, J. & Luckring, J.M. 1996. ***Experimental Surface Pressure Data Obtained on 65^0 Delta Wing across Reynolds Number and Mach number Ranges.*** NASA Technical Memorandum 4645.

11) Cipolla, K.M. & Rockwell, D. 1995. ***Flow Structure on Stalled Delta Wing subjected to Small Amplitude Pitching Oscillations.*** AIAA Journal. Vol. 33, No.7, Page 1256-1262.

12) Crichton M.L., Czarnecka Z, Green R.B. & Coton F.N. (2005). ***A Systematic Study of Side-Wall Interference effects on Delta Wing Aerodynamics.*** *A1AA 2005-498.*

13) Crippa, S. 2008. ***Chapter 30 – Numerical Solutions for the VFE-2 Configuration on Unstructured Grids at KTH, Sweden.*** RTO-TR-AVT-113. Page 30-2 – 30-34.

14) Cummings, R.M. & Schutte, A. 2008. ***Chapter 32. Numerical Solutions for the VFE-2 Configuration on Unstructured Grids at USAFA***. RTO-TR-AVT-112. Page 32-1 – 32-28.

15) Dēlery, J.M. 1992. ***Physics of Vortical Flow.*** Journal of Aircraft. Vol 29 (5). Page 856-876.

16) Dieterle, L., Kompenhans, J., Peiter, U. & Pengel, K. 1998. ***Flow Field Investigations on a Large Delta Wing Using LSI and PIV.*** 8th International Symposium on Flow Visualization.

17) Drikakis, D., Li, N., Turner, J.T., Jaworski, A.J. & Wood, N. 2003. ***Highly Swept Leading Edge Separations.*** MSTTAR DARP Report.

18) Earnshaw, P.B. 1962. ***An Experimental Investigation of the Structure of a Leading-Edge Vortex.*** Aeronautical Research Council Reports and Memoranda, No 3281.

19) Elle, B.J. 1958. ***An Investigation at Low Speed of the Flow near the Apex of Thin Delta Wings with Sharp Leading Edges.*** Aeronautical Research Council Reports and Memoranda, No. 3786.

20) Elle, B.J. 1960. ***On the Breakdown at High Incidences of the Leading Edge Vortices on Delta Wings.*** Journal of the Royal Aeronautical Society. Vol. 64. Page 491-493.

21) Engler, R.H., Hartmann, K & Sculze, B. 1991***. Aerodynamics Assessment of an Optical Pressure Measurement System (OPMS) by Comparison with Conventional Pressure Measurements in a High Speed Wind tunnel.*** IEEE, CH3028-8/91/0000-0017.

22) Erickson, G.E. 1981. ***Water Tunnel Studies of Leading-edge Vortices. Journal of aircraft.*** Vol. 19, No. 6, Page 442 – 448.

23) Erickson, G.E. 1991. ***Wind Tunnel Investigation of the Interaction and Breakdown Characteristics of Slender-Wing Vortices at Subsonic, transonic and Supersonic Speeds***. NASA Technical Paper 3114.

24) Erickson, L.E. & King, H.H.C. 1992. ***Effect of Leading-Edge Geometry on Delta Wing Unsteady Aerodynamics. Journal of Aircraft.*** Vol. 30, No. 5. Page 793 – 795.

25) Faler, J.H. & Leibovich, S. 1977. ***Disrupted States of Vortex Flow and Vortex Breakdown***. The physics of Fluids, Vol. 20, No. 9.

26) Fink, P.T.1966. ***Some Early Experiments on Vortex Separation, Part 1: Some Low Speed Aerodynamic Properties of Cones***. Aeronautical Research Council Reports and Memoranda, No. 3489.

27) Fletcher, H.S. 1958. ***Low-Speed Experimental Determination of the Effects of Leading-Edge Radius and Profile Thickness on Static and Oscillatory Lateral Stability Derivatives for a Delta Wing with 60^0 of Leading-Edge Sweep***. NASA Technical Note 4341.

28) Fritz, W. 2008. ***Chapter 25 – Numerical Solutions for the VFE-2 Configurations on Structured Grids at EADS-MAS, Germany***. RTO-TR-AVT-113. Page 25-1 – 25-21.

29) Fritz, W. & Cummings, R.M. 2008. ***Chapter 34 – Lessons Learned From the Numerical Investigations on the VFE-2 Configuration.*** RTO-TR-AVT-113. Page 34-1 – 34-31.

30) Furman, A. & Breitsamter, C. 2008. ***Experimental Investigations on the VFE-2 Configurations at TU Munich, Germany***. RTO-TR-AVT-113.

31) Gad-El-Hak, M. & Blackwelder, R.F. 1985. ***The discrete Vortices from a Delta Wing.*** Technical Report 1985. Vol 23, 961-962

32) Gad-el-Hak, M. & Ho, C.M.1985. ***The Pitching Delta Wing***. Vol. 23, No. 11, Page 1660-1665.

33) Garg, A.K. & Leibovich, S. 1979. ***Spectral Characteristics of Vortex Breakdown Flowfields.*** Physic Fluid 22(11).

34) Greenwell, D.I. & Wood, N.J. 1992. ***Determination of Vortex Burst Location on Delta Wings from Surface Pressure Measurements.*** AIAA Journal, Vol.30, No. 11, Page 2736-2739.

35) Gurdamar, E., Ortakaya, Y., Kaya, S. & Korkem, B. 2008. ***Chapter 28 – Numerical Solutions for the VFE-2 Configurations on Structured Grids***. TRO-TR-AVT-113. Page 28-1 – 28-25

36) Gursul, I. 2004. ***Recent Developments in Delta Wing Aerodynamics.*** The Aeronautical Journal. Page 437-452.

37) Gursul, I., Allan, M.R. & Badcock, K.J. 2005a. ***Opportunities for the integrated use of Measurement and Computations for the Understanding of Delta Wing Aerodynamics.*** Aerospace Science and Technology, Vol. 9. Page 181-189.

38) Gursul, I., Gordnier, R. & Visbal, M. 2005b. ***Unsteady Aerodynamics of Nonslender Delta Wings.*** Progress in Aerospace Science, 41. Page 515 – 557.

39) Gursul, I. & Xie, W. 1999. ***Buffeting Flows over Delta Wings.*** AIAA journal, Vol. 37, No. 1, Page 58 - 65

40) Hall, M.G. 1972. ***Vortex Breakdown***. Annual Review Fluid Mechanics. Vol 4. Page 195-218.

41) Henderson, W.P. 1976. ***Effects of Wing Leading-Edge Radius and Reynolds Number on Longitudinal Aerodynamics Characteristics of Highly Swept Wing-Body Configurations at Subsonic Speeds.*** NASA Technical note TN – D – 8361.

42) Honkan, A & Andreopoulos, J. 1997. ***Instantaneous Three-Dimensional Vorticity Measurements in Vortical Flow over a Delta Wing***. AIAA Journal, Vol. 35. Page 1612- 1620.

43) Huang, A, Folk, C., Silva, C., Christensen, B., Chen, Y., Ho, C.M., Jiang, F., Grosjean, Tai, Y.C., Lee, G.B., Chen, M. & Newbern, S. 2001. ***Application of MEMS Devices to Delta Wing Aircraft: From Concept Development to***

Transonic Flight Test. 39th AIAA Aerospace Sciences Meeting & Exhibit. AIAA 2001-0124.

44) Hummel, D. 2004. ***Effects of Boundary layer Formation on the vortical Flow above Slender Delta Wings. RTO specialist Meeting on Enhancement of NATO military Flight Vehicle Performance by Management of Interacting Boundary Layer transition and Separation.*** Meeting Proceedings RTO-MP-AVT-111, Page 30-1 to 30-2.

45) Hummel, D.2006. ***The Second International Vortex Flow Experiment (VFE-2): Objectives and First Results.*** Proc.ImechE Vol. 220 Part G: J. Aerospace Engineering.

46) Hummel, D. 2007. ***The Second International Vortex Flow Experiment (VFE-2): Objectives and Present Status.*** 25th AIAA Applied Aerodynamics Conference. AIAA 2007-4446.

47) Hummel, D. 2008a). ***Chapter 17 – The International Vortex Flow Experiment 2 (VFE-2): Objectives and Overview.*** RTO-TR-AVT-113, Page 17-1 – 17-20.

48) Hummel, D. 2008b). ***Chapter 35 – Final Results of the International Vortex Flow Experiments – Résumé and Outlook.*** RTO-TR-AVT-113, Page 35-1 – 35-25.

49) Hummel, D. & Srinivasan, P.S. 1967. ***Vortex Breakdown Effects on the Low-Speed Aerodynamics Characteristics of Slender Delta Wings in Symmetrical Flow.*** Journal of the Royal Aeronautical Society, Vol 71. Page 319-322.

50) Jiang, F., Lee, G.B., Tai, Y.C. & Ho, C.M. 2000. ***A flexible Micromachine-based Shear Stress sensor array and its application to separation point detection.*** Sensors and Actuators, Vol. 79. Page 194-203.

51) Kegelman, J.T. & Roos, F.W. 1989. ***Effects of Leading Edge Shape and Vortex Burst on the Flowfield of a 70-Degree-Sweep Delta Wings***. 27th Aerospace Science Meeting. AIAA-1989-86

52) Klein, K., Sachs, W.E., Henne, U., Engler, R.H., Wiedemann, A. & Konrath, R. 2006. ***Development of PSP Technique for Application on the VFE-2 65^0 Delta Wing Configuration.*** 44th AIAA Aerospace Sciences Meeting and Exhibit. AIAA 2006-59.

53) Kompenhans, J. 2007. ***Experimental Methods for Multi Diagnostics of Flow Fields in Wind Tunnel.*** Journal of Visualization, Volume 10, No. 1/2007, Page 25-28.

54) Konrath, R., Klein, C., Engler, R.H. & Otter, D. 2006a. ***Analysis of PSP Results Obtained for the VFE-2 65^0 Delta Wing Configuration at Sub- and Transonic Speeds.*** 44th AIAA Aerospace Sciences Meeting and Exhibit. AIAA 2006-60

55) Konrath, R., Schröder, A. & Kompenhans, J. 2006b. ***Analysis of PIV Results Obtained for the VFE-2 65^0 Delta Wing Configuration at Sub- and Transonic Speed.*** 24th Applied Aerodynamics Conference. AIAA 2006-3003.

56) Konrath, R., Klein, C., Henne, U., Sachs, W., Wiedemann, A., Otter, D. Schroder, A., Agocs, J., Mattner, M., Egami, Y., Fey, U. & Groot, K.D. 2008a. ***The International Vortex Flow Experiment 2 in the DNW-TWG and the DNW-KKK***. DNW Report.

57) Konrath, R., Klein, C., Schröder, A. & Groot, K.D. 2008b. ***Chapter 19 – Experimental Investigations on the VFE-2 configuration at DLR, Germany***. RTO-TR-AVT-113. Page 19-1 – 19-37.

58) Kurun, S. 2008. ***Chapter 23 – Experimental Investigations on the VFE-2 Configuration at TUBITAK-SAGE, TURKEY.*** RTO-TR-AVT-113. Page 23-1 – 23-18.

59) Lamar, J.E. 1990. ***Vapour-Screen Technique Applied to a Delta-Wing Aircraft***. NASA-Langley Research Center.

60) Lamar, J.E. & Hummel, D. 2008. ***Chapter 1 – RTO Task Group AVT-113 "Understanding and modelling Vortical Flows to Improve the Technology readiness Level for Military Aircraft": Objectives and Overview***. RTO-TR-AVT-113

61) Lamar, J.E. & Obara, C.J. 2008. ***Chapter 3 – The Cranked Arrow Wing Aerodynamics Project (CAWAP) and Its Extension to the International Community AS CAWAPI: Objectives and Overview***. RTO-TR-AVT-113

62) Lambourne, N.C. & Bryer, D.W.1961. ***The Bursting of Leading-Edge Vortices – Some Observations and Discussions of the Phenomenon.*** Aeronautical Research Council Reports and Memoranda, No. 3282.

63) Lang, N. 1998. ***PIV Measurements in Sub- and Supersonic Flow over the Delta Wing Configuration ELAC.*** 8th International Symposium on Flow Visualization.

64) Leibovich, S. 1978.***The Structure of Vortex Breakdown.*** Rev. Fluid Mech., Vol 10.

65) LeMay, S.P., Batil, S.M. & Nelson, R.C. 1990. ***Vortex Dynamics on a Pitching Delta Wing.*** Journal of Aircraft. Vol. 27, No. 2, Page 131-139.

66) Le Roy, J.F. & Riou, J. 2008. ***Chapter 26 – Numerical Solutions for the VFE-2 Configuration on Structured Grids at ONERA, France.*** RTO-TR-AVT-113. Page 26-1 – 26-24.

67) Luckring, J.M. 2002. ***Reynolds Number and leading-Edge Bluntness Effects on a 65^0 Delta Wing.*** AIAA-2002-0419

68) Luckring, J.M. 2004a. ***Reynolds Number, Compressibility, and Leading Edge Bluntness Effects on Delta Wing Aerodynamics.*** 24th International Congress of the Aeronautical Sciences

69) Luckring, J.M. 2004b. ***Compressibility and Leading-Edge Bluntness Effects for a 65^0 Delta Wing.*** AIAA-2004-0765.

70) Luckring, J.M. 2008. ***Chapter 18 – Initial Experimental and Analysis of Blunt-Edge Vortex Flows.*** RTO-TR-AVT-113

71) Luckring, J.M. & Hummel, D. 2008. ***Chapter 24 – What Was Learned From The New VFE-2 Experiments.*** RTO-TR-AVT-113.

72) Mabey, D.G. 1992. ***Review of the Normal Force Fluctuations on Aerofoils with Separated Flow.*** Progress in Aerospace Science. Vol. 29. Page 43 – 80.

73) May, C. & Gutmark, E. J. 2005. ***High Angle of Attack Flight Control of Delta Wings Using Vortex Actuators.*** AIAA Conference Proceeding. AIAA-2005-1232.

74) Miau, J.J, Kuo, K.T., Liu, W.H., Hsieh, S.J. & Chou, J.H. ***Flow Developments Above 50-Deg Sweep Delta Wings with Different Leading-Edge Profiles.*** Journal of Aircraft, Vol. 32, No. 4. Page 787 – 794.

75) Moigne, Y.L., Rizzi, A. & Johansson, P. 2001. ***CFD Simulations of a Delta Wing in High-Alpha Pitch Oscillations.*** 39th Aerospace Science Meeting & Exhibit, AIAA 01-0862.

76) Narayan, K.Y. & Hartman, K. 1988. ***Transonic and Supersonic Flow Past a 65^0 Delta Wing with Rounded Leading Edge.*** DFVLR-FB 88-44 Report.

77) Narayan, K.Y. & Seshadri. 1997. ***Types of Flow on the Lee Side of Delta Wings.*** Progress of Aerospace Science, Vol. 33, Page 167-257.

78) Nelson, R.C. & Pelletier, A. 2003. ***The Unsteady Aerodynamics of Slender Wings and Aircraft Undergoing Large Amplitude Maneuvers.*** Progress in Aerospace Science. Vol 39. Page 185-248.

79) Nelson, R.C. & Visser, K.D. 1990. ***Breaking Down the Delta Wing Vortex: The Role of Vorticity in the Breakdown Process.*** AGARD symposium on Vortex Flow Aerodynamics.

80) O'Neil, P.J., Ross, F.W., Kegelmen J.T., Barnet, R.M., Hawk J.D., ***Investigations of flow characteristics of a developed vortex.*** Naval Air Development Center, Report NADC-89114-60, 1989

81) Pashilkar, A.A. 2001. ***Surface Pressure Model for Simple Delta Wings at High Angle of Attack.*** Sâdhana, Vol. 26, Part 6. Page 495-515.

82) Payne F.M. ***The structure of the leading edge vortex flows including vortex breakdown***. PhD dissertation, University of Notre Dame, May 1987

83) Payne, F.M., Ng, T.T., Nelson, R.C. 1987. ***Experimental Study of the Velocity Fields on Delta Wings***, *AIAA Journal*.1-14.

84) Payne, F.M., Ng, T.T., Nelson, R.C. 1989. ***Seven hole probe measurement of Leading Edge Vortex Flows***. Experiments in Fluids 7, 1-8.

85) Peake, D.J. & Tobak, M. 1980. ***Three-Dimensional Interactions and Vortical Flows with Emphasis on High Speeds.*** AGARD-AG-252.

86) Peckham, D. H. 1958. ***Low Speed Wind Tunnel Tests on a Series of Uncambered Slender Pointed Wings with Sharp-Edges***. Aeronautical Research Council Reports and Memoranda, No. 3186.

87) Peckham, D.H. & Atkinson, S.A. 1960. ***Preliminary Results of Low Speed Wind Tunnel Tests on a Gothic Wing of Aspect Ratio 1.0.*** Aeronautical Research Council Technical Report. R21836.

88) Polhamus E.C. 1966. ***A Concept of the vortex Lift of Sharp-Edged Delta Wings Based on a Leading-Edge Suction Analogy.*** NASA TN-D-3767.

89) Renac F., Barberis D. & Molton P. 2005. Control of Vortical Flow over a Rounded Leading- Edge Delta Wing. *AIAA Journal*. Vol. 43, No. 7, Page 1409-1417

90) Riley, A.J. & Lowson, M.V. 1998. ***Development of a Three-dimensional Free Shear Layer.*** J. Fluid Mechanics. Vol 369. Page 49-89.

91) Rizzi, A. & Muller, B. 1989. ***Large-Scale Viscous Simulation of Laminar Vortex Flow over a Delta Wing.*** AIAA Journal, Vol. 27, No. 7. Page 833 – 840.

92) Ronoie, K. 1996a. ***Low Speed Aerodynamics Characteristics of 60^0 Rounded Leading-Edge Delta Wing with Vortex Flaps: Part 1: 457 mm Span Delta Wing. Cranfield University.*** COA Report No. 9611.

93) Rinoie, K. 1996b. ***Low Speed Aerodynamics Characteristics of 60^0 Rounded Leading-Edge Delta Wing with Vortex Flaps: Part 2 1.15m Span Delta Wing.*** Cranfield University. COA Report No. 9612.

94) Rodriguez, O. 2008. ***Chapter 20 – Experimental Investigation on the VFE-2 Configuration at ONERA, France.*** RTO-TR-AVT-113.

95) Özörem, M. & Sahin, B 2002. ***The Effect of Pitching Delta Wing on Vortex Structures with and Without Impingement Plate.*** Turkish J.Eng. Env. Sci. 26 (2002), Page 325-345.

96) Sawyers, D. 2005. ***Testing For Laminar Flow on New Aircraft.*** European Telfona Report on Aircraft Development.

97) Sarpkaya, T. 1971. ***On Stationery and travelling Vortex Breakdown***. AIAA Journal, Vol.9.

98) Schiavetta, L.A., Boelens, O.J., Crippa, S., Cummings, R.M., Fritz, W. & Badcock, K.J. 2008. ***Chapter 29 – Shock Effects on Delta Wing Vortex Breakdown.*** RTO-TR-AVT-113. Page 29-1 – 29-24.

99) Schröder, A., Agocs, J., Frahnert, H., Otter, D., Mattner, H., Kompenhans, J. & Konrath, R. 2006. ***Application of Stereo PIV to the VFE-2 65^0 Delta Wing Configuration at Sub- and Transonic Speed.*** 24^{th} Applied Aerodynamics Conference. AIAA 2006-3486.

100) Schutte, A. & Ludeke, H. 2008. ***Chapter 31 – Numerical Solutions for the VFE-2 Configuration on Unstructured Grids at DLR, Germany.*** RTO-TR-AVT-113. Page 31-1 – 31-16.

101) Spall, R.E. 1996. ***Transition from Spiral-to Bubble-type Vortex Breakdown.*** Physics Fluids 8 (5), Page 1330 – 1332.

102) Squire, L.C. 1970. The Motion of a Thin Oil Sheet under the Boundary Layer on a Body. AGARD-AG-70. Page 70-28.

103) Szodruch, J. 1978. ***Reynolds Number Influence on Leeside Flowfields***. AIAA Journal, Vol. 16, No. 12, Page 1306 – 1308.

104) 2004. ***Technology Facts: F-16 XL Supersonic Laminar Flow.*** Dryden Flight Research Center Report. TF-2004-12 DFRC.

105) Thompson, S.A. & Nelson, R.C. 1992. ***Wind Tunnel Blockage Effects on slender Wings Undergoing Large Amplitude Motion.*** 17th AIAA Aerospace Ground Testing Conference. AIAA 92-3926.

106) Tsang, K.K.Y., So, R.M.C., Leung, R.C.K. & Wang, X.Q. 2008**.** ***Dynamic Stall Behaviour from Unsteady Force Measurements.*** Journal of Fluids and Structures. Vol 24. Page 129 – 150.

107) Visbal, M. & Gordnier, R. 2003. ***On the Structure of the Shear Layer Emanating from a Swept Leading Edge at Angle-of-Attack.*** AIAA paper 2003-4016.

108) Wang, J.J. & Lu, S.F. 2005. ***Effects of Leading-Edge bevel Angle on the Aerodynamic Forces of a Non-Slender 50^0 Delta Wing.*** The Aeronautical Journal. Paper No. 2918. Page 403 - 407

109) Wang, J. & Zhan, J. 2005**.** ***New Pair of Leading-Edge Vortex Structure for Flow over Delta Wing.*** Journal of aircraft. Vol. 42. Page 718-721.

110) Wentz, W.H. & Kohlman, D.L. 1970. ***Vortex Breakdown on Slender Sharp-Edged Wings.*** Journal of Aircraft. Vol. 8. No. 3.

APPENDIX A – WING AND STING PROFILES

A1 Delta Wing and Near-Field Sting Profiles

The delta wing leading edges, trailing edge and near-field sting profiles were defined by the general equations provided by Chu & Luckring (1996). These general equations; $\varphi(\xi)$, were used to define the leading edge semi-thickness, the flat plate semi-thickness, the trailing edge closure semi-thickness and the transverse radius of the sting fairing. The availability of these equations made it relatively easy to replicate the NASA model. The equations are;

$$\varphi(\xi) = \pm x_1(a\sqrt{\xi} + b\xi + c\xi^2 + d\,\xi^3), \text{ for } 0 \leq \xi \leq 1 \quad \text{---------- (1)}$$

$$\psi(\xi) = \pm x_1[l / x_1 + m(\xi-1) + nx_1/2\,(\xi-1)^2], \text{ for } 1 \leq \xi \text{ ---------- (2)}$$

A2 Leading Edge

The leading edge region is defined as extending from the leading edge itself to 15% of span inboard, where the profile blends smoothly into the flat plate region. The longitudinal coordinates of the leading edge contour are shown in figure A.1

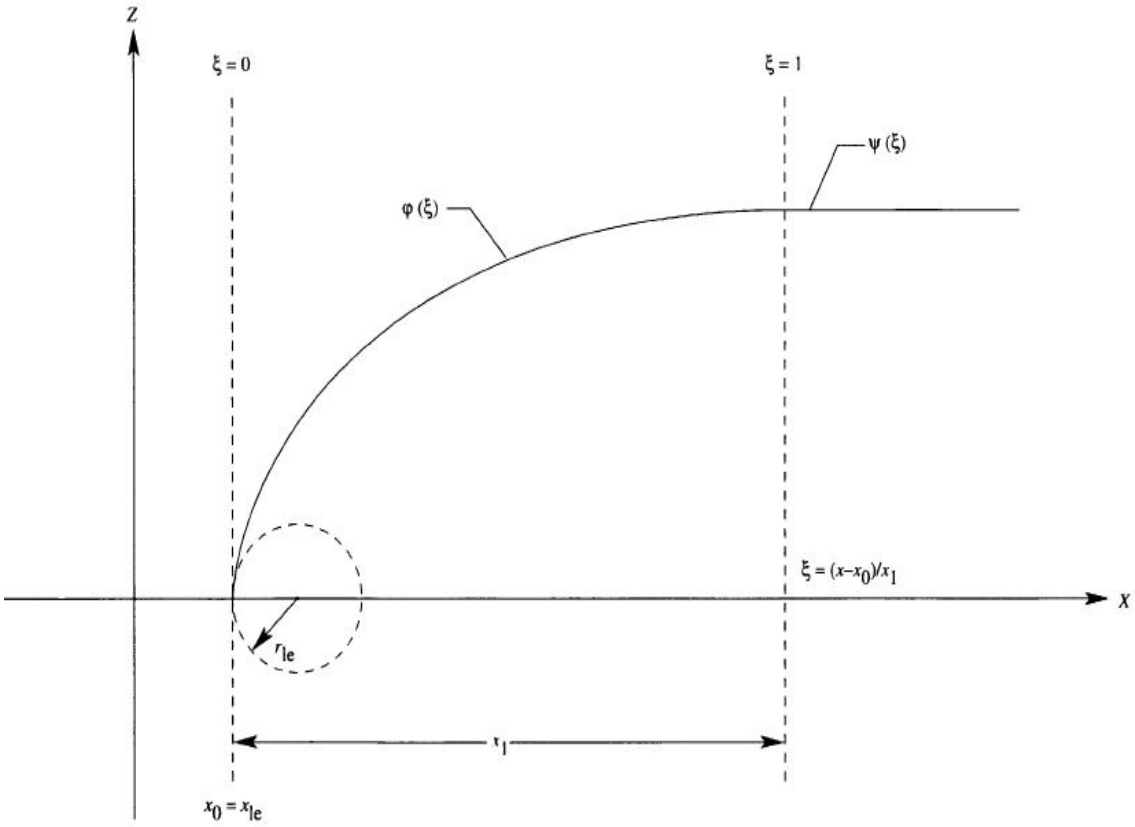

Figure A.1: Delta wing semi thickness functions [Chu & Luckring, 1996]

All four sets of leading edge profiles can be normalized using the φ (ξ) equation and the normalized coefficients (a, b, c and d) for the different sets of leading edges are given in table A.1 below. The plot of the four leading edge profiles is shown in figure A.2.

r/c, percent	a	b	c	d
0	0	3d	-b	0.113338668
0.05	0.066666667	0.215016000	-0.256682667	0.0883386669
0.15	0.11547005384	0.1235096497	-0.195678433	0.070037397
0.30	0.1632993161	0.0338297828	-0.135891855	0.0521014233

Table A.1: Leading-edge coefficients for equation (1)

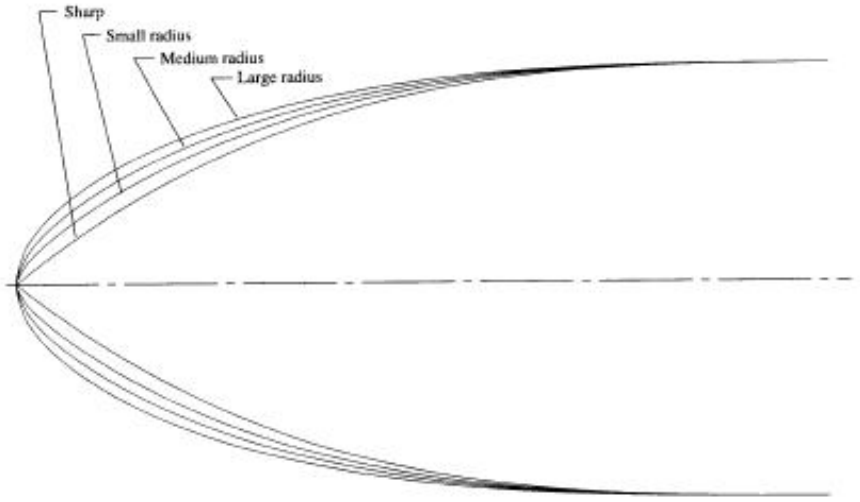

Figure A.2: A contour of leading edge profiles for all wings (Not to scale) [Chu & Luckring, 1996]

The sharp leading edge and the inner flat portion are shown in figure A.3 a) & b) respectively. All the leading edges were machined with an extra slit on the bottom surface. Several holes were drilled on the slit as shown in figure A.3 a). The leading edges were then bolted through to the inner flat portion forming a complete delta wing model as shown in figure A.3 c).

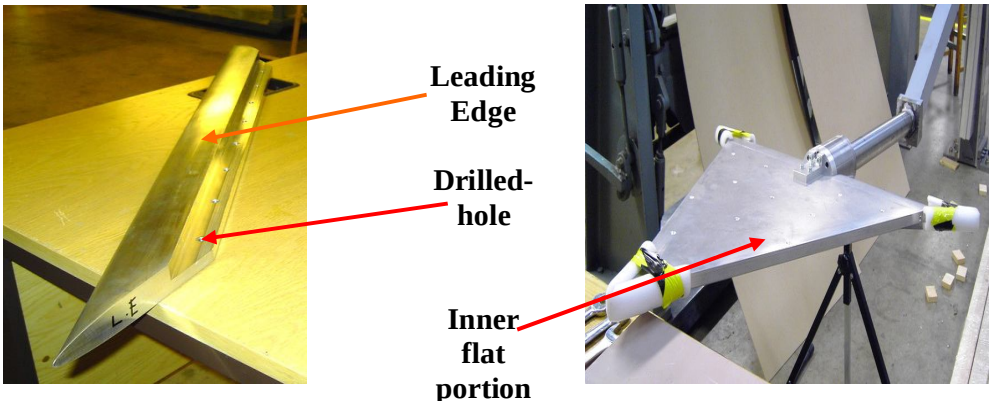

a) Leading edge b) Inner flat portion

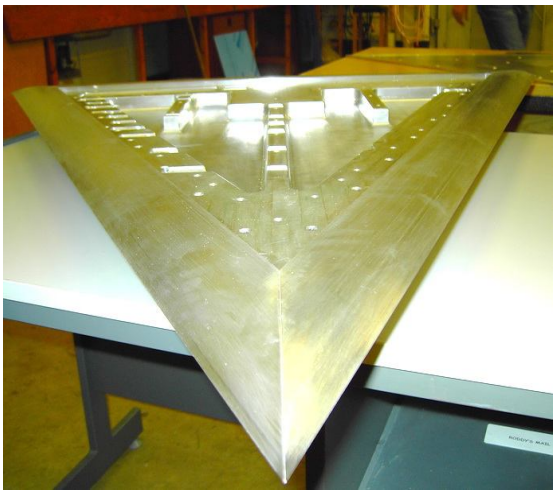

c) Leading edge attached to the flat portion

Figure A.3: Arrangement of leading edges and flat portion of the delta wing

A3 Trailing-Edge Closure Region

The trailing edge portion is designed to produce a sharp edge at the trailing edge termination point. The trailing edge curvature starts at 90% of the wing root chord where it blends smoothly into the flat plate region. The trailing-edge coefficients for equation (1) are tabulated in table A.2.

r/c, percent	a	b	c	d
0	0	3d	-b	0.170008000

Table A.2: Trailing-edge Coefficients for equation (1)

A4 Sting Fairing and Fore-Sting

The sting fairing or wing interface is designed to start at 61.05% of the root chord from the apex. The curvature of the sting fairing extends to 97.97 % of the root chord from the apex where it joins the short sting, or *fore sting*, further aft. The radius to chord ratio used to define the curvature is 0.2791026 and the coefficients for the first-blending function equation are tabulated in table A.3.

r/c, percent	a	b	c	d
0.2791026	0.100402348	0.332798228	-0.39554969	0.136033329

Table A.3: Sting fairing Coefficient for equation (1)

The sting fairing is then connected to the short-sting that extends 175.8% of the root chord downstream. The short sting (figure A.4) can be divided into four regions as shown in the figure and as defined in table A.4. Beyond region 4, the NASA sting profile was rather complicated and an analytic function for this was not provided in the report of Chu & Luckring (1996).

Region	Taper, deg	x/c_R	φ
1	0^0	From 0.9797	0.06412
		To 1.175	0.06412
2	Radius	From 1.175	0.06412
		To 1.253	0.06564
3	2.25^0	From 1.253	0.06564
		To 1.684	0.08258
4	0^0	From 1.684	0.08258
		To 1.758	0.08258

Table A.4: Short-sting transverse radius

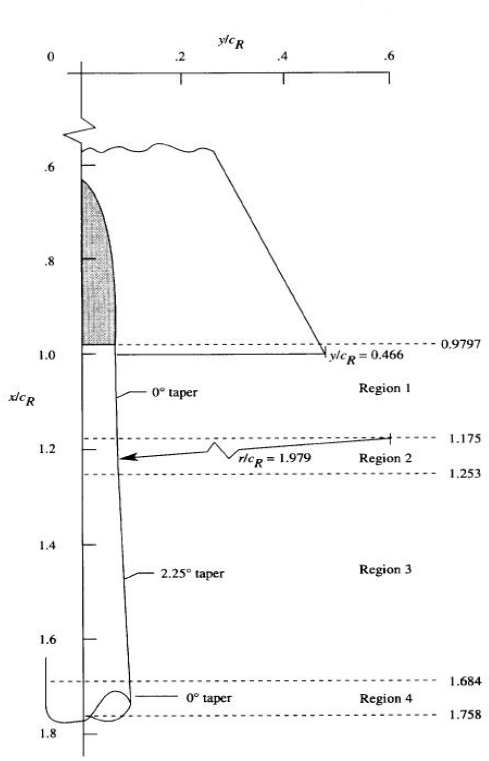

Figure A.4: Delta wing model short-sting detail [Chu & Luckring, 1996]

APPENDIX B